PhD thesis

Generation of non-classical states in a hybrid spin-optomechanical system

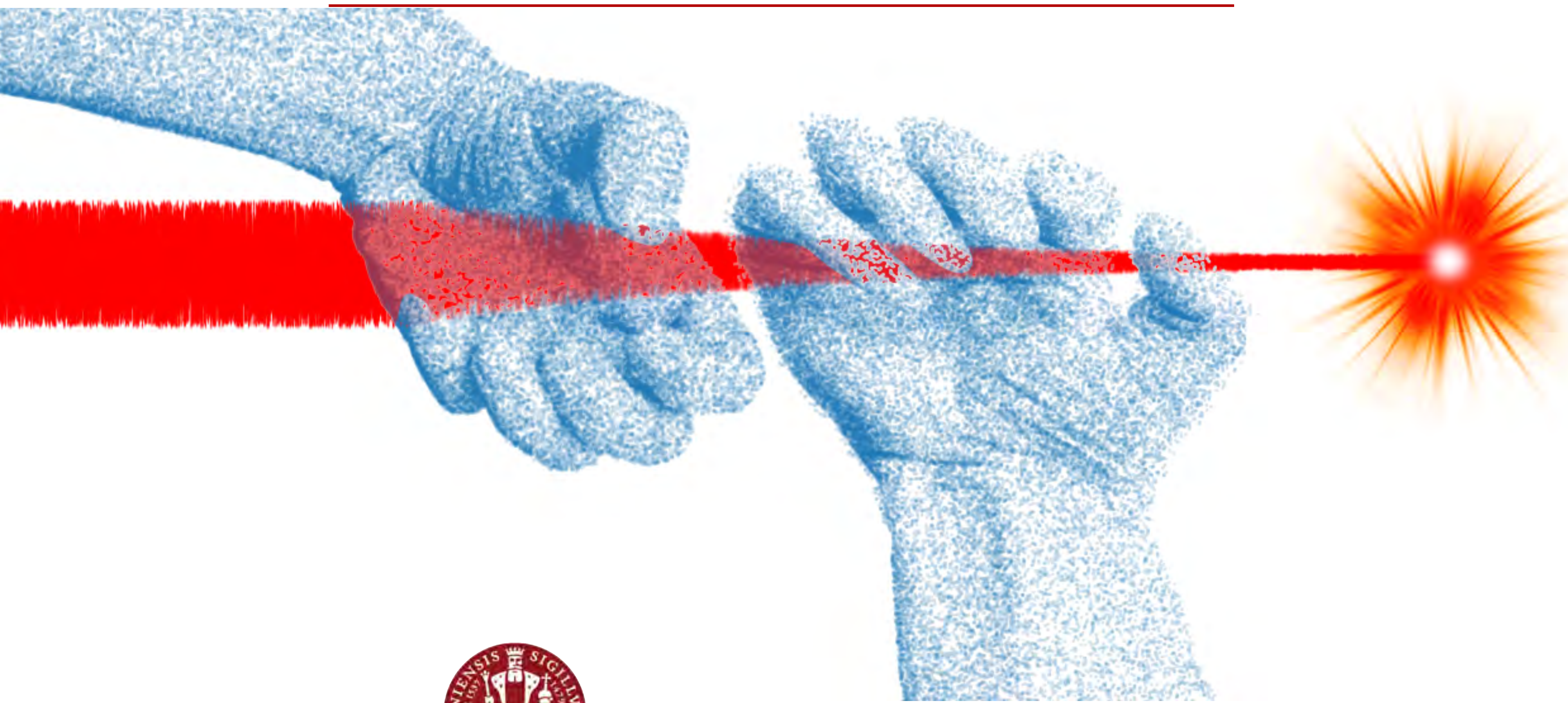

UNIVERSITY OF COPENHAGEN

Christian Folkersen Bærentsen

Generation of non-classical states in a hybrid spin-optomechanical system

Quantop
The Danish Center for Quantum Optics
The Niels Bohr Institute

This thesis has been submitted to the PhD School of
The Faculty of Science, University of Copenhagen
May 19th 2023

Author	Christian Folkersen Bærentsen
Academic supervisor	Prof. Eugene S. Polzik

Abstract

This thesis covers the generation of non-classical states in a hybrid spin-optomechanical system. The macroscopic spin oscillator comprises cesium atoms confined in a hot vapor cell of 330 K, coupling to light through the Faraday effect. The optomechanical system is a highly stressed silicon nitride membrane positioned in an optical cavity within a 4 K cryostat.

Due to quantum back-action, the parts of the hybrid system are dominated by the interaction with the probing light field. The spin system can be prepared in the highest energy state, effectively creating a negative mass oscillator. The interaction between the sub-systems mediated by the light field generates a quantum back-action evading measurement, suppressing the quantum back-action noise by 4.6 dB. This allows for an entangled link for the hybrid system, estimated by a continuous variable Einstein-Podolsky-Rosen state with a conditional variance $V_c = 0.83 \pm 0.03 < 1$, below the separability limit. This establishes a new benchmark for the achieved quantum links between hybrid quantum systems.

In addition, an enhanced coupling to the spin oscillator has been accomplished by improved motional averaging attained by spatially shaping the probe beam into a square tophat, realizing a continuous measurement of light squeezing for two advanced regimes of readout. A measurement slower than the oscillation frequency generates $11.5^{+2.5}_{-1.5}$ dB of squeezing and detects $8.5^{+0.1}_{-0.1}$ dB of squeezing, and a measurement faster than the oscillation frequency detecting 4.7 dB of squeezing spanning more than one order of magnitude below the oscillation frequency, demonstrating a new milestone for the performance of quantum sensors, which enables strong coherent coupling to other material systems.

The conceived hybrid system opens avenues for teleportation protocols in a spin-optomechanical system and quantum back-action evading measurements. Furthermore, the spin system constitutes a new regime for the performance of quantum oscillators, upholding the spin system's esteemed reputation as a quantum platform.

Sammenfatning

Denne afhandling dækker genereringen af ikke-klassiske tilstande i et hybrid spin-optomekanisk system. Oscillatoren som udgøre det makroskopiske spin består af cæsium-atomer fastholdt i en varm celle ved 330 K, som kobles til lys gennem Faraday-effekten. Den Optomekanisk membran er en højt spændt siliciumnitrid membran, som er placeret i en optisk kavitet og nedkølet i en 4 K kryostat.

På grund af kvantemekanisk tilbagevirkning domineres de hybride systemer af interaktionen med det interagerende lysfelt. Spin-systemet kan forberedes i den højeste energitilstand og skabe en negativ masse-oscillator. Interaktionen mellem under-systemerne, som er medieret af lyset, genererer en ophævende kvantemekanisk tilbagevirkning på målingen. Dette undertrykker den kvantemekaniske tilbagevirkningsstøj med 4.6 dB, hvilket tillader et sammenfiltret/entangled link til hybrid-systemet, som estimeres med en kontinuerlig variabel Einstein-Podolsky-Rosen tilstand med en betinget varians $V_c = 0.83 \pm 0.03 < 1$, som er under separationsgrænsen. Dette fastsætter en ny standard for de opnåede kvanteforbindelser mellem hybride kvantesystemer.

Derudover er en forbedret kobling til spin-oscillatoren opnået ved hjælp af en forbedret bevægende middelværdi, opnået ved rumligt at forme lysstrålen til en firkantet tophat, som realiserer en kontinuerlig måling af lys-komprimering/squeezing for to avanceret målinger af udlæsningshastigheden: En måling langsommere end oscillationsfrekvensen, hvilket genererer $11.5^{+2.5}_{-1.5}$ dB lys-komprimering og måler $8.5^{+0.1}_{-0.1}$ dB lys-komprimering, og en måling hurtigere end oscillationsfrekvensen, hvilket måler 4.7 dB lys-komprimering, som spænder mere end en størrelsesorden under oscillationsfrekvensen. Dette demonstrerer en ny milepæl for ydeevnen af kvante-sensorer, som muliggør stærk kohærent kobling til andre kvante-systemer.

Det konstruerede hybrid-system åbner muligheder for teleporteringsprotokoller i et spin-optomekanisk system og kvantemekaniske tilbagevirkningsmålinger. Desuden udgør spin-systemet en ny grænse for ydeevnen af kvanteoscillatorer og opretholder spin-systemets velrenommerede position som en kvanteplatform.

List of Publications

Peer-reviewed articles:

Rodrigo A. Thomas, Michał Parniak, Christoffer Østfeldt, Christoffer B. Møller, **Christian Bærentsen**, Yeghishe Tsaturyan, Albert Schliesser, Jürgen Appel, Emil Zeuthen, and Eugene S. Polzik. *Entanglement between distant macroscopic mechanical and spin systems.* Nature Physics. 17, 228–233 (2021).

Rodrigo A. Thomas, Christoffer Østfeldt, **Christian Bærentsen**, Michał Parniak, and Eugene S. Polzik, *Calibration of spin-light coupling by coherently induced Faraday rotation.* Optics Express 29, 23637-23653 (2021)

Manuscripts in review:

Christian Bærentsen, Sergey A. Fedorov, Christoffer Østfeldt, Mikhail V. Balabas, Emil Zeuthen, and Eugene S. Polzik *Squeezed light from an oscillator measured at the rate of oscillation.* arXiv. 2302.13633 (2023).

List of abbreviations

AOM Acousto-optic modulator.

BA Back-action noise.

BBN Broadband noise.

CIFAR Coherent induced Faraday rotation.

EPR Einstein–Podolsky–Rosen.

FFT Fast Fourier transform.

MORS Magneto-optical resonance signal.

NBN Narrowband noise.

OMIT Optomechanically-induced transparency.

PCB Printed circuit board.

PSD Power Spectral Density.

RF Radio frequency.

SLM Spatial light modulator.

SN Shot noise.

SNR Signal to noise ratio.

TH Thermal noise.

Preface

My interest in Quantum optics was sparked as an undergraduate physics student when introduced to the course Optical Physics and Lasers lectured by Eugene Polzik in 2016. I was profound by the research performed at Quantop, and I knew from this point that Quantop was meant to be a stop in my academic journey. However, the train had already left the station as I was deeply involved in the field of metrology - working on atomic clocks since I was plotting to do my specialization at l'Observatoire de Paris - PSL. Fortunately, I maintained contact with Eugene while researching in Paris, and I was offered a PhD position starting at Quantop in October 2019.

The efforts of my research presented in this dissertation are thanks to the staff at Quantop that contributes to a supportive culture where help is an unlimited resource. Therefore, I have a list of people that I would like to acknowledge.

Foremost I thank Eugene for giving me the opportunity to work under his supervision. You have always taken the time to give guidance and support when needed. When everything comes to an end, you will always stand up for your employee's well-being when a crisis hits. I experienced this when covid-19 hit since I was in a group of particular risk. No one could have given me more support than you gave, for which I am grateful beyond words.

Joining a new field of quantum physics has been challenging, especially a hybrid experiment requiring an understanding of two material systems. However, I have been surrounded by helpful colleagues who have always been willing to help. Rodrigo Thomas introduced me to the atomic part of the setup, taking me under his wing. You are always positive and inclusive. It was very tough when you left the experiment, as you were highly valued personally and professionally. Christoffer Østfeldt introduced me to the optomechanical part of the setup. I have always felt at ease with you being responsible for the optomechanics, as your work is held to a very high standard. It was only emphasized during your leave since your presence was highly missed.

Sergey Fedorov, you are the smartest and hardest-working person that I know. I have learned a lot from you, especially your trade doubting already endorsed solutions, which has changed how I approach problems. Thank you for being extremely helpful; you are an invaluable colleague.

Emil Zeuthen, you have been extremely friendly and humble. You have remarkable patience and have, in many ways, served as a mentor that has helped me grasp the physical principles. I could not have had a better person to share the office.

Michal Parniak, Ivan Galinskiy, and Jörg Helge Müller, every one of you work

as you have three full-time positions, two dedicated to helping others. You have all been incredibly helpful in assisting others, myself included. The gratitude towards you is only cemented by the fact that you are being praised in almost every PhD thesis at Quantop.

I also thank the single-photon experiment by Karsten Dideriksen, Michael Zugenmaier, and Rebecca Schmieg. You have always been willing to share knowledge and take time out of your calendar to help with work other than your own. Rebecca, we became the most senior people working with the atomic ensembles when the long-serving PhDs and postdocs left. I have enjoyed our mutual support; it has been a pleasure.

Still, there are many people at Quantop with whom I have collaborated closely; Georg Enzian, Peyman Malekzadeh, Chao Meng, Ryan Yde, Jun Jia, Tulio Brito Brasil, Valerii Novikov, Jonas Mathiassen. Thanks for everything from the help in the laboratory to the talk over the coffee machine.

Last, I thank the person who has endured the most. Camilla, I feel incredibly blessed to have you as my partner in life. These have been the most stressful years of my life for which you always supported me, living in covid isolation for almost a year without seeing your family or friends. In addition, we got our Dalmatian Lucky, we built a house from scratch, we got married, we got our daughter Magnolia, and we have a second one coming. The past three and a half years must have had more than 24 hours in a day for us to complete everything, even though the day seemed to be over before it even started. I love you.

Scope of the thesis

This thesis has been written to convey the research performed in the work of this PhD with the scientific community and the evaluation committee as the recipient. But, equally important, it is meant to preserve knowledge within the group at Quantop, especially the work presented in part II and part III, which is mainly original to this thesis; therefore, the contribution from others will be stated in these parts if it has been collaborative work.

Contents

Part I

Overview

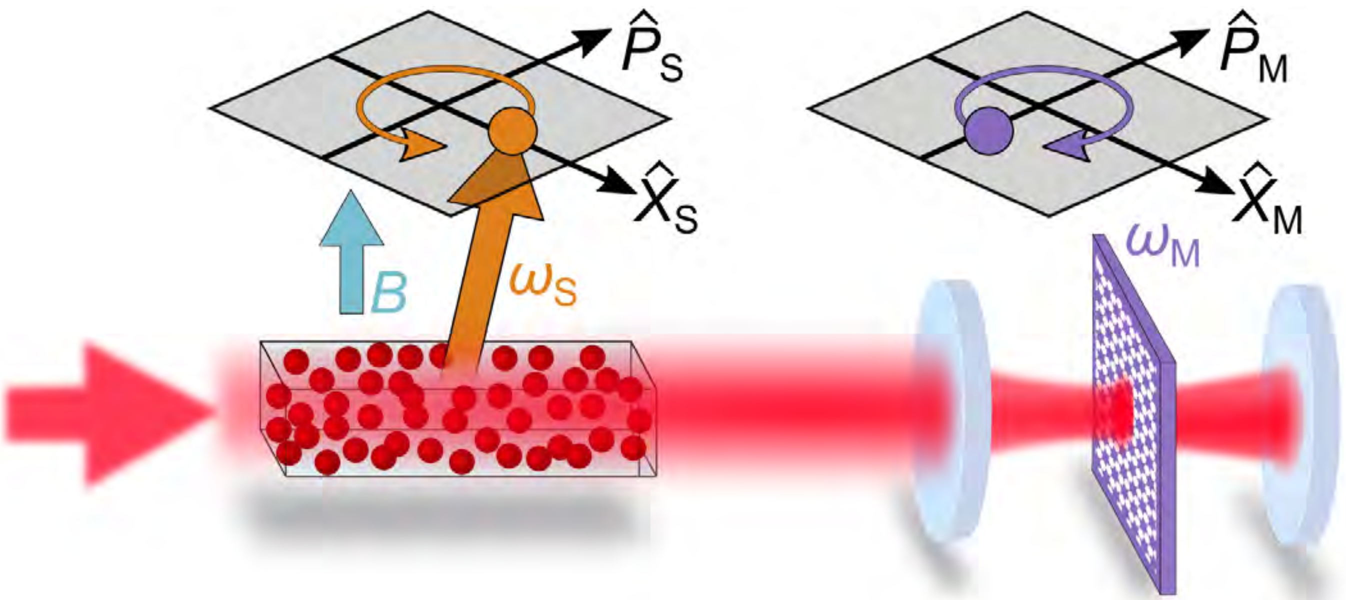

CHAPTER 1

Introduction

Why are non-classical states in a hybrid spin-optomechanical system interesting? To answer this question, we must understand a more fundamental question; why are quantum systems interesting? What makes a spin system interesting? What makes an optomechanical system interesting? And what capabilities come with the interplay between hybrid spin-optomechanical systems?

At the Niels Bohr Institute, we are currently exploring the possibilities of quantum systems, which can be traced back to the early formulation of quantum mechanics by Niels Bohr as one of its founding fathers. Quantum mechanics opened many physical possibilities, which was invalid to classical physics, most famously by Einstein, Podolsky, and Rosen in [Einstein et al., 1935], arguing that quantum mechanics must be an incomplete theory because it implied that particles at a distance could instantaneously determine the state of the other, violating the principle of locality, calling it "spooky action at a distance." Moreover, the probabilistic behavior of quantum mechanics was discomforting to Einstein, connected to his famous quote, "God does not play dice with the universe." Later, Bell proposed to test the Einstein-Podolsky-Rosen Paradox [Bell, 1964], first to be demonstrated by the violation of Bell's inequality in the Aspect's experiment [Aspect et al., 1982], notably a part of the work awarded by the recent 2022 Nobel Prize.

Quantum mechanics is already a part of our every day in the transistors of our computers, the atomic clocks taking care of our time connected to GPS devices tracking our position, the medical imaging in x-rays, MRI and PET scanners, the solar cells giving electricity, here only mentioning a small fraction of the implication that quantum mechanics has had on our lives. The effects that made Einstein uncomfortable with quantum mechanics is the foundation of quantum mechanics, making it interesting, illustrated by the capabilities to surpass classical boundaries in quantum-enhanced sensing, quantum key distribution, quantum computing, etc. We are starting to breach "the second quantum revolution" [Dowling and Milburn, 2003], referred to as the period surpassing the passive use of quantum mechanics, where it was used to understand properties of something already existing. We are starting to employ quantum mechanics actively for "the second quantum revolution" in the use of quantum dots, quantum engineered materials (phononic membranes), quantum-enhanced sensing, and the initial appearance of quantum supremacy in quantum computers [Arute et al., 2019] [Madsen et al., 2022], and so forth. The possible technologies within quantum mechanics are astronomical, with an almost continuous flow of new proposed applications [Kimble, 2008, Wehner et al., 2018].

1.1 Atomic spins

Measurements of the atomic spin state is a well-explored platform used in various metrology fields for hybrid entanglement measurements [Thomas et al., 2020], Bell-inequalities [Hensen et al., 2015], single photon sources with built in memory towards quantum repeaters [Cao et al., 2020, Dideriksen et al., 2021], magnetometers [Dang et al., 2010], quantum simulators [Ebadi et al., 2021, Bernien et al., 2017], and so forth. The measurements of atoms have evolved from having a strong coupling to single or few atoms [Kimble, 1998] and for non-classical measurement [Aspect et al., 1981] to a theoretical proposal for a weak interaction (off-resonant Faraday rotation) with large atomic ensembles [Kuzmich et al., 1997] with one of the first experimental implementations [Julsgaard et al., 2001]. The method of off-resonant Faraday rotation is less detrimental for conserving the quantum state, which can be measured in a quantum non-demolition regime that is less constrained by the unwanted perturbations that often follow with resonant probing [Kuzmich et al., 1998].

The energies of a spin ensemble are quantized to the Zeeman levels set by the magnetic field, evolving the system at the Larmor precession, meaning that the system is sensitive to magnetic perturbations, consequently making spin ensembles an esteemed platform for quantum-enhanced magnetometry [Dang et al., 2010, Wasilewski et al., 2010]. The interaction of light with a large ensemble of atomic spins through the Faraday rotation is a popular choice due to the quantum non-demolition alike measurements, along with a long memory time [Kozhekin et al., 2000, Julsgaard et al., 2004], in addition to the properties of a negative mass for the spin ensembles [Julsgaard et al., 2001]. This thesis utilizes a hot paraffin-coated cesium vapor cell for the spin system described in chapter 2.

1.2 Mechanical resonators

Optomechanical phenomena were observed long before the birth of quantum mechanics. Kepler discovered radiation pressure by noticing that the comets' tails point away from the sun [Kepler, 1619]. The optomechanical coupling first got a renewed interest for optical interferometry measurements for gravitational wave sensing, with the first theoretical proposal of radiation-induced ponderomotive forces on mechanical object [Braginsky and Manukin, 1967], later to be experimentally verified [Braginskiǐ et al., 1970], formalizing the theoretical concept of quantum non-demolition measurements [Braginsky et al., 1980], and experimental ground state cooling of a mechanical object [Chan et al., 2011].

The field of quantum optomechanics enables quantum-enhanced force and positional sensing. It has been shown to produce ultra-coherent quantum oscillators [Tsaturyan et al., 2017] that can be utilized as long-lived quantum memories.

This thesis utilizes cavity optomechanics [Aspelmeyer et al., 2014] to position a mechanical membrane in the-middle design outlined in chapter 3.

1.3 Hybrid spin-optomechanics

Quantum links between hybrid systems aim at combining the advantages of different material systems [Kurizki et al., 2015]. This includes systems of large coherence, like phononic membranes, for memory and systems easily manipulated, like superconducting qubits, for quantum computing, to get a more robust and versatile quantum system. More specifically to the material systems of this thesis, teleportation between spin and optomechanical systems would open the possibility of teleporting an engineered quantum state on the mechanical system, enabling new tests of fundamental physics, enhanced force sensing, long-lived quantum memory, and the transduction of quantum signals between the optical and microwave domains [Wehner et al., 2018].

A hybrid spin-optomechanical system might even solve the problem that the field of optomechanics originated from - enhancing the sensitivity of gravitational wave detectors, which is limited by quantum back-action arising from the light-driven measurements of suspended mirrors. The measurement of quantum back-action can be evaded using a negative-mass spin system [Zeuthen et al., 2019, Khalili and Polzik, 2018], thereby enhancing the sensitivity of gravitational wave detection. The path towards such enhancement has been recently demonstrated in a proof-of-the-principle experiment using a spin ensemble and an optomechanical cavity [Møller et al., 2017].

This thesis focuses on developing the spin ensemble for the hybrid spin-optomechanical system. The thesis structure is the following:

In part I, we give an overview of the material systems, describing the spin system for the relevant dynamics when interacting with light, and an outline of the optomechanical system introducing the mechanical behavior in the interface of light.

In part II, we demonstrate our most treasured characterization methods for the atomic spin ensemble: magneto-optical resonance signal and coherent induced Faraday rotation. Additionally, we investigate the procedure of preparing the spin ensemble in the ground state.

In part III, we introduce the concept of motional averaging with related challenges to overcome for improving the homogeneity of the magnetic field that determines the Larmor precession generated by a new coil design and a reduction of fast-decaying modes from an inhomogeneous atomic probing through the generation of a square tophat beam. We complete the topic on motional averaging by simulating the presented effects for different regimes to better understand the limitations in measurements of our spin ensemble.

In part IV, we are laying out the phenomena of spin-induced light squeezing for different measurement regimes, showcasing state of the art spin induced light squeezing and measurement rates larger than the Larmor precession, demonstrating the culmination of advancements for the spin ensemble.

In part V, we outline the hybrid spin-optomechanical system for generating a conditional entanglement, creating an Einstein-Podolsky-Rosen state [Einstein et al., 1935] with a variance below the inseparability limit, declaring the first entanglement generation between a spin ensemble and a mechanical resonator. Finally, to establish a new direction for our hybrid system in the quest to demonstrate quantum teleportation between a spin ensemble and a mechanical resonator.

In part VI, we summarize the results of this thesis, centered on the results of spin-induced light squeezing and entanglement generation. In the outlook, we discuss the new opportunities in hybrid spin-optomechanical systems opened by the experimental advances.

CHAPTER 2

Macroscopic spin systems of cesium atoms

This chapter serves the purpose of describing the macroscopic atomic spin system of cesium atoms. It describes the platform of cesium atoms confined in a glass cell that was perfected in the group of my supervisor Eugene Polzik over the last two decades. Much of the theory and methodology that are presented overlap with the great work of Brian Julsgaard [Julsgaard, 2003], as the theory of polarized spin ensembles that we present still provides a comprehensive description of the dynamics that we observe experimentally. Together with this, we have adopted a more convenient basis for the quadratures of the light introduced by [Thomas, 2020].

The following chapter lays out the theory needed to understand the atomic spin system, which is the quantum oscillator of primary focus in this thesis. This provides theoretical references for the experimental chapters, as most experimental techniques probe the same underlying physics.

2.1 Atomic spin state of cesium

Cesium-133 is a widely used isotope in metrology. In particular, the second is defined as the hyperfine splitting for $(6^2\mathrm{S}_{1/2}, F = 3) \rightarrow (6^2\mathrm{S}_{1/2}, F = 4)$ of cesium oscillating at 9 192 631 770 Hz [Newell and Tiesinga, 2019]. Cesium-133 is the only stable isotope of cesium, which makes the most sense for optical purposes since it is the only cesium species found naturally with almost $\approx 100\%$ abundance. Moreover, it is easy to achieve a high vapor density for cesium at temperatures around room temperature due to its low melting point at $28.4\,°\mathrm{C}$ [Steck, 1998]. Another advantage of cesium is the wide availability of lasers for the wavelength of the D_1 line $(6^2\mathrm{S}_{1/2} \rightarrow 6^2\mathrm{P}_{1/2})$ and the D_2 line $(6^2\mathrm{S}_{1/2} \rightarrow 6^2\mathrm{P}_{3/2})$ at $894\,\mathrm{nm}$ and $852\,\mathrm{nm}$, respectively. The relevant level scheme for this can be seen in figure 2.1. We are interested in the atoms populated in $6^2\mathrm{S}_{1/2}, F = 4$ for one of the outermost m_F levels for this work, which is treated as our ground state. The repump laser transfers atoms from $F = 3 \rightarrow F = 4$ by shining σ-light from $F = 3$ to the frequency midpoint between $F' = 2$ and $F' = 3$. All the allowed transitions:

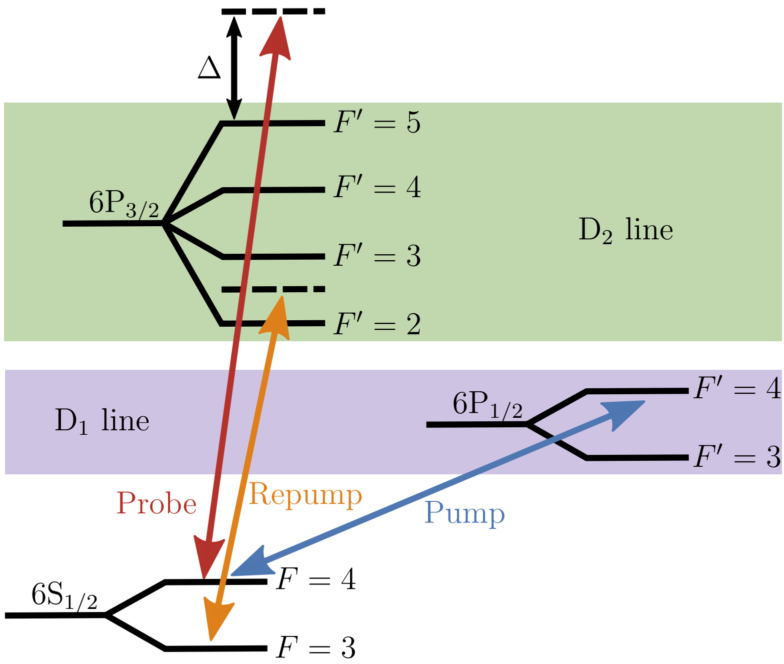

Figure 2.1: Cesium hyperfine transitions for the D_1 line and D_2 line. The repump is stabilized in between $F = 3 \rightarrow F' = 2, 3$ on the D_2 line at a wavelength of 852 nm, the pump is stabilized from $F = 4 \rightarrow F' = 4$ on the D_1 at a wavelength of 894 nm and the probe is detuned to $F = 4 \rightarrow F' = 5$ for the D_2 line. A positive detuning Δ corresponds to a higher laser frequency of the probe laser to the transition frequency ($F = 4 \rightarrow F' = 5$).

$F' = 2$, $F' = 3$ and $F' = 4$ are within the Doppler width of the repump for cesium atoms at room temperature[1]. It is, therefore, not easy to see the logic behind this non-trivial choice of repumping as it has shown empirically to be the best (see chapter 5 for further explanation). The pump laser transfers atoms to the outermost m_F level by shining σ-polarized light resonant with the transition $F = 4 \rightarrow F' = 4$. This creates a dark state in the outermost m_F level, increasing the populations in the extreme projections of the spin. The pumping beam can have disadvantages compared to the repump since it pumps directly on the ground state, significantly broadening the probed transitions.

The sign of the circularity of light being σ^- or σ^+ is either populating $m_F = -4$ or $m_F = 4$, respectively. This determines the sign of the effective mass of the oscillator, where atoms pumped towards $m_F = -4$ result in a positive mass oscillator and atoms pumped towards $m_F = 4$ result in a negative mass oscillator (the negative mass reference frame is explained in the following section 2.1.1).

The probe beam is tuned off-resonance. Usually, 3 GHz blue detuned to the $F = 4 \rightarrow F' = 5$ transition. This is because we are interested in a weak interaction without absorption(losses), so we can have a nondestructive measurement of the spin state of the cesium atoms through the interaction of the Faraday rotation.

[1]The Doppler width for atoms at room temperature on the D_2 line: $\Delta\nu_{\mathrm{FWHM}} \approx 375\,\mathrm{MHz}$. The relevant hyperfine splittings for $6^2P_{3/2}$: $\nu_{F'=2\leftrightarrow F'=3} = 151\,\mathrm{MHz}$, $\nu_{F'=3\leftrightarrow F'=4} = 201\,\mathrm{MHz}$ [Steck, 1998].

2.1.1 Effective negative mass oscillator

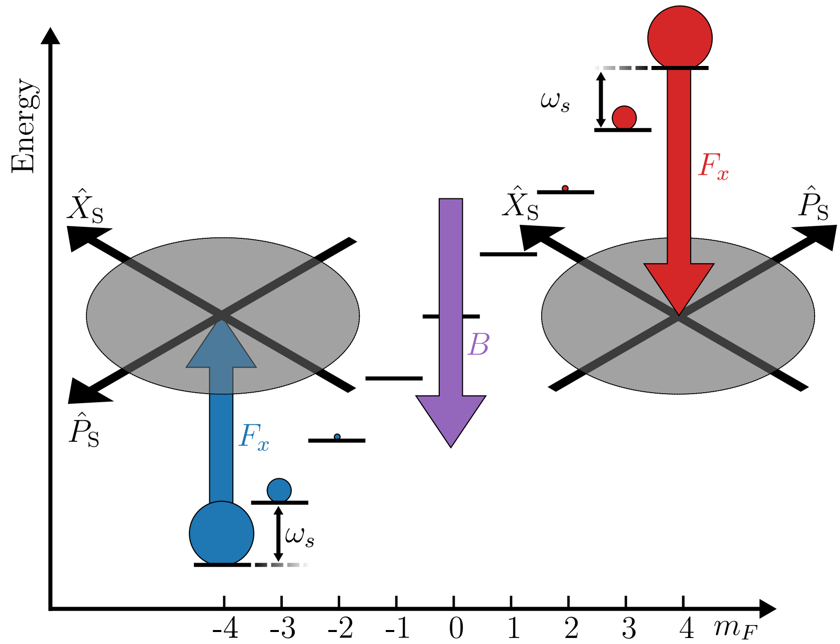

Figure 2.2: Illustration of the an effective negative mass oscillator. The blue spin vector illustrates an atomic ensemble pumped to the lowest energy state in $m_F = -4$, referred to as an effective positive mass oscillator. The red spin vector illustrates an atomic ensemble pumped to the highest energy state in $m_F = 4$, referred to as an effective negative mass oscillator. $\hat{X}_S$ and $\hat{P}_S$ are the canonical observables (see equation 2.4 for definition) and B is the magnetic field.

The atomic spin state can realize an effective negative-mass oscillator. However, an oscillator with effective negative mass can be also looked at as an oscillator with negative resonance frequency, which is often more convenient in theoretical calculations. This is interesting because the sign change of light-spin induced force, quantum back-action, that can be canceled when interacting with other material systems. This opens the possibility for measurements free of noise contributions arising from the quantum back-action [Polzik and Hammerer, 2015].

An illustration of the negative-mass oscillator is shown in figure 2.2. The oscillator in the negative(positive) mass reference frame is in the highest(lowest) energy state, where the magnetic field is parallel(anti-parallel) oriented to the mean spin F_x in red(blue). The atoms are pumped to the outermost m_F level, which is the corresponding ground state of the system. The usual description of a system in the ground state is the lowest energy state, where excitations increase the oscillator energy. The atoms have a finite number of excited levels, in contrast to a mechanical membrane with infinite levels, which makes it possible for an atomic ensemble to be prepared in the highest-energy state. Therefore, an excitation of the system lowers the energy of the system. Manipulating our system to treat the highest energy state as our prepared ground state changes the coupling between the oscillator and the light. The oscillator frequency changes sign, giving an opposite response for the susceptibilities.

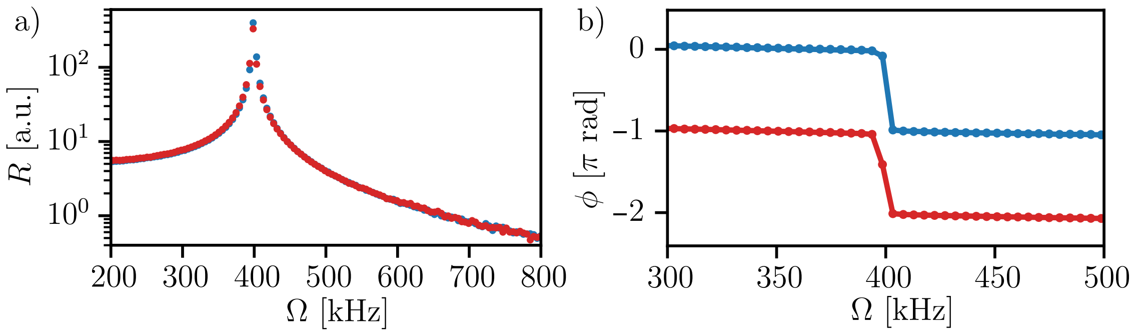

Figure 2.3: Driven measurement of the spin ensemble prepared as a positive and negative mass oscillator. The positive and negative mass is represented in blue and red, respectively. a) the amplitude response is identical in an ideal situation. b) the phase of the response has a π phase shift due to the sign change of the mass. The figure has been reproduced from [Thomas, 2020].

A measurement of a negative and positive mass oscillator can be seen in figure 2.3. The measurement of the amplitude response is unaltered from the mass change between the positive and negative mass, shown in figure a). The phase response of the oscillator is changed by π at all frequencies when changing the mass of the oscillator, shown in figure b). This means that the oscillator response is exactly the opposite when changing the oscillator's mass.

2.1.2 Cesium in a vapor cell

We want to have the cesium atoms encapsulated as we need a way to confine the cesium vapor to measure its spin state. Furthermore, we want to have an encapsulation that reinforces the ability to prepare our system in a quantum state without decaying, as well as the ability to read the quantum state out. Here is a listing of the characteristics that are desirable for our encapsulated spin system but also most other similar quantum systems:

1. Preparation of atoms in the ground state.
2. Low decay rate such the quantum state can be maintained (long memory).
3. A strong collective interaction with light - high optical depth.
4. Readout of quantum state with low optical losses.

The 1st point involves the ability to access the atomic ensemble with a beam of pure polarization for the repump and pump light with either σ_+ or σ_- polarization. This is achieved by choosing a square channel to host the atomic ensemble. This can be seen in figure 2.4, where a small channel is shown in the center of the chip. The cell is made of Borofloat, which is very transparent at the wavelengths of the D_1 and D_2 lines of cesium. The square channel geometry does not create any lensing effects, unlike a circular channel that would change the angle of light rays with respect to the magnetic field. It is essential to keep a clean polarization and parallelism of pumping beams to the magnetic field, as this controls the repumping and pumping

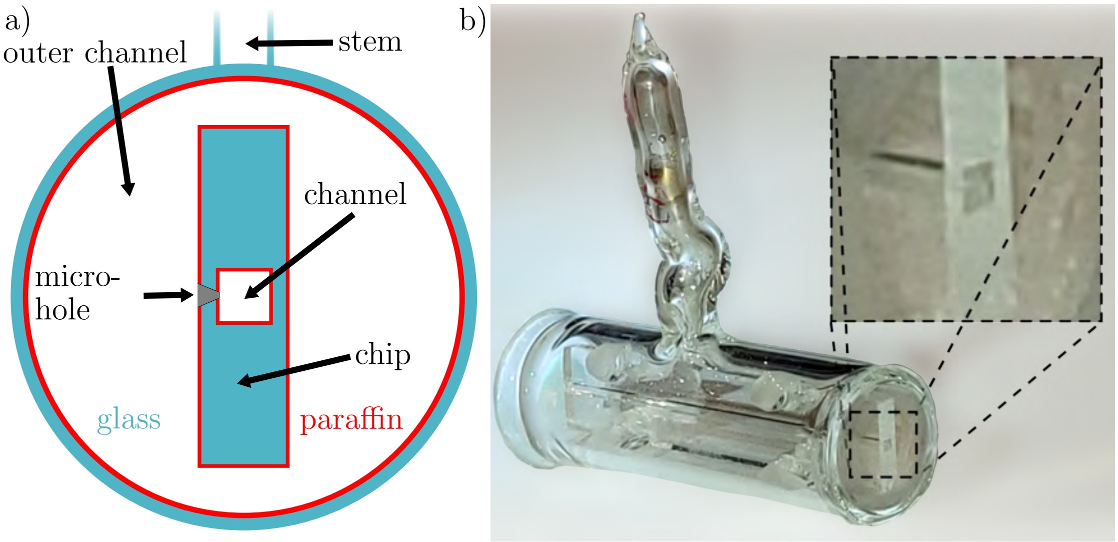

Figure 2.4: Cesium captured in a glass cell. a) The geometry of the cesium vapor cell. The glass is made of Borofloat and coated with paraffin as a spin anti-relaxation coating. The input and output windows are coated with anti-reflection coatings for 852 nm. b) A picture of our latest generation cell with a geometry of 1 mm × 1 mm × 40 mm.

rates. The outer channel has a round encapsulation, which is for convenience of the fabrication. The lensing effects can also be accounted for more easily because of the larger radius of curvature of the outer channel. The encapsulation of the outer channel has a diameter of 25.4 mm. The (inner) channel varies in size depending on the needed characteristics of the cell, the optimization of which is a complex topic that is covered in part III: Experimental realizations and simulations of motional averaging in a hot vapor cell. In the latest generation, the channel cross-section size varies from 0.5 mm by 0.5 mm to 5 mm by 5 mm.

The 2nd point on the list is the decay of the atomic state. It is critical for treating a spin ensemble as a collective oscillator that atoms are indistinguishable with regards to interaction with light, therefore it is important that the decay rate is slower than the motional averaging of light. The primary decay rate of a spin state when encapsulating an alkali specie in a glass channel is the wall collisions since the decay rate goes as $\frac{\gamma_S}{2\pi} = 1/\tau$, where τ is the average transit time across the channel. The transit time is $\tau \approx 7\ \mu$s for a square channel with a side length of 1 mm. A memory time equal to the transit time gives a decay rate of $\frac{\gamma_S}{2\pi} \approx 0.14$ MHz, which is unacceptably short in the regime that we are working in where a longer memory time is desirable. Memory time can be vastly improved by introducing a paraffin coating to the atomic cell. It covers the cell surfaces as illustrated by the red lines in figure 2.4a. The paraffin coating protects the spin coherence, so the spin coherence lasts $\sim 10^4$ wall collision before decaying, bringing the memory time from a few microseconds to a few tenths of milliseconds [Corsini et al., 2013, Balabas et al., 2010]. The paraffin used in this work is C30, which is paraffin containing 30 carbon atoms, having shown the best experimental results.

The 3rd point is the requirement of a large number of atoms for the interaction. The cell is designed with a storage of cesium atoms confined in the stem, seen in figure 2.4b by the brown color of the stem (the glass finger sticking up from the glass cylinder). The stem functions as a reservoir of cesium atoms that releases them to supply the inner channel with new cesium atoms. A small hole named the micro-hole has been made to create a small bridge between the outer and the inner channel for the cesium atoms to pass. The micro-hole is either a small drilled hole into the chip or a scratch on the surface between the chip and the window enclosing cell ends. The number of cesium atoms in the channel can then be controlled by raising the cell temperature such that the cesium in the stem vaporizes. The temperature is limited by the reaction of paraffin to raised temperature, where it starts to clump at high temperatures. This problem starts to be pronounced above a temperature of 50 °C, and temperatures never exceed 60 °C during measurements to protect the cells. The cells have at times exceeded a temperature of 60 °C in the process of curing the cell, which is the process of restoring the cell that is explained in appendix B. The last requirement for achieving a large atomic number is to have elongated cells along the probing direction. This enhances the interaction between light and the spin as it enhances the optical depth of the measurement (see chapter 6 for the measurement of the readout rate).

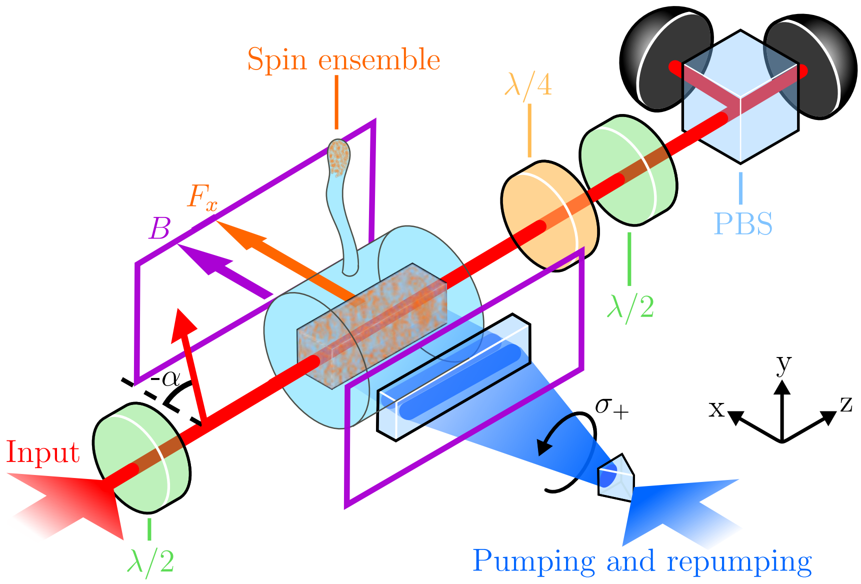

Figure 2.5: Optical setup for spin preparation and readout. The atomic ensemble is prepared in a homogeneous magnetic field, B, along the x-axis, where it is pumped and repumped into $F = 4, m_F = 4$ with σ_+ light. A linearly polarized beam with an angle α to the mean spin, F_x, probes the atomic ensemble. The beam quadratures of light are measured with homodyne detection that reuses the virtually unaltered local oscillator for detection. The phase angle of the homodyne detection is adjusted with a combination of $\lambda/4$ and $\lambda/2$ plates.

The 4th point is the ability to produce atomic cells with a high transmission. The chip is compressed between two windows to stay fixated inside the glass cylinder (outer channel). These windows are coated with anti-reflection (AR) coating optimized for the D_2 line at 852 nm. The highest observed transmission is 98% for this type of cell, but it usually ranges within $91 - 98\%$. The main reason for a decreased transmission is the collection of paraffin spots on the windows, resulting in light scattering. This is also one of the main reasons why the cells need to be cured since it releases paraffin spots from the windows[2].

The atomic cell in a simple optical setup for preparation and readout is shown in figure 2.5. The setup shows a cell placed in a homogeneous magnetic field along the x-axis, where it is pumped and repumped with a beam that is traveling parallel to the B-field with σ_+ light to prepare the ensemble in $m_F = 4$. The total mean spin is parallel to the magnetic field setting the quantization axis of the experiment. The input light is linearly polarized and can be tuned by a $\lambda/2$ waveplate with the input polarization angle denoted as α. The input light is then probing the atomic ensemble, where the state of the atomic spin is read out into the quadratures of light. The light is at last measured in a homodyne configuration.

The homodyne configuration of this experimental setup benefits from the local oscillator that probes the system since it is virtually unaltered in transmission. The interaction between light and spin is imprinted into orthogonal polarizations of light. Waveplates differ in phase delay depending on the quantization axis of the input polarization. This means that the light phase can be adjusted between the polarizations of light; here, the local oscillator and the quadratures of interest. Two waveplates are placed so the homodyne detection phase can be tuned with a $\lambda/4$ waveplate, and the balancing between the two detectors with a $\lambda/2$ waveplate.

2.2 Spin and light interactions

We want to describe the theory behind a collective atomic spin in an external bias magnetic field. The atoms are weakly probed by a far-detuned optical light field, where the interaction of interest is due to the polarization-dependent AC Stark shifts of the sub-m_F levels. The reader should consider the atomic system presented previously in this chapter.

The atoms are described by the spin operators $\{\hat{F}_x, \hat{F}_y, \hat{F}_z, \hat{F}_0\}$[3], and the light is described by the Stokes operators $\{\hat{S}_x, \hat{S}_y, \hat{S}_z, \hat{S}_0\}$. The spin operator is an operator for the collective macroscopic spin $\hat{F}_{x,y,z} = \sum_{i=1}^{N} \hat{F}^{(i)}_{x,y,z}$ with N ranging from 10^7 to 10^{11} depending on the cell geometry and the vapor pressure. $\hat{F}^{(i)}_{x,y,z}$ is the total angular momentum projection quantum number for a single atom.

We want to begin describing the full model by first taking our standpoint in the Hamiltonian for a single atom placed in a bias magnetic field oriented along

[2]The atomic cells have been fabricated by Mikhail V. Balabas using glass blowing techniques.

[3]The notation in this group (Quantop) has historically been using $\hat{J}$ as the spin operator, which is not to be confused with the quantization of the spin and orbital angular momentum. $\hat{F}$ is, therefore, a more appropriate operator as it includes the nuclear spin to describe the hyperfine splitting.

the x-direction[4]:

$$\begin{aligned}\hat{H}_{\mathrm{S}}/\hbar = \pm\,\omega_{\mathrm{S}}\hat{F}_x^{(i)} + g_{\mathrm{S}}\Bigg[& a_0\hat{S}_0 + a_1\hat{S}_z\hat{F}_z^{(i)} + \\ & 2a_2\Big[\hat{S}_0(\hat{F}_z^{(i)})^2 - \hat{S}_x((\hat{F}_x^{(i)})^2 - (\hat{F}_y^{(i)})^2) - \hat{S}_y(\hat{F}_x^{(i)}\hat{F}_y^{(i)} + \hat{F}_y^{(i)}\hat{F}_x^{(i)})\Big]\Bigg],\end{aligned} \tag{2.1}$$

with the angular frequency of the spin precession, ω_{S}, determined by the Zeeman splitting between the adjacent m_F levels, where the sign denotes the positive or negative spin orientation to the magnetic field. This is referred to as the positive and negative mass of the oscillator because it mathematically resembles a negative mass by having a mean spin vector oppositely orientated to the bias magnetic field. Next, g_{S} is the single-photon coupling rate:

$$g_{\mathrm{S}} = -\frac{c\gamma_{\mathrm{cs}}\lambda_{\mathrm{cs}}^2}{16\pi A\Delta} \quad \text{if } |\Delta| \gg \gamma_{\mathrm{cs}}, \tag{2.2}$$

where c is the speed of light, $\gamma_{\mathrm{cs}}/(2\pi) = 5.22\,\mathrm{MHz}$ is the natural linewidth, λ_{cs} is the wavelength, Δ is the detuning to the optical transition, and A is the cross-section area of the ensemble.

We have three coefficients in equation 2.1 that we refer to as the scalar, vector, and tensor contributions arising from a_0, a_1 and a_2, respectively [Deutsch and Jessen, 2010]. The three coefficients can be calculated from the Clebsch–Gordan coefficients for a given atomic level and the individual laser detuning to the atomic transitions[5], and the result is

$$\begin{aligned} a_0(\Delta) &= \frac{1}{4}\left(\frac{1}{1+\Delta_{35}/\Delta} + \frac{7}{1+\Delta_{45}/\Delta} + 8\right) \xrightarrow[\Delta\to\pm\infty]{} 4, \\ a_1(\Delta) &= \frac{1}{120}\left(-\frac{35}{1+\Delta_{35}/\Delta} - \frac{21}{1+\Delta_{45}/\Delta} + 176\right) \xrightarrow[\Delta\to\pm\infty]{} 1, \\ a_2(\Delta) &= \frac{1}{240}\left(\frac{5}{1+\Delta_{35}/\Delta} - \frac{21}{1+\Delta_{45}/\Delta} + 16\right) \xrightarrow[\Delta\to\pm\infty]{} 0, \end{aligned} \tag{2.3}$$

where Δ_{35} is the detuning between $F' = 3$ and $F' = 5$ in $6^2\mathrm{P}_{3/2}$, and Δ_{45} is the detuning between $F' = 4$ and $F' = 5$ in $6^2\mathrm{P}_{3/2}$[6].

The terms proportional to a_1 give rise to a vectorial rotation between two polarization states resulting in a circular birefringence for the probe light, and the quantum back-action noise acting on the spin oscillator. The terms involving a_2 also affect the probe light similarly to a_1 inducing a tensorial rotation between all three polarization states due to the linear birefringence from a_2. The interaction type coming from a_2 results in dynamical back-action amplifying or dampening the oscillator.

[4]The derivation for this Hamiltonian can be found in [Julsgaard, 2003].

[5]The complete calculation for the three a-coefficients can be found in [Julsgaard, 2003], where the a-coefficients for atoms prepared in $F = 3$ also can be found.

[6]The relevant frequencies: $\Delta_{35}/2\pi = 452.24$ MHz and $\Delta_{45}/2\pi = 251.09$ MHz [Steck, 1998].

We want to understand the contributions associated with the tensor contribution (a_2) since some terms can be neglected when describing the evolution of the spin. We are only interested in the frequency components oscillating at ω_S. We follow the derivations and arguments in section 6.4 of [Julsgaard, 2003] to understand the arising effects coming from the tensor contributions in the Hamiltonian equation 2.1:

- Let us look at the first two terms of the tensor contribution: $\hat{S}_0(\hat{F}_z^{(i)})^2$ and $\hat{S}_x((\hat{F}_x^{(i)})^2 - (\hat{F}_y^{(i)})^2)$. These terms can be rewritten into identity matrices when approximating a spin-$\frac{1}{2}$ system for the polarized ensemble (see equation A.2 for details). The identity matrices only contribute to a frequency shift of the oscillator, which results in a higher order AC Stark shift changing the energy splitting between the sub-m_F levels.
- The last term in the tensor contribution: $(-\hat{S}_y(\hat{F}_x^{(i)}\hat{F}_y^{(i)} + \hat{F}_y^{(i)}\hat{F}_x^{(i)}))$ can be rewritten into $-(2m+1)\hat{S}_y\hat{F}_y$ (see equation A.1 and A.2 for details). This gives rise to a rotation of the quadratures that we refer to as the tensor interaction term. It later appears in the normalized form as $\zeta_S\hat{P}_S\hat{P}_L$ in the normalized Hamiltonian for the collective spin (see equation 2.12).

The Holstein-Primakoff approximation can be applied for a collective spin, normalized to the mean angular momentum F_x, because we map the mean spin to bosonic ladder operators $\hat{F}_x = F_x - \hat{b}^\dagger\hat{b}/2$ [Holstein and Primakoff, 1940]. A visual illustration of the Holstein-Primakoff approximation is shown in figure 2.6, where the change of F_x is negligible[7] in the regime: $\langle\hat{F}_y\rangle, \langle\hat{F}_z\rangle \ll F_x$. The illustration shows a mapping of the quadratures onto a 2-dimensional plane instead of a sphere because of the large length differences between the directions of angular momentum.

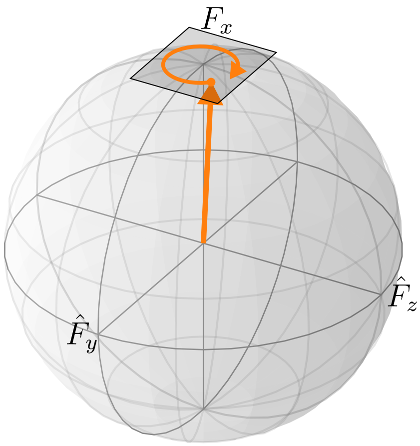

Figure 2.6: Illustration of the effect of the Holstein-Primakoff approximation on the Bloch sphere. F_x is independent of the excursions in F_y and F_z for the Holstein-Primakoff approximation.

The Hamiltonian can be simplified by linearizing the spin and light operators. The atomic ensemble is prepared in the ground state such the steady-state spin is

[7] It is essential to note that this approximation may not be valid in case of large $\hat{F}_y$ or $\hat{F}_z$, resulting in a small spin polarization.

$F_x = |\langle \hat{F}_x \rangle|$. We assume small fluctuations from the mean spin in the transverse spin components: $\langle \hat{F}_y \rangle, \langle \hat{F}_z \rangle \ll F_x$. The spin quadratures and their commutation relation are defined as

$$\hat{X}_{\mathrm{S}} = \hat{F}_z / \sqrt{|F_x|}, \tag{2.4}$$

$$\hat{P}_{\mathrm{S}} = -\operatorname{sgn}(F_x) \hat{F}_y / \sqrt{|F_x|}, \tag{2.5}$$

$$[\hat{X}_{\mathrm{S}}, \hat{P}_{\mathrm{S}}] = i. \tag{2.6}$$

There is a need for a change of basis for the Stokes vectors to simplify the scenario of a rotated input polarization of the light field. We want to define our basis such that the strong linear field of our probe is the classical mean photon flux: $\langle \hat{S}_{\|} \rangle = \langle \hat{S}_0 \rangle = S_{\|}$ with quantum variables being the orthogonal zero-mean variables: $\hat{S}_{\perp}$ and $\hat{S}_z$. The rotation of the basis can be written as

$$\hat{S}_{\|} = \hat{S}_x \cos 2\alpha - \hat{S}_y \sin 2\alpha, \tag{2.7}$$

$$\hat{S}_{\perp} = \hat{S}_x \sin 2\alpha + \hat{S}_y \cos 2\alpha, \tag{2.8}$$

where $\hat{S}_z$ and $\hat{S}_0$ are unaffected by the rotation, and α is the angle to the mean spin F_x that has been previously depicted in figure 2.5. The light quadratures and their commutation relation can then be defined from the above basis change:

$$\hat{X}_{\mathrm{L}} = \hat{S}_z / \sqrt{|S_{\|}|}, \tag{2.9}$$

$$\hat{P}_{\mathrm{L}} = -\hat{S}_{\perp} / \sqrt{|S_{\|}|}, \tag{2.10}$$

$$[\hat{X}_{\mathrm{L}}, \hat{P}_{\mathrm{L}}] = (i/2)\delta(t - t'). \tag{2.11}$$

Following the Hamiltonian in equation 2.1 for a single atom, where the above quadrature basis is used to rewrite the Hamiltonian for a collective spin:

$$\hat{H}_{\mathrm{S}}/\hbar = \mp \frac{\omega_{\mathrm{S}}}{2}(\hat{X}_{\mathrm{S}}^2 + \hat{P}_{\mathrm{S}}^2) - 2\sqrt{\Gamma_{\mathrm{S}}}(\hat{X}_{\mathrm{S}}\hat{X}_{\mathrm{L}} \mp \zeta_{\mathrm{S}}\hat{P}_{\mathrm{S}}\hat{P}_{\mathrm{L}}). \tag{2.12}$$

We have neglected a term in the Hamiltonian $-2\sqrt{\Gamma_{\mathrm{S}}}\zeta_{\mathrm{S}} \tan(2\alpha)\hat{S}_{\|}/\sqrt{|S_{\|}|}\hat{P}_{\mathrm{S}}$ since the contribution from this term has negligible effects for our working regime. It is only important when having laser amplitude noise at the oscillation frequency, ω_{S}, for which it drives $\hat{X}_{\mathrm{S}}$. In such a case, the transduction of amplitude noise can be avoided by choosing a linear polarization of the probe along x or y, where the term is zeroed[8]. The readout rate (Γ_{S}) and the tensor interaction coefficient (ζ_{S}) are defined as

$$\Gamma_{\mathrm{S}} = g_{\mathrm{S}}^2 a_1^2 S_{\|} F_x, \tag{2.13}$$

$$\zeta_{\mathrm{S}} = -14\frac{a_2}{a_1} \cos\ 2\alpha. \tag{2.14}$$

[8] We are operating with a titanium-sapphire laser(MSquared SolsTiS 7W-SRX-F) in our experiment. It is pumped with low power of 2 W to have the relaxation oscillations of the laser at 300 kHz, so we have shot noise limited measurements from around 1 MHz [Østfeldt, 2022].

The readout rate, Γ_S, characterizes the ability to measure the atomic state via Faraday interaction, as well as it determines the strength of the quantum back-action of such a measurement. The tensor interaction coefficient, ζ_S, describes the ratio between the linear birefringence (dynamical back-action) to the circular birefringence (quantum back-action) type of interactions. The tensor interaction also determines the asymmetry in the creation of Stokes and anti-Stokes photons by scattering from probe beam[9]. The tensor interaction is maximized at $\alpha = n\pi/2,\ n \in \mathbb{Z}$ because the tensor effect arises from the Larmor-induced oscillation in $\hat{S}_y$. These are maximized when $\hat{S}_y$ is orthogonal or parallel to the classical drive, which follows from the defined basis in equation 2.8. The strength of the tensor interaction is different for an imperfectly polarized ensemble, where the tensor interaction for the other m_F levels has a scaling following

$$\zeta_\mathrm{S}(m) = \zeta_{\mathrm{S},m=-4} \cdot (2m+1)/7. \tag{2.15}$$

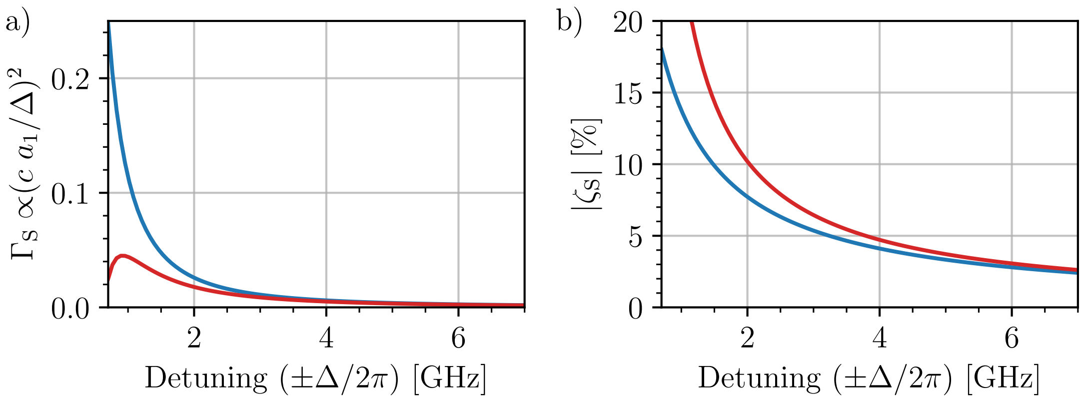

Figure 2.7: Readout rate and tensor interaction dependency on the detuning. Blue and red colors denote a positive and negative detuning, respectively. A positive detuning corresponds to higher laser frequency compared to the transition $F = 4 \to F' = 5$. a) shows the detuning dependency of the vector coefficient responsible for the readout rate Γ_S. b) shows the detuning dependency of the tensor interaction in the outermost m_F level. Note that the sign of the tensor can easily be flipped accordingly to equation 2.14.

Γ_S and ζ_S depend on $a_1(\Delta)$ and $a_2(\Delta)$. This means that the readout rate and tensor terms can be changed by tuning the probe laser with respect to the $F = 4 \to F' = 5$ transition. We mostly work far from resonance, where the atomic absorption is low with respect to the coupling since the absorption falls off as $1/\Delta^2$ and the coupling as $g_\mathrm{S} \propto 1/\Delta$. The full dependency of the readout rate on the detuning can be seen in figure 2.7. We have mostly been working at $\Delta/2\pi = 3\,\mathrm{GHz}$ blue detuned in this work, where the probe-induced decay is low compared to the readout[10]. Most of our experiments have also favored having a low

[9] This process creates the two interaction types that are known as entanglement generation (Stokes) and beam-splitter interaction (anti-Stokes) that are used in quantum protocols.

[10] This is conditioned on a high resonant optical depth for our measurements.

tensor interaction coefficient, as the tensor creates couplings between the P and X quadrature as well as coupling between m_F sublevels adding more complexity to the model.

2.2.1 Frequency of the spin precession

The spin precession, denoted as ω_S, arises from the torque imposed on the atomic angular moment by the bias magnetic field. This phenomenon is understood well both theoretically and experimentally [Steck, 1998], especially for the historical reason that the hyperfine splitting of cesium is used in the definition of the unit of time. This section explains the phenomena behind the observed spin precession with the underlying physics behind the equations further explained in [Julsgaard, 2003].

We want to express the energy splitting between subsequent m_F levels. The first effect to consider, and the main contributor to the Larmor frequency, is the weak field Zeeman effect, also known as the Larmor precession, which is a linear energy shift between the energy levels:

$$\frac{\omega_\mathrm{Z}}{2\pi} = \frac{g_F \mu_\mathrm{B} B}{h} = \gamma_e B, \tag{2.16}$$

where g_F is the hyperfine Landé g-factor, μ_B is the Bohr magneton, h is plack constant and B is the magnetic field. γ_e is called the gyromagnetic ratio with the size of $350.5\,\mathrm{kHz/G}$ for $F = 4$. We often work in the regime $1 - 2\,\mathrm{MHz}$, meaning that a field of $3 - 6$ Gauss is applied to the atomic ensemble. The gyromagnetic ratio for $F = 3$ is $-351.6\,\mathrm{kHz/G}$, which is essential to note as the interaction with the atoms left in $F = 3$ is visible at Larmor frequencies $3 - 6\,\mathrm{kHz}$ above the frequencies of interest for $F = 4$.

The second contribution affection the Larmor frequency is the quadratic Zeeman splitting that scales quadratically with the strength of B-field:

$$\frac{\omega_\mathrm{QZ}}{2\pi} = -\frac{\omega_\mathrm{Z}^2}{2\pi\omega_\mathrm{HFS}}, \tag{2.17}$$

where ω_HFS is the hyperfine splitting between $F = 3$ and $F = 4$ with the value of $\omega_\mathrm{HFS}/2\pi \approx 9.193\,\mathrm{GHz}$[11]. The quadratic Larmor frequency scales according to the projection of the spin, which means that the transitions between neighboring m_F levels have different Larmor frequencies

$$\omega_\mathrm{S}(m) = \omega_\mathrm{Z} + m\omega_\mathrm{QZ}. \tag{2.18}$$

An illustration of the resulting level splitting described by equation 2.18 can be seen in figure 2.8. The gray dashed lines are the energy levels without quadratic energy shift, and the red solid lines are the energy levels with quadratic energy shift. The 9 energy levels give rise to the 8 transitions that we observe experimentally.

The quadratic effects become significant for an imperfectly polarized ensemble as they can be used to separate the frequencies of different m_F levels. However, it can also be the case that these quadratic splittings are unwanted as the total

[11]It is the hyperfine transition of cesium that is used to define the second as an exact frequency at 9.192 631 770 GHz [Steck, 1998].

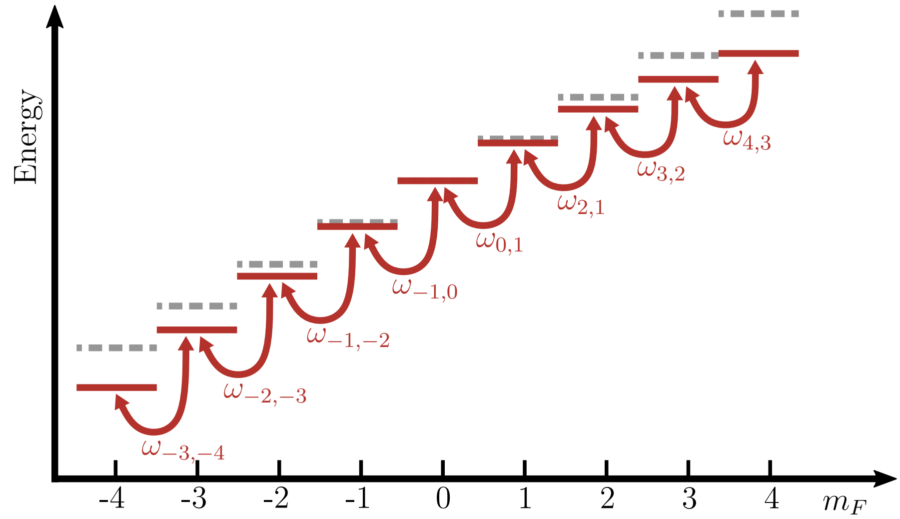

Figure 2.8: Illustration of splittings between atomic levels. Energy levels for the different m_F levels in $F = 4$. The dashed gray lines are the energy levels only accounting for the linear shift. The solid red lines are the full energy splitting accounting for quadratic effects. Linear and quadratic splittings are not to scale for illustrative purposes.

interaction between all m_F levels is favorable. Figure 2.9 shows the effect of the quadratic splitting on the spectrum. The red curve shows a spectrum for which the resonance frequency is 1.3 MHz with a quadratic Zeeman splitting of $\omega_{\mathrm{QZ}} \approx 370\,\mathrm{Hz}$, where all the transitions can be distinguished from each other. The blue curve shows a response without a quadratic splitting of the levels, where all the transitions contribute constructively to the signal. This configuration cannot distinguish the levels, enhancing the overall resonance signal strength.

We want to be able to control the quadratic splitting between m_F levels. This is briefly mentioned in section 2.2 when discussing the effects arising from terms proportional to a_2 for the Hamiltonian in equation 2.1. Some terms give rise to polarization-dependent identity operators equivalent to energy shifts. These shifts are higher-order AC Stark shifts that we refer to as the tensor Stark shift

$$\frac{\omega_{\mathrm{TSS}}}{2\pi} = \frac{\gamma_{\mathrm{cs}}\lambda_{\mathrm{cs}}^3}{32\pi^3 hc} \cdot \frac{a_2(\Delta)}{\Delta} \cdot \frac{P}{A} \cdot (1 + 3\cos(2\alpha)). \tag{2.19}$$

The tensor Stark shift can be tuned by the laser power P, the polarization angle of the input light α, or by the detuning Δ. This is one of the most commonly used formulas for sanity checks as it can estimate α and the detuning dependent parameters for calculating ζ_{S}. It is, therefore, convenient to have the numbers written up for the scaling of terms in equation 2.19: $\frac{\gamma_{\mathrm{cs}}\lambda_{\mathrm{cs}}^3}{32\pi^3 hc} = 6.47 \cdot 10^{11}$ [Hz $\cdot$ rad $\cdot$ $\mathrm{m}^2/(\mathrm{W} \cdot \mathrm{s})$][12]. We are often working at the same detuning at $\Delta/2\pi = 3\,\mathrm{GHz}$, therefore, giving the detuning dependent scaling for a detuning of 3 GHz: $\frac{a_2(\Delta)}{\Delta} = 2.14 \cdot 10^{-13}$ [s/rad)]. The tensor Stark shift can be zeroed for an angle

[12]The confusing units only emphasize the importance between angular frequencies and frequencies. Δ needs to be given in angular frequencies to have the result, $\frac{\omega_{\mathrm{TSS}}}{2\pi}$, as a frequency.

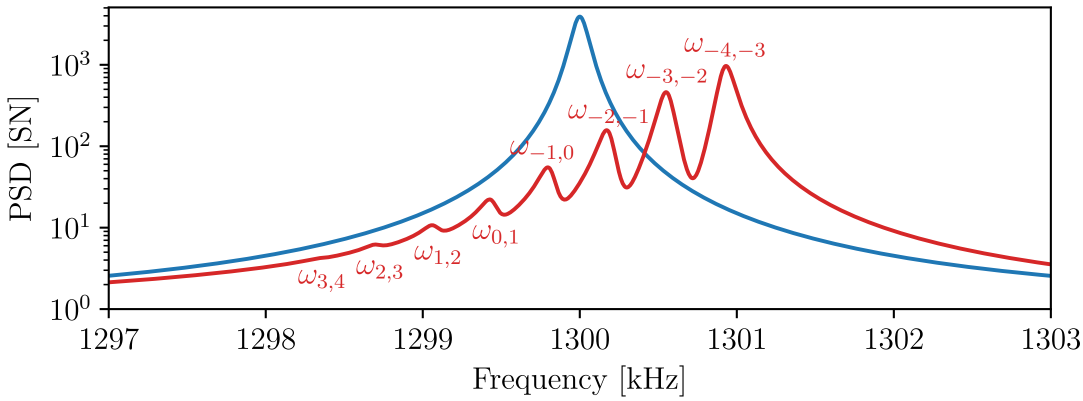

Figure 2.9: Impact on the power spectral density for a quadratic energy splitting. Atoms prepared in a thermal distribution with a spin polarization of $p = 85\%$ (see chapter 5 for the definition of the spin polarization) for both red and blue. The red curve has a quadratic splitting of 370 Hz, and the blue curve is without a quadratic splitting.

of $\alpha = 54.7°$. The tensor Stark shift only takes a negative value for $-1 > 3\cos(2\alpha)$, which is the regime that cancels the quadratic Zeeman splitting. ζ_S also has a dependency on $\cos(2\alpha)$ (see equation 2.14), meaning that the optimum in polarization angle depends on the requirements of the experiment. It is only for a pulsed experiment, where a pin polarization close to perfect can be achieved (see chapter 5 for ground state preparation), for which quadratic frequency effects do not have to be considered.

2.2.2 Input-output relations

The time evolution of the quadratures can be calculated from the Hamiltonian in equation 2.12 in the Heisenberg picture. The time evolution for a negative mass oscillator can be written as

$$\begin{aligned} \frac{\mathrm{d}}{\mathrm{d}t}\begin{pmatrix}\hat{X}_\mathrm{S}\\ \hat{P}_\mathrm{S}\end{pmatrix} &= \begin{pmatrix}-\gamma_{\mathrm{S}0}/2-\zeta_\mathrm{S}\Gamma_\mathrm{S} & \omega_\mathrm{S}\\ -\omega_\mathrm{S} & -\gamma_{\mathrm{S}0}/2-\zeta_\mathrm{S}\Gamma_\mathrm{S}\end{pmatrix}\begin{pmatrix}\hat{X}_\mathrm{S}\\ \hat{P}_\mathrm{S}\end{pmatrix} \\ &+ 2\sqrt{\Gamma_\mathrm{S}}\begin{pmatrix}0 & -\zeta_\mathrm{S}\\ 1 & 0\end{pmatrix}\begin{pmatrix}\hat{X}_\mathrm{L}\\ \hat{P}_\mathrm{L}\end{pmatrix} + \begin{pmatrix}\hat{F}_\mathrm{S}^X\\ \hat{F}_\mathrm{S}^P\end{pmatrix}, \end{aligned} \tag{2.20}$$

where $\hat{F}_\mathrm{S}^X$ and $\hat{F}_\mathrm{S}^P$ are the effective Langevin forces, and $\gamma_{\mathrm{S}0}$ is the decay rate of spin including broadening effects. We are interested in the solution for the differential equation to get the steady state solution for the quadratures of light in the frequency space.

We use the Fourier transform: $\{\mathcal{F}(\frac{\mathrm{d}}{\mathrm{d}t}\hat{X}_\mathrm{S}) = -i\omega\hat{X}_\mathrm{S},\ \mathcal{F}(\frac{\mathrm{d}}{\mathrm{d}t}\hat{P}_\mathrm{S}) = -i\omega\hat{P}_\mathrm{S}\}$. The atoms are experiencing motional averaging for interaction with light, which comes from the coherence of the atoms being much larger than the timescale for motionally coupling through the light beam. This means we can treat the light field that the atoms are experiencing as an average of the light operators. Therefore, we can write the solution for the atomic spin in the frequency space as

$$\begin{pmatrix}\hat{X}_\mathrm{S}\\ \hat{P}_\mathrm{S}\end{pmatrix} = 2\sqrt{\Gamma_\mathrm{S}}\mathbf{L}\mathbf{Z}\begin{pmatrix}\hat{X}_\mathrm{L}^\mathrm{in}\\ \hat{P}_\mathrm{L}^\mathrm{in}\end{pmatrix} + \mathbf{L}\begin{pmatrix}\hat{F}_\mathrm{S}^X\\ \hat{F}_\mathrm{S}^P\end{pmatrix}. \tag{2.21}$$

The light interacting with the oscillator results in the output field:

$$\begin{pmatrix}\hat{X}_\mathrm{L}^\mathrm{out}\\ \hat{P}_\mathrm{L}^\mathrm{out}\end{pmatrix} = \begin{pmatrix}\hat{X}_\mathrm{L}^\mathrm{in}\\ \hat{P}_\mathrm{L}^\mathrm{in}\end{pmatrix} + \sqrt{\Gamma_\mathrm{S}}\mathbf{Z}\begin{pmatrix}\hat{X}_\mathrm{S}\\ \hat{P}_\mathrm{S}\end{pmatrix}, \tag{2.22}$$

where the matrices in the equations are defined as

$$\mathbf{Z} = \begin{pmatrix}0 & -\zeta_\mathrm{S}\\ 1 & 0\end{pmatrix}, \tag{2.23}$$

$$\mathbf{L} = \begin{pmatrix}\gamma_\mathrm{S0}/2+\zeta_\mathrm{S}\Gamma_\mathrm{S}-i\omega & \omega_\mathrm{S}\\ -\omega_\mathrm{S} & \gamma_\mathrm{S0}/2+\zeta_\mathrm{S}\Gamma_\mathrm{S}-i\omega\end{pmatrix}^{-1} = \begin{pmatrix}\rho_\mathrm{S}(\Omega) & \chi_\mathrm{S}(\Omega)\\ -\chi_\mathrm{S}(\Omega) & \rho_\mathrm{S}(\Omega)\end{pmatrix}. \tag{2.24}$$

The spin susceptibilities χ_S and ρ_S are defined as

$$\chi_\mathrm{S}(\Omega) = \frac{\omega_\mathrm{S}}{\omega_\mathrm{S}^2-\Omega^2-i\Omega(\gamma_\mathrm{S0}+2\Gamma_\mathrm{S}\zeta_\mathrm{S})+(\gamma_\mathrm{S0}+2\Gamma_\mathrm{S}\zeta_\mathrm{S})^2/4}, \tag{2.25}$$

$$\rho_\mathrm{S}(\Omega) = \frac{(\gamma_\mathrm{S0}+2\Gamma_\mathrm{S}\zeta_\mathrm{S})/2-i\Omega}{\omega_\mathrm{S}^2-\Omega^2-i\Omega(\gamma_\mathrm{S0}+2\Gamma_\mathrm{S}\zeta_\mathrm{S})+(\gamma_\mathrm{S0}+2\Gamma_\mathrm{S}\zeta_\mathrm{S})^2/4}. \tag{2.26}$$

The entity; $\gamma_\mathrm{S} = \gamma_\mathrm{S0} + 2\Gamma_\mathrm{S}\zeta_\mathrm{S}$, is the full linewidth accounting for the dynamical broadening ($2\Gamma_\mathrm{S}\zeta_\mathrm{S}$) due to the tensor effect. Combining the solutions in equations 2.21 and 2.22 to write the solution for the output light field quadratures:

$$\begin{aligned}\begin{pmatrix}\hat{X}_\mathrm{L}^\mathrm{out}\\ \hat{P}_\mathrm{L}^\mathrm{out}\end{pmatrix} =& \left[\mathbf{1}_2 + 2\Gamma_\mathrm{S}\mathbf{ZLZ}\right]\begin{pmatrix}\hat{X}_\mathrm{L}^\mathrm{in}\\ \hat{P}_\mathrm{L}^\mathrm{in}\end{pmatrix} + \sqrt{\Gamma_\mathrm{S}}\mathbf{ZL}\begin{pmatrix}\hat{F}_\mathrm{S}^X\\ \hat{F}_\mathrm{S}^P\end{pmatrix}\begin{pmatrix}\hat{X}_\mathrm{L}^\mathrm{out}\\ \hat{P}_\mathrm{L}^\mathrm{out}\end{pmatrix}\\ =&\left[\mathbf{1}_2 + 2\Gamma_\mathrm{S}\begin{pmatrix}-\zeta_\mathrm{S}\rho_\mathrm{S} & -\zeta_\mathrm{S}^2\chi_\mathrm{S}\\ \chi_\mathrm{S} & -\zeta_\mathrm{S}\rho_\mathrm{S}\end{pmatrix}\right]\begin{pmatrix}\hat{X}_\mathrm{L}^\mathrm{in}\\ \hat{P}_\mathrm{L}^\mathrm{in}\end{pmatrix}\\ &+\sqrt{\Gamma_\mathrm{S}}\begin{pmatrix}\zeta_\mathrm{S}\chi_\mathrm{S} & -\zeta_\mathrm{S}\rho_\mathrm{S}\\ \rho_\mathrm{S} & \chi_\mathrm{S}\end{pmatrix}\begin{pmatrix}\hat{F}_\mathrm{S}^X\\ \hat{F}_\mathrm{S}^P\end{pmatrix}.\end{aligned} \tag{2.27}$$

We can rotate the detected quadratures by adding waveplate(s) after the atomic cell. This works similarly to having a local oscillator in a Mach–Zehnder interferometer, where one path is changed by ΔL, which results in a change of homodyne phase $\Delta\phi$. The local oscillator, $S_\parallel$, propagates through the atomic ensemble in a polarization mode that does not interact with the spins. The waveplate(s) introduce a phase change between $S_\parallel$ and the orthogonal polarization quadratures that change the homodyne phase. This can be expressed with a rotation matrix $\mathbf{M}_\phi$:

$$\begin{pmatrix}\hat{X}_\mathrm{L}^\mathrm{det}\\ \hat{P}_\mathrm{L}^\mathrm{det}\end{pmatrix} = \mathbf{M}_\phi\begin{pmatrix}\hat{X}_\mathrm{L}^\mathrm{out}\\ \hat{P}_\mathrm{L}^\mathrm{out}\end{pmatrix} = \begin{pmatrix}\cos(\phi)\hat{X}_\mathrm{L}^\mathrm{out} - \sin(\phi)\hat{P}_\mathrm{L}^\mathrm{out}\\ \sin(\phi)\hat{X}_\mathrm{L}^\mathrm{out} + \cos(\phi)\hat{P}_\mathrm{L}^\mathrm{out}\end{pmatrix}, \tag{2.28}$$

$$\mathbf{M}_\phi = \begin{pmatrix} \cos(\phi) & -\sin(\phi) \\ \sin(\phi) & \cos(\phi) \end{pmatrix}. \tag{2.29}$$

We can then take $\hat{P}_{\mathrm{L}}^{\mathrm{det}}$ as our detected quadrature (for the case of non-squeezed input quadratures) for calculating the power spectral density (PSD):

$$\overline{S}_{\mathrm{PP}}^{\mathrm{det}}(\Omega) = \tfrac{1}{2}\langle \hat{P}_{\mathrm{L}}^{\mathrm{det}}(\Omega)\hat{P}_{\mathrm{L}}^{\mathrm{det},\dagger}(\Omega) + \hat{P}_{\mathrm{L}}^{\mathrm{det},*}(\Omega)\hat{P}_{\mathrm{L}}^{\mathrm{det},\intercal}(\Omega)\rangle. \tag{2.30}$$

We can calculate from the above equation the spectral contributions for the input quadratures of the light, calculated from the commutation relation of the light in equation 2.11:

$$\overline{S}_{\mathrm{PP}}(\Omega)\delta(\Omega-\Omega') = \tfrac{1}{4}\delta(\Omega-\Omega'), \tag{2.31}$$

and the spectral contributions for the thermal bath of the spin, $F_{\mathrm{S}}(\Omega)$, calculated from the commutation relation of the spin in equation 2.6:

$$\overline{S}_{\mathrm{FF}}(\Omega)\delta(\Omega-\Omega') = \gamma_{\mathrm{S0}}(n_{\mathrm{S}}+\tfrac{1}{2})\delta(\Omega-\Omega'). \tag{2.32}$$

The introduced variable, n_{S}, is the mean number of thermal excitation, experimentally often conceived below 1 ($n_{\mathrm{S}} < 1$). The number of thermal excitations is not directly related to the number of atoms in the ensemble as the number of atoms is incorporated into the definition of the readout rate, see equation 2.13, in the form of the length of the spin F_x. The number of thermal excitations can be calculated from the distribution of atoms from the relation:

$$n_{\mathrm{S}} = \frac{N_m}{N_{m+1}-N_m}, \tag{2.33}$$

where N_m is the number of atoms in a given m_F level. The theory behind measuring and calculating n_{S} is derived in section 5.1.5. The factor $\frac{1}{2}$ added to the thermal excitation in equation 2.32 is the ground state noise, often called the projection noise.

We can use the expressions in 2.30 and 2.31 to write the full model for a spin oscillator

$$S_{\mathrm{PP}}^{\mathrm{det}}/SN = \overbrace{\left|\sin(\phi)(1-2\Gamma_{\mathrm{S}}\zeta_{\mathrm{S}}\rho_{\mathrm{S}})+\cos(\phi)2\Gamma_{\mathrm{S}}\chi_{\mathrm{S}}\right|^2+\left|\cos(\phi)(1-2\Gamma_{\mathrm{S}}\zeta_{\mathrm{S}}\rho_{\mathrm{S}})-\sin(\phi)2\Gamma_{\mathrm{S}}\zeta_{\mathrm{S}}^2\chi_{\mathrm{S}}\right|^2}^{\mathrm{BA+SN}} \\ \underbrace{+\,4\gamma_{\mathrm{S0}}\Gamma_{\mathrm{S}}\left(|\rho_{\mathrm{S}}|^2+|\chi_{\mathrm{S}}|^2\right)\left(n_{\mathrm{S}}+\tfrac{1}{2}\right)\left(\cos^2(\phi)+\sin^2(\phi)\zeta_{\mathrm{S}}^2\right)}_{\mathrm{TH}}. \tag{2.34}$$

The spectral density in the model is normalized to the shot noise (SN), where the brackets help to identify the shot noise, the quantum back-action noise (BA), and thermal noise (TH). The full model can be hard to comprehend at first glance without taking parameters in certain limits to simplify the model.

We want to take the following limit of $\gamma_{\mathrm{S}} \ll \omega_{\mathrm{S}}$ and the limit of measuring close to resonance ($\Omega \sim \omega_{\mathrm{S}}$). This makes the following approximation true for the susceptibilities:

$$\begin{aligned} \chi_{\mathrm{S}}(\Omega) &\approx \frac{1}{2}\frac{1}{\omega_{\mathrm{S}} - \Omega - i\gamma_S/2}, \\ \rho_{\mathrm{S}}(\Omega) &\approx -i\chi_{\mathrm{S}}(\Omega). \end{aligned} \tag{2.35}$$

We refer to the above expression for the susceptibilities as the near resonance limit.

There is no readout into the X quadrature of light in the case of no dynamical back-action ($\zeta_{\mathrm{S}} = 0$). This is clear from equation 2.27, where the following is true $\hat{X}_{\mathrm{L}}^{\mathrm{out}} = \hat{X}_{\mathrm{L}}^{\mathrm{in}}$ for $\zeta_{\mathrm{S}} = 0$. Looking at the PSD of light when measured at $\phi = 0$ is a measurement of the P quadrature of light:

$$S_{\mathrm{PP}}^{\mathrm{det}}/SN(\phi \to 0^\circ) = 1 + \overbrace{4|\chi_{\mathrm{S}}(\Omega)|^2\Gamma_{\mathrm{S}}^2}^{\mathrm{BA}} + \overbrace{4\gamma_{\mathrm{S0}}\Gamma_S(|\rho_{\mathrm{S}}(\Omega)|^2 + |\chi_{\mathrm{S}}(\Omega)|^2)\Big(n_{\mathrm{S}} + \tfrac{1}{2}\Big)}^{\mathrm{TH}}. \tag{2.36}$$

The terms arising from the ζ_{S} in equation 2.34 have been neglected, which gives rise to an expression equal to $4|\rho_{\mathrm{S}}(\Omega)|^2\Gamma_{\mathrm{S}}^2\zeta_{\mathrm{S}}^2 - 4\mathrm{Im}[\rho_{\mathrm{S}}(\Omega)]\Gamma_{\mathrm{S}}\zeta_{\mathrm{S}}$. This term is close to zero, contributing less than 1% to the readout in the parameter regime operating at 3 GHz detuning. Therefore, the tensor contribution can be considered insignificant for amplifying the quantum back-action effects of the spin when measuring the P quadrature.

Next, we introduce the important quantity called the quantum cooperativity of our oscillator:

$$C_{\mathrm{Q}} = \frac{\mathrm{BA}}{\mathrm{TH}} = \frac{\Gamma_{\mathrm{S}}}{2\gamma_{\mathrm{S0}}(n_{\mathrm{S}} + \frac{1}{2})}. \tag{2.37}$$

Quantum cooperativity is the ratio between the readout rate and the rate of thermal decoherence. This can be seen from equation 2.36 by dividing the two expressions for the quantum back-action noise by the thermal noise when setting the dynamical broadening to zero ($\zeta = 0$) and taken in the near resonance limit ($|\rho_{\mathrm{S}}(\Omega)|^2 \approx |\chi_{\mathrm{S}}(\Omega)|^2$). Quantum cooperativity is a figure of merit for the sensitivity of the oscillator to external forces, in particular, it determines the strength of the quantum correlations that can enhance the signal-to-noise (SNR) ratio in force measurements.

The simplest imaginable system is the spin oscillator free from the dynamical back-action $\zeta_{\mathrm{S}} = 0$, which can be calculated using equation 2.34:

$$\begin{aligned} S_{PP}^{\mathrm{det}}/\mathrm{SN} =& 1 + \overbrace{4\Gamma_{\mathrm{S}}^2|\chi_{\mathrm{S}}(\Omega)|^2\cos^2(\phi) + 2\Gamma_{\mathrm{S}}\mathrm{Re}[\chi_{\mathrm{S}}(\Omega)]\sin(2\phi)}^{\mathrm{BA}} \\ &+ \overbrace{4\gamma_{\mathrm{S0}}\Gamma_S\Big(|\rho_{\mathrm{S}}(\Omega)|^2 + |\chi_{\mathrm{S}}(\Omega)|^2\Big)\Big(n_{\mathrm{S}} + \tfrac{1}{2}\Big)\cos^2(\phi)}^{\mathrm{TH}}. \end{aligned} \tag{2.38}$$

Interestingly, the back-action depends on the real part of the susceptibility having a sign change for the two sides of the resonance. This means there are frequencies for back-action noise to contribute negatively to the measurement caused by the negative cross-correlational between the X quadrature of the atomic spin and the quadratures of light. The regime in which the total noise of a frequency range goes below 1 gives rise to light squeezing. This means that a polarization state of light can be measured better than the standard quantum limit, i.e. with a resolution below the shot noise. There is likewise an orthogonal polarization state of light that is anti-squeezed such the Heisenberg uncertainty principle is obeyed $\Delta P_{\mathrm{L}} \Delta X_{\mathrm{L}} \geq \frac{1}{4}$.

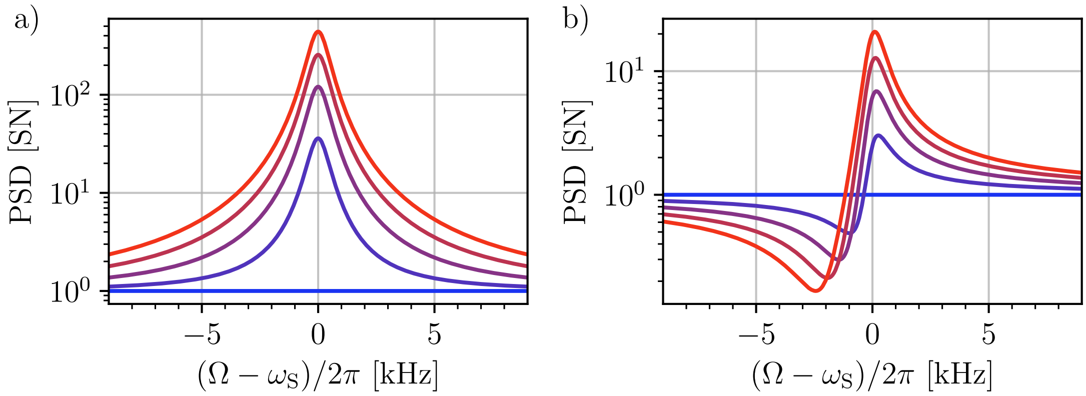

Figure 2.10: Spin noise dependency on the quantum cooperativity. The power spectral density for $\phi = 0°$ in a) and $\phi = 102°$ in b). There is no dynamical back-action ($\zeta_{\mathrm{S}} = 0$), the spin system is in the ground state $n_{\mathrm{S}} = 0$ and $\gamma_{\mathrm{S0}}/2\pi = 1\,\mathrm{kHz}$. The readout rate is increased from blue to red as $\Gamma_{\mathrm{S}}/2\pi = [0,\ 2.5,\ 5.0,\ 7.5,\ 10]\,\mathrm{kHz}$, which gives a quantum cooperativity of $C_{\mathrm{Q}} = [0,\ 2.5,\ 5.0,\ 7.5,\ 10]$.

The readout of the atomic spin onto the light for increased quantum cooperativity can be seen in figure 2.10. The P quadrature ($\phi = 0°$) is the measured state of light showcasing strongest atomic signal, shown in figure 2.10a. The fraction of thermal noise in the measurement is gradually reduced as the quantum cooperativity is increased, as well as an increase of signal strength due to the increase of readout rate. This type of growth in the readout rate could be achieved by heating the cell such the vapor pressure would increase, resulting in an increased number of atoms for the interaction[13]. A measurement of an intermediate quadrature at a measurement angle of $\phi = 102°$ is shown in figure 2.10b, where the response goes below shot noise of 1, meaning that the light is in a squeezed state. The squeezing level highly depends on the quantum cooperativity, which determines the minimum value of noise relative to the shot noise for perfect detect efficiency, in which the squeezing value of the figure results in $\mathrm{SQ} = [0,\ 3.1,\ 5.3,\ 6.7,\ 7.8]$ dB for quantum cooperativity of $C_{\mathrm{Q}} = [0,\ 2.5,\ 5.0,\ 7.5,\ 10]$. The phenomenon of light squeezing is extensively described in Part IV Spin induced light squeezing.

It is also interesting to show the contributions from a nonzero tensor, which is the operation regime for most of our experiments. The most distinct measurement for the nonzero tensor, $\zeta_{\mathrm{S}} \neq 0$, is the X quadrature of light $\phi = 90°$ since a zero

[13] Increasing the vapor pressure also increases the intrinsic linewidth of the atomic ensemble due to increased rate of atom-atom collisions, but this is often a small contribution compared to other broadening processes, therefore, neglected in this context.

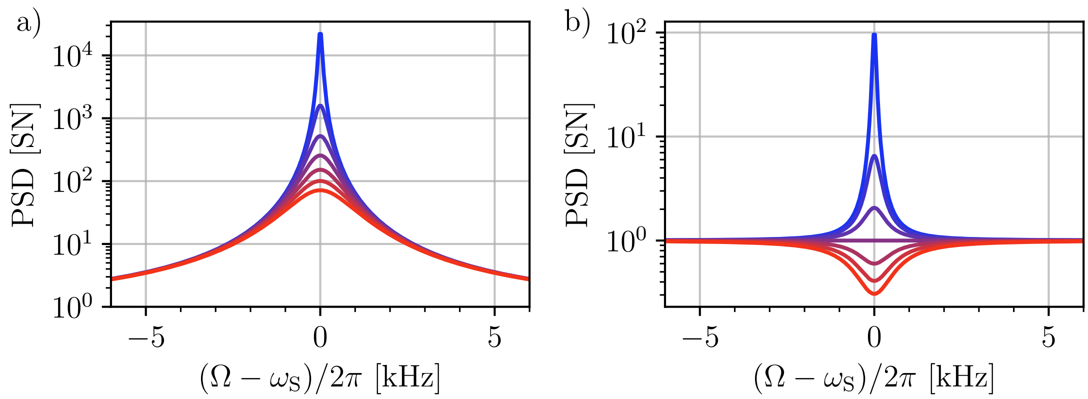

Figure 2.11: Spin noise dependency on the dynamical back-action. The power spectral density for $\phi = 0$ in a) and $\phi = 90°$ in b). The spin system is in the ground state with the parameters; $n_S = 0$, $\gamma_{S0}/2\pi = 1$ kHz and $\Gamma_S/2\pi = 7.5$ kHz, which gives a quantum cooperativity of $C_Q = 7.5$. The tensor interaction coefficient is increased from blue to red as $\zeta_S = [-6,\ -4\ -2,\ 0,\ 2,\ 4,\ 6] \times 10^{-2}$.

tensor does not have any spectral contribution. We can write the expression for the X quadrature computed using equation 2.34:

$$\begin{aligned} S_{\mathrm{PP}}^{\mathrm{det}}/SN(\phi \to 90°) =& 1 + \overbrace{4|\chi_S(\Omega)|^2\Gamma_S^2\zeta_S^2 - 4\mathrm{Im}[\chi_S(\Omega)]\Gamma_S\zeta_S}^{\mathrm{BA}} \\ &+ \overbrace{8\gamma_{S0}\Gamma_S|\chi_S(\Omega)|^2\left(n_S + \tfrac{1}{2}\right)\zeta_S^2}^{\mathrm{TH}}. \end{aligned} \tag{2.39}$$

We have neglected the terms proportional to ζ_S^4. It can be seen from the above equation that we can both have back-action and thermal noise on the X quadrature for nonzero tenor interaction ($\zeta_S \neq 0$). We can also be in a situation having a negative back-action noise contribution on the X quadrature, which results in squeezed light on the oscillator resonance for a positive tensor interaction ($\zeta_S > 0$).

Figure 2.11 shows the spin noise dependency on the tensor interaction coefficient. All parameters are fixed for both figures with a quantum cooperativity of $C_Q = 7.5$. The figures show the P quadrature and the X quadrature in figures a) and b), respectively. The first pronounced feature arising from the tensor contribution can be seen in figure a), where the spin response is only affected by the change of the total linewidth. This is because of the dynamical broadening: $\gamma_S = \gamma_{S0} + 2\Gamma_S\zeta_S$. Therefore, the spin is narrowed for the negative tensor interaction coefficient in blue and broadened for the positive tensor interaction coefficient in red. The narrowing and broadening are also visible for the X quadrature in figure b), where the light is squeezed in red for a positive tensor and amplified in blue for a negative tensor. Therefore, the sign of the tensor interaction coefficient can easily be predicted by looking at the X quadrature as it has a $\Gamma_S\zeta_S$ scaling.

We are concluding this chapter, having outlined the description of macroscopic spin systems of cesium atoms. The following parts of the thesis showcase the experimental capabilities of the spin oscillators: in part II Experimental methods for characterization of an atomic spin ensemble in a hot vapor cell, part III Experimental realizations and simulations of motional averaging in a hot vapor cell, and part IV Spin induced light squeezing.

CHAPTER 3

Outline of membrane in the-middle optomechanics

An exemplary quantum oscillator requires two traits; the ability to decouple the oscillator from the environment - the memory time, and the ability to interact with the quantum system - the coupling rate. Using a semitransparent membrane to couple the motion of a mechanical resonator (phonons) to the radiation pressure (photons) seems like a crazy idea at first glance. However, the membrane can be decoupled from the thermal surroundings by introducing a phononic band gap structure that isolates the desired modes of the membrane from thermalizing. The latest design of such a membrane used in these studies can be seen in figure 3.1a, designed and fabricated by [Tsaturyan et al., 2017]. The membrane is made from silicon nitride (Si_3N_4) in a structure referred to as a soft-clamped membrane because the spatial region of the membrane and the phononic structure has a soft spatial transition giving it its name. The advantage of the soft-clamped membrane is to reduce the bending losses, otherwise limiting designs with sharp spatial mode cut-off.

The excellence of the membranes is often characterized by the quality factor calculated from the ratio of the total energy over the lost energy per oscillation, also estimated from the ratio: $Q \approx \Omega_\mathrm{M}/\gamma_\mathrm{M}$, where Ω_M is the mechanical frequency and γ_M is the decay rate. The quality factor intuitively represents the amount of oscillation that the membrane oscillates after excitation before relaxing to a steady state. The membranes used in our experiments have a quality factor of $Q > 10^7$ with the previous best of this design; $Q = 1.555 \cdot 10^9$ at frequencies ~ 1.3 MHz [Tsaturyan, 2019].

To enhance the coupling between light and mechanics, the membrane is placed inside an optical cavity to increase the strength of the interaction. A cartoon illustration of a membrane in the-middle configuration is shown in figure 3.1b. This design relies on stable confinement of the Gaussian beam, which is the case for the beam propagating between the two curved mirrors and the two sub-cavities created by the surface of the reflective membrane and the nearby mirrors. Therefore, the membrane is placed in the center of the concave cavity to fulfill the conditions for a stable optical resonator. Another typical design is to have the membrane placed

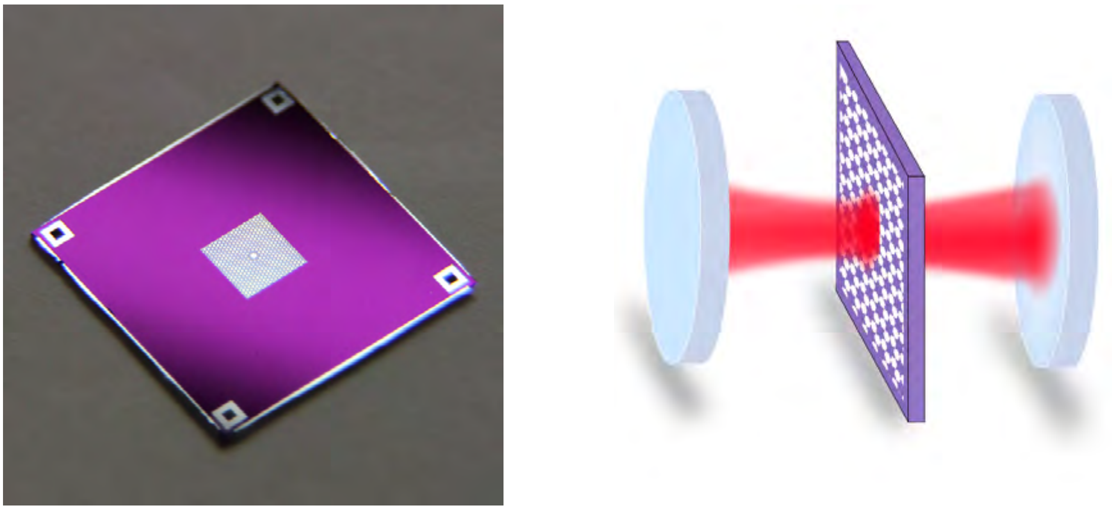

a) b)

Figure 3.1: Visual representation of the silicon nitride membrane. a) showing the design of the soft-clamped membranes. The figure is reproduced from [Møller, 2018]. b) visualization of a membrane placed inside an optical cavity, also known as a membrane in the-middle optomechanics.

in a plano-concave cavity with the membrane placed close to or on top of the flat mirror, as this constructs a stable cavity geometry. Earlier experiment stages used a plano-concave cavity design [Møller, 2018]. However, it left the cavity design with less motional degrees of freedom to position the membrane, which decided to migrate to a concave cavity design. See section 3.2 for further explanation.

3.1 Theoretical layout of a membrane in the-middle optomechanics

Optomechanics is the physical dynamics of coupling of light to mechanical objects. We are using the derivations of [Nielsen, 2016, Møller, 2018] for the description of our mechanical system. Our mechanical object, represented by a membrane, is described by a damped harmonic oscillator. Introducing the susceptibility for a damped harmonic oscillator:

$$\chi(\Omega) = \frac{\omega_{\mathrm{M}}}{\omega_{\mathrm{M}}^2 - \Omega^2 + i\Omega\gamma_{\mathrm{M}}}. \tag{3.1}$$

The angular oscillation frequency ω_{M} and the damping rate γ_{M} describe the damped oscillator. The notable difference concerning the spin system is the asymmetrical decay process for the mechanical object, only inducing decay for the position of the membrane and not the momentum. In contrast, the spin system has a symmetric decay into both spin quadrature, showcasing a slightly different oscillator response for the spin system (see equation 2.25 and 2.26 for spin susceptibility).

A simple illustration of an optomechanical system is illustrated in figure 3.2a, showing a cavity with an end-mirror attached to a spring. The field strength and the spring energy can describe the energy for such a system:

$$\hat{H}_{\text{opt}}/\hbar + \hat{H}_{\text{mech}}/\hbar = \omega_{\text{C}}(\hat{a}^\dagger\hat{a} + 1/2) + \omega_{\text{M}}(\hat{b}^\dagger\hat{b} + 1/2), \tag{3.2}$$

where $\hat{a}^\dagger\hat{a}$ and $\hat{b}^\dagger\hat{b}$ are the photon and phonon numbers, respectively, described by the creation and annihilation operators. ω_{C} is the angular frequencies of the light field in the cavity. The optomechanical configuration with a movable end mirror has been unpromising due to the limited reflection coefficient of conceived membranes (the swinging mirror) restricted by the index of refraction of the dielectric, $r_{\text{m}} \ll 1$, except for recent promising results for a high Q photonic-crystal membrane realized with a reflectivity of $r_{\text{m}} = 99.89\%$ [Enzian et al., 2022].

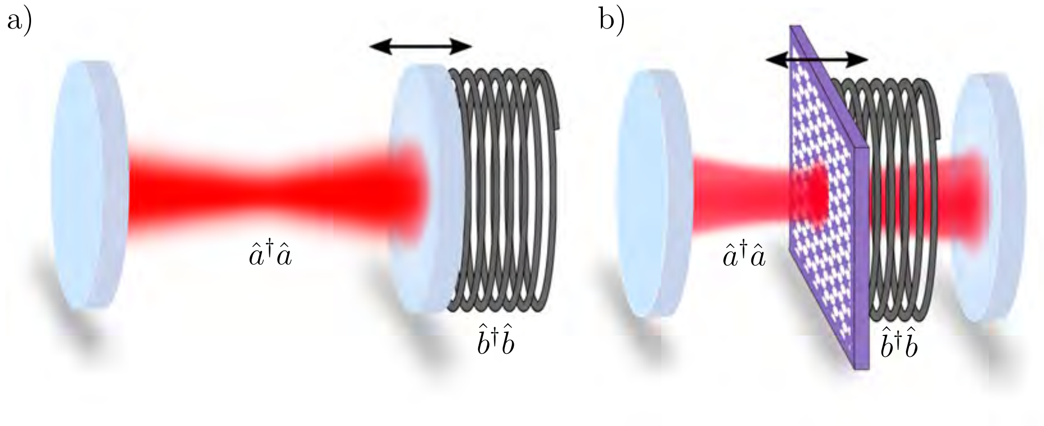

Figure 3.2: Illustration of an optomechanical system. $\hat{a}^\dagger\hat{a}$ is the photon number and $\hat{b}^\dagger\hat{b}$ is the phonon number. a) a canonical optomechanical system. b) a membrane in the-middle optomechanical system.

The approach to enhance the intra-cavity optical field has been a membrane in the-middle design shown in figure 3.2b. The membrane is positioned in a concave cavity, creating two sub-cavities. The membrane is a small defect centered in the phononic structure. The entire membrane is not moving, as shown for illustrative purposes. The membrane inside the cavity gives experimental freedom by detuning the coupling to the sub-cavities and tuning the photon to phonon coupling. Listing all the dynamics for our optomechanical system:

$$\hat{H} = \hat{H}_{\text{opt}} + \hat{H}_{\text{mech}} + \hat{H}_{\text{int}} + \hat{H}_{\text{drive}}. \tag{3.3}$$

We have included the photon-phonon interaction $\hat{H}_{\text{int}}$, and the drive being the in-coupling of light to the cavity $\hat{H}_{\text{drive}}$. The interaction Hamiltonian can be calculated for a linear approximation having small fluctuations from the mean: $\hat{a} = \alpha + \delta\hat{a}$ and $\hat{b} = \beta + \delta\hat{b}$, with α and β representing the mean field.

$$\begin{aligned} \hat{H}_{\text{int}}/\hbar &= \sqrt{2}g(\delta\hat{a} + \delta\hat{a}^\dagger)(\delta\hat{b} + \delta\hat{b}^\dagger) \\ &\propto \underbrace{\delta\hat{a}\delta\hat{b} + \delta\hat{a}^\dagger\delta\hat{b}^\dagger}_{\text{Stokes}} + \underbrace{\delta\hat{a}\delta\hat{b}^\dagger + \delta\hat{a}^\dagger\delta\hat{b}}_{\text{Anti-stokes}}, \end{aligned} \tag{3.4}$$

where g is the optomechanical coupling rate. The interaction Hamiltonian gives rise to Stokes or anti-Stokes dynamics. The Stokes process is associated with annihilating(creation) a phonon and photon pair amplifying/heating the membrane, giving rise to entanglement generation. The anti-Stokes process is associated with annihilating(creation) a phonon and creating(annihilating) a photon, cooling the membrane, giving rise to a beam-splitter type of interaction.

The last term to describe the dynamics of the optomechanical system is the drive describing the input light feeding the cavity with light.

$$\hat{H}_{\text{drive}}/\hbar = i\sqrt{\kappa}(\bar{s}_{\text{in}}\delta\hat{a}^{\dagger} - \bar{s}_{\text{in}}^{*}\delta\hat{a}), \tag{3.5}$$

where κ is the cavity linewidth and $\bar{s}_{\text{in}}$ is the normalized amplitude of the drive field.

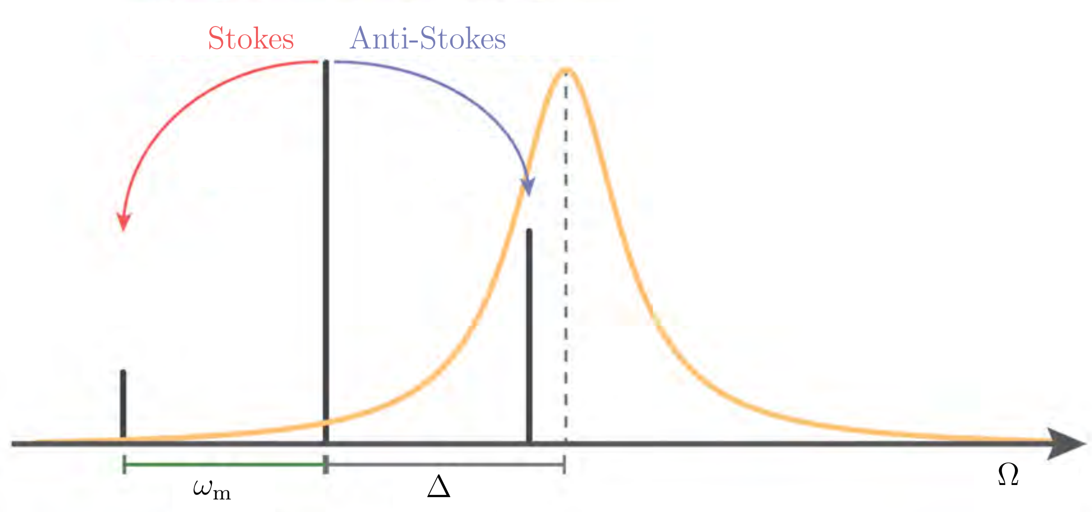

Figure 3.3: Dynamical side-band asymmetry of cavity optomechanics. The yellow curve shows the cavity mode. The large peak is the input laser detuned by Δ to the cavity, having side-bands for the Stokes and anti-Stokes process generated by the light-membrane interaction. The figure have been reproduced from [Tsaturyan, 2019].

The cavity has a complex Lorentzian describing the frequency response of the input light for the effective cavity detuning Δ, following

$$L(\Omega) = \frac{\kappa/2}{\kappa/2 - i(\Omega + \Delta)}. \tag{3.6}$$

The cavity response can be used to control the coupling of modes to the membrane. This can be seen in controlling the process of the Stokes and anti-Stokes dynamics described by the interaction Hamiltonian. Figure 3.3 shows the cavity response in yellow, demonstrating the suppression of the Stokes process and amplification of the anti-Stokes process by red detuning the laser frequency to the cavity response. This favors the anti-Stokes process over the Stokes process, resulting in a cooling of the membrane. The presented cooling broadens the oscillator, which under the proper condition yields ground state cooling $n_{\text{M}} < 1$, provided there is a sufficient sideband asymmetry to cool the oscillator. Important parameters describing both sideband asymmetry and the readout rate of the membrane [Thomas, 2020]:

$$\begin{aligned} \zeta_{\mathrm{M}} &= \frac{|L(\omega_{\mathrm{M}})| - |L(-\omega_{\mathrm{M}})|}{|L(\omega_{\mathrm{M}})| + |L(-\omega_{\mathrm{M}})|}, \\ \Gamma_{\mathrm{M}} &= \frac{4g^2}{\kappa}(|L(\omega_{\mathrm{M}})| + |L(-\omega_{\mathrm{M}})|)^2. \end{aligned} \tag{3.7}$$

The two parameters are essential for understanding the relation to the spin system for a later description of the hybrid system covered in part V Hybrid spin-optomechanical systems, which relies on matching parameters for the hybrid spin-optomechanical system. In addition, the quantum cooperativity can also be defined for the optomechanical cavity described by the quantum back-action to thermal noise:

$$C_{\mathrm{Q}} = \frac{4g^2}{\kappa\gamma_{\mathrm{M}}(n_{\mathrm{bath}} + 1/2)}, \tag{3.8}$$

where n_{bath} is the thermal occupancy of the bath being; $n_{\mathrm{bath}} \approx 10^5$ at the membrane thermalization temperature of 10 K.

For more information, the input-output relation and mechanical response for the described system can be found in the following dissertations [Nielsen, 2016, Møller, 2018, Tsaturyan, 2019, Østfeldt, 2022].

3.2 Implementation of a membrane in the-middle optomechanics

The transition to a concave-concave cavity design has been to match the optimal laser frequency for probing the optomechanical system and the spin system. The position of the membrane is chosen to maximize the photon-phonon coupling is in between the maximum and minimum of a node in the standing wave of the cavity. The membrane positioned in the maximum photon-phonon coupling can be seen in figure 3.4c. The cavity design incorporates two piezo crystals, so the entire cavity can be moved, effectively moving the fixed membrane in the standing wave to accommodate the position of the maximum photon-phonon coupling. Previous cavity designs had a plano-concave cavity design; the membrane was fixed relative to the flat mirror dividing the cavity into a long and a short sub-cavity. The position of the maximum photon-phonon coupling was here adjusted by tuning the laser frequency, which is incompatible with the fixed frequency of the spin system, being unsuited for large frequency tunings. Figure 3.4a and 3.4b show a picture and detailed drawing of the cavity design. The detailed experimental considerations for the design of the cavity holder can be found in [Mathiassen, 2019, Østfeldt, 2022].

It is essential to extract the parameters of the optomechanical system for quantum protocols. Three methods are realized to characterize the optomechanical cavity:

- **Optomechanically-induced transparency (OMIT)**
  OMIT measures induced transparency by driving the optomechanical cavity with phase-modulated light [Weis et al., 2010], giving rise to effects similar

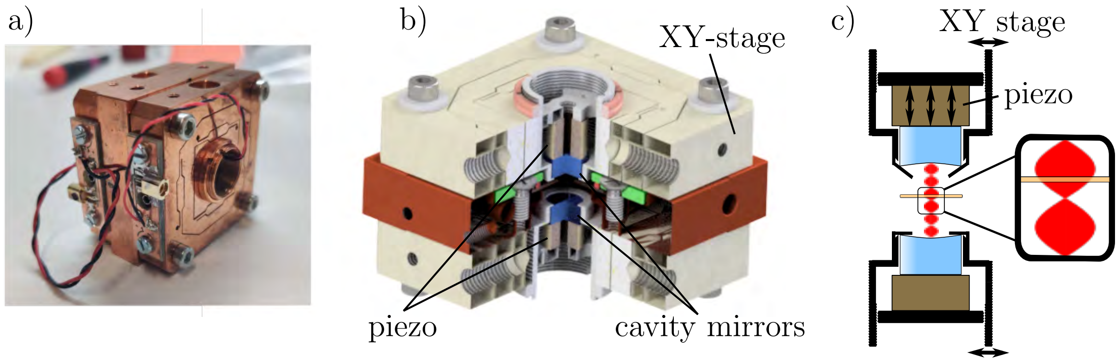

Figure 3.4: Optomechanical cavity design. a) a picture of the holder for the optomechanical cavity. b) a sketch of the optomechanical cavity with a cutout. c) An illustrative drawing of the position alignment for the holder, maximizing the photon-phonon coupling. Figures have been reproduced from [Mathiassen, 2019].

to electromagnetically induced transparency. OMIT allows to extract the following parameters: the cavity linewidth κ, the effective detuning Δ, and the optomechanical coupling rate g, all important for characterizing the optomechanical cavity. OMIT is covered in [Østfeldt, 2022].

- **Ringdown technique**
  The ringdown technique is measured by driving the membrane with amplitude modulated light or a piezo drive of the cavity length. This excites the membrane leaving the mode of the membrane in a decaying excited state. The decaying envelope allows for the extraction of the quality factor Q of the membrane, which estimates the decay rate γ_{M}. The ringdown technique is covered in [Tsaturyan, 2019].

- **Ponderomotive squeezing**
  The measurement of ponderomotive squeezing for the optomechanical cavity is the measurement of optomechanical induced light squeezing, arising from the quantum back-action process [Purdy et al., 2013] similar to the spin induced light squeezing briefly covered in section 2.2.2 and later investigated in part IV Spin induced light squeezing. The ponderomotive squeezing estimates the last parameters necessary for a complete system model of the optomechanical cavity; the thermal occupancy of the bath n_{bath} and the detection efficiency η.

We are concluding this chapter on membrane in the-middle optomechanics, which is further explained in the context of the hybrid spin-optomechanical system in part V Hybrid spin-optomechanical systems for the entanglement generation between a hybrid spin-optomechanical system in chapter 11, and for the quest towards hybrid spin-optomechanical teleportation in chapter 12.

Part II

Experimental methods for characterization of an atomic spin ensemble in a hot vapor cell

CHAPTER 4

Outline of spin ensemble characterizations

This chapter presents the experimental methods for characterizing an atomic spin ensemble in a hot vapor cell. These methods are paramount for quantum experiments since they allow for translating the signals observed in the laboratory into the outcomes of measurements on quantum states.

We present the advancements in and the technical implementation of the protocols for the atomic ground state preparation and verification via optical pumping and magneto-optical resonance, and the readout calibration via coherently-induced Faraday rotation. The presented methods allow estimating the parameters: the readout rate (Γ_S), the intrinsic decay rate (γ_{S0}), the thermal occupancy (n_S), and the tensor interaction coefficient (ζ_S). These are the main parameters to characterize the atomic system as they determine its quantum cooperativity and dynamical back-action.

The significance of the magneto-optical resonance signal and the coherent induced Faraday rotation are due to their self-sufficient implementation. The two methods are independent of the detection efficiency, a generic problem in quantum characterization since calculating losses is a cumbersome and challenging task. The knowledge about the losses can be calibrated from a fully understood quantum oscillator. The two methods can therefore be used to estimate the losses after calibration.

There is a number of other characterization methods that are not described in detail. Still, they deserve to be mentioned as they have been used in the work of this thesis, and they are essential in the characterization of atomic cell performance. The experimental methods:

- **Atomic absorption measurement**
  The optical depth, and the associated density of the atomic vapor, can be measured with the atomic absorption measurement. This method relies on atomic absorption, recorded when scanning the frequency over the resonances of the D_2 line. The absorption depth can then be calculated as a function of the atomic density. The method of the atomic absorption measurement is covered in [Schmieg, 2018].

- **AC Faraday angle**
  The quantum cooperativity for a perfectly-polarized ensemble can be estimated from the AC Faraday angle. This method relies on a $\pi/2$-excitation of the atomic spin, upon which the total spin is rotated perpendicular to the magnetic field and modulates the output polarization with the amplitude proportional to the mean value of F_x. The amplitude of this oscillation can then be used to estimate the quantum cooperativity for $n_\mathrm{S} = 0$. The method of the AC Faraday angle is covered in [Thomas, 2020].

- **Relaxation of the Faraday angle**
  The decay of the longitudinal spin (T_1) can be calculated from the relaxation of the Faraday angle. This method is based on the same principles as the AC Faraday angle, upon which the total spin is rotated perpendicular to the magnetic field. It results in a signal decaying at the rate T_1. The method of relaxation of the Faraday angle is covered in [Schmieg, 2023].

CHAPTER 5

Atomic ground state preparation

Preparing the collective spin in the ground state is important to reduce the thermal noise. Ground state preparation corresponds to preparing all atoms of the ensemble in one of the outermost m_F levels of $6S_{1/2}$, $F = 4$ by optical pumping.

This chapter showcases the techniques to measure the thermal occupancy or the equivalent measure being the spin polarization, which is the ratio of the spin projection and the maximum spin length. We are using the magneto-optical resonance signal (MORS) to characterize the spin polarization. This chapter also describes the consideration we have made in our endeavor to optimize the spin polarization.

All the equations in this chapter are described by preparing a positive mass configuration, where the atoms are prepared in $|F = 4, m_F = -4\rangle$. The equations can also be applied for a negative mass configuration, where the sign of the spin projection is opposite (see section 2.1.1 for the definition of a negative mass reference frame).

5.1 Magneto-optical resonance signal

The magneto-optical resonance signal (MORS) technique is used for the measurement of the distribution of atoms over magnetic sublevels, by utilizing a coherent displacement of the oscillator created by a magnetic drive at the oscillator's frequency. The drive excites the transverse spin creating a coherent displacement, which creates signals much larger than the levels of all quantum noises. The physical dynamics for the coherent displacement of the spin oscillator are described in the original paper presenting the MORS technique [Julsgaard et al., 2003]. The MORS can both be analyzed in the time domain as well as in the Fourier domain with equivalent accuracy on the determination of the spin polarization[1]. The MORS technique exploits the quadratic splittings of m_F levels to decouple the amplitudes of the different modes that represent the transitions between adjacent m_F levels.

[1]The analysis in the Fourier domain can make it easier to visualize differences between signals for different spin polarizations because the strengths of the transitions between the m_F levels are more visually decoupled from each other in the Fourier domain.

The MORS spectrum is described by the expression:

$$\mathrm{MORS}(\Omega_{RF}) = A \cdot \left| \sum_{m=-F}^{F-1} C(F,m)\chi(\Omega_{RF},m)(P_m - P_{m+1}) \right|^2. \tag{5.1}$$

Here, A is a constant proportional to the strength of the drive and the total number of atoms, P_m is the fractional population in a m_F level of the total population, $\chi(\omega,m)$ is the susceptibility of a transition between two m_F levels (see equation 2.35 for the simplified spin susceptibility), C is the Clebsch-Gordan coefficients for the transition between the m_F levels:

$$C(F,m) = F(F+1) - m(m+1). \tag{5.2}$$

The spin modes are separated due to the quadratic energy shifts (see equation 2.18), giving rise to a m-dependency on the Larmor frequency.

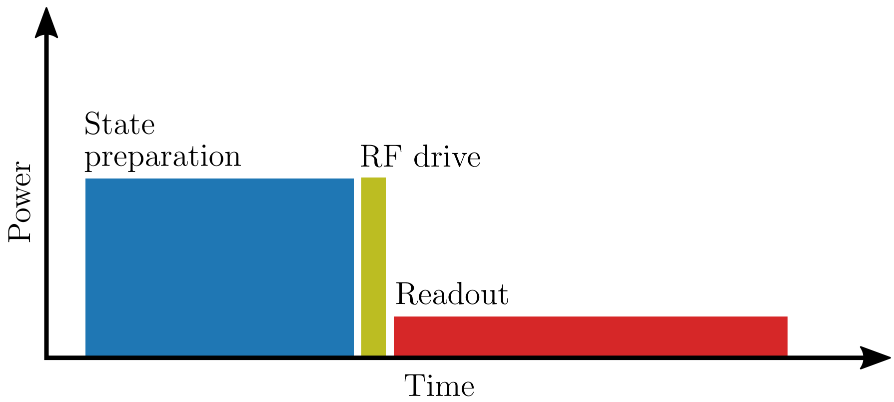

Figure 5.1: Experimental pulse sequence for MORS measurements. The atoms are 1. prepared by optical pumping, 2. coherently displaced with a RF drive, and 3. readout by homodyne detection.

The experimental sequence for performing a MORS measurement can be seen in figure 5.1. First, the atomic ensemble is prepared under the same conditions as the experiment in that the spin polarization is desired to be measured. The system is then displaced using a short coherent excitation of the transverse spin, which is performed by a RF excitation of the magnetic field along one of the spin quadratures (perpendicular to bias magnetic field). The excitation field is shown for the experimental drawing in figure 5.2 by the olive-colored arrow pointing out of the plane (along the y-axis). The final step is to readout the displacement of all the m_F levels, in which the signal strengths of different transitions are related to the numbers of atoms occupying different m_F levels according to equation 5.1.

RF drive

Two methods can be exploited to perform the MORS measurements in the Fourier domain for the RF drive of the magnetic field, by applying either a short or long coherent pulse:

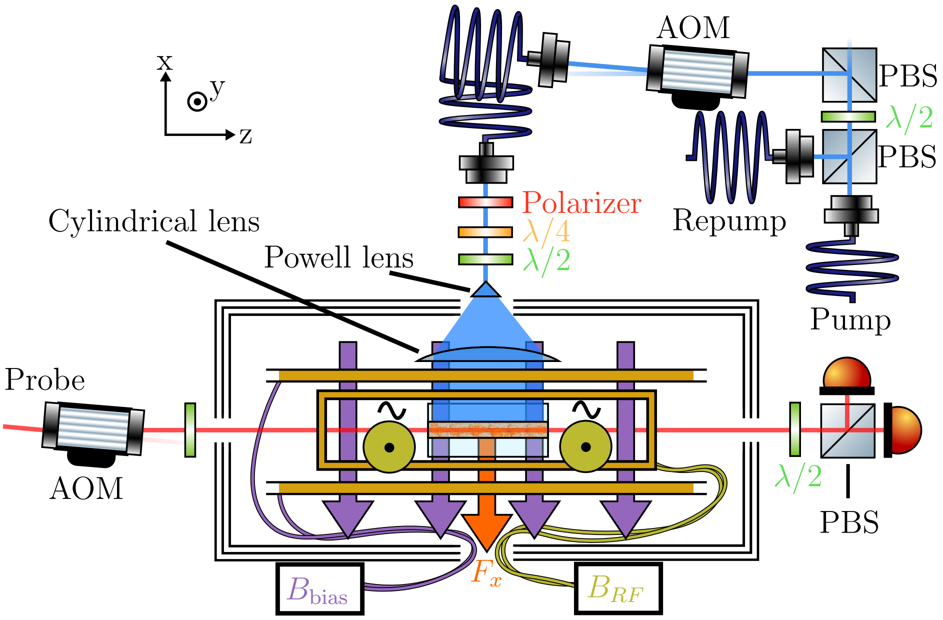

Figure 5.2: Experimental setup for MORS. All the beams can be pulsed by virtue of AOMs; all the beams can therefore be used for state preparation. The pump and repump are passed through a telescope to fill the entire cell channel. The magnetic RF drive points along the y-axis. After interacting with the atomic ensemble, the probe is measured by a homodyne detector.

1. All the atomic modes can be driven at once by applying a very short pulse - making a broad frequency band for the excitation. This excites all the atomic modes within the band of the excitation, where the excitation bandwidth needs to be much broader than the entire frequency span of all the m_F levels: $2\pi/\tau_{\text{RF}} \gg 2F \cdot \omega_{\text{QZ}}$.

2. A long coherent pulse can collect the oscillator responses at individual frequencies. The driving pulse demodulates the measurements to extract sine and cosine components of the excitation.

The two methods result in analogous spectra. The 1. method is the most used technique of our experiment, therefore, the method presented in the succeeding outline of the MORS technique[2].

Readout

It is essential to have a long readout since this determines the resolution of the frequency spacing for the fast Fourier transform (FFT) $\Delta f = 1/T$. The readout should extend beyond the characteristic decay time of the spin, $T \gg 2/\gamma_{\text{S0}}$, to maximize the resolution of the transformation.

[2]The 2. method may succeed in measuring low frequencies as it can be less susceptible to low-frequency noise but requires a Lock-in amplifier to demodulate the signal.

Data collection

The readout of the MORS technique is measured through homodyne detection (realization of the measurement is explained in the following section 5.1.1). The data collected from the homodyne detection is the photocurrent $i(t)$. The PSD can be found by: $S_{ii}(f) = \frac{1}{T}\left|\mathrm{FFT}[i(t)]\right|^2$, where T is the measurement time. Single-shot measurements are usually not sufficient because of their low SNR, therefore we average MORS over multiple repetitions of the same experimental sequence. The best approach to collect the MORS measurement is to take the average of all the time measurements before computing the PSD because all the MORS measurements are in phase with each other. This has the same effect as averaging the collected data before taking the Fourier transform: $\mathrm{MORS}(f) = \frac{1}{T}\left|\mathrm{FFT}[\langle i(t)\rangle]\right|^2$. This process eliminates uncorrelated noise like shot noise and other noise processes, increasing the SNR of the final measurement.

5.1.1 Experimental implementation

The optical setup for measuring the MORS can be seen in figure 5.2. The atomic ensemble is in a magnetic shield with the total spin oriented towards the bias magnetic field. The probe reading out the atomic state is linearly polarized, where the P-quadrature of the probe is detected using balanced homodyne detection, where balancing is accomplished using a $\lambda/2$ waveplate. The pumping beams are circularly polarized and propagate in the same spatial mode, which is shaped to maximize the overlap of the beams with the cell. A detailed description of the pumping is outlined in section 5.1.4.

MORS measurements require the ability to pulse lasers to perform the sequence shown in figure 5.1. The on-off switching of the optical beams is implemented using AOMs in the probe and the pump paths. The AOMs enables the control over the power of the probe beam, which can be used to minimize the probe-induced decay for the readout. A strong probe beam can introduce decay of the population distribution or the transverse spin known as T_1 or T_2, respectively. T_1 is the decay of the longitudinal spin (decay of F_x) and T_2 is the decay of the transverse spin (decay of $\hat{X}_\mathrm{S}$ and $\hat{P}_\mathrm{S}$). T_1 is not of great interest in this thesis as we typically observe $T_1 > T_2$, and we are in our measurements mostly influenced by transverse decay: $\gamma_{\mathrm{S}0} = 2/T_2$, since the transverse spin is readout into the light. The decoherence of the longitudinal spin is mostly interesting when performing measurements limited by the dark decoherence time, where we have the following equality, $2T_1 = T_2$ when excluding dephasing [Thomas, 2020].

The RF drive for the MORS measurement requires a very short and weak pulse of only a few µs to have a driving pulse spanning over a large frequency band that has a flat frequency spectrum in the frequency band of interest. We have in the theoretical description of our spin-model neglected loss of spin polarization due to large fluctuations in $\hat{X}_\mathrm{S}$ or $\hat{P}_\mathrm{S}$, because of the Holstein Primakoff approximation (see figure 2.6 for illustration). The Holstein-Primakoff approximation is not valid in the case of a strong drive of $\hat{X}_\mathrm{S}$ and $\hat{P}_\mathrm{S}$. The loss of spin polarization can be accommodated by having a weak RF drive. The effect of a strong drive can be seen in figure 5.3. The figure illustrates that the total spin is maintained but is rotated into the transverse spin, reducing F_x, which reduces the spin polarization.

The effect of the drive strength can be tested by increasing the RF drive until the measurements enter the regime, where the loss of spin polarization becomes apparent. The strength of the drive required for degrading the spin polarization due to the RF pulse varies depending on the design of the excitation coils - a number for strength is, therefore, not universal. We are using a RF drive with the magnitude of $\sim$0.1 V peak to peak in the current iteration of the experimental setup.

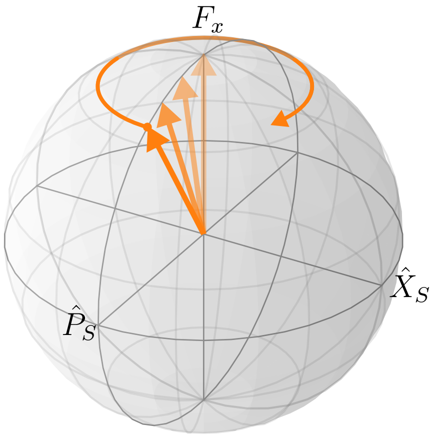

Figure 5.3: Illustration of the Bloch sphere dynamics following after the application of a coherent displacement via a RF pulse. The mean spin F_x is rotated into the transverse spin when applying a RF excitation along one of the transverse directions of the bias magnetic field.

It is essential to have the three sequences of the MORS measurement separated in time, especially it important to isolate the interval of the state preparation. An overlap between the state preparation and the RF drive causes decoherence and dephasing to the coherent displacement of the oscillator due to the pump and repumping beams. The decoherence and dephasing are less pronounced for the probe. Therefore, a weak probe can overlap with the other sequences without degrading the measurement.

MORS measurement exploit the quadratic Zeeman splitting to distinguish the ratio of the different m_F transitions. The SNR, or accuracy, of the MORS measurement can be improved by increasing the Larmor frequency, where the splittings of the different transitions are further increased. It can therefore be advantageous to perform the MORS measurement at higher Larmor frequencies than those in the final experiment. The main concern with increasing the Larmor frequency is the impact of the earth's magnetic field as it alters the direction of the bias magnetic field. An increase in the Larmor frequency may therefore alter the direction of the bias magnetic field if the magnetic shield does not cancel the earth's magnetic field. An altered direction of the bias magnetic field changes the alignment of the pumping beams, because the bias magnetic field sets the quantization axis, implying a change in the spin polarization.

5.1.2 Evaluation of a continuous state

Continuous state preparation is the preparation of a spin ensemble in a steady state. The steady state preparation of the spin state is favorable because it is compatible with a continuous readout of the spin state.

We want to prepare the atoms in the steady state configuration to evaluate the spin polarization. In this case, the repump, the pump, and the probe are continuously on until a steady state is achieved for the mean spin. This is the initial process of the continuous MORS measurement, which is the first step (state preparation) seen in figure 5.1. The following procedure is as described in section 5.1.1.

The population of atomic levels are distributed following a thermal distribution if all the levels are pumped with equal rates. The thermal occupancy is the same for all m_F levels in the case of a thermal distribution. The thermal distribution is described by the level distribution: $P_m = e^{\beta m}/\sum_{m=-F}^{F-1} e^{\beta m}$, where β is the spin temperature: $\beta = 1/(k_\mathrm{B}T_\mathrm{S})$ [Appelt et al., 1998]. Later derived in equation 5.10, the thermal distribution has the thermal occupancy:

$$n_\mathrm{S} = \frac{e^\beta}{1-e^\beta}. \tag{5.3}$$

The spin polarization is defined as the length of the F_x normalized to the total length of the spin, $p = |\langle F_x\rangle|/F$; later defined in equation 5.14, the thermal distribution result in the spin polarization:

$$p = \frac{1}{F}\frac{\left|\sum_{m=-F}^{F-1} m e^{\beta m}\right|}{\sum_{m=-F}^{F-1} e^{\beta m}}. \tag{5.4}$$

The distribution of atoms over the levels is not thermal in presence of dark states. The pump beam has $|F=4, m=-4\rangle$ for a positive mass configuration as a dark transition, which means that $e^{\beta m}$ cannot be used to model the distribution. The thermal occupancy, n_S, has to be considered more thoroughly in this incidence as the thermal occupancy varies on the different transitions between the m_F levels.

The expression for MORS assuming a thermal distribution of atoms is

$$\mathrm{MORS}(\Omega) = A\cdot\left|\sum_{m=-F}^{F-1} e^{-i\phi_m}\left(e^{\beta m} - e^{\beta(m+1)}\right)\frac{C(F,m)}{\omega_\mathrm{Z} + m\omega_\mathrm{QZ} - \Omega - i\gamma_m/2}\right|^2 + B. \tag{5.5}$$

A is the overall scaling, B is the background, e^β is the thermal distribution, ω_Z is the linear Zeeman splitting, ω_QZ is the quadratic Zeeman splitting, γ_m are the transverse decay rates and ϕ_m are the oscillator phases as fitted parameters. The transverse decay rates are not fitted with a separate rate for each mode, as many modes experience the same decay rate. Because of spin exchange, the atom-atom collisions change the coherence between m_F levels differently depending on the projection m [Savukov and Romalis, 2005]. The highest populated m_F levels are less affected since collision of atoms with equal spin does not alter the projection of the atoms involved[3]. Therefore, the highest populated m_F levels are fitted with a different decay rate.

[3] These effects are more thoroughly studied in [Thomas, 2020].

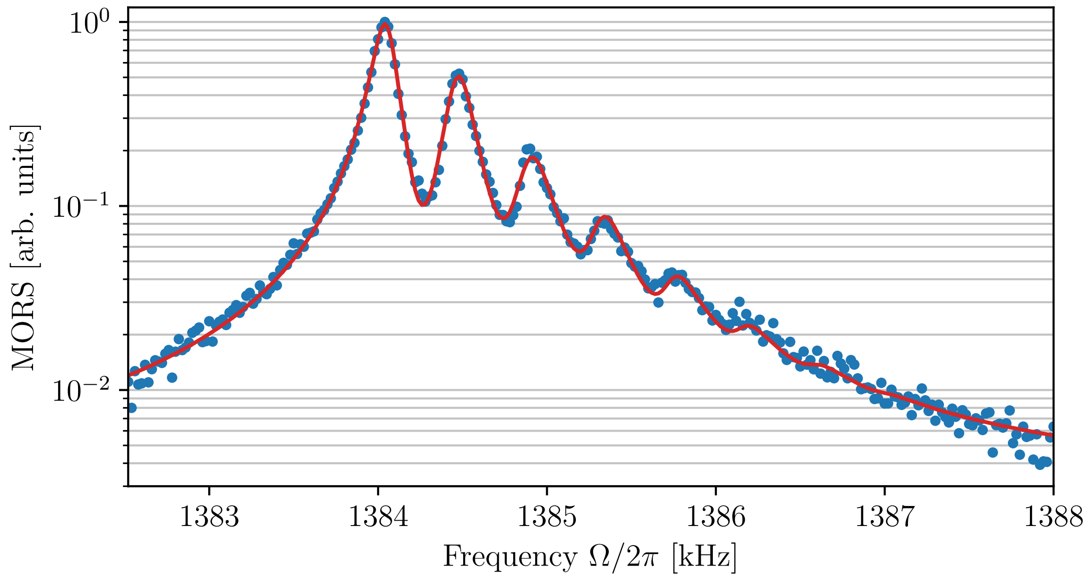

Figure 5.4: MORS for continuous state evaluation with repump and probe. The repump and probe each has a power of 10 mW. The spin polarization is $79.0 \pm 0.4\%$, and the thermal occupancy is $n_\mathrm{S} = 0.85 \pm 0.02$ for atoms populated towards $|4, 4\rangle$ in the negative mass configuration.

The continuous MORS is often fitted for 3 decay rates (in case of a positive mass oscillator); γ_{-4}, γ_{-3}, and $\gamma_{-2\ +}$. The oscillator phase ϕ_m describes the interference between different modes. The main mode has the largest signal contribution with which the other modes interfere, meaning that the phases of less populated modes result in an over fitting. Therefore, we fit over 3 phases for the continuous state evaluation ϕ_{-4}, ϕ_{-3} and ϕ_{-2} with the other phases being zero. The fit over phases can be reduced to one phase if the signal is heavily dominated by one mode, which is the case for the pulsed state evaluation in section 5.1.3.

The decoherence(broadening) process must be considered in preparing the atomic ensemble into a steady state for a continuous readout. The broadening induced by the repump is minimal since it does not address $F = 4$. On the other hand, the pump beam addresses $F = 4 \rightarrow F' = 4$, which causes significant broadening of all the m_F levels in $F = 4$. The advantage of using the pump beam for ground state preparation depends on the experimental requirements. The decision depends on whether the added thermal noise from an elevated thermal occupancy or an elevated decoherence rate is most detrimental to the experiment.

The presented MORS measurement for an experimental configuration relying on the continuous readout of the atomic state is shown in figure 5.4. The measurement is performed with a state preparation of 10 mW repump power and 10 mW probe power. The state preparation is of 30 ms, RF drive is of 5 µs and the readout is of 5 ms with a full cycle length of 50 ms. The probe is attenuated to 0.1 mW for the readout. The spin polarization of this measurement is $p = 79.0 \pm 0.4\%$ with a thermal occupancy of $n_\mathrm{S} = 0.85 \pm 0.02$, which has shown to be an upper limit when only using the repump for state preparation. The uncertainties of the spin polarization and the thermal occupancy are statistical uncertainties.

A higher spin polarization of $\approx 98\%$ can be achieved in a steady-state configuration using a pumping beam. The added broadening from the pumping beam is around 2 kHz applying approximating 3 mW of pump power. The added decoherence cannot justify the improvement in the thermal occupancy. The pump beam is, therefore, often only a few tenth of µW when applied in a continuous measurement to limit the amount of broadening.

5.1.3 Measurements in the pulsed regime

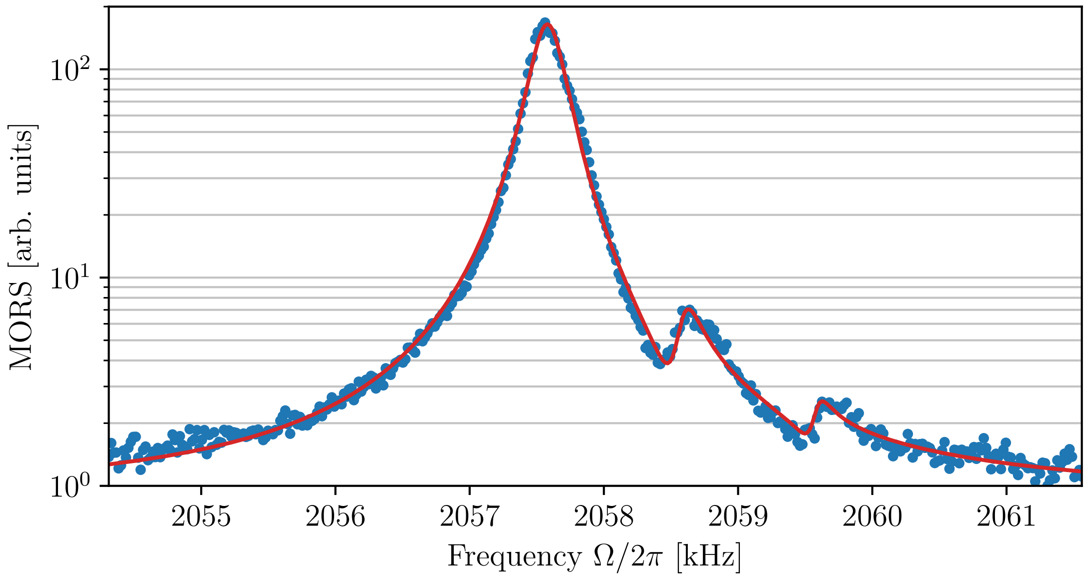

Figure 5.5: MORS of the best spin polarization in a pulsed regime. The spin polarization is $98.7 \pm 0.3\%$, and the thermal occupancy of the transitions between the (negative mass) ground state coherence $|4,4\rangle\langle 4,3|$ is $n_\mathrm{S} = 0.042 \pm 0.004$ for atoms populated towards $|4,4\rangle$. The measurement has been driven with a RF pulse with a duration of 5 µs.

The pulsed state preparation is the preparation of a spin ensemble in a non-stationary state that can be probed over a short period after the preparation. The technique of pumping atoms into a high spin polarization ($p > 98\%$) has been thoroughly investigated in [Dideriksen, 2021, Schmieg, 2019] for which the 3-peak model was developed. The 3-peak model refers to the presence of only 3 modes in the measured MORS spectrum, corresponding to the coherences $|4,-4\rangle\langle 4,-3|$, $|4,-3\rangle\langle 4,-2|$ and $|4,-2\rangle\langle 4,-1|$. The 3-peak model uses the following formula for the MORS measurement[4]:

$$\mathrm{MORS}(\Omega) = \left| \sum_{m=-F}^{2-F} e^{-i\phi_m} A_m \frac{C(F,m)}{\omega_\mathrm{Z} + m\omega_\mathrm{QZ} - \Omega - i\gamma_m/2} \right|^2 + B. \tag{5.6}$$

[4]The expression for the 3-peak model can be adapted to the experimental configuration, if a lower spin polarization is realized requiring the fitting of 4-peaks.

It is only ϕ_{-4} that is fitted in the 3-peak model since the interference between the two minor modes is negligible compared to the interference with the main($|4, -4\rangle\langle 4, -3|$) mode because the main mode has the largest spectral contribution. The other phases are fixed to zero. The amplitudes A_m and the decay rates γ_m are fitted for each mode. The 3-peak model is applied to the data in figure 5.5. The data represent the largest spin polarization achieved in our experimental configuration. The atoms are pumped to the negative mass configuration with a spin polarization of $98.7 \pm 0.3\%$. The spin polarization can be calculated using equation 5.14 and 5.15.

The thermal occupancy is only relevant for the main mode for a high spin polarization. The thermal occupancy of the main mode ($|4, 4\rangle\langle 4, 3|$) is $n_\mathrm{S} = 0.042 \pm 0.004$ calculated using equation 5.16. The spectral contributions from the other modes are small and, therefore, not interesting.

The spin polarization and thermal occupancy uncertainty are estimated from the statistical uncertainties of the amplitudes. This is feasible because there is only a weak correlation between the fitted amplitudes $|C(A_i, Aj)| \approx 0.1$.

5.1.4 Experimental challenges in ground state preparation

The main challenge in preparing the atomic ensemble in the ground state is generating a beam of circularly polarized light, propagating co-aligned to the magnetic field. In addition, the repumping and pumping scheme is vital to understand the dynamics for transferring atoms into the ground state.

The optical transitions used for preparing atoms into the ground state of the positive-mass configuration ($|4, -4\rangle$) are shown in figure 5.6. The repump and pump are σ_- polarized to create a preferred direction for the change of the atomic spin upon absorption events. The repump and pump beams are frequency stabilized in separate optical setups using the method of saturation polarization spectroscopy [Harris et al., 2006, Pearman et al., 2002].

Repump

The most important function of the repump is to transfer atoms from $F = 3$ to $F = 4$. The transfer of atoms to $F = 4$ is achieved using the transitions $|4', m_F - 1\rangle\langle 3, m_F|$ and $|3', m_F - 1\rangle\langle 3, m_F|$ of the D_2 line. The repump also transfer atoms towards a lower (higher negative projection) m_F state due to the σ_- polarization.

The repump only affects the atoms in $F = 3$, which means it may be favorable to keep them in $F = 3$ until they are pumped toward a lower spin projection. The atoms excited to $F' = 2$ only decays into $F = 3$. The transition $|2', m_F - 1\rangle\langle 3, m_F|$ can transfer atoms towards a lower spin projection without repumping the atoms to $F = 4$. The transition $|3', m_F - 1\rangle\langle 3, m_F|$ like wise has a higher probability of decaying into $F = 3$ than $|4', m_F - 1\rangle\langle 3, m_F|$. The transition $|3', m_F - 1\rangle\langle 3, m_F|$ can, therefore, also be used to transfer atoms towards a lower spin projection.

It has been concluded empirically that the largest spin polarization is realized by positioning the repump frequency between $F' = 2$ and $F' = 3$, where all the

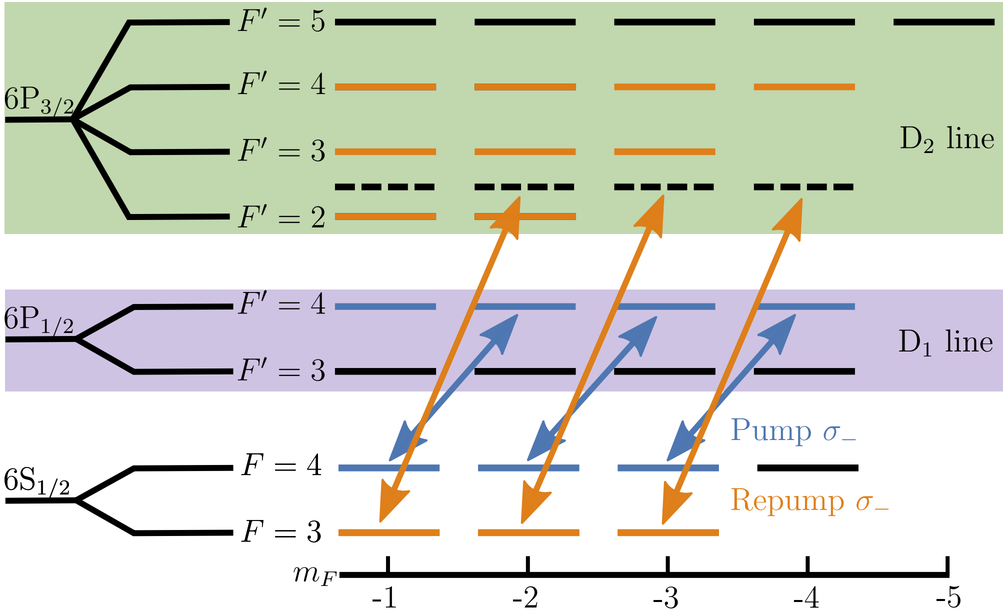

Figure 5.6: Optical transitions addressed by the pump and repump beams. The levels the pump and repump address are colored to show the appropriate level dynamics. This illustration is for preparing a positive mass oscillator realized with a σ_- polarization of the light.

transitions $F' = 2$, $F' = 3$ and $F' = 4$ are within Doppler width for atoms at room temperature. All the addressed transitions for the repump are colored orange in figure 5.6. The frequency of the repump is only to change the rates between excitation probabilities of the three excitations of the D_2 line. For maximizing spin polarization, it is favorable to address the transitions $|2', m_F - 1\rangle\langle 3, m_F|$ and $|3', m_F - 1\rangle\langle 3, m_F|$, so the repump favors a pumping of the spin projection more than pumping of atoms to the $F = 4$ manifold.

Pump

The pump only transfers atoms to a lower spin projection by the D_1 line using the transition $|4', m_F - 1\rangle\langle 4, m_F|$. The pumping beam has the disadvantage of addressing $F = 4$. Pumping on $F = 4$ manifold adds decoherence from spontaneous emission, contrary to the repump beam that is 9 GHz detuned from the transitions involving the $F = 4$ manifold.

Beam shaping of the pumping beams

It is necessary to have a pumping beam covering a large section of the atomic ensemble. This maintains a homogeneous and high spin polarization by addressing all the atoms. The remaining atoms not covered by the pumping beams are addressed through motional averaging for the hot atomic vapor. The atomic cell is elongated in the plane of pumping, having a cross-section of 1 mm×40 mm. We use a telescope in a combination with a Powell lens (line-generator) and a cylindrical lens to accommodate the elongated shape of the cell. Figure 5.7 shows the optical

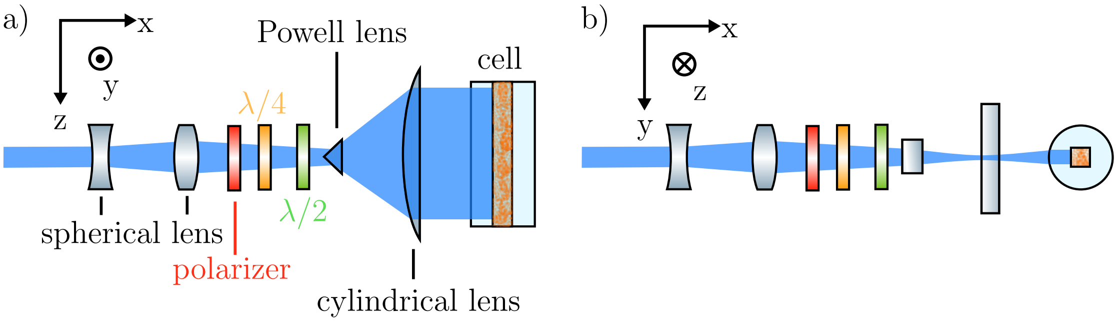

Figure 5.7: Optical system for generation of collimated pumping beams. a) the optical setup and beam propagation in the xz-plane. b) the optical setup and beam propagation in the xy-plane. Powell Lens: Thorlabs - LGL130.

system for generating the pumping beams. Figure a) shows the xz-plane, where the Powell and cylindrical lenses enlarge the beam profile. Figure b) shows the xy-plane shaped by two spherical lenses and adjusted to cancel the focusing of the outer channel such the collimation of the beam is maintained. The objective of the lens system is to have a uniform coverage of the pumping beam with the beam rays being aligned to the magnetic field. The optical system has a lot of coupled alignment degrees of freedom for achieving this, which is an experimental challenge addressed with mirrors and translation stages for the two spherical lenses and the Powell lens.

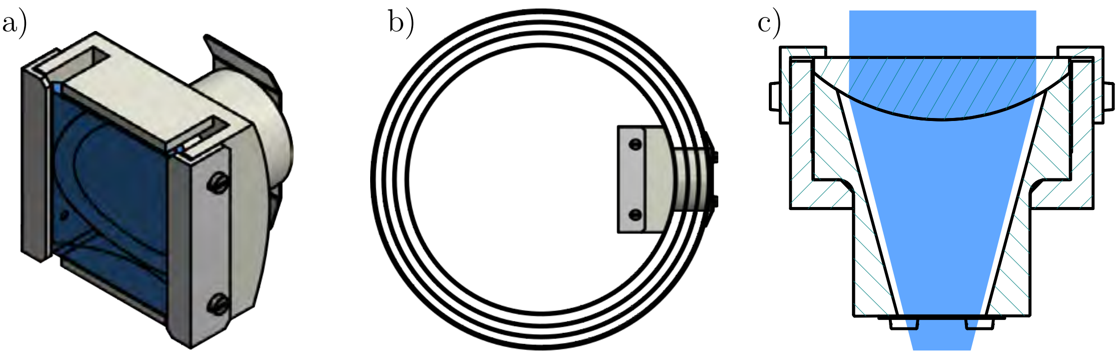

Figure 5.8: Cylindrical lens holder for collimating the pumping beams. a) the cylindrical lens holder. b) the cylindrical lens holder positioned inside the magnetic shield. c) a top view of a two-dimensional slice of the cylindrical lens holder to illustrate how the lens holder accommodates a diverging beam.

The magnetic shield used in this experiment has a round pumping hole of 25 mm in diameter. This is insufficient for a pumping beam covering the entire cell with the cell length of the z-axis being 40 mm. Therefore, the cylindrical lens is positioned inside the magnetic shield, so a pumping beam covering the entire cell can be generated. The mount for holding the lens inside the magnetic shield can be seen in figure 5.8. The mount is made of the plastic material PEEK due to its magnetic and electric properties as well as mechanical properties[5]. The atomic

[5]The lens holder has been fabricated in collaboration with the technical support group at the Niels Bohr institute.

ensemble is very sensitive to magnetic disturbances that induce classical noise into the measurement. Therefore, we only use plastics and ceramics inside the magnetic shield, excluding the coil systems for generating the bias magnetic and the RF drive. A cone structure is engraved into the lens holder to accommodate the divergence of the optical beam and the small hole of the magnetic shield. The cone structure follows the diverging angle of the beam shown in figure 5.8c.

The beam size of pumping beams is too large for a camera to image the beam profile. A picture of a fluorescence paper is instead used to show the beam shape. The shape of the pumping beam is uniform over the elongated direction shown in figure 5.9a. The uniformity is achieved by the optical properties of the Powell lens that generates a uniform line. Using two cylindrical lenses creates an elliptical beam, where the edges experience a lower intensity than the center, illustrated in figure 5.9b. The use of a Powell lens for shaping the pumping beams allows for uniformly addressing all the atoms of the ensemble, contrary to the use of cylindrical lenses, therefore increasing the spin polarization and making the spin polarization more uniform.

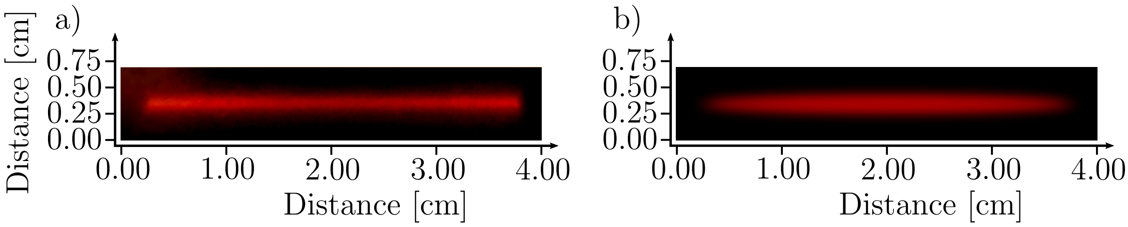

Figure 5.9: Beam shape of pumping beam measured on a fluorescence paper. a) beam shape of the pumping beam measured with a fluorescence paper. The beam is generated by the optical setup in figure 5.7. The beam size is slightly enlarged vertically due to light scattering on the fluorescence paper. b) illustration of pumping beams using Gaussian optics for comparison.

The scattering of light on the cell walls hitting the ensemble addresses other transitions resulting in a depolarization of the atoms. Therefore, it is essential not to have a beam larger than the probed channel since the clipping on the cell walls decreases the spin polarization. It is also essential to have a polarization state of the pumping beam as purely σ_- polarized as possible. This is achieved by having a polarizer to generate a clean linear polarization of light followed by an achromatic $\lambda/4$ waveplate compatible with both the wavelengths of the D_1 and D_2 line, 894 nm and 852 nm, respectively. This should, in theory, generate a perfect beam of circular polarized light, but the real-world $\lambda/4$ waveplates are not perfect. Therefore, an achromatic $\lambda/2$ waveplate is placed after the $\lambda/4$ waveplate to cancel any slight imperfection of the waveplate. The waveplate combination can be seen in figure 5.7 positioned just before the Powell lens. The degradation of the beam polarization due to the Powell and cylindrical lenses is below our detection resolution for measuring depolarized optical beams. The high achieved spin polarization of 98.7% can only be achieved with a good beam polarization, inferring that the effect of beam polarization degradation from the telescope must be low.

A consideration to further improve the spin polarization past this work could be to pulse shape the repump and pump. A rapid extinguishing of the beams introduces a lot of broadband frequency noise, where the broadband frequency noise is inversely proportional to the cut-off time. The rapid extinguishing of the beams has been shown to diminish the spin polarization in the work of [Dideriksen, 2021, Schmieg, 2023, Bao et al., 2020], where spin polarization is improved by smoothening the extinguishing of the beams.

5.1.5 Thermal occupancy

We want to derive the expression for the added thermal noise from the thermal occupancy n_S in our system. We derive it for preparing the system in the ground state $|4,-4\rangle$. The same derivation can be used for a system prepared in $|4,4\rangle$ being aware of sign changes for the projection of the spin[6]. Following the derivation of [Bærentsen et al., 2023], we can define the ladder operators for the system summing over N atoms:

$$\begin{aligned} \hat{\Sigma} &= \sum_{i=1}^{N} \hat{\sigma}^{(i)}_{m-1,m}, \\ \hat{\Sigma}^\dagger &= \sum_{i=1}^{N} \hat{\sigma}^{(i)}_{m,m-1}. \end{aligned} \tag{5.7}$$

The density operator is defined as $\hat{\sigma}_{a,b} = |a\rangle\langle b| = |F,a\rangle\langle F,b|$. The ladder operators can give the total number of atoms: $N_m = \langle \hat{\Sigma}^\dagger \hat{\Sigma}\rangle$, and it has the commutation: $[\hat{\Sigma}, \hat{\Sigma}^\dagger] = N_{m-1} - N_m$. The bosonic ladder operators are defined to have the commutation relation:

$$[\hat{b}, \hat{b}^\dagger] = 1. \tag{5.8}$$

We can write up bosonic ladder operators for our system by normalizing our ladder operators:

$$\hat{b} = \frac{\hat{\Sigma}}{\sqrt{N_{m-1} - N_m}} \tag{5.9}$$

We can then calculate the number for the thermal occupancy by using the definition:

$$n_\mathrm{S} = \langle \hat{b}^\dagger \hat{b}\rangle = \frac{N_m}{N_{m-1} - N_m}. \tag{5.10}$$

We want to calculate the distribution over the levels from the MORS measurement to infer the spin polarization and the thermal occupancy in our calibration. We measure the difference of distribution between two subsequent m_F levels when measuring a transition with the MORS technique:

$$\alpha A_m = \Delta N_m = N_m - N_{m+1}, \tag{5.11}$$

where A_m is the measured transition amplitude between two m_F levels, and α is a constant. We can assume for a pumped ensemble that the projection oppositely

[6]Equation 5.10 changes in the negative mass configuration change to $n_\mathrm{S} = \frac{N_m}{N_{m+1} - N_m}$.

oriented to pumped transition has a population of zero $N_4 = 0$. Therefore, we have the boundary condition $\alpha A_3 = N_3$. This makes it possible for us to write up the population for each level:

$$\begin{aligned} N_m &= \alpha \sum_{k=m}^{F-1} A_k, \\ N_{\text{total}} &= \alpha \sum_{m=-F}^{F-1} \sum_{k=F-1}^{m} A_k = \alpha \sum_{k=-F}^{F-1} (k+5) A_k. \end{aligned} \tag{5.12}$$

We can, from the above formulas, calculate fraction of atoms in a m_F level:

$$N_m / N_{\text{total}} = P_m = \frac{\sum_{k=m}^{F-1} A_k}{\sum_{k=-F}^{F-1} (k+5) A_k}. \tag{5.13}$$

The spin polarization is the length of F_x compared to the total length of the spin:

$$p = \frac{|\langle F_x \rangle|}{F} = \frac{1}{F} \left| \sum_{k=-F}^{F-1} m P_m \right|. \tag{5.14}$$

High spin polarization

We can practically not measure A_{-1} for a high spin polarization. It is often only 3 peaks that are measurable, which also motivated the 3-peak model earlier described in this chapter. We can write up the boundary condition for the 3-peak model as $N_{-1} \approx 0 \rightarrow \alpha A_{-2} = N_{-2}$. In this regime, we use the following formula for the calculation of the level distribution:

$$P_m = \frac{\sum_{k=m}^{2-F} A_k}{\sum_{k=-F}^{2-F} (k+5) A_k}. \tag{5.15}$$

When running the experiment in the high spin polarization regime, we only measure the mode between the ground and the first excited state. Therefore, we only consider the thermal occupancy between the ground state and the first excited state:

$$n_{\text{S}} = \frac{N_m}{N_{m-1} - N_m} = \frac{A_{-2} + A_{-3}}{A_{-4}}. \tag{5.16}$$

CHAPTER 6

Atomic readout: Calibration of spin-light coupling by coherently induced Faraday rotation

This chapter introduces the experimental technique of calibrating the atomic readout with the method of coherently induced Faraday rotation (CIFAR) presented in the published work:

Rodrigo A. Thomas, Christoffer Østfeldt, **Christian Bærentsen**, Michał Parniak, and Eugene S. Polzik, *Calibration of spin-light coupling by coherently induced Faraday rotation.* Optics Express 29, 23637-23653 (2021).

The published work can be found in appendix F.

6.1 Introduction to the CIFAR technique

This introduction presents key aspects of the published work [Thomas et al., 2021]. The full text of the paper can be found in appendix F.

The technique of calibrating the readout rate, Γ_S, is paramount for calibrating the oscillator. Determining the coupling strength between spin and light is highly coupled to the detection efficiency, making it challenging to measure. Previous calibration of the readout rate in [Møller et al., 2017] used a noise modeling of an increased probe power to extrapolate the ratio of noise processes through the difference of noise scaling to the readout rate[1]. On the other hand, the CIFAR method relies on a coherent drive of the spin oscillator that is self-sufficient and does not rely on any other calibrations.

The CIFAR method is motivated by the optomechanical method known as optomechanically-induced transparency (OMIT) [Weis et al., 2010], where a phase-modulated drive induces a signal that enables extraction of the coupling strength

[1]The method uses the scaling presented in equation 2.36 of the quantum back-action noise and the thermal noise, where they scale quadratically and linearly with the readout rate, to calibrate the quantum cooperativity.

between light and the mechanical oscillator without being sensitive to neither the detection efficiency nor the driving strength.

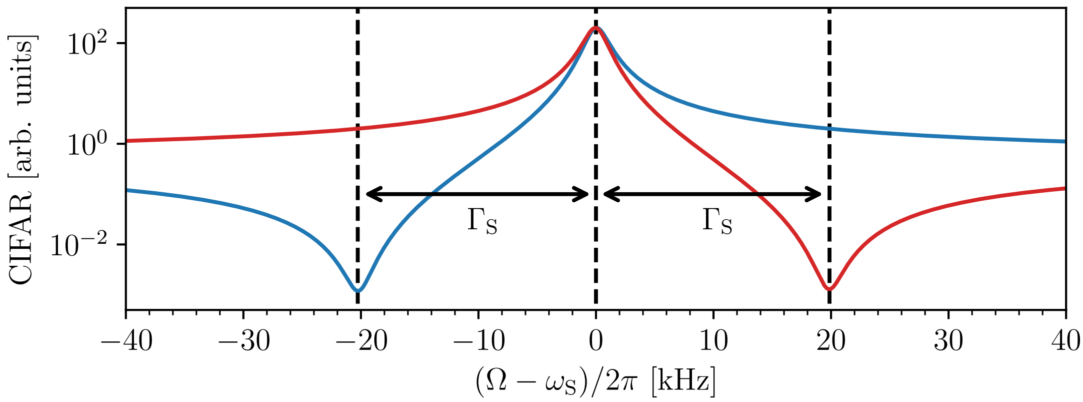

Figure 6.1: Illustration of the CIFAR signal. The spin system is driven with a polarization modulation having equal amplitudes for the two orthogonal light polarization. The drives are phase shifted by $\pi/2$ for the curves in red and blue. The curves illustrate an ensemble with a readout rate of $\Gamma_S = 20\,\text{kHz}$ and a decay rate of $\gamma_S = 2\,\text{kHz}$.

The CIFAR technique relies on a drive on the transverse quadratures of light, X_L^{in} and P_L^{in}. Therefore, only addressing/amplifying the light components associated with the transverse input drive. The input-output relation of the spin in equation 2.27 can be rewritten, showing the case without dynamical back-action, to only incorporate the terms, including the quadratures of light:

$$\begin{aligned} X_L^{out} &= X_L^{in}, \\ P_L^{out} &= P_L^{in} + 2\Gamma_S \chi_S X_L^{in}. \end{aligned} \tag{6.1}$$

The thermal noise processes are neglected due to the classical drive dominating the signal. The classical drive modulates the orthogonal linear polarization and the orthogonal circular polarization of the input light. The method relies on having an equal classical drive for the two quadratures; $P_L^{in} = \pm X_L^{in} = G$, giving us the ability to rewrite the above equation:

$$P_L^{out} = (1 \pm 2\Gamma_S \chi_S) G. \tag{6.2}$$

Giving rise to the characteristic spectrum of the CIFAR method:

$$\text{CIFAR}(\Omega) = |P_L^{out}(\Omega)|/G|^2 = 1 + 4\Gamma_S^2 |\chi_S(\Omega)|^2 \pm 4\Gamma_S \text{Re}[\chi_S(\Omega)]. \tag{6.3}$$

The CIFAR signal arises from the same dynamics of the spin-light interface as the spin-induced light squeezing. This can be seen for the shot noise and quantum back-action noise in equation 2.38 illustrating the squeezing signal. The characteristic dip of the CIFAR signal emerge from the negative cross-correlational between the X-quadrature of the atomic spin and the modulation drive.

The strength of the CIFAR method is its ability to convert the readout associated with a scaling of the noise spectrum into a frequency dependent variable, making the detected signal independent of detection losses. An illustration of the model and how it converts the readout rate into a frequency dependent parameter can be seen in figure 6.1. The distance between the minimum and the maximum of the CIFAR signal is $|\Omega_{\text{min}} - \Omega_{\text{max}}| = \sqrt{\Gamma_{\text{S}}^2 + \gamma_{\text{S}}^2}$, where the separation can be approximated to be the readout rate, $|\Omega_{\text{min}} - \Omega_{\text{max}}| \approx \Gamma_{\text{S}}$, for a high quantum cooperativity, $\Gamma_{\text{S}} \gg \gamma_{\text{S}}$.

We are concluding the introduction to the CIFAR technique - a robust method for measuring the coupling between spin and light that benefits from being a self-sufficient characterization technique. The experimental results and detailed description are presented in appendix F.

Part III

Experimental realizations and simulations of motional averaging in a hot vapor cell

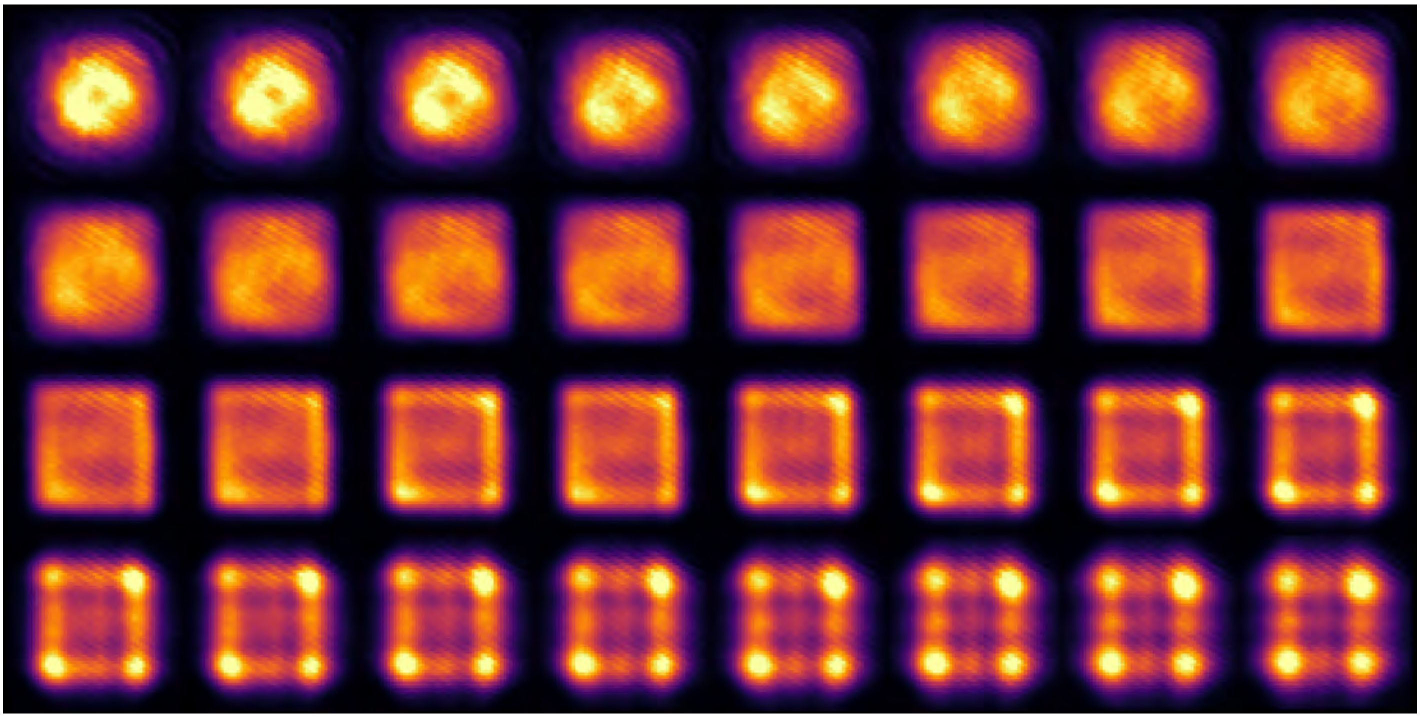

In the following chapters, we cover the influence of motional averaging for the readout of the atomic state and the effect of magnetic inhomogeneities of the bias magnetic field.

Motional averaging relates to the individual atoms of the hot vapor moving inside the cell with a velocity dictated by the Maxwell-Boltzmann distribution. As a result, the atoms encounter inhomogeneities in the dynamics that characterize the ensemble. The inhomogeneities are averaged over the motion of the atoms. The critical time scale of these effects is for the coherence time to be longer than the time of the motional averaging, $1/\gamma_{S0} > \tau_{\text{motion}}$.

The motional averaging comes with a price in the form of dephasing of the atomic ensemble for the magnetic inhomogeneities and excess noise from the decay in the dark for the atomic readout. We have addressed these issues by innovating new experimental techniques uncovered in the succeeding chapters: implementing a new coil system to improve dephasing processes and implementing a square tophat beam to improve the fast decaying modes arising from imperfect motional averaging.

At last, simulations of the motional averaging processes are covered, which have been used to investigate experimental boundaries of motional averaging, effect of cell geometries, and the practical benefits of implementation. Finally, the experimental results are compared to the simulated results assessing the quality of the simulated forecasting, which is used as a decision tool for experimental implementations.

CHAPTER 7

Magnetic inhomogeneities

When an atomic ensemble resides in a static magnetic field, the Larmor precession of the atomic spin is determined by the strength of the magnetic field. Due to the spatial extent of our ensemble, the strength of the magnetic field varies across the cell dimensions resulting in a spatial variation of the local Larmor frequency. The velocity of the atomic ensemble is thermally distributed with a mean velocity along one axis of 142 [m/s] for a cesium ensemble at 50 °C. As a result, the atoms experience a variation in the Larmor frequency as they move through the magnetic field of varying strength. The shifting Larmor frequency induces dephasing of the ensemble, broadening the oscillator's response. The effect of dephasing can be accommodated by improving the homogeneity of the magnetic field.

We have, in the work of this thesis, changed our cell geometry from a cell with a cross-section of 300 µm × 300 µm and a length of 10 mm to a cell with a cross-section of 1 mm × 1 mm and a length of 40 mm[1]. The biggest concern regarding the magnetic inhomogeneities is the elongated geometry since it is experimentally harder to ensure a high magnetic field homogeneity over the entire cell length. The geometry change has therefore elevated our sensitivity to the magnetic inhomogeneities, introducing a need for design change of the coil system generating the magnetic field.

We are in the following of this chapter, detailing the change of coil design and experimental characterization of the new coil system.

7.1 Magnetic field generation

The atomic ensemble is positioned in a magnetic shield of 4 layers: aluminum, μ-metal, μ-metal, and iron from the inside and out. The aluminum is good at shielding electromagnetic radiation at higher frequencies in the RF domain. The μ-metal is a ferromagnetic alloy of high permeability that can shield the cell from an external magnetic field. The iron also has some magnetic shielding effect like the μ-metal, but it also serves as a cheaper outside protection of the other layers. The magnetic shield serves the purpose of canceling the effect of the earth's magnetic

[1]The reasoning for the change of geometry is explained thorough chapter 8 and 9.

field and magnetic fields from laboratory equipment. The shield is cylindrically shaped with an inner diameter of 150 mm and an inner length of 350 mm.

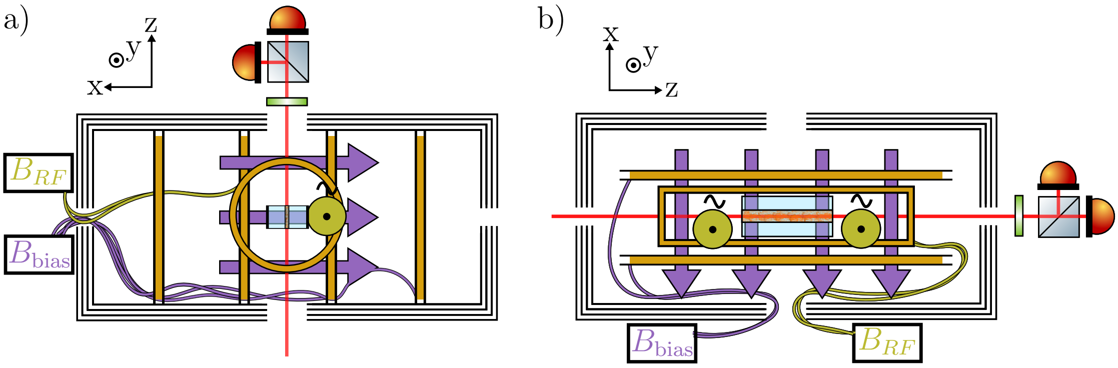

Figure 7.1: Rotating the experimental setup for a more homogeneous magnetic field. The purple arrow is the bias magnetic field, and the olive arrow, pointing out of the plane, is the coil for the coherent RF drive. a) the previous experimental setup in a Lee-Whiting coil configuration. b) the current experimental setup to accommodate the larger cell size.

We were in a position where it was required of us to reduce the magnetic inhomogeneities over the cell geometry. The previous experimental configuration was using a Lee-Whiting coil configuration [Kirschvink, 1992], where a series of Helmholtz coils are applied to cancel the magnetic inhomogeneities over the cell geometry. Figure 7.1a shows the previous experimental configuration. The cell's long axis was orthogonal to the long axis of the shield. The magnetic inhomogeneities increase for this configuration when you are getting closer to the diameter/edge of the Helmholtz coils, which would not be suitable for a larger cell geometry. The current experimental setup can be seen in figure 7.1b, where the cell is rotated to align the magnetic shield's long axis to the cell's long axis. This gives some technical challenges of a new coil design, but also for all the optical beams, especially the pumping beams, addressed in section 5.1.4.

Jürgen Appel first started investigating magnetic inhomogeneities to simulate complex coil shapes imprinted onto printed circuit boards (PCB). The efforts into using PCB coils for magnetic field generation was picked up by [Yde, 2020] and later joined by Jun Jia for the experimental testing of the PCB coils. The PCB coil system can be seen in figure 7.2a. The figure shows the EXCITATION PCB coil on top used for coherent displacements and the CAP PCB coil on the side to generate the bias magnetic field. The EXCITATION PCB coil has a c-shaped design such that the coil system can be removed easily so that we can get access to the atomic cell. The CAP PCB coil has an elongated cutout in the center to accommodate the access of the pumping beams to the atomic cell.

The PCB coils work similarly to Helmholtz coils, where two identical coils are displaced, having the current flowing in the same direction of the two coils. The PCB coils are simulated to generate a perfect homogeneous magnetic field for a given volume. This also works when measuring the generated magnetic field of the PCB coils. The PCB coils can then be positioned in a magnetic shield, where the reflected field of the shield walls alters the magnetic field generated by the PCB coils. All the PCB coils are simulated by [Yde, 2020] for this experiment.

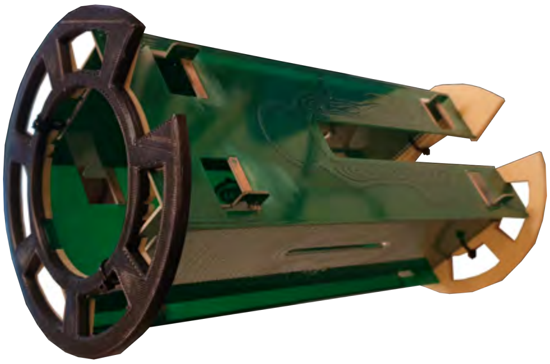

a)

b)

Figure 7.2: Mounted coil systems. a) PCB coil system showing the EXCITATION PCB coils and CAP PCB coils. b) RECTANGLE coil system with the geometry of 320 mm×100 mm and a separation between the coils of 60 mm.

7.2 Experimental characterization of the coil system

The magnetic field has to be characterized inside the magnetic shield to account for the effect of the shield on the magnetic field. The setup for characterizing the magnetic field inhomogeneities can be seen in figure 7.3. A cubic cell with a volume of 5 mm×5 mm×5 mm is attached to a hollow glass rod on a translation stage. This hollow glass rod allows us to move the cell without obscuring the probe beam path for measuring the interaction with the atoms using homodyne detection. The repump laser is expanded to cover the full measured range, transferring atoms to the $F = 4$ manifold. The Larmor frequency can then be calculated from the detected signal for each cell position. This technique uses atoms as a precise magnetometer to measure the positional dependency on the magnetic field. The spin oscillator is driven by white noise applied using an orthogonal pair of coils in order to increase the SNR in the detection of the Larmor frequency. The central Larmor frequency of the cell is determined for each position for magnetic field strength determination.

The most homogeneous magnetic field generated by the PCB coils in a magnetic shield is generated by the CAP PCB coils[2]. The shape of the magnetic field generated by the PCB coils strongly depends on the separation between the two coils. The magnetic field also depends on the geometry and the shield's permeability. This means that characterization of the PCB coils must be remeasured when implemented into a new magnetic shield. The magnetic field generated by the CAP PCB coils can be seen in figure 7.4, where the separations between the PCB coils are 82 mm and 86 mm in a) and b), respectively. The magnetic field is first measured in

[2]The PCB coils are named after their curvature with the CAP PCB coils having a negative second-order curvature - forming a cap shape.

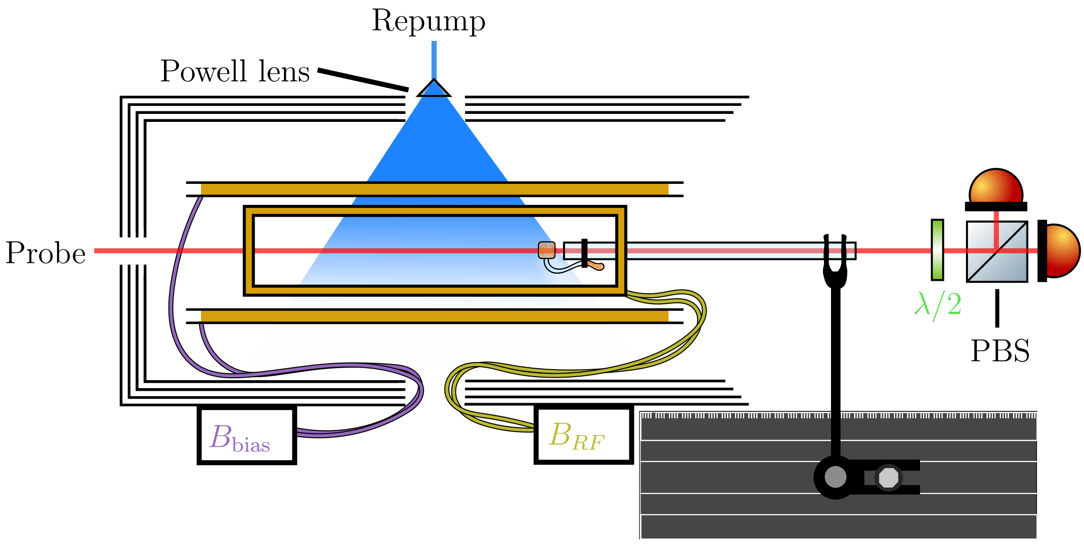

Figure 7.3: Experimental setup for measuring the magnetic inhomogeneities. A cubic cell is used as a magnetometer on a translation stage to map the positional dependency of the Larmor frequency. The probe interacts with the cubic cell and is measured through homodyne detection.

one direction, represented by the blue dots, where the magnetic field is flipped by an equal alternating current, represented by the orange dots. This process removes the background by taking the average of the two measurements, primarily influenced by the earth's magnetic field. The alignment of the magnetic moment to the earth's magnetic field is achieved with demagnetization or degaussing by resetting the alignment with a strong magnetic field [Thiel et al., 2007]. This explains the big difference in the background between figure 7.4a and 7.4b. The red fit is a polynomial applied to quantify the curvature of the field: $f(x) = a_0 + a_2x^2 + a_3x^3 + a_4x^4$. The most essential magnetic field parameters are a_2 and a_4 for the characterization of the field homogeneity. The parameter a_3 has a minor scaling that probably comes from the wiring and the shield's opening required for translating the cubic cell.

The magnetic field performed by the CAP PCB coils is insufficient. The idea is, therefore, to generate a set of PCB coils with opposite curvature that we refer to as the CUB PCB coils. The opposite curvature can then cancel the second-order scaling of the inhomogeneities of the CAP PCB coils, using the same principle as a Lee-Whiting coil configuration to cancel the magnetic inhomogeneities. The magnetic inhomogeneities of the CUB PCB coils can be seen in figure 7.5 for a PCB coil separation of 74 mm and 78 mm in a) and b), respectively. The fitted curves can be seen in table 7.1, for which the CUB PCB coils can be compared with CAP PCB coils.

The best combination of the PCB coils for a homogeneous magnetic field is the CAP - 82 mm and the CUP - 78 mm calculated from the fitted magnetic profiles. The theoretical best magnetic field generated by combining the CAP and the CUP can be seen in figure 7.6. The standard deviation of the magnetic field homogeneity over the central 40 mm (the length of our atomic cell) is $\sigma = 27$ ppm. This was considered acceptable for the application resulting in a broadening of

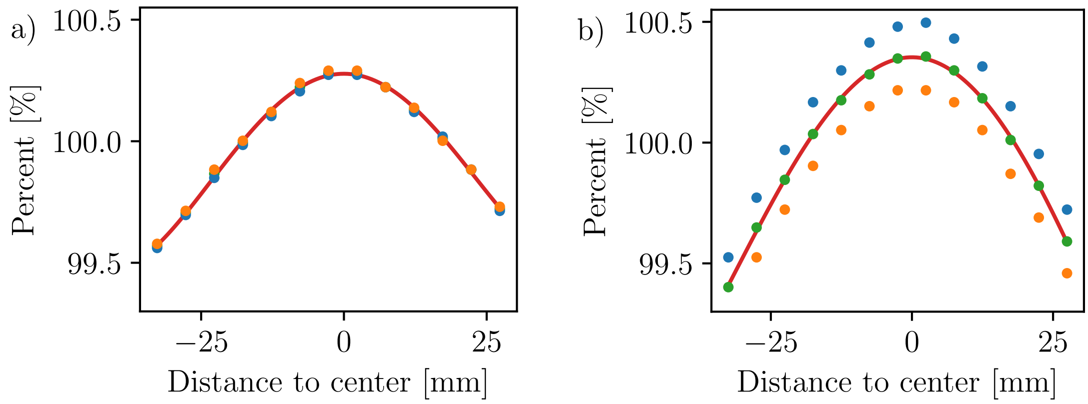

Figure 7.4: Magnetic inhomogeneities of the CAP PCB coil design. The magnetic field is measured for two field directions in blue and orange dots, where the green dots are averages. The measurement is normalized to the mean Larmor frequency. a) measurement of the CAP PCB coils with a separation of 82 mm. b) measurement of the CAP PCB coils with a separation of 86 mm. The values for the fitted red curves can be seen in table 7.1.

Coils - separation	a_2	a_3	a_4
CAP - 82 mm	$-9.7 \cdot 10^{-4}$	$2.6 \cdot 10^{-7}$	$3.0 \cdot 10^{-7}$
CAP - 86 mm	$-1.2 \cdot 10^{-3}$	$-1.2 \cdot 10^{-6}$	$1.8 \cdot 10^{-7}$
CUP - 74 mm	$8.9 \cdot 10^{-3}$	$-5.5 \cdot 10^{-6}$	$-2.4 \cdot 10^{-7}$
CUP - 78 mm	$7.9 \cdot 10^{-3}$	$-1.6 \cdot 10^{-6}$	$-4.8 \cdot 10^{-7}$
RECTANGLE - 60 mm	$7.4 \cdot 10^{-5}$	$1.8 \cdot 10^{-7}$	$2.3 \cdot 10^{-8}$
EXCITATION - 110 mm	$-9.4 \cdot 10^{-3}$	$-1.3 \cdot 10^{-4}$	$-1.7 \cdot 10^{-6}$

Table 7.1: Fit of the magnetic inhomogeneities: $f(x) = a_0 + a_2x^2 + a_3x^3 + a_4x^4$. a_0 approximates to 100 for all the coils as the data is normalized to the average field strength.

$\gamma_{\text{dephasing}} \approx 200\,\text{Hz}$ at 1.37 MHz. However, the number for the broadening comes with a notable uncertainty, which comes from an inherent heating limitation for the PCB coils, resulting in a heating of the cell inducing other broadening processes, making the estimation of the broadening challenging.

The strength of the magnetic field generated by the PCB coils is very low compared to the applied current and resistance of the coils. The required currents for reaching 1.37 MHz for the PCB coils are 0.6 A and 1 A for the CUP PCB coils and CAP PCB coils, respectively. This results in a heat dissipation of 135 W from the coils. The magnetic shield works as a heat insulator around the coils from having the 4 layers of metal. An equilibrium temperature of 50 °C is achieved by having 15 watts dissipated inside the magnetic shield. This is one order of magnitude below the dissipated power of the PCB coils. The problem of the heat dissipation arises from the original design of the PCB coils, where it was meant to be used in the work of [Yde, 2020] having a much lower Larmor frequency around

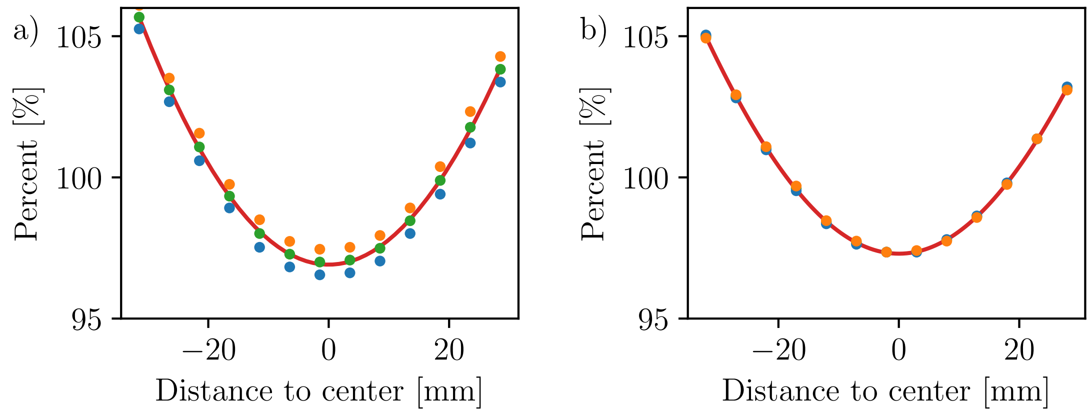

Figure 7.5: Magnetic inhomogeneities of the CUP PCB coil design. The magnetic field is measured for two field directions in blue and orange dots, where the green dots are the averages. The measurement is normalized to the mean Larmor frequency. a) measurement of the CUP PCB coils with a separation of 74 mm. b) measurement of the CUP PCB coils with a separation of 78 mm. The values for the fitted red curves can be seen in table 7.1.

50 kHz. The heating of the coils scales quadratically to the amount of current, but the magnetic field strength only scales linearly to the current. This means that the heat dissipation scales quadratically to the Larmor frequency, giving a heat dissipation for a 50 kHz Larmor frequency of 0.2 W.

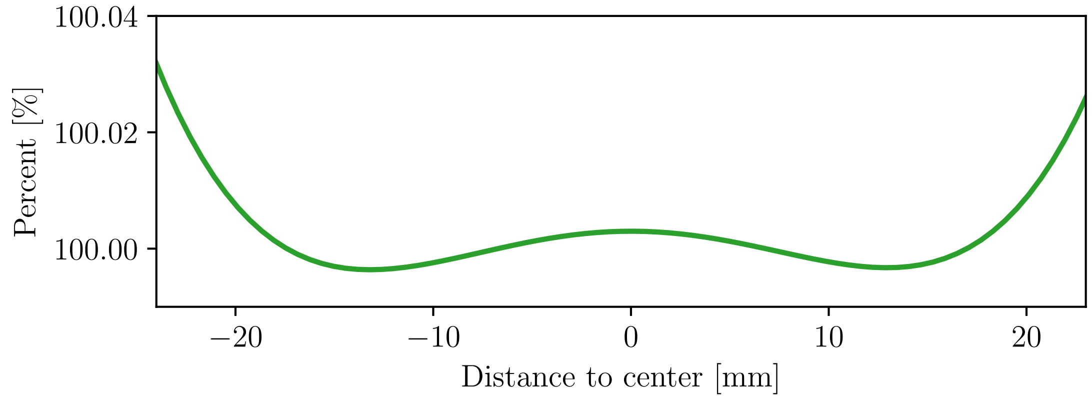

Figure 7.6: Best magnetic field homogeneity by combining the CAP - 82 mm and the CUP - 78 mm. The curve is generated from an optimal ratio between the fitted polynomials for the two coils. The standard deviation of the magnetic field over the central 40 mm is $\sigma = 27$ ppm.

We came up with a new idea for a design of a coil system using a RECTANGLE coil design. The idea was based on the boundary condition of having an infinite elongated rectangular coil design. This theoretical limit would create an infinite homogeneous magnetic field along the elongated axis of the coils. The coil design should therefore be an elongated RECTANGLE coil stretching as far as possible in the cylindrical shield. Another addition to creating a more homogeneous field was implementing the Python simulation using the software package *bfieldtools*[3]. This made it possible to simulate the effect of the magnetic shield on the coil system to first order before implementing them experimentally. Unfortunately, it was not directly possible to design PCB coils using *bfieldtools* since the PCB simulation software's physical principles were incompatible with the package, where the entire software would have to be rewritten to include the package.

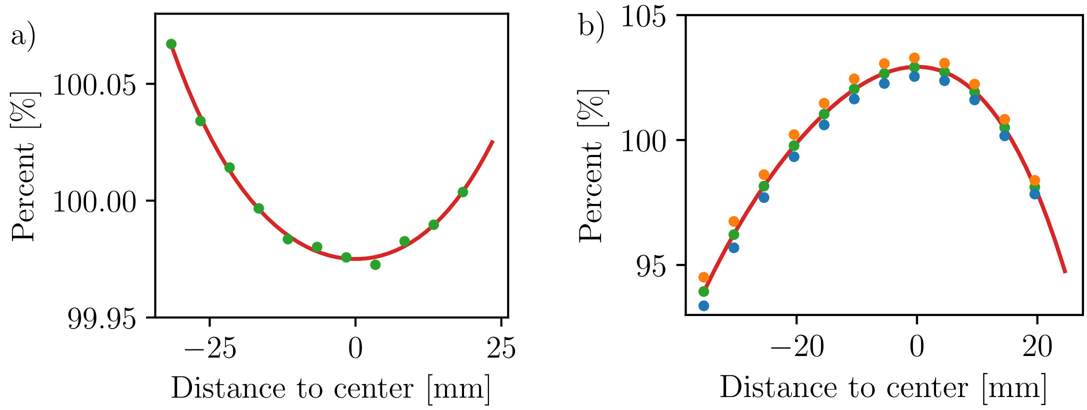

Figure 7.7: Magnetic inhomogeneities of the RECTANGLE coil design and the EXCITATION PCB coil design. The magnetic field is measured for two field directions in blue and orange dots, where the green dots are the averages. The measurement is normalized to the mean Larmor frequency. a) measurement of the RECTANGLE coils with a 60 mm separation. b) measurement of the EXCITATION PCB coils with a separation of 110 mm. The standard deviation of the EXCITATION field over the cell length is $\sigma = 1\%$. The values for the fitted red curves can be seen in table 7.1.

Implementing the RECTANGLE coil design was collaborative work with Sergey A. Fedorov in designing and experimental testing the coil system. The design of the RECTANGLE coil system can be seen in figure 7.2b. The coil system has a RECTANGLE geometry of 320 mm$\times$100 mm and a separation of 60 mm. We also designed a much smaller winded compensation coil seen in figure 7.2b, but it did not show promising results. The measured magnetic field of the RECTANGLE coil design can be seen in figure 7.7a, showing a magnetic field homogeneity close to that generated by the CAP and CUP coils combined. The background subtraction from the orange and blue dots can not be seen in figure 7.7a because the background is much larger than the inhomogeneities of the RECTANGLE coils. The fitted curves can be seen in table 7.1, where the RECTANGLE coils show homogeneity levels one order of magnitude better than the CAP PCB coils.

The magnetic inhomogeneities can be improved even more by combining the design of the RECTANGLE coils and the CAP PCB coils since the quadratic term for the two coils is opposite. The heat dissipation of the CAP PCB coils

[3]https://bfieldtools.github.io/authors.html created by Joonas Iivanainen, Antti Mäkinen, and Antti Mäkinen.

is not a problem because of the large difference in homogeneity between the two coil systems, such only a tenth of the current is going through the CAP PCB coils. This generates around 2 watts of dissipated power at 1.37 MHz, below the 15 watts that saturates the temperature of the cell at 50 °C. The coil system for a hybrid coil system by combining the RECTANGLE coils, the CAP PCB coils, and the EXCITATION PCB coils can be seen in figure 7.8. The theoretical magnetic field from combining the RECTANGLE coils and the CAP PCB coils can be seen in figure 7.9, where the standard deviation of the magnetic field over the central 40 mm is $\sigma = 5$ ppm. The added broadening from this magnetic field is $\gamma_{\text{dephasing}} \approx 90\,\text{Hz}$ at 1.37 MHz. The small amount of dephasing achieved is acceptable for the experiment, which is lower than the atom-atom collisional and wall collisional broadening that is $\gamma_{\text{collisional}} \approx 110\,\text{Hz}$. The dominant decay process for the atomic spin in our experiment is probe induced decay, which exceeds the decay rate in the dark at about 0.5 mW of probe power at 3 GHz detuning, where the probe induced decay is $\gamma_{\text{probe}} \approx 200\,\text{Hz}$.

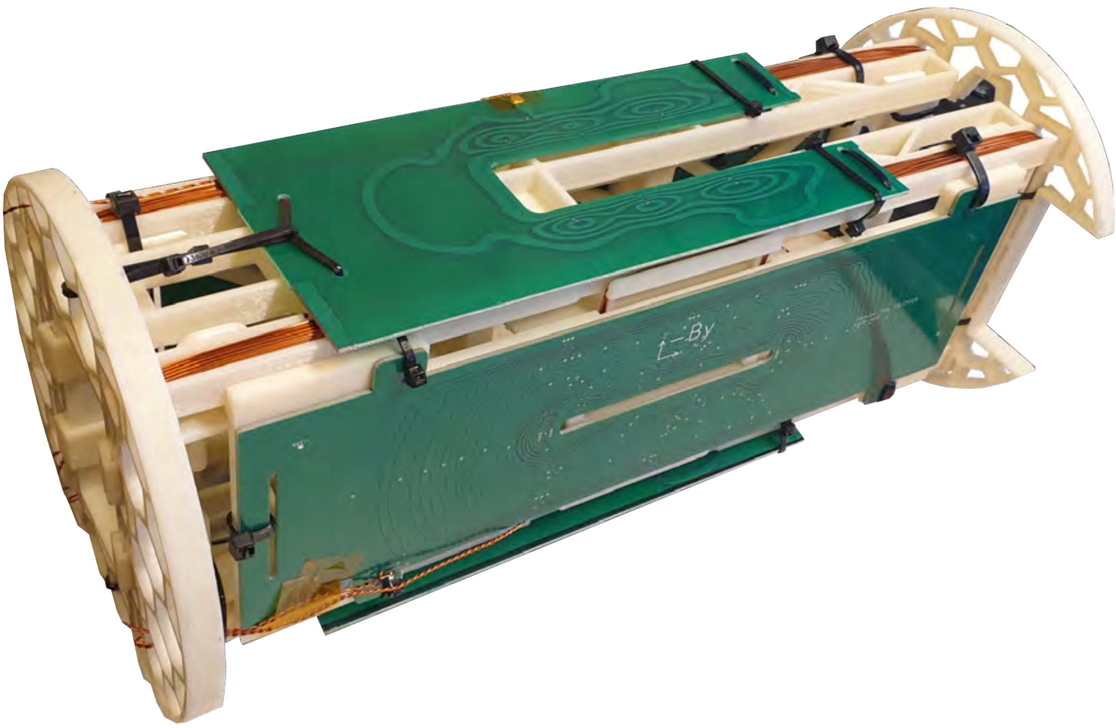

Figure 7.8: Mounted hybrid coil system. The PCB coils are mounted on the RECTANGLE coil frame. The EXCITATION PCB coils are placed on top and below the frame with a separation of 110 mm, and the CAP PCB coils are placed on both sides of the RECTANGLE coils with a separation for the CAP PCB coils of 86 mm.

The magnetic field homogeneity of the EXCITATION PCB coil is also relevant since it determines the homogeneity of the coherent displacement when driving the atoms. The requirement for field homogeneity is much lower than that of the bias magnetic field. The measurement of the field homogeneity for the EXCITATION PCB coil is performed similarly to the bias coils, where the CAP PCB coils are used for white noise driving to enhance the atomic signal instead of using the EXCITATION PCB coils for this process since the EXCITATION PCB coils serve the purpose of the bias magnetic field for this measurement. The measured magnetic field for the EXCITATION PCB coils can be seen in figure 7.7b. The fitted red curve can be seen in table 7.1, showing that the homogeneity of the magnetic field is limited by the uneven (a_3) parameter because of the c-shape of the coils. The standard deviation of the magnetic field over the central 40 mm is $\sigma = 1\%$ ($\sigma = 10^4$ ppm), which means that the coherent displacement when driving the atomic ensemble is uniformly displaced within 1% standard deviation. This is considered to be acceptable.

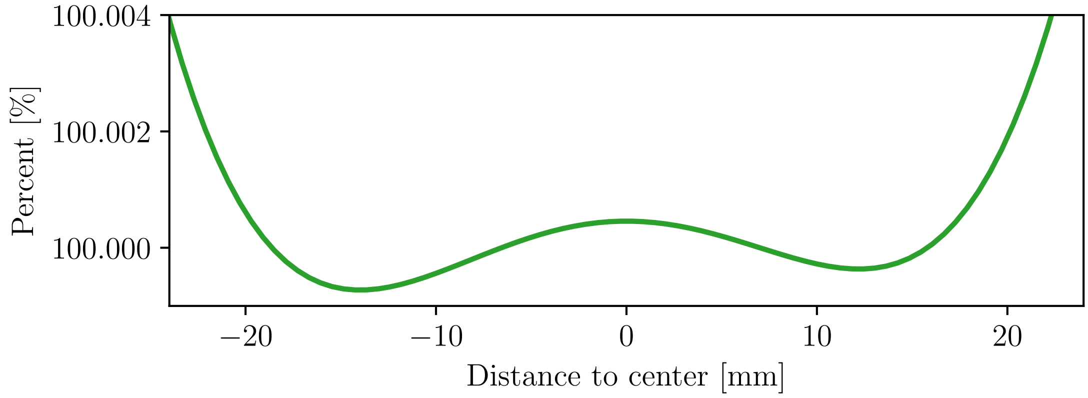

Figure 7.9: Best magnetic field homogeneity by combining the RECTANGLE - 60 mm and the CAP - 86 mm. The curve is generated from an optimal ratio between the fitted polynomials for the two coils. The standard deviation of the magnetic field over the central 40 mm is $\sigma = 5$ ppm.

Figure 7.10: Heating pad for temperature regulation of the atomic ensemble. Product: OMEGA PLM-106/10-P. Image reused from product website: *https://sea.omega.com/ph/pptst/PLM-SERIES.html*.

We had to implement a new heating system to elevate the cell temperature, in a range of 50−70 °C, without alternating the magnetic field inside of the shield. The previous heating of the cell was introduced by having a wire made of a semiconducting material to heat the shield. The wire was folded in half and twisted to cancel the magnetic field generated by the wire. The wire was wrapped around the coil frame giving it good thermal contact. This was not possible with the new coil frame made of the plastic material ABS. The new method was to heat the shield with a heating pad (OMEGA PLM-106/10-P) shown in figure 7.10. The heating pad was placed in the bottom of the magnetic shield to have good thermal contact and to create a gradient between the channel of the cell and the stem of the cell (the cell terminology for the cell geometry is explained in figure 2.4). The temperature gradient makes the cesium condense back in the stem, which is desired for avoiding cell clogging (see appendix B for explaining clogging of the cell) or cesium condensing on the windows of the cell. The stem points upwards away from the heating pad, creating a heating gradient of $1-2\,^{\circ}\mathrm{C}$ between the cell's body and the stem. The advantage of this heating pad is the wire configuration aligned to have the forward and alternating current co-aligned for magnetic field cancellation.

CHAPTER 8

Fast decaying spin-modes from an inhomogeneous readout

In this chapter, we investigate the effect of motional averaging on the light-spin interaction arising from the uneven probing, consequently, an uneven readout for the state of the spin ensemble. The atoms decaying in the dark give rise to fast decaying spin-modes, referred to as one unity named the broadband noise (BBN) due to its broad spectral profile. The single atom response, resembling the mode of the long-lived oscillator response, is referred to as the narrowband noise (NBN) due to its narrow spectral mode profile.

Through experimental investigation, the BBN has been shown to consist of uncorrelated noise, raising the overall extrinsic noise level in detection. It is treated similarly to shot noise because it is much broader than the NBN, therefore, considered to be flat around the oscillation frequency.

The BBN arises from the lack of information about the atoms in the dark; therefore, the BBN can be reduced by increasing the filling factor of the probe beam. This is shown for a cell with a cross-section of $0.5\,\mathrm{mm} \times 0.5\,\mathrm{mm}$ and a length of $25\,\mathrm{mm}$ in figure 8.1 for a varying beam size. The data around the oscillation frequency is removed to focus on the BBN. The figure illustrates the reduction of BBN resulting from an increase in beam size, showing a reduction from 8 to 2 shot noise units. This is for increasing the Gaussian beam size by a factor of 2, reducing the BBN by a factor of 4 for this measurement.

The size of the Gaussian beam is limited by the geometry of the atomic channel, limiting the reduction of BBN without introducing significant clipping losses for the Gaussian beam. This chapter introduces the use of a non-Gaussian beam for an increased filling factor by implementing a square tophat beam profile.

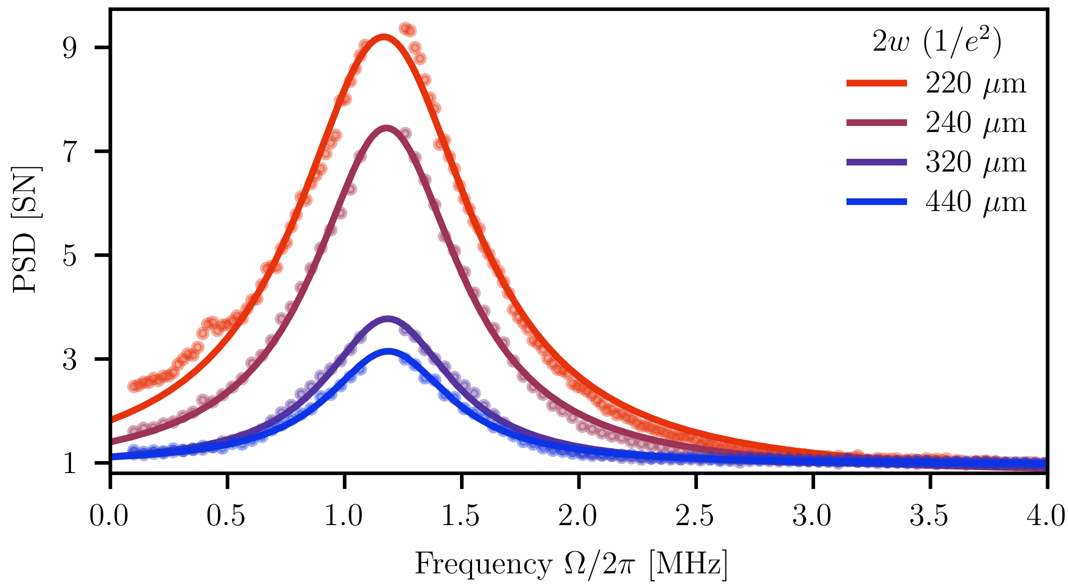

Figure 8.1: Broadband noise dependency on the size of the Gaussian probe beam. Data and fit of the BBN for a varying beam size with the data for the NBN removed. The atomic channel has a cross-section of 0.5 mm × 0.5 mm and a length of 25 mm. The Gaussian width $2w$ is the beam's diameter $(1/e^2)$. The figure has been reproduced from [Thomas, 2020].

8.1 Theoretical interpretation of the broadband noise

The BBN can be described from a mode picture of spatial beam modes with decay rates set by the mean free path. A similar approach is taken in [Shaham et al., 2020], where an elevated noise level is described from an inhomogeneous spin-decay, focusing on the inhomogeneous spin-decay from wall collisions. Another approach to describe the BBN is a time of flight model [Borregaard et al., 2016], following the derivation presented in [Bærentsen et al., 2023] by computing the time-domain correlation function of the atomic motion:

$$R(\tau) = e^{i\omega_S t}\langle x(t)x(t+\tau)\rangle = \langle g(t)g(t+\tau)\rangle, \tag{8.1}$$

where $x(t)$ is the atomic signal and $g(t)$ is the demodulated atomic signal by the oscillation frequency. The correlation function results in the NBN for a large delay $R(\tau \gg \tau_{\mathrm{BBN}}) \to \langle g(t)\rangle^2$, where τ_{BBN} is the decay time of the fast decaying modes. We can write the correlation function of the fast-decaying modes as

$$R(\tau)_{\mathrm{BBN}} = \langle \Delta g(t)\Delta g(t+\tau)\rangle, \tag{8.2}$$

described by the deviation from the mean: $\Delta g(t) = g(t) - \langle g(t)\rangle$. The correlation function for the BBN mathematically expresses the added frequency components emerging from atoms traveling in and out of the beam. We can from the correlation function in equation 8.2 write up the spectrum for the BBN:

$$S_{\mathrm{BBN}}(\Omega) = \int_{-\infty}^{\infty} \langle \Delta g(t)\Delta g(t+\tau)\rangle e^{i(\Omega-\omega_S)\tau} d\tau. \tag{8.3}$$

The width of the BBN is closely related to the transition time of an atom in the channel, approximating the decay rate of the BBN; $1/\tau_{\mathrm{BBN}} = v_{\mathrm{avg}}/(2w) \approx \gamma_{\mathrm{BBN}}/2\pi$, where $2w$ is the beam diameter and v_{avg} is the average transverse speed of an atom. The power ratio between the BBN and the NBN can be written up using the defined correlation functions:

$$\frac{P_{\mathrm{BBN}}}{P_{\mathrm{NBN}}} = \frac{\langle \Delta g(t)^2 \rangle}{\langle g(t) \rangle^2}. \tag{8.4}$$

A more uniformly distributed probe beam can minimize the coupling to the BBN. However, this is challenging due to the propagating mode following Laguerre-Gaussian modes, which makes it challenging to have a large filling factor for the probe beam when having a square chip. The investigation into having a larger filling factor is covered in the succeeding section 8.2.

The BBN arises from the uncorrelated atoms moving in and out of the beam. It is important to note that correlated atoms have a different scaling for the BBN. For example, a collective displacement achieved by the excitation of the transverse spin (see section 5.1 for details about the coherent displacement) excites the BBN less than the NBN because the excitation is correlated for different atoms.

The BBN appears in the spin equation of motion (see section 2.2.2 for details about the spin equation of motion) similar to the NBN with a changed susceptibility. The BBN has a very broadband spectral profile, which puts it in the regime; $\Gamma_{\mathrm{BBN}} \ll \gamma_{\mathrm{BBN}}$, where the readout is much smaller than the decay rate[1]. This entails that the BBN is predominantly thermal noise, whereas the quantum back-action contribution in the spectra of the BBN is negligible. The atomic motion is largely diffusive, which results in a BBN profile being Gaussian. The broadband response can therefore be approximated to have the following relation measured at the P quadrature of light:

$$S_{PP}^{\mathrm{BBN}}/\mathrm{SN} = A_{\mathrm{BBN}} e^{-\frac{1}{2}(\Omega - \omega_{\mathrm{S}})^2/\gamma_{\mathrm{BBN}}^2}, \tag{8.5}$$

where γ_{BBN} is Gaussian width of the BBN and A_{BBN} is the height of the BBN in shot noise units. The BBN changes its shape towards a Lorentzian susceptibility for ballistic motion [Borregaard et al., 2016], which can be seen for vapor cells operating at lower temperatures, having a lower gas pressure.

8.2 Implementation of a square tophat beam

We want to increase the filling factor of the probe beam reading out the atomic ensemble. This can be accommodated by a square tophat beam, which is a beam that resembles a square transverse intensity profile, similar to a super-Gaussian beam profile [Mielec et al., 2018] being a round tophat beam. The square tophat beam profile is to accommodate the square channel size of the atomic cell.

[1]The only operational regime, where this is not the case is presented in part IV Spin induced light squeezing. Demonstrating measurements for maximized readout by tuning closer to resonance.

8.2.1 Tophat beam shaper

There are several methods for generating an arbitrary beam shape. A spatial light modulator is a popular choice for generating arbitrary beam shapes with the disadvantage of optical losses and finite resolution. Therefore, the choice for generating a tophat beam has been a special lens named a tophat beam shaper with a high spatial resolution and low optical losses.

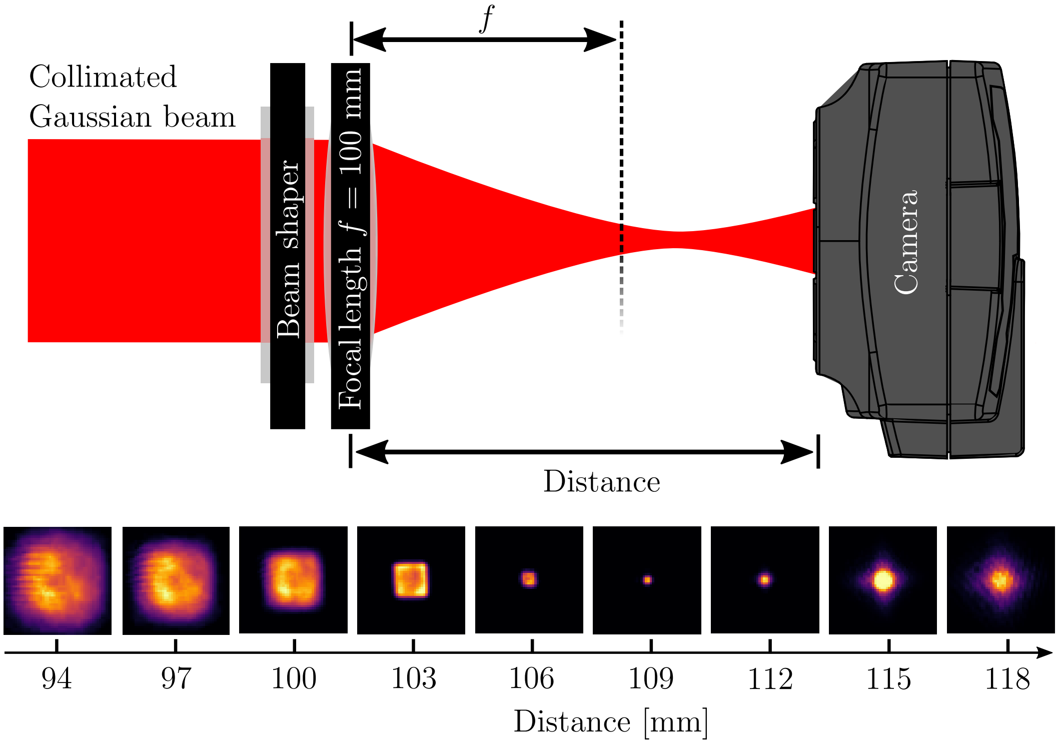

Figure 8.2: Beam shaper generated beam profiles. Optical setup specified by the manufacturer for tophat beam generation. The beam profile is imaged with a Thorlabs camera DCC1545M for distances close to the generation of the best tophat beam and the beam waist. The images have a size of 520 µm × 520 µm.

The beam shaper[2] for the generation of a square tophat beam is primarily designed for high-intensity laser precision welding/cutting, where a focused beam is desirable to have for a sharp square beam profile. Therefore, the beam shaper is designed to have a focusing lens positioned after the beam shaper to determine the size of the tophat and the position of the tophat beam generation, see figure 8.2 for an illustrative optical setup. By design, the most flat/square tophat beam profile is generated one focal length after the focusing lens, referred to as the position of the best tophat beam. The waist of the beam is displaced further away than the best tophat beam, such the beam keeps converging after the best tophat beam generation.

The optical setup for showcasing the beam propagation in the optical setup specified by the manufacturer can be seen in figure 8.2. The distance specifies the

[2]The beam shaper used in this thesis: Topag GTH-3.6-1.75FA.

displacement from the focusing lens, where the best tophat beam is positioned the focal length of lens, $f = L_{\text{best}} = 100\,\text{mm}$, away from the lens, keeping in mind that the focal length of lens may deviate slightly from the manufacturer specification of the lens and the systematical errors of measuring distances from a lens to a camera. The beam has a Gaussian intensity profile after the combination of the beam shaper and lens since the first optical elements only changes the phase front such the beam propagates/converges into a square tophat beam. It is not possible to maintain a square tophat beam profile over a long propagation distance due to the decomposition of the tophat beam into Gaussian modes, where the beam waist is approximately at a distance of 109 mm from the lens. The focusing lens determines the size of the tophat beam, where the size of the best tophat beam is linearly proportional to the focal length of the focusing lens.

The mismatch between the position of the beam waist and the best tophat beam is a manufacturing design giving the beam shaper a slight divergence of 1.75 mrad for our beam shaper. This divergence angle is known as the full fan angle, see manual for details [Eksmaoptics-manual, 2023]. The input beam is a Gaussian beam with a waist of 1.8 mm (radius $1/e^2$).

8.2.2 The generation of a collimated tophat beam

The designed scheme provided by the manufacturer is insufficient for creating a beam that uniformly fills an elongated cell. An illustration of a conceivable optical scheme resulting in a tophat beam with an overlap of the beam waist and the best tophat beam can be seen in figure 8.3a. A negative lens can be placed in the position of the best tophat beam changing the waist position to coincide with the best tophat beam referred to as a collimated tophat beam. The focal length can be calculated from lens equations using the full fan angle of the beam shaper ϕ_{FA}, the input beam size w_{in}, and the focal length of the focusing lens f_1:

$$f_2 = \frac{\phi_{\text{FA}}/w_{\text{in}} f_1}{\phi_{\text{FA}}/w_{\text{in}} - 1/f_1}. \tag{8.6}$$

The lens system shown in figure 8.3a would require the last lens to be positioned inside the cell for a good tophat beam generation making it disadvantageous. The course has been to decompose the intuitive/conceivable lens system into a ray transfer matrix $\mathbf{M}_a$, where a more advantageous optical scheme can generate with the same ray transfer matrix. The optical scheme in figure 8.3b shows a non-intuitive optical scheme for generating a tophat beam. The optical scheme has three free variables L_1, L_2, and L_3, where the focal length of the lenses F_1 and F_2 are fixed. Having more free parameters than minimally required is useful because the ray transfer matrix can be matched to fulfill the condition $\mathbf{M}_a = \mathbf{M}_b$ while giving us the flexibility to choose the lens positions suited for our experimental setup. We can write the ray transfer matrices for the two systems as

$$\begin{aligned} \mathbf{M}_a &= \mathbf{L}(f_2)\mathbf{S}(f_1)\mathbf{L}(f_1), \\ \mathbf{M}_b &= \mathbf{S}(L_3)\mathbf{L}(F_2)\mathbf{S}(L_2)\mathbf{L}(F_1)\mathbf{S}(L_1). \end{aligned} \tag{8.7}$$

We use ray transfer matrices for propagation in free space, $\mathbf{S}$, and passing through

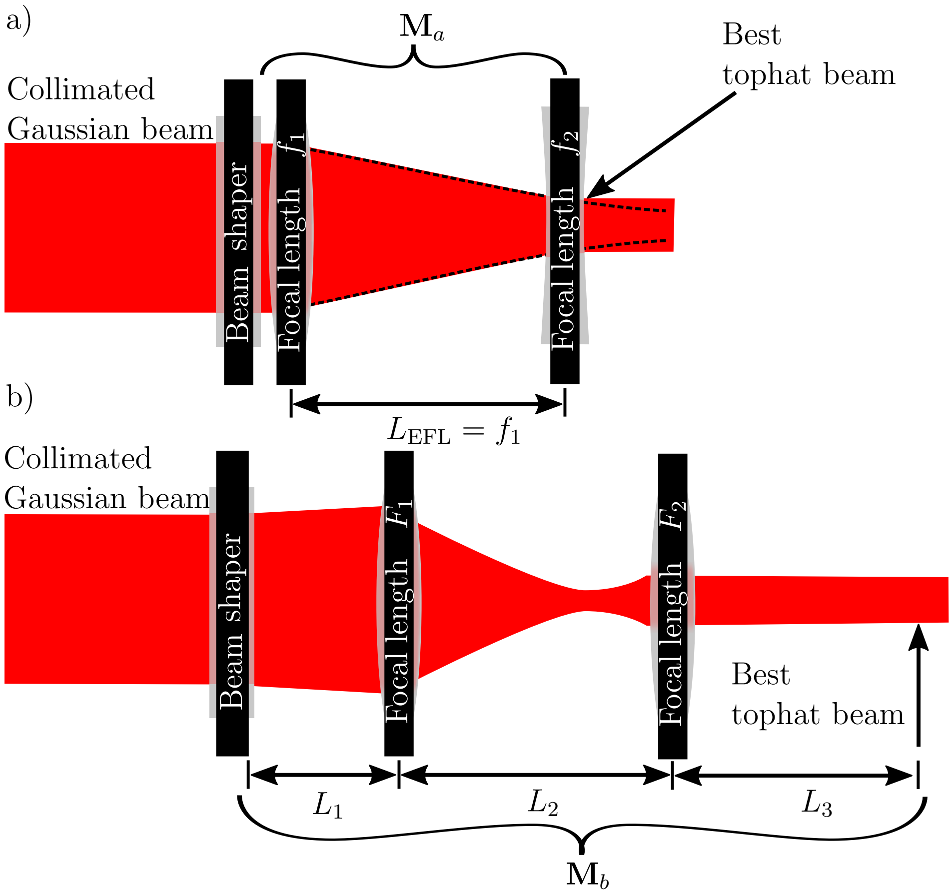

Figure 8.3: Optical setups for generating a collimated tophat beam. a) an intuitive optical scheme for generation of a collimated tophat beam, having a ray transfer matrix $\mathbf{M}_a$. The black dashed lines show the beam convergence without putting the negative lens f_2. b) a non-intuitive optical scheme for generating a collimated tophat beam, having a ray transfer matrix $\mathbf{M}_b$. The optical scheme in b) fulfills the condition $\mathbf{M}_a = \mathbf{M}_b$ to generate the same transformation of the input optical beam as the optical scheme in a).

a thin lens, $\mathbf{L}$:

$$\begin{aligned} \mathbf{S}(L) &= \begin{bmatrix} 1 & L \\ 0 & 1 \end{bmatrix}, \\ \mathbf{L}(f) &= \begin{bmatrix} 1 & 0 \\ -1/f & 1 \end{bmatrix}. \end{aligned} \tag{8.8}$$

The full solution for $\mathbf{M}_a$ and $\mathbf{M}_b$ in equation 8.7 using the ray transfer matrices in 8.8:

$$\begin{aligned} \mathbf{M}_a &= \begin{bmatrix} 0 & -f_1 \\ \frac{1}{f_1} & \frac{f_1+f_2}{f_2} \end{bmatrix}, \\ \mathbf{M}_b &= \begin{bmatrix} \frac{F_1(F_2-L_3)+L_2L_3-F_2(L_2+L_3)}{F_1F_2} & \frac{L_1L_2L_3-F_1L_3(L_1+L_2)-F_2L_1(L_2+L_3)+F_1F_2(L_1+L_2+L_3)}{F_1F_2} \\ -\frac{F_1+F_2-L_2}{F_1F_2} & \frac{F_1(F_2-L_1-L_2)+L_1(-F_2+L_2)}{F_1F_2} \end{bmatrix}. \end{aligned} \tag{8.9}$$

The ray matrix $\mathbf{M}_a$ has practically been complemented with the addition of a 4f-system[3], which creates an inversion in the plane of the transverse beam profile, resulting in more flexible solutions for the choice of lenses and positions. The matrix operation gives a solution for the lens positions, the focal length of the lenses can then be adjusted to accommodate the experimental geometry. The optimization of lenses has been focused on the position for the last lens, F_2, such that it is positioned outside the magnetic shield, having L_3 larger than half the shield length, additionally making the total distance of the beam generation as short as possible.

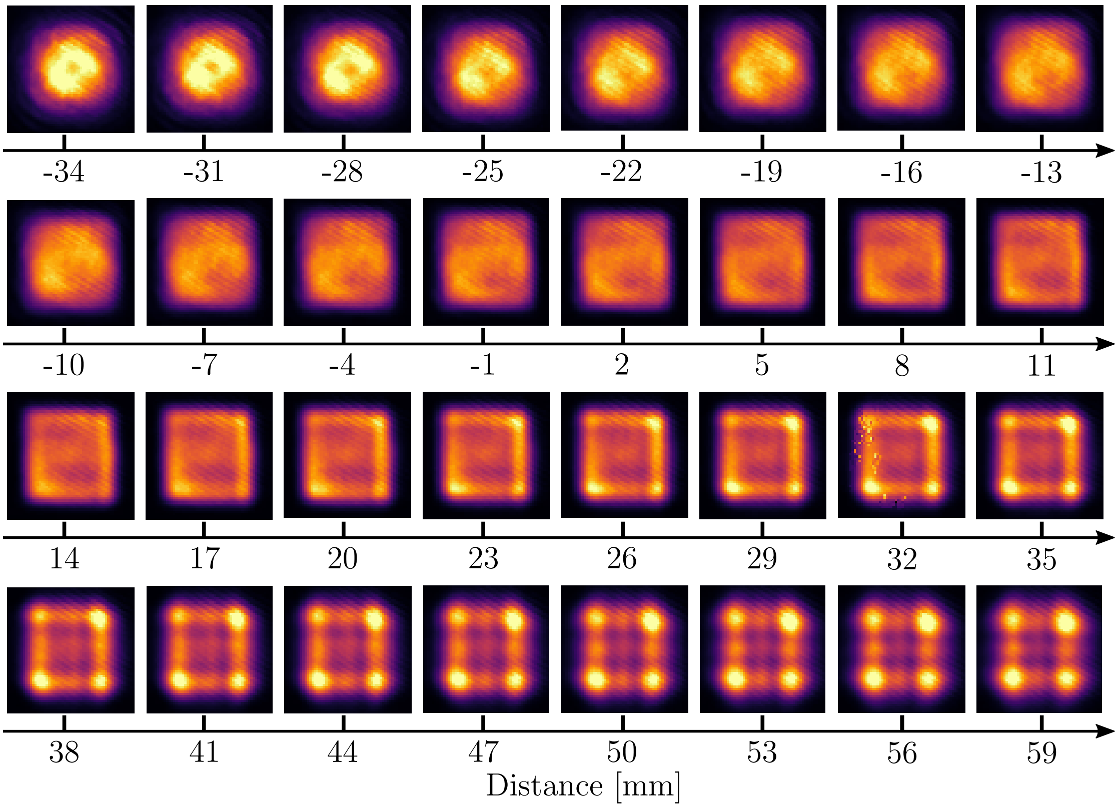

Figure 8.4: Camera pictures of a collimated square tophat beam. The beams are measured with L_3 as a zero reference point. The images have a size of 0.8 mm × 0.8 mm. The optical scheme follows the presented scheme in figure 8.3b, having the parameters: $L_1 = 343\,\mathrm{mm}$, $L_2 = 400\,\mathrm{mm}$, $L_3 = 100\,\mathrm{mm}$, $F_1 = 300\,\mathrm{mm}$ and $F_2 = 50\,\mathrm{mm}$.

The generation of a collimated tophat beam using the optical scheme shown in figure 8.3b can be seen in figure 8.4. The zero reference point for the distance is the calculated position of the best tophat beam being a distance of L_3 after F_2 in figure 8.3b. The imaginary lens in figure 8.3a, setting the beam size is $f_1 = 300\,\mathrm{mm}$ using $F_1 = 300\,\mathrm{mm}$ and $F_2 = 50\,\mathrm{mm}$ as lenses for the beam generation with a total length for the optical setup of $L_1 + L_2 + L_3 = 843\,\mathrm{mm}$. The beam propagates from a beam assembling a Gaussian beam towards a square tophat beam and then

[3]The ray transfer matrix of a 4f-system: $\mathbf{S}(f)\mathbf{L}(f)\mathbf{S}(2f)\mathbf{L}(f)\mathbf{S}(f)$.

towards a beam profile named the donkey ears because of the sharp corner peaks imitating donkey ears when looking along a cut of one of the beam profile axes. The objective is to have the flattest and most homogeneous beam profile generated around the position of the best tophat beam, in theory minimizing the BBN the most.

The rapid intensity oscillation, giving noisy patterns to the beam pictures, should be neglected since they are generated by a glass piece protecting the camera sensor, introducing interference patterns to the measurement for all beam profiles presented in this thesis.

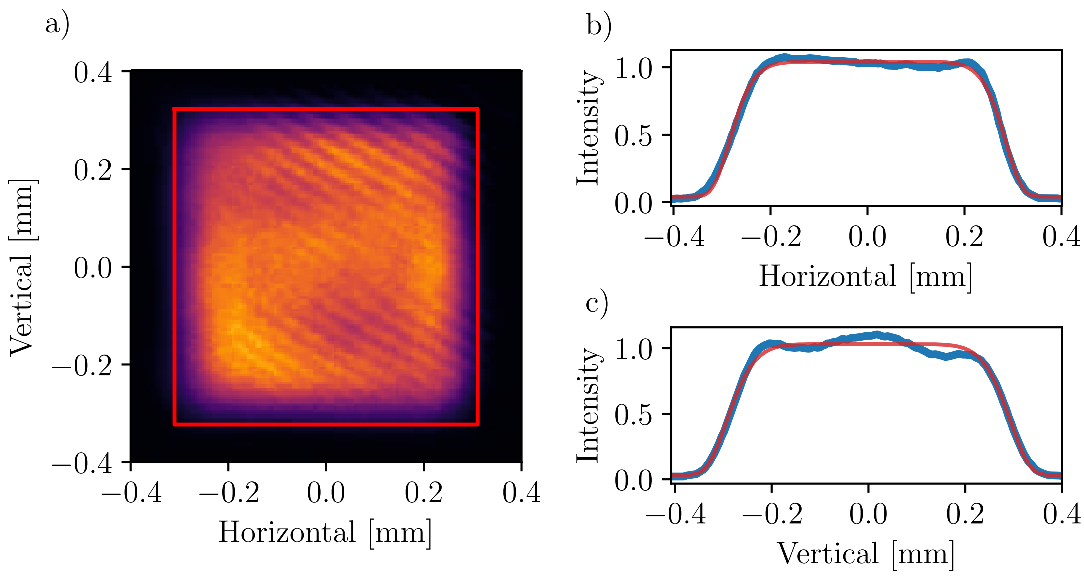

Figure 8.5: Parameters characterizing a tophat beam. Tophat beam at a distance of 5 mm in figure 8.4. a) image of the tophat beam with a red square marking an intensity drop to $1/e^2$. b) the accumulated intensity of the vertical axis. c) the accumulated intensity of the horizontal axis. The red curve is a fit of the blue data with a super-Gaussian. The fitted super-Gaussian power is $n = 4.5$, and the diameter is $2w = 0.63$.

The beam size of the generated tophat beam in figure 8.4 can be seen in figure 8.5 for the tophat beam at a distance of 5 mm. Figure a) shows the beam profile with a red square symbolizing the drop to an intensity of $1/e^2$ for the power level of the flat plateau. Figures b) and c) are the accumulated intensity over the vertical and horizontal axis, respectively. The red curve is a fit of the blue data using a super-Gaussian distribution:

$$Ae^{-2[(x-x_0)^2/w^2]^n}, \tag{8.10}$$

where $n = 1$ resembles a Gaussian intensity distribution. The fitted width w is the radius $(1/e^2)$ determining the red square in figure 8.5a. The power of the super-Gaussian is $n = 4.5$ and the diameter is $2w = 0.63$ mm. The figure of merit for a well-collimated tophat beam is having a constant width w for the propagating

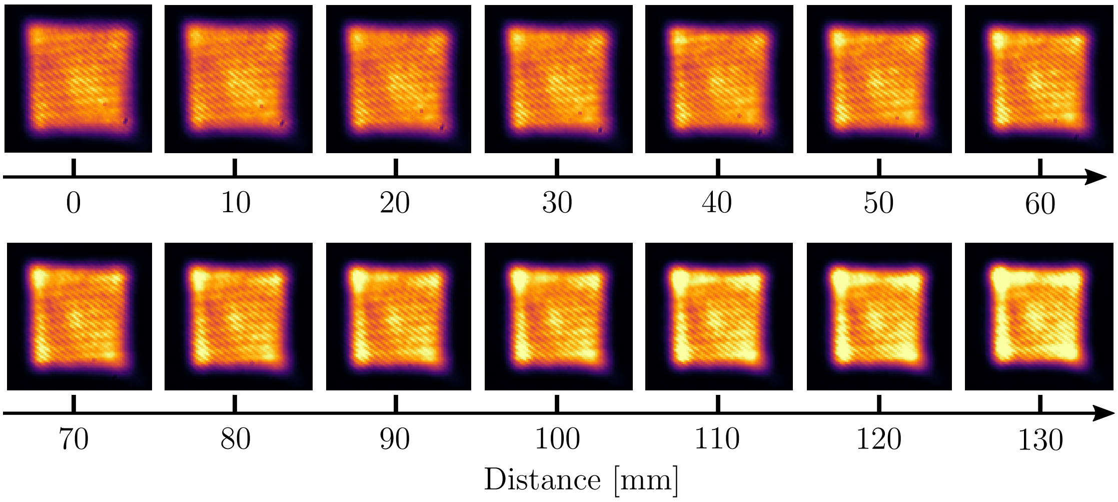

Figure 8.6: Camera pictures of a large square tophat beam. The images have a size of 3 mm × 3 mm. The beam at a distance of 0 mm has a fitted super-Gaussian power of n=4.1 and a diameter $2w = 2.3$ mm converging to $2w = 2.1$ mm for the beam at a distance of 130 mm.

tophat beam, which insures the maximum filling factor. This is also defined as the overlap between the waist potion and the position of the best tophat beam.

The size of the tophat beam determines the distance it takes to evolve from the Gaussian beam profile over to the beam profile of the donkey ears. The tophat beam is discomposed of propagating Gaussian modes, therefore, the beam propagates accordingly to the Rayleigh length of the Gaussian modes. Because of this, a smaller beam profile propagates at a shorter distance from the Gaussian beam toward the donkey ears. The Rayleigh length scales quadratically with the beam waist, implying that the tophat beam maintains 4 times the distance for twice the size. The distance for maintaining the tophat beam limits the use case since the tophat beam is hard to maintain for a small channel size. The tophat beam has been tested on an atomic channel with a cross-section of 0.5 mm × 0.5 mm and length 25 mm. This was a challenging task, where a smaller channel size used in chapter 11 with a cross-section of 0.3 mm × 0.3 mm and length 1 mm would be even harder to implement the tophat beam, making the disadvantages over shine the advantages of the tophat beam. The cell length would have to be shrunk in order to maintain the beam profile, limiting the quantum cooperativity of the atomic ensemble due to the restricted propagation length of the tophat beam, emphasizing that the tophat beam is best to be implemented at cell geometries with a square side length of 0.5 mm or larger.

Propagation of a larger tophat beam can be seen in figure 8.6 with the displayed distance of the beam profiles being equal to the distance from the calculated best tophat beam position. The beam is generated from the same optical scheme as in figure 8.4 using an expanding telescope to resize the tophat beam. The beam is enlarged by a factor ≈ 3.5 generating a tophat beam with a size of $2w = 2.3$ mm with a slight convergence of the tophat beam having a beam size at 130 mm of $2w = 2.1$ mm. The propagation of the tophat beam can be compared with the first presented tophat beam in figure 8.4. Maintaining the large tophat beam over the 130 mm would compare to maintaining the small tophat beam for ≈ 11 mm by making the Rayleigh length comparison. The tophat beam is maintained the best in the collimated configuration, which would put the large tophat beam at disadvantage since it has a slightly converging beam. Still, the enlarged tophat beam demonstrates that the tophat beam is maintained for a longer distance when enlarging the beam profile.

8.3 The noise improvement upon changing to a square tophat beam

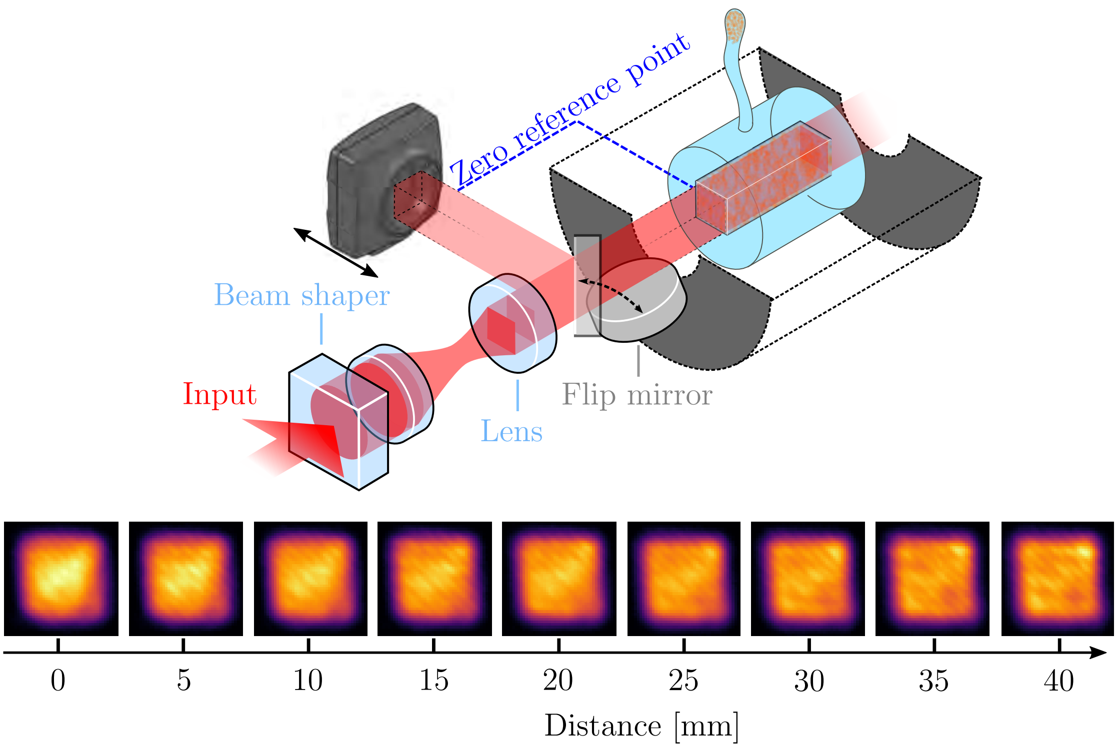

Figure 8.7: Optical setup for implementing a square tophat beam. The square tophat beam is generated using a ray transfer matrix for the lens positions. The flip mirror directs the tophat beam towards a camera to measure the beam profile. Camera model: IDS - UI-1220LE-M-GL Rev.2. The beam positions are measured from the first window of the cell as the zero reference point.

The tophat beam's worth must be determined by its ability to reduce the BBN. The optical setup for implementing and testing a square tophat beam on our atomic ensemble is depicted in figure 8.7, showing a square tophat beam transmitted through our atomic ensemble with a flip mirror for measuring the tophat beam profile. The distance for pictures of the tophat beams is referenced to the zero reference point determined by the first window of the atomic cell. The best tophat beam is optimized to be in the cell center at 20 mm. The cross-section of the atomic channel is 1 mm × 1 mm with a length of 40 mm. The image size of the tophat beams is 1 mm × 1 mm to match the size of the cell cross-section for better visualization.

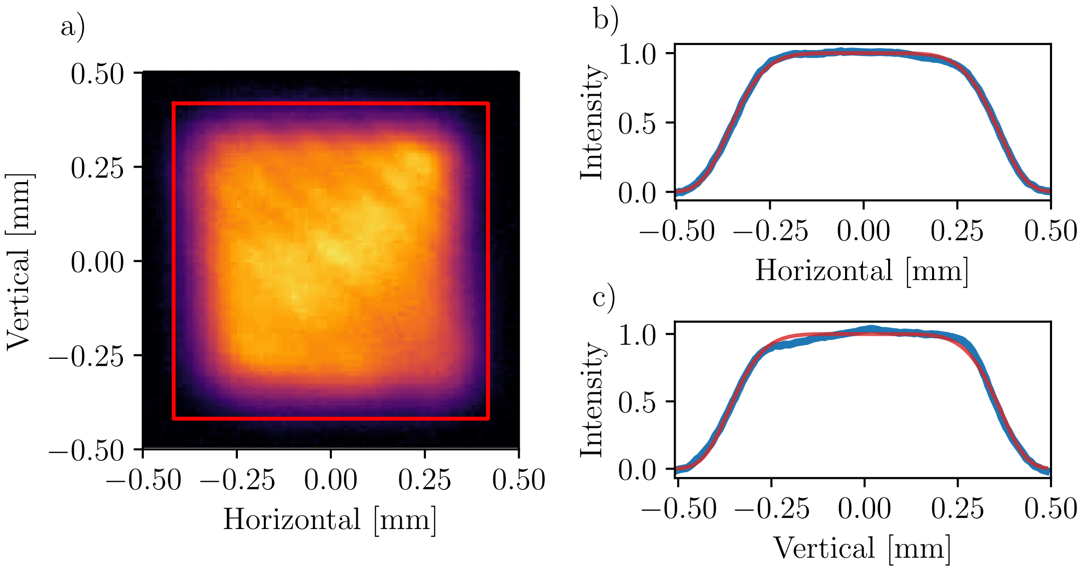

Figure 8.8: Characterization of the tophat beam for cell testing. Tophat beam measured for the center of the cell, $L = 20$ mm, in figure 8.7. a) image of the tophat beam with a red square marking an intensity drop to $1/e^2$. b) the accumulated intensity of the vertical axis. c) the accumulated intensity of the horizontal axis. The red curve is a fit of the blue data with a super-Gaussian. The fitted super-Gaussian power is $n = 3.2$ and the diameter is $2w = 0.84$ mm.

The tophat beam at the center of the cell has a diameter of $2w = 0.84$ mm with the beam profile shown in figure 8.8. The tophat beam has a transmission through the cell of 96.8% similar to the transmission of a small Gaussian beam, demonstrating the absence of clipping losses. The optical transmission losses occur due to reflections of the anti-reflection-coated windows as well as paraffin collecting on the channel windows[4].

A comparison between the spectra for a Gaussian beam and a square tophat beam can be seen in figure 8.9. The spectra are measured for the P-quadrature of light with shot noise subtracted. The response from probing with a Gaussian beam is shown in red, and the square tophat beam is shown with a reduced BBN in blue. The width of the Gaussian beam is maximized to have the largest value allowed by the cell without incurring a significant clipping loss. The Gaussian beam has a diameter of $2w = 0.80$ mm shown in figure 8.10. The Gaussian beam has a transmission of 95%, meaning that it has more clipping losses than the tophat beam, illustrating that the tophat beam could be enlarged even further for a fair comparison. Therefore, the presented results are a lower bound of the

[4]A transmission of 96.8% is considered high for paraffin coated cesium vapor cells at QUANTOP with cell transmissions of the newest generation non-discarded cells ranging from 91% to 97% [Schmieg, 2023].

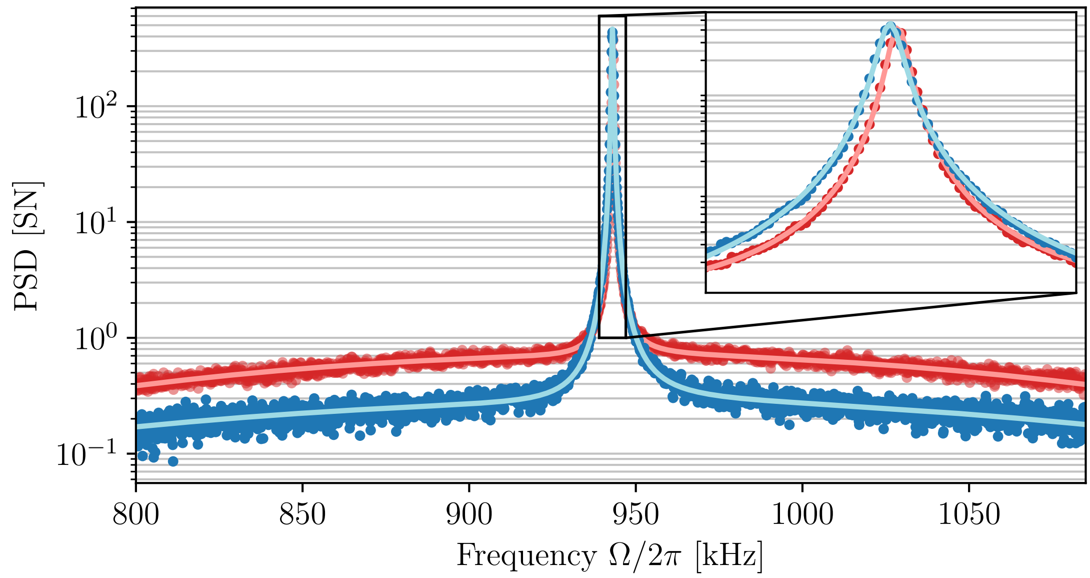

Figure 8.9: Spectral comparison between atomic noise arising from Gaussian and tophat beam profiles. The spectrum for probing with a Gaussian beam profile is shown in red, and with a square tophat beam profile in blue. The bright curves show the spectra fits. The fit shows an increased readout rate: $\Gamma_{\mathrm{S}}^{\mathrm{TH}}/\Gamma_{\mathrm{BBN}}^{\mathrm{Gaus}} = 1.33$, and a reduction of the BBN: $A_{\mathrm{BBN}}^{\mathrm{Gaus}}/A_{\mathrm{BBN}}^{\mathrm{TH}} = 2.55$ when probing with a square tophat beam.

improvements gained by transiting to a square tophat beam.

The fitted bright curves in figure 8.9 include the full spin model for a single spin oscillator in the dynamical back-action free regime, $\zeta_{\mathrm{S}} = 0$, presented in equation 2.38. The detection angle is the same for the measurement of the Gaussian beam and the tophat beam, completed for the same experimental configuration resulting in an equal number for the amount of thermal excitations. The BBN is modeled accordingly to equation 8.5 having a Gaussian shape for the BBN. The comparison between a Gaussian beam and a square tophat beam in figure 8.9 shows a reduction of the BBN by a factor of $A_{\mathrm{BBN}}^{\mathrm{Gaus}}/A_{\mathrm{BBN}}^{\mathrm{TH}} = 2.55$ when changing the beam profile to a square tophat beam. The Gaussian width, γ_{BBN}, of the BBN is increased by 12% for the square tophat beam, which can be understood in the mode model to describe the BBN since the tophat beam consists of higher order spatial modes compared to the Gaussian beam. The higher order modes will have a higher decay rate, broadening the the spectral profile of the BBN.

The increase of the probe filling factor has also been shown to increase the readout rate, which has been confirmed for separate measurements. The increase of readout in figure 8.9 comparing the probing of a Gaussian beam with a square tophat beam, results in a readout rate increase by a factor of $\Gamma_{\mathrm{S}}^{\mathrm{TH}}/\Gamma_{\mathrm{S}}^{\mathrm{Gaus}} = 1.33$ when changing to a square tophat beam, calculated from the fitted spectra of figure 8.9. The increase of coupling to NBN is a phenomenon still to be understood theoretically, which may relate to inhomogeneous stark shifts.

The total reduction of the added thermal noise introduced by the BBN by combining the enhanced coupling to the NBN and the reduced level of the BBN gives an improvement by a factor of 3.4 when changing to a square tophat beam.

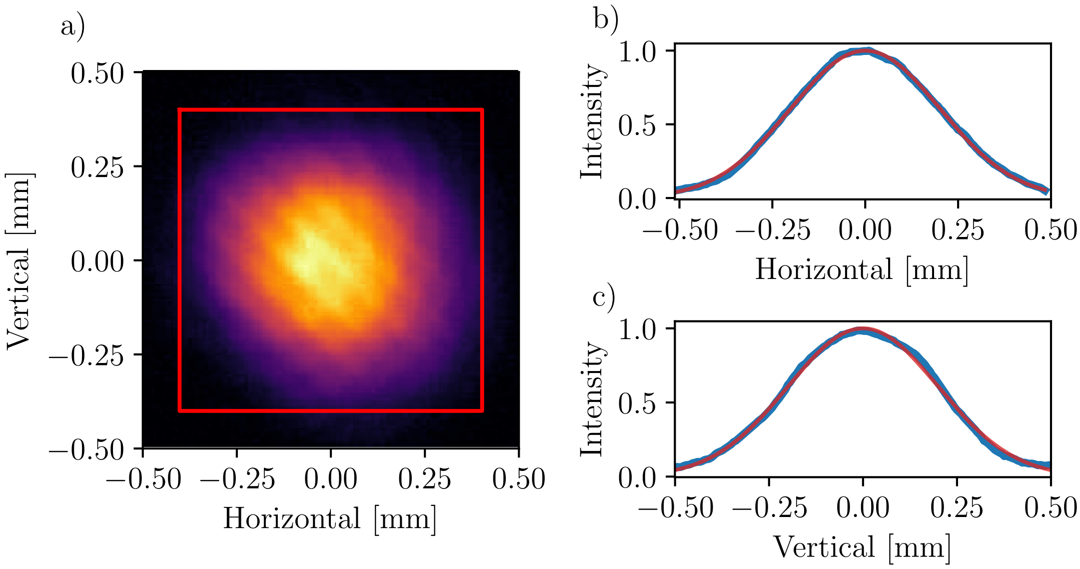

Figure 8.10: Characterization of the Gaussian beam for BBN comparison. a) image of the Gaussian beam with a red square marking an intensity drop to $1/e^2$ for the horizontal and vertical axis. b) the accumulated intensity of the vertical axis. c) the accumulated intensity of the horizontal axis. The red curve is a fit of the blue data with a Gaussian fit. The fit diameter is $2w = 0.80\,\mathrm{mm}$.

Disadvantages of tophat beams include potential difficulties of coupling them into optical fibers (i.e., for photon counting) and interacting them with other material systems after the atomic ensemble for which they were optimized. In addition, other systems, like a cavity using spherical mirrors, are incompatible with the mode profile of a square tophat beam. Therefore, the transmission of a cavity with a square tophat beam would introduce a lot of losses. However, this is not a problem for the homodyne detection method using the local oscillator in the orthogonal polarization for detection, similar to our experimental configuration.

The advantage of using a round tophat beam (super-Gaussian) to a square tophat is the flat phase front generated around the waist of the beam. The square tophat beam is not rotationally symmetric, meaning it does not produce a flat phase front at any plane. The flat phase front allows for converting the beam back into a Gaussian beam by reflecting the flat phase front [Mielec et al., 2018]. It is non-trivial to convert a square tophat beam back into a Gaussian beam. It would require an optical element with an opposite phase pattern of the beam shaper, which multiple beam shaping companies have declined to produce; therefore, a proposal for converting a tophat beam into a Gaussian beam is presented in appendix C.

Finally, we want to evaluate the overall improvement of fast-decaying modes compared to previous experimental configurations. We have previously used a smaller cell geometry, $0.3\,\mathrm{mm} \times 0.3\,\mathrm{mm} \times 10\,\mathrm{mm}$, probed with a Gaussian beam as it will be explained that smaller cell geometries are less affected by the BBN in section 9.4. The previous ratio for the smaller cell was $\Gamma_{\mathrm{S}}/A_{\mathrm{BBN}} \approx 7.5 \cdot 10^4$ and for the new experimental configuration $\Gamma_{\mathrm{S}}/A_{\mathrm{BBN}} \approx 15 \cdot 10^4$, estimating an overall reduction of the BBN for the new configuration by a factor of 2.

CHAPTER 9

Simulation of a hot spin ensemble in a hot vapor cell

This chapter covers the simulations of effects arising from motional averaging. Rebuilding an experimental setup after having exchanged spatial beam shapes, cell geometries, or changed magnetic fields is time-consuming and can take weeks to months to implement. Consequently, having a theoretical tool to optimize the parameters is vital to save time. Additionally, simulations give the possibility of independently looking into the different aspects of the dynamics to get a better understanding of the underlining physics.

We want to simulate a thermal gas interacting with light with the same physical parameters as the spin ensemble. The simulation assumes atoms with velocities determined through the Maxwell–Boltzmann velocity distribution. The dynamics of atoms, $s(t)$, can be simulated by the Euler method

$$s(t+\tau) = s(t) + \frac{\mathrm{d}s}{\mathrm{d}t}\tau. \tag{9.1}$$

The system evolves in a stochastic way over each time step τ; therefore our approach is a Monte-Carlo simulation of the Euler method. The Euler method gives rise to errors due to the exclusion of higher-order terms, which is insignificant due to the stochastic behavior of the system. The Euler method can also be applied for the dynamics for the evolution of the spin and the readout into light, as long as the time steps are smaller than the time scale of the dynamics[1].

9.1 Thermal motion and physical boundaries

We want to simulate a physical system whose dynamics resemble the thermal motion of cesium atoms moving around in a paraffin-coated cell.

The velocity of an ensemble corresponds to the thermal motion following a

[1]This chapter partially overlaps with the bachelor thesis of Martin Krehbiel since I supervised the implementation of a thermal gas in a hot vapor cell.

Maxwell–Boltzmann distribution [Schroeder, 2014]:

$$P(v) = \left(\frac{m}{2\pi k_{\mathrm{B}} T}\right)^{3/2} 4\pi v^2 e^{-\frac{mv^2}{2k_{\mathrm{B}}T}}, \tag{9.2}$$

described by the particle's mass m, the temperature T, the Boltzmann constant k_{B}, and the total velocity v. The distribution can be alternatively parameterized by the three-dimensional velocity vector with each component distributed according to a Gaussian:

$$P(v_x) = \sqrt{\frac{m}{2\pi k_{\mathrm{B}} T}} e^{-\frac{mv_x^2}{2k_{\mathrm{B}}T}}, \tag{9.3}$$

therefore, we can initialize a thermal ensemble following a Gaussian distribution of the velocity vectors for our simulation:

$$\mathbf{v} = \begin{pmatrix} P(v_x) \\ P(v_y) \\ P(v_z) \end{pmatrix}. \tag{9.4}$$

The spatial positions of the atoms are initialized evenly distributed across the cell, after which the atoms propagate along classical trajectories calculated from their instantaneous velocities using the Euler method.

9.1.1 Wall collisions

The atoms are confined inside a cell and therefore experience collisions with the cell walls. The simplest form of wall collision is a perfect reflections from the wall, which inverts the velocity component parallel to the normal vector, $\mathbf{n}$, of the wall, as can be seen in figure 9.1a. The angle parallel to the plane ϕ is maintained, $\phi_2 = \phi_1$, and the angle to the normal vector is reflected $\theta_2 = -\theta_1$.

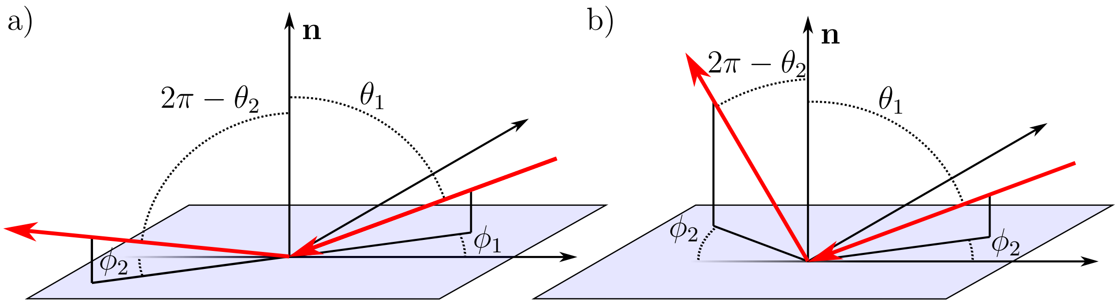

Figure 9.1: Velocity vector after wall collision. (a) reflection of the velocity vector after wall collision $\phi_2 = \phi_1$ and $\theta_2 = -\theta_1$. (b) outgoing velocity vector being independent of the incoming velocity vector.

Reflective wall collisions are not a physically accurate description for rough surfaces since we have the cells coated with paraffin, which consists of long carbon chains and thus creates irregular surfaces at the scale of an atom. A more accurate description of reflection is provided by Knudsen's cosine law [Knudsen, 1967], predicting a randomized outgoing angle described by a cosine distribution. Figure

9.1b depicts a randomized outgoing velocity, which is independent of the incoming vector to illustrate the behavior of Knudsen's cosine law. Knudsen's cosine law has been experimentally proven for alkali atoms reflected of paraffin-coated films [Sekiguchi et al., 2018]. Implementation of Knudsen's cosine law into Monte-Carlo simulation is thoroughly described in [Greenwood, 2002], demonstrating that the angle distribution follows

$$P(\theta) = \sin^2(\theta). \tag{9.5}$$

The distribution of ϕ for Knudsen's cosine law is uniform over the interval $[0,\ 2\pi]$, independent of the incoming beam. The outgoing vector has a modulus distributed accordingly to the Maxwell–Boltzmann distribution in equation 9.2.

Knudsen's cosine law redistributes the atoms with a complete loss of momentum memory after a wall collision, maintaining the spin and the positional coherence. In simulations, occasionally an atom overshoots a wall due to the finite time steps, which is corrected for by tracing back the point of collision for all wall-colliding atoms, dragging each of them back to the position of collision with a wall.

9.1.2 Atom-atom collisions

Modeling atom-atom collisions is a computationally expensive problem, as it would require us to model the atomic density of our ensemble consisting of a few million to a few billion atoms. Furthermore, we would have to compute all the atoms' dependency on each other, which would be a computational task proportional to $\propto N^2$. However, the motion of atoms can be computed for fewer atoms assuming Brownian motion, implemented by the Langevin equation [Dean, 1996]:

$$\frac{\mathrm{d}v}{\mathrm{d}t} = -\lambda v + \eta(t)/m, \tag{9.6}$$

where λ corresponds to the rate of velocity-changing collisions, and $\eta(t)$ is a stochastic force that has no memory, shown by the correlation function; $\langle \eta_i(t)\eta_j(t+\tau)\rangle = 2\lambda k_\mathrm{B} T \delta_{ij}\delta(\tau)$. Resulting in a Gaussian probability distribution of η with a width of $\sigma^2 = 2\lambda k_\mathrm{B} T/\tau$. η is implemented using the Euler-Maruyama method [Bayram et al., 2018].

Experimental findings for rubidium vapor cells coated with paraffin at room temperature [Sekiguchi and Hatakeyama, 2016] show a rate of velocity-changing collisions, $\lambda \approx 10^6\,\mathrm{s}^{-1}$; therefore, we have chosen the same value for our simulation at room temperature, corresponding to a mean free path of $L_\mathrm{mean} = \langle v\rangle/\lambda = 0.2\,\mathrm{mm}$.

9.2 Light-atom interaction

The spin dynamics are described in the Heisenberg picture in equation 2.20. However, modeling the quantum back-action for the spin-light coupling is non-trivial. Therefore, the focus of the simulations has been to model the thermal noise of the spin, which is adequate for modeling broadband noise (BBN) and dephasing due to magnetic inhomogeneities. The simulated spin dynamics, excluding quantum back-action, follow

$$\frac{\mathrm{d}}{\mathrm{d}t}\begin{pmatrix}\hat{X}_{\mathrm{S}}\\ \hat{P}_{\mathrm{S}}\end{pmatrix} = \begin{pmatrix}-\gamma_{\mathrm{S0}}/2 & \omega_{\mathrm{S}}\\ -\omega_{\mathrm{S}} & -\gamma_{\mathrm{S0}}/2\end{pmatrix}\begin{pmatrix}\hat{X}_{\mathrm{S}}\\ \hat{P}_{\mathrm{S}}\end{pmatrix} + \begin{pmatrix}\hat{F}_{\mathrm{S}}^{X}\\ \hat{F}_{\mathrm{S}}^{P}\end{pmatrix}. \tag{9.7}$$

The effective Langevin forces, $\hat{F}_{\mathrm{S}}$, are stochastic variables, assuming equal size of the Langevin forces for both quadratures and an oscillator in the ground state, the correlation function for the Langevin forces; $\langle \hat{F}_{\mathrm{S}}(t)\hat{F}_{\mathrm{S}}(t+\tau)\rangle = \gamma_{\mathrm{S0}}\delta(\tau)$, showing a Gaussian probability distribution of $\hat{F}_{\mathrm{S}}$ with a width of $\sigma^2 = \gamma_{\mathrm{S0}}/\tau$. $\hat{F}_{\mathrm{S}}$ is implemented using the Euler-Maruyama method similar to η for the modeling of the Brownian motion.

The intrinsic decay rate γ_{S0} is mainly dominated by atom-atom collisions for the regime of this thesis, meaning that the decay rate is uniformly distributed in the cell. However, other vapor cells operate with wall collisions as the primary decay channel, which would open the possibility of simulating the noise behavior assuming an inhomogeneous decay rate similar to the theoretical description by [Shaham et al., 2020].

The readout of the atomic spin is only into the P quadrature of light, neglecting dynamical back-action from equation 2.22;

$$\hat{P}_{\mathrm{L}}^{\mathrm{out}} = \hat{P}_{\mathrm{L}}^{\mathrm{in}} + \sqrt{\Gamma_{\mathrm{S}}}\hat{X}_{\mathrm{S}}. \tag{9.8}$$

The quadratures of light are normalized to $\sqrt{S_{||}}$ (shot noise) accordingly to equation 2.9, correspondingly the interaction needs to be scaled by $\sqrt{S_{||}}$ for the measurement:

$$i(t) = \sqrt{S_{||}}\sqrt{\Gamma_{\mathrm{S}}}\hat{X}_{\mathrm{S}} = \sqrt{S_{||}}\sqrt{g_{\mathrm{S}}^2 a_1^2 S_{||} F_x}\hat{X}_{\mathrm{S}} \approx A\frac{S_{||}}{\Delta}\hat{X}_{\mathrm{S}}, \tag{9.9}$$

where A is a overall scaling. The interaction strength with the X quadrature of the spin depends on the detuning Δ, affected by Doppler broadening from the atomic velocity, v_z, in the direction of the light propagation, and the effect of inhomogeneous probing, $S_{||}$, from atoms moving in and out of the beam. The varying probing strength of individual atoms is setting the dynamics of interest to measured by $i(t)$.

9.2.1 Normalization

The measurements are scaled by $1/\sqrt{N}$, where N being the number of atoms in the simulation. This normalizes the measurements accordingly to Gaussian statistics, ensuring that simulations are independent of the number of atoms. The number of simulated atoms is in the range of 10^4 to 10^6, which is determined by the statistical requirements of the investigated dynamics.

The intensity of the light is normalized to the total light inside of the cell $S_{\mathrm{norm}}(x,y,z) = S_{||}(x,y,z)/(\int\int\int_D S_{||}(x,y,z)\ \mathrm{d}x\mathrm{d}y\mathrm{d}z)$. This fixes the beam power inside the cell in the simulations, allowing for a meaningful comparison between the simulations with different beam shapes. The normalized measurement signal from the spin ensemble summing over all the atoms is

$$i(t) = \frac{1}{\sqrt{N}}\sum_{j=1}^{N}\frac{S_{\mathrm{norm}}^{j}[x^j(t), y^j(t), z^j(t)]}{\Delta^j[v_z^j(t)]}\hat{X}_{\mathrm{S}}^{j}(t). \tag{9.10}$$

The normalization of the atomic number and the probe power ensures that the coupling to the narrow mode of the atomic ensemble is independent of the simulation parameters for a specific cell geometry.

9.3 Simulations of magnetic inhomogeneities

The simulations of magnetic inhomogeneities model the dynamics of atoms experiencing a positionally-dependent Larmor frequency, $\omega_S(z)$, inside the cell. We have used the simulations of magnetic inhomogeneities in our work to understand the requirements for improving the design of the coil systems described in chapter 7 and for understanding the physical dynamics better.

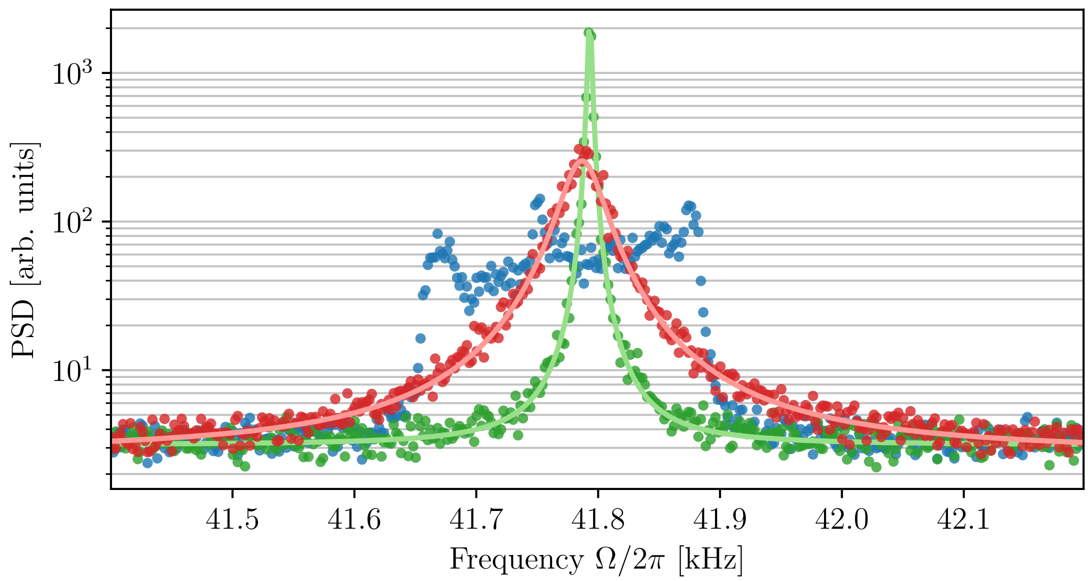

Figure 9.2: Simulation of magnetic inhomogeneities. The simulated cell geometry is 5 mm × 5 mm × 80 mm at room temperature. The green data is simulated with a perfectly homogeneous magnetic field, the red data is simulated with the magnetic field of the CUB PCB coils, and the blue data is simulated with $v_z = 0$ in the magnetic field of the CUB PCB coils. The bright colored curves are fits showing $\gamma_{S0} = 4\,\mathrm{Hz}$ and $\gamma_{S0} = 37\,\mathrm{Hz}$ in green and red, respectively.

We used the simulations in the initial development of the new coil system, using the CUB PCB coils for the bias magnetic field generation with a similar positional dependence as presented in figure 7.5. The cell employed in the initial testing was a cell of geometry 5 mm × 5 mm × 80 mm operated at 24 °C with an intrinsic decay rate; $\gamma_{S0} = 7\,\mathrm{Hz}$. The dephasing due to the magnetic inhomogeneities was evaluated experimentally at a Larmor frequency of 42 kHz, showing a broadening of the linewidth by $\approx 30\,\mathrm{Hz}$[2].

[2]The experimental measurement of the magnetic inhomogeneities was performed by Ryan Yde and Jun Jia.

We implemented the same experimental parameters in our simulation to test agreements with our experimental findings. The simulations are shown in figure 9.2, where the green data is in the absence of magnetic inhomogeneities and the red data is with the magnetic inhomogeneities of the CUB PCB coils. The fitted data of the simulations show a broadening due to magnetic inhomogeneities of $\approx 33\,\mathrm{Hz}$, close to the dephasing experimentally verified. The broadening due to magnetic inhomogeneities showed a dependency on the parameter for the rate of velocity-changing collisions, λ, since it introduces Brownian motion to the ensemble, increasing the transit time of an atom to cross the z-direction (the elongated direction). We get a value near the experimentally verified result, which confirms a reasonable number for the rate of velocity-changing collisions in the simulations: $\lambda = 10^6\,\mathrm{s}^{-1}$.

Additionally, we wanted to understand better the effect of atoms motionally averaging when moving through a changing magnetic field. The z component of the velocity was removed in the simulation whose result is shown by the blue curve in figure 9.2. The atomic response is shaped by the magnetic field, not resembling a Lorentzian anymore, but dominated by the magnetic inhomogeneities, showing the effect of the motional averaging. The simulations gave insight into the effect of the transit time when considering the broadening due to magnetic inhomogeneities. Enlarging the cell's long axis increases the transit time, increasing the time for motional averaging, further broadening the spin response. The requirements for the inhomogeneities of the magnetic fields are consequently even larger when enlarging the cell length.

Simulations for investigating oscillation frequencies in the megahertz range that resolves narrow features, like the broadening due to magnetic inhomogeneities, start to be limited by the computational speed, making it more cumbersome to compute. It is required for the time steps to be below the oscillation frequency, while the spectral resolution is determined by the entire computation time $\Delta f = 1/T_{\mathrm{total}}$. It is necessarily increasing the computation time proportional to the fastest-evolving dynamic of the simulation. This can be solved by outsourcing the computation to more powerful computers.

9.4 Simulations of fast decaying spin-modes

The simulations of fast decaying spin-modes model the dynamics of atoms moving through a positionally-dependent probe intensity, $S_{||}(x, y, z)$, inside the cell. The simulations of the fast decaying spins modes have been used to determine the employed cell geometry of this thesis: $1\,\mathrm{mm} \times 1\,\mathrm{mm} \times 40\,\mathrm{mm}$, which made the decision of experimentally implementing a square tophat beam into our setup, described in chapter 8.

The typical operating temperature of our ensemble is approximating $55\,^\circ\mathrm{C}$, which is higher than the simulations in section 9.3. The rate of velocity changing collisions can be assumed to be linear with the atomic number for a fixed volume, elevating the temperature to $55\,^\circ\mathrm{C}$ changes the atomic number by one order of magnitude, therefore a velocity changing collision rate of $\lambda(55\,^\circ\mathrm{C}) \approx 10^7\,\mathrm{s}^{-1}$ is implemented for the simulations in this section.

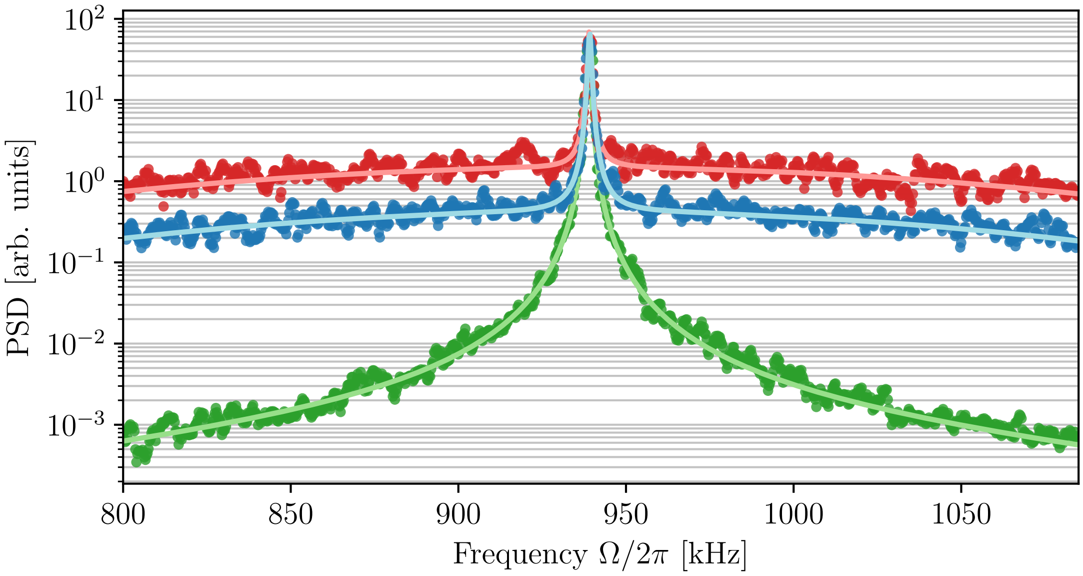

Figure 9.3: Simulation of broadband noise arising from Gaussian and tophat beam profiles. The simulation for a Gaussian beam profile is shown in red, a square tophat beam profile in blue, and a uniform filling in green. The bright curves show the spectra fits. The simulation shows the BBN comparison: $A_{\text{BBN}}^{\text{Gaus}}/A_{\text{BBN}}^{\text{TH}} = 3.5$. The Gaussian beam has a diameter of $2w = 0.80\,\text{mm}$, and the tophat beam has a diameter of $2w = 0.84\,\text{mm}$ with a super-Gaussian power; $n = 3.2$.

We want to compare our simulation to the experimental results of implementing a square tophat beam, presented in chapter 8. Figure 9.3 shows a simulation to be compared with the experimental result of figure 8.9, with a beam profile for the Gaussian beam having a diameter of $2w = 0.80\,\text{mm}$ in red, and for the tophat beam having a diameter of $2w = 0.84\,\text{mm}$ with a super-Gaussian power; $n = 3.2$ in blue. The fitted curves for the simulations show a ratio for the BBN of $(A_{\text{BBN}}^{\text{Gaus}}/A_{\text{BBN}}^{\text{TH}})_{\text{sim}} = 3.5$. This is larger than the ratio of $(A_{\text{BBN}}^{\text{Gaus}}/A_{\text{BBN}}^{\text{TH}})_{\text{exp}} = 2.55$ achieved for experimental realizations in figure 8.9 but close to the experimental value of the overall reduction of thermal noise introduced by the BBN of 3.4. The deviation in the height of the BBN, $A_{\text{BBN}}^{\text{Gaus}}/A_{\text{BBN}}^{\text{TH}}$, between the experimental data and the simulation is not to be explained by our current model since we are looking into the effects that increase the readout rate for increased homogeneous probing, and we are still to implement quantum back-action into the simulations. However, the simulation agrees with the experimental results for the overall thermal noise reduction of the BBN, showing that the simulation gives a reasonable estimate for the overall improvement by converting from a Gaussian beam to a tophat beam profile. Furthermore, a simulation of uniform coverage of the entire cell for the probe is shown by the green data in figure 9.3 for comparison, showing the lack of BBN when having an equal probing of all the atoms, illustrating the importance of homogeneous probing.

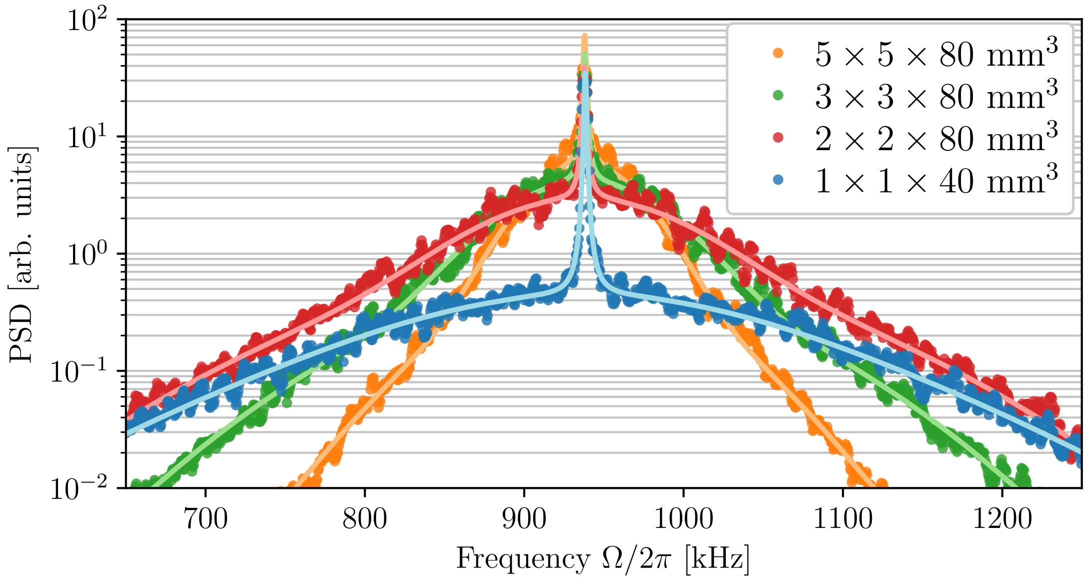

Figure 9.4: Simulation of broadband noise dependency on the cell size. All the simulations are under the same conditions, except for the cell geometry and the size of the probing tophat beam to have the same filling factor for all the cell geometries. The bright curves show the spectra fits. The spectra are normalized to the lowered local intensity and decreased atomic density for an increased cell geometry to have an equal coupling to the narrow response for all the spectra.

There are trade-offs when optimizing the cell geometry, here focusing on the fast decaying modes and the optical depth. The optical depth is proportional to the length of the cell geometry, which means it is beneficial to have a longer cell only concerning the optical depth. However, the divergence of a beam is set by the Rayleigh length; therefore, a small cross-section is ultimately limited to a shorter cell length, in addition, having fabrication challenges in producing long cells of small cross-sections. The 80 mm cell have consequently been limited to cells with cross-sections larger than 1 mm $\times$ 1 mm.

To estimate the optimal cell geometry, we want to compare the BBN between different cell geometries. A comparison of the BBN for relevant cell geometries is shown in figure 9.4. The simulations are implemented with a tophat beam of size $2w = 0.84 \cdot L_{\text{side}}$ with a super-Gaussian power $n = 3.2$, therefore maintaining the same filling factor for all the simulations, where L_{side} is the transverse side length. The decay rate of the BBN, γ_{BBN}, is inversely proportional to the transit time of an atom in the transverse direction of the channel, resulting in an elevated BBN on resonance for an increased transverse cell geometry. This can be seen in figure 9.4, showing a smaller width and an elevated noise level for the BBN. The BBN is best described by a Gaussian response within a few sigmas of the Gaussian distribution; an additional Gaussian distribution is implemented to model the BBN due to the cross-section 5 mm $\times$ 5 mm having a smaller decay rate: $\gamma_{\text{BBN}}^{5\times5} = 31$ kHz, consequently spanning more deviations of the Gaussian distribution when fitting the BBN. We evaluate the amplitude of the BBN by the combined amplitude of the two Gaussian distributions as A_{BBN}. The increase in BBN comparing it to the BBN for the cell geometry of 1 mm × 1 mm: $A^{2\times2}_{\mathrm{BBN}}/A^{1\times1}_{\mathrm{BBN}} = 6.6$, $A^{3\times3}_{\mathrm{BBN}}/A^{1\times1}_{\mathrm{BBN}} = 9.2$ and $A^{5\times5}_{\mathrm{BBN}}/A^{1\times1}_{\mathrm{BBN}} = 12.6$, showing a large discrepancy in amplitude between the BBN when enlarging the cell, which is not favorable for our experimental requirements as the BBN is one of the experimental bottlenecks. It can be concluded that it would not be beneficial for us to increase the cross-section of the cell based on the simulated findings. Other experimental configurations often benefit from a larger coherence time achieved by enlarging the cell geometry due to fewer wall collisions. Consequently, the elevated BBN should be strongly considered when enlarging the cell geometry.

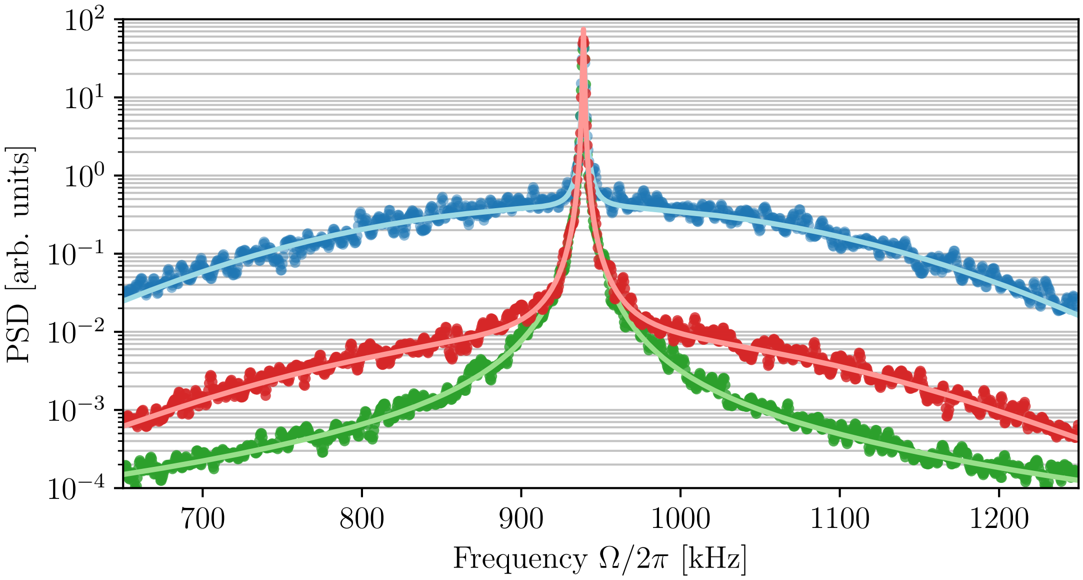

Figure 9.5: Simulations of the probe Doppler broadening. The probe is uniformly filling the channel for data in red and green for a detuning of 0.7 GHz and 3 GHz, respectively. The blue data is probing with a square tophat beam that has a diameter of $2w = 0.84$ mm with a super-Gaussian power $n = 3.2$ for a detuning of 3 GHz. The bright curves show the spectra fits.

We have started to operate closer to resonance when probing the atomic ensemble, see chapter 10 for details, having a detuning for the probe laser of $\Delta/(2\pi) = 0.7$ GHz, which starts to be close to the Doppler width of $\Delta\nu_{\mathrm{FWHM}}(55\,^\circ\mathrm{C}) = 396$ MHz. The effect of inhomogeneous probing due to the velocity-dependent detuning induces fast decaying modes similar to a non-uniform filling factor of the probe beam. The effect of Doppler-induced broadband noise would be hard to test experimentally, therefore benefiting from the simulation to test the noise contribution, motivating the use of the simulations to understand the underlying dynamics.

A simulation has been performed to investigate the influence of the Doppler broadening shown in figure 9.5, where the green data is for a probe detuning of $\Delta/(2\pi) = 3$ GHz and the red data is for a probe detuning of $\Delta/(2\pi) = 0.7$ GHz both of uniform probing, showing an elevated noise level for the detuning of

$\Delta/(2\pi) = 0.7\,\mathrm{GHz}$. The data in blue is a tophat beam for a probe detuning of $\Delta/(2\pi) = 3\,\mathrm{GHz}$ for comparison. The elevated noise level due to the Doppler broadening is only $A_{\mathrm{BBN}}^{\mathrm{Doppler}}/A_{\mathrm{BBN}}^{\mathrm{TH}} = 2\%$ of the elevated noise level due to the broadband noise from an inhomogeneous filling factor. Concluding that the induced noise due to the Doppler broadening can be considered insignificant compared to other noise processes.

9.5 Computational challenges and implementation

This last section on the simulation describes computational challenges associated with propagating an extensive variable system for many iterations. The correct implementation is crucial for the speed of a simulation, which is vital for practicable purposes. This is especially important for the knowledge transfer for the future use of the simulation script. The simulation script is open access: `https://github.com/CBaerentsen/Simulation-gas-in-cell.git`

The presented simulations of this thesis would have taken each a few months to compute for a laptop with a processing power of $\sim 2\,\mathrm{GHz}$ for the first implemented simulation. Many efforts have gone into accelerating the computation speed, limited by the programming language of choice, Python. The resulting accelerated process has gained on the computational time by a factor of $\sim 10^3$, which means a simulation only takes a few hours to compute on a laptop.

The simulations of motional averaging dynamics can be performed by having a single atom propagating inside the cell for many iterations. However, this is disadvantageous, requiring huge loops to collect statistical knowledge, where it is more advantageous to simulate many atoms at once. Instead, the many atoms can be made into a vector, implementing the dynamics by vector and matrix multiplication, making it possible to perform the calculation by quicker programming languages like C or C^{++} for the multiplication, only requiring a single loop to run in Python for the Euler steps. The package performs the vector and matrix multiplication: NumPy `https://numpy.org/` programmed in C and C^{++}, decreasing the computation time by ~ 100 compared to looping the computation in Python.

The last addition to the speed up of the computation time is the implementation of multi-core processing. This is not a compatible process to run in one execution for Python, which has been bypassed by summoning several executions with separate local storages, combining all the results after completion of the simulation. This is implemented by a large number of atoms $10^4 - 10^6$, dividing them into equal sizes and computed on separate cores, later combing the result after computation, which increased the computation time by the number of logical cores 7 (excluding one since the operating system would crash when using all the logical cores). Implementing multi-core processing has also opened the possibility of ruining the simulation on remote computers utilizing many logical cores in supercomputers.

Part IV

Spin induced light squeezing

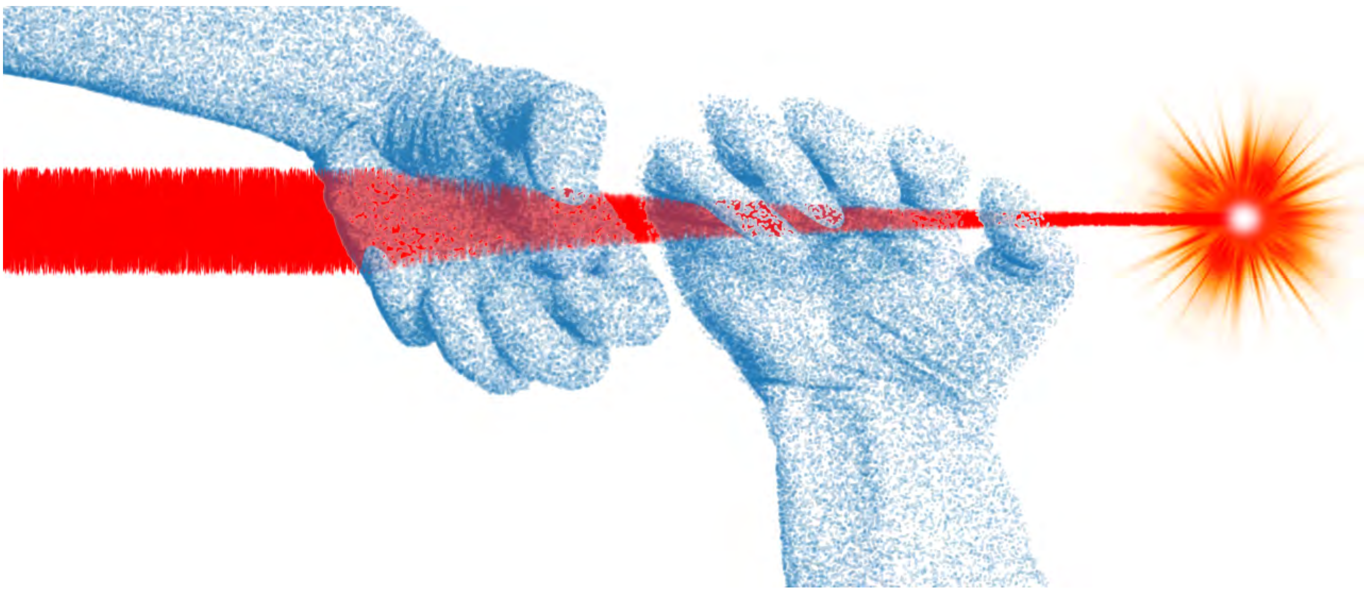

CHAPTER 10

Squeezed light from an oscillator measured at the rate of oscillation

This chapter outlines the realization of squeezed light from a spin ensemble achieving an unprecedented spin-induced light squeezing level and a new measurement regime measuring the spin ensemble faster than the rate of oscillation presented in the published work:

Christian Bærentsen, Sergey A. Fedorov, Christoffer Østfeldt, Mikhail V. Balabas, Emil Zeuthen, and Eugene S. Polzik *Squeezed light from an oscillator measured at the rate of oscillation.* arXiv. 2302.13633 (2023).

The paper submitted for publication [Bærentsen et al., 2023] is appended in appendix D.

10.1 Outline of spin-induced light squeezing

This outline presents key results of the published work [Bærentsen et al., 2023]. The full text of the paper can be found in appendix D.

The phenomenon of spin-induced light squeezing has been introduced in section 2.2.2. It originates from negative cross-correlations between the spin oscillator and the light, which reduces the fluctuation of light below the shot noise level.

The squeezing measurements demonstrated in [Bærentsen et al., 2023] were performed in two measurement regimes:

1. $\Gamma_S < \omega_S$. In this regime, the highest light squeezing is generated, reaching $11.5^{+2.5}_{-1.5}$ dB at the output of the cell and $8.5^{+0.1}_{-0.1}$ dB at the detection. The squeezing exists in a narrow bandwidth, which, however, can be freely tuned by changing the magnetic field.

   This showcases a new benchmark for the highest achieved light squeezing obtained from a spin oscillator. The quantum cooperativity reaches $C_Q = 15$, and the measurement rate reaches $\Gamma_S/(2\pi) = 52$ kHz. The measurement is performed at a detuning of $\Delta/(2\pi) = 3$ GHz with a tunable band for the Larmor frequency between 0.8 MHz and 5 MHz without having a significant change for the maximum squeezing.

2. $\Gamma_S > \omega_S$. In this regime, the light squeezing spans over a MHz bandwidth and reaches 6.5 dB at the its maximum.

   This showcases a new benchmark for measurement rates faster than the oscillation frequency obtained for a hot spin ensemble while obtaining a large quantum cooperativity of $C_Q = 8$, and measured at a readout rate of $\Gamma_S/(2\pi) \approx 2.2$ MHz. The measurement is achieved at a detuning of $\Delta/(2\pi) = 0.7$ GHz with a Larmor frequency of $\omega_S/(2\pi) = 1.09$ MHz. In addition, realizing a back-action imprecision product close to the Heisenberg limit, elevated 20% above the limit at frequencies higher than $\omega_S > 100$ kHz.

Measurements of an oscillator faster than the rate of oscillation conditionally prepare a spin state with the variance of one quadrature below the variance of the zero-point motion. On the contrary, in a measurement slower than the rate of oscillation, the oscillator is projected on coherent states, because the oscillator position is averaged over several oscillation periods.

The measurement of an oscillator faster than the oscillation rate opens the possibility for continuous positional squeezing of the oscillator [Meng et al., 2020]. The fast measurement squeezes light to low frequencies inducing an effectively instantaneous oscillator response to the back-action, which is necessary for continuous positional squeezing of the oscillator, resulting in a broad squeezing level for the measurement.

10.1.1 Experimental setup

The experimental setup for the realized spin-induced light squeezing is built using the results of the investigations displayed in this thesis: the improved pumping of the atomic ensemble presented in chapter 5, the reduced magnetic inhomogeneities presented in chapter 7, and the improved filling factor for implemented square tophat beam presented in chapter 8.

Figure 10.1 shows the experimental setup, including all the optical elements required for measuring the spin-induced light squeezing but excluding mirrors. A linearly polarized square tophat beam uniformly probes the atomic ensemble, prepared with the repump (D_2-line) in a negative mass configuration, with the atomic spin F_x aligned along the magnetic field B. The spin noise imprinted on the light polarization is measured by polarization homodyning. The pump (D_1-line) is turned off to reduce broadening, which increases the thermal noise for the squeezing spectra. Still, the spin polarization is maintained at the level $p = F_x/F \approx 78\%$.

The experiment only requires ≈ 20 mW of light at the D_2 transition, meaning low power requirements compared to bulk nonlinear crystals. Those setups, which are currently the standard for squeezed light generation [Vahlbruch et al., 2016], generally require optical powers in the watt range and large complicated experimental setups. The probe beam is aligned along the y-axis, $\alpha = \pi/2$, to maximize ζ_S. This improves the squeezing spectra, primarily due to the hybridization of the oscillator modes (explained in the following section 10.1.2). The classical laser amplitude noise driving the oscillator is also eliminated for input polarization along the y-axis, making it a favorable polarization axis for squeezing measurements,

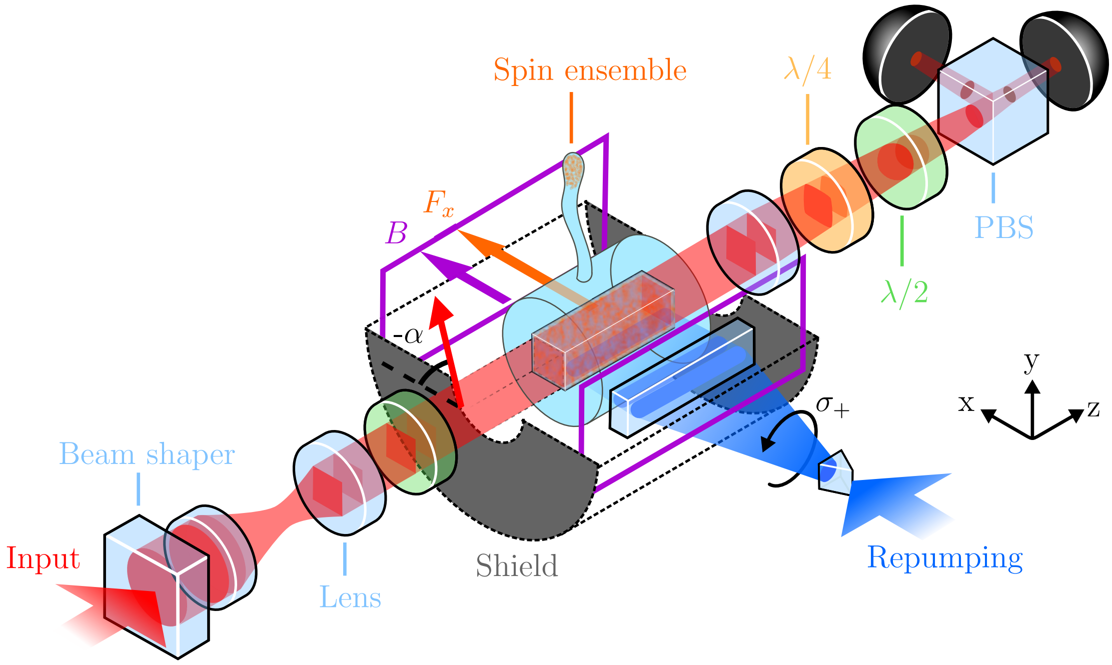

Figure 10.1: Experimental setup for spin-induced light squeezing. The atomic ensemble is pumped with the repump beam aligning the spin, F_x, to bias magnetic field, B. The atomic ensemble is probed with a linear polarized square tophat beam and detected by polarization homodyning.

arising from the otherwise neglected dynamical term for the Hamiltonian presented after equation 2.12. The optical detection efficiency after the interaction with the atomic ensemble, from the last window to detection, is $91 \pm 3\%$, only exhibiting a transmission loss of 1.6% per cell window; therefore, the losses are primarily introduced by the detection setup.

10.1.2 Hybridization of the oscillator modes

The spin modes are coupled due to dynamical effects altering the common optical bath, which hybridizes the spin modes. The expression for the multi-spin-mode Heisenberg equation is analogous to the expression for a single oscillator, derived in equation 2.20, with the addition of the coupling between oscillators (see appendix D for complete derivation):

$$\begin{aligned}\frac{\mathrm{d}}{\mathrm{d}t}\begin{pmatrix}\hat{X}_i\\ \hat{P}_i\end{pmatrix} &= \begin{pmatrix}-\gamma_{i,0}/2-\zeta_i\Gamma_i & \omega_i\\ -\omega_i & -\gamma_{i,0}/2-\zeta_i\Gamma_i\end{pmatrix}\begin{pmatrix}\hat{X}_i\\ \hat{P}_i\end{pmatrix}\\ &\quad + 2\sqrt{\Gamma_i}\begin{pmatrix}0 & -\zeta_i\\ 1 & 0\end{pmatrix}\begin{pmatrix}\hat{X}_\mathrm{L}\\ \hat{P}_\mathrm{L}\end{pmatrix} + \begin{pmatrix}\hat{F}_i^X\\ \hat{F}_i^P\end{pmatrix}\\ &\quad \underbrace{-\sum_{j=1}^{N_\mathrm{modes}}\left[\begin{pmatrix}\zeta_i\sqrt{\Gamma_i\Gamma_j} & 0\\ 0 & \zeta_j\sqrt{\Gamma_i\Gamma_j}\end{pmatrix}\begin{pmatrix}\hat{X}_j\\ \hat{P}_j\end{pmatrix}\right]}_{\text{coupling}}.\end{aligned} \tag{10.1}$$

The dynamical processes rotate the light polarization proportional to the readout rate, Γ, and the tensor interaction coefficient, ζ, of the spin modes (see equation 2.15 for the tensor interaction coefficient dependency on the mode number), changing the drive light along the propagation of the cell due to the linear birefringence of the dynamical effects.

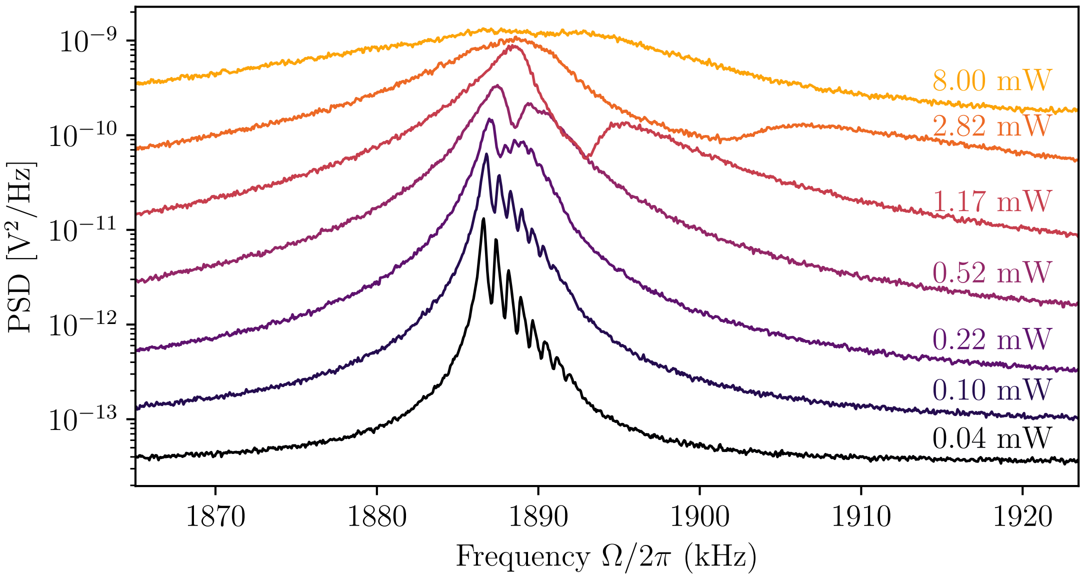

Figure 10.2: Hybridization of spin modes. The spin modes are prepared in a negative mass configuration, driven with white noise for an elevated signal, demonstrating a hybridization of spin modes for an increased probe power, measured at a detuning of $\Delta/(2\pi) = 0.7\,\text{GHz}$.

The hybridization is illustrated in figure 10.2, which shows the measurements of the spin being driven by white classical noise at different probe powers. The detuning is brought close to the resonance $\Delta/(2\pi) = 0.7\,\text{GHz}$, realizing an increased tensor interaction ζ_S (the tensor interaction dependency on the detuning is visualized in figure 2.7), to increase the effect of hybridization. The spin is prepared in the negative mass configuration, with $m_F = 4$ being the highest populated state. The black trace measured with a probe power of $0.04\,\text{mW}$ shows the strongest signal for the transition $|F = 4, m_F = 4\rangle\langle F = 4, m_F = 3|$ for thermal populated states shown by the 8 transitions, having all the spin modes spectrally separated. Three dynamics are responsible for the change of the spectral appearance when increasing the probe power; the tensor Stark shift (see equation 2.19 for details), the dynamical broadening $2\Gamma_i\zeta_i$, and the coupling of the spin modes. It is important to note that the spin polarization is independent of probe power, which was verified using the MORS technique[1]. The probe power is progressively increased, initially showing the tensor Stark shift pushing the modes together. First, starting to show the hybridization of modes at a probe power of $0.22\,\text{mW}$. The mode position in the spectra flips having $|F = 4, m_F = 4\rangle\langle F = 4, m_F = 3|$ to the right and $|F = 4, m_F = -3\rangle\langle F = 4, m_F = -4|$ to the left in the spectra when exceeding

[1]See chapter 5 for details about the MORS technique.

probe powers of 0.52 mW, where the two effects of dynamical broadening $2\Gamma_i\zeta_i$ and the coupling of modes starts to dominate, finally hybridizing the modes into the manifestation of two peaks that can be modeled by two coupled oscillators.

We model the hybridization of modes by two coupled modes accordingly to the dynamics in equation 10.1 with $N_{\text{modes}} = 2$ for the presents of two peaks in the spectrum, only introducing a third mode for high readout measurements ($\Gamma/(2\pi) > 1\,\text{MHz}$), where the broadband noise starts to be dominated by the quantum back-action, $C_{\text{Q}}^{\text{BBN}} \gtrsim 1$.

10.1.3 Characterization of the squeezing spectra

The characterization of the spin system is done via quadrature sweeps, where the detection angle, ϕ, is changed for the measurements of several spectra. The quadrature sweep is fitted with the full model describing the frequency behavior of interaction with the atomic ensemble by a global fit for all the detection angles. This is achieved using three model descriptions:

1. A single oscillator model, achieved by tuning the tensor Stark shift to the quadratic Zeemann splitting for a detuning of $\Delta/(2\pi) = 7\,\text{GHz}$. This process aligns all the oscillators to have the same Larmor frequency. This can be seen in figure 10.3a, demonstrating 7.5 dB of squeezing for a quantum cooperativity of $C_{\text{Q}} = 11$, measured for a readout of $\Gamma/(2\pi) = 13\,\text{kHz}$.

2. A two oscillator model fitted to the hybridization of the modes into two peaks, realized when tuning the detuning to $\Delta/(2\pi) = 3\,\text{GHz}$. This can be seen in figure 10.3b, detecting $8.5^{+0.1}_{-0.1}$ dB of squeezing for a quantum cooperativity of $C_{\text{Q}} = 15$, and a readout rate of $\Gamma/(2\pi) = 52\,\text{kHz}$, with the generated squeezing level of $11.5^{+2.5}_{-1.5}$ dB accounting for the detection losses. This measurement also constitutes a high level of fraction coherent spin readout reaching $\Gamma_{\text{S}}/\gamma_{\text{S0}} = 42$.

3. A three oscillator model similar to the "two oscillator model" with the addition of an oscillator representing the broadband noise because the broadband mode starts to be back-action dominated, realized when tuning the detuning to $\Delta/(2\pi) = 0.7\,\text{GHz}$. This can be seen in figure 10.3c, detecting 5.3 dB of squeezing for a quantum cooperativity of $C_{\text{Q}} = 8$, and readout rate of $\Gamma/(2\pi) = 1.77\,\text{MHz}$. This measurement is used to calibrate the spin parameters for a lower Larmor frequency seen in figure 10.4 since classical low-frequency noise increases the model error for fits of the quadrature sweep at lower frequencies.

The stability of the experimental configuration when performing the quadratures sweep is only affected by the fluctuations of the probe power varying within 3% between the measurements of the spectra.

Additional methods are applied for verification of experimental parameters, using the theoretical optimum-quadrature squeezing spectrum, derived in appendix D:

$$S_{\min}(\Omega)/\text{SN} = 1 - 2\eta\frac{\Gamma}{\Gamma + \gamma_{\text{S0}}(1+2n)}\,D\left(\frac{\Omega - \omega_{\text{S}}}{\Gamma + \gamma_{\text{S0}}(1+2n)}\right), \tag{10.2}$$

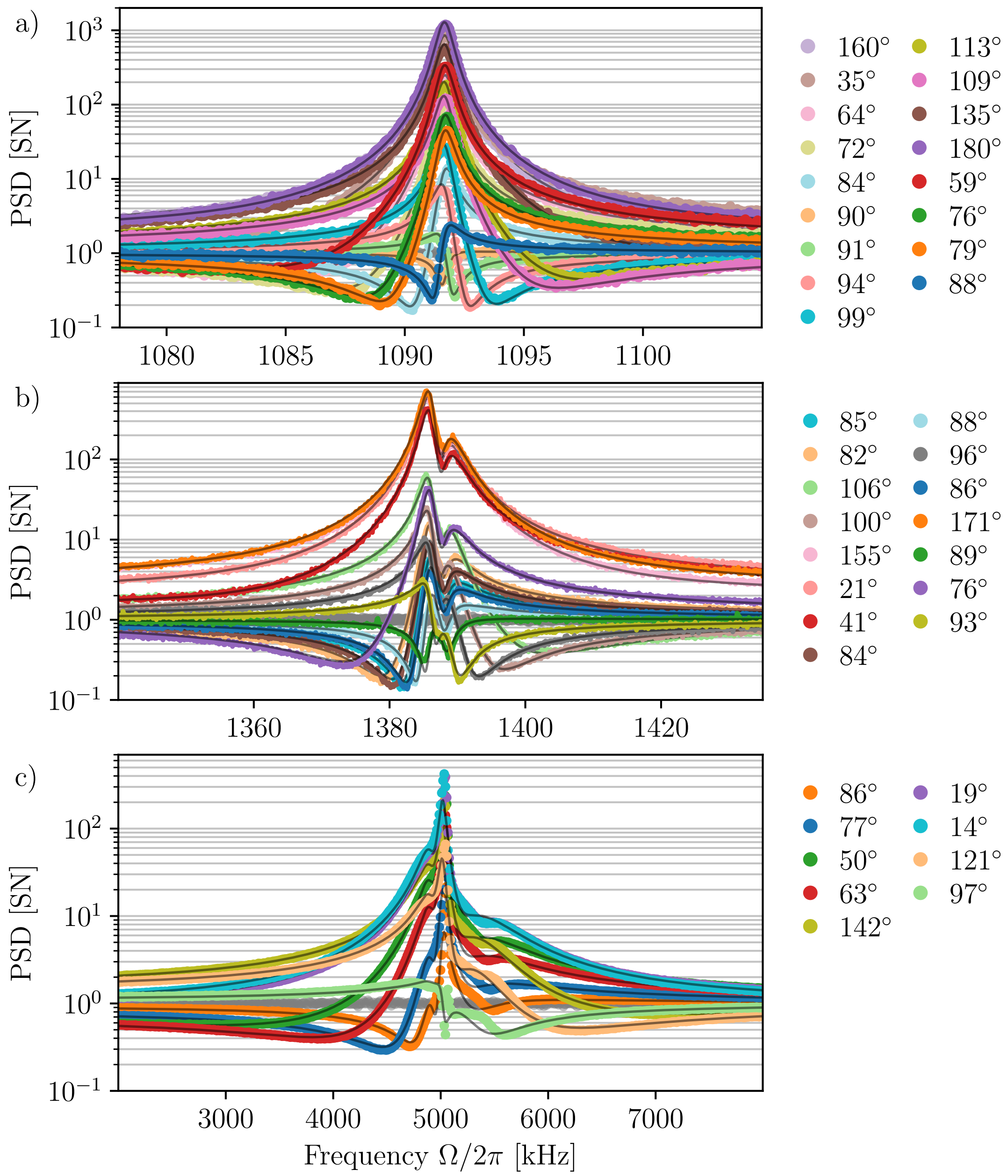

Figure 10.3: Squeezing spectra in three regimes. The black curve is a global fit of all the spectra calculated for three models. The colors represent the different detection angles ϕ. The gray curve shows the shot noise. a) single oscillator model measured at $\Delta/(2\pi) = 7\,\mathrm{GHz}$. b) two oscillator model measured at $\Delta/(2\pi) = 3\,\mathrm{GHz}$. c) three oscillator model measured at $\Delta/(2\pi) = 0.7\,\mathrm{GHz}$. The figure is revisited in the supplementary information in appendix D.

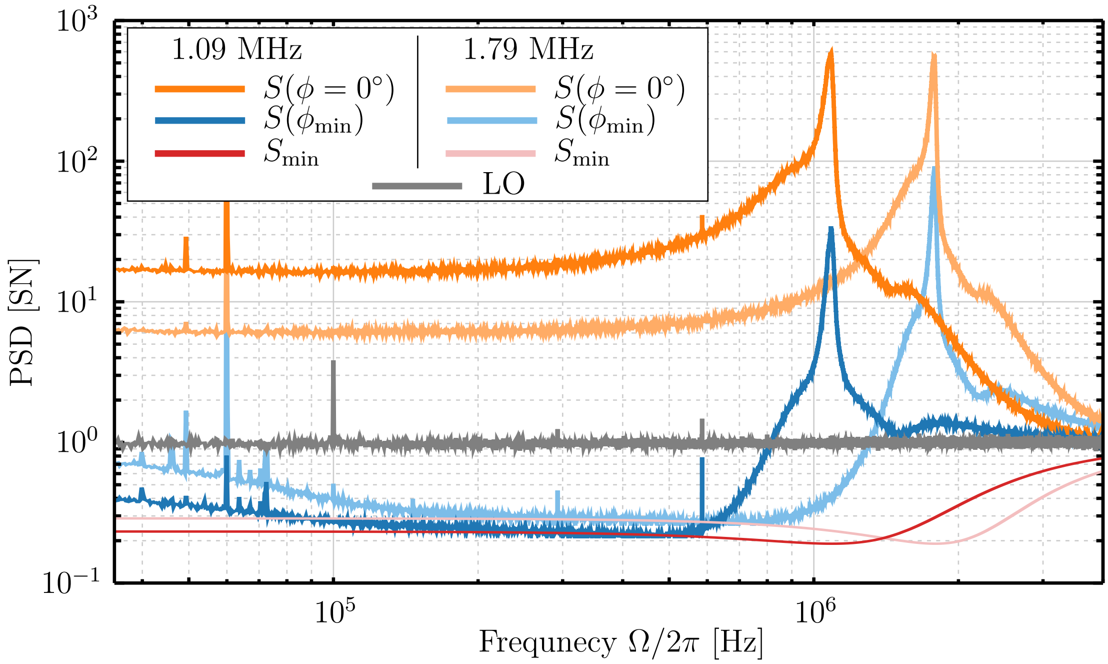

Figure 10.4: Spectra for measurements faster than the rate of oscillation. The measurements in orange are measured at the P quadrature, the measurements in blue are the best squeezing levels measured close to the X quadrature, and red is the theoretical optimum-quadrature squeezing spectrum. The spectra demonstrate a readout rate of $\Gamma/(2\pi) \approx 2.2\,\text{MHz}$. The figure is revisited in appendix D.

with the function $D(x) = 1/\left(1 + \sqrt{1 + 4x^2}\right)$. This model can be used to determine the maximum squeezing for all frequencies. Furthermore, a model for the level of oscillator response at zero frequency measured for the P quadrature of light, relevant for measurements faster than the rate of oscillation:

$$S_{\phi=0}(0)/\text{SN} = 1 + 4\eta \left(\Gamma/\omega_{\text{S}}\right)^2 . \tag{10.3}$$

These two models aid the parameter estimation in combination with the global quadrature sweep to determine the relevant parameters of the spin oscillator. This is especially useful for the measurements at the detuning $\Delta/(2\pi) = 0.7\,\text{GHz}$ having a significant contribution from the dynamical back-action $\zeta = 0.18$, which makes the fits more demanding due to strong coupling between the modes.

Figure 10.4 shows the measurement of the spin oscillator faster than the rate of oscillation for a Larmor frequency of 1.09 MHz and 1.79 MHz, performed at the detuning of $\Delta/(2\pi) = 0.7\,\text{GHz}$. The measurements of the P quadrature are presented in orange for establishing the readout rate using the model in equation 10.3. The blue curve presents the best squeezing with a Larmor frequency of 1.09 MHz reaches a flat squeezing level of 6.5 dB, aligned with the red curve for the theoretical optimum-quadrature squeezing spectrum detailed in equation 10.2. These measures confirm a readout rate of $\Gamma/(2\pi) \approx 2.2\,\text{MHz}$. The measurements are performed with 12.8 mW of probe power concerning a probe power of 10.2 mW for the quadrature sweep presented in figure 10.3c. Accounting for the readout rate being proportional to the probe power allows us to conclude that the measurements of the readout rates are in agreement $[\Gamma_{10.2\,\mathrm{W}}/(2\pi)]\cdot[12.8\,\mathrm{mW}/10.2\,\mathrm{mW}] \approx 2.2\,\mathrm{MHz}$, demonstrating the robustness of our model.

We are concluding the measurements of the spin-induced light squeezing constituting a new regime for the performance of quantum oscillators in generating light squeezing. Additionally, a new regime for the oscillator capabilities for measurements faster than the rate of oscillation while still achieving a high quantum cooperativity for the measurements.

Part V

Hybrid spin-optomechanical systems

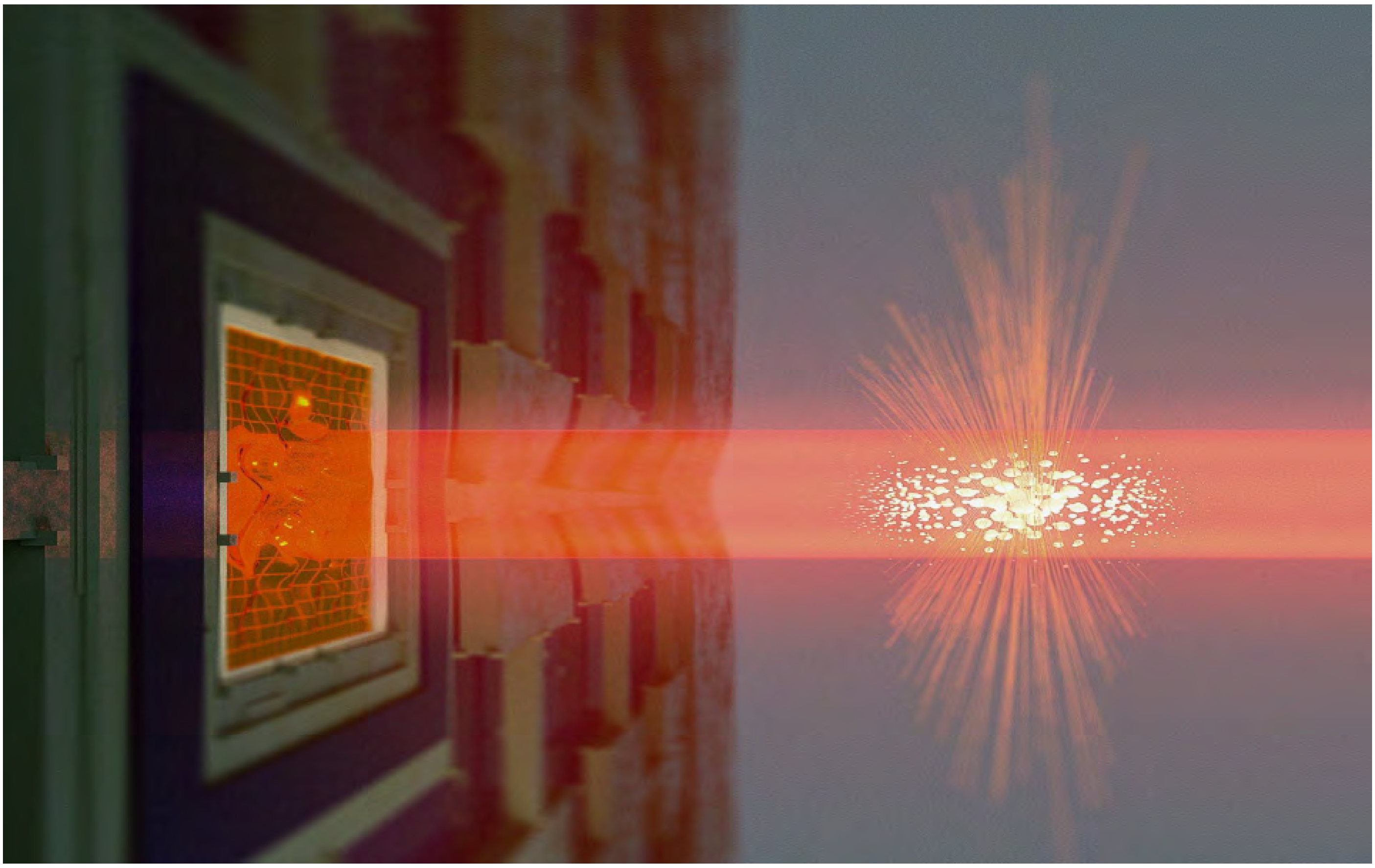

Illustration by Bastian Leonhardt Strube and Mads Vadsholt.

CHAPTER 11

Entanglement

This chapter outlines the experimental realization of entanglement generation and verification between the macroscopic spin ensemble and the membrane in the-middle optomechanical cavity presented in the published work:

Rodrigo A. Thomas, Michał Parniak, Christoffer Østfeldt, Christoffer B. Møller, **Christian Bærentsen**, Yeghishe Tsaturyan, Albert Schliesser, Jürgen Appel, Emil Zeuthen, and Eugene S. Polzik. *Entanglement between distant macroscopic mechanical and spin systems.* Nature Physics. 17, 228–233 (2021).

The published work can be found in appendix E.

11.1 Outline of hybrid spin-optomechanical entanglement

This outline presents key results of the published work [Thomas et al., 2020]. The full text of the paper can be found in appendix F.

Entanglement is essential for quantum protocols such as quantum-enhanced sensing and quantum teleportation. [Kurizki et al., 2015] presents the prospect of using hybrid systems in order to benefit from the strengths of the physical properties in different material platforms. The missing link between atomic spin ensembles and mechanical resonators described in that reference is resolved by the realization of entanglement between hybrid spin-optomechanical systems presented by our published work [Thomas et al., 2020].

Hybrid spin-optomechanical entanglement was initially proposed in [Hammerer et al., 2009], using back-action evading measurements for creating an entangled state between an atomic spin ensemble and a mechanical resonator. The initial proposal differs from the realized experimental entanglement scheme presented here by assuming the absence of dynamical back-action processes. This is not feasible within the parameter constraints in our setup; moreover, dynamical back-action can be beneficial for increasing the degree of entanglement.

11.1.1 Einstein–Podolsky–Rosen state

The quadratures for the spin and mechanical systems are non-commuting variables:

$$[\hat{X}_{\mathrm{S,M}}, \hat{P}_{\mathrm{S,M}}] = i. \tag{11.1}$$

The boundary sets a minimum uncertainty for our ability to predict system variables set by the Heisenberg uncertainty limit. This is not the limit to the precision for suitable measurements of the combined system that prepares an Einstein–Podolsky–Rosen (EPR) state [Einstein et al., 1935]. This is possible for the EPR combinations of the two systems:

$$\begin{aligned} \hat{X}_{\mathrm{EPR}} &= \frac{1}{\sqrt{2}}(\hat{X}_{\mathrm{M}} - \hat{X}_{\mathrm{S}}), \\ \hat{P}_{\mathrm{EPR}} &= \frac{1}{\sqrt{2}}(\hat{P}_{\mathrm{M}} + \hat{P}_{\mathrm{S}}), \\ [\hat{X}_{\mathrm{EPR}}, \hat{P}_{\mathrm{EPR}}] &= 0. \end{aligned} \tag{11.2}$$

The commutation relation of zero implies that the pair of EPR variables can be prepared in simultaneously well-defined values without violating the Heisenberg uncertainty limit. An EPR state for a pair of systems violate the locality principle manifested by entanglement (non-separability) between the two systems. Therefore, the variance of the combined system can go below the inseparability limit for an entangled state [Duan et al., 2000]:

$$V = \mathrm{Var}[\hat{X}_{\mathrm{EPR}}] + \mathrm{Var}[\hat{P}_{\mathrm{EPR}}] < 1. \tag{11.3}$$

More generally, EPR variables with unequal weights on the two subsystems, as arises in our experimental setting, can also exhibit inseparability according to equation 11.3 (see also the discussion of the full model for the hybrid system in appendix E)

11.1.2 Simplified hybrid model

The spin and optomechanical systems have similar behaviors when interacting with light. The atomic ensemble is characterized by canonical quadratures ($\hat{X}_{\mathrm{S}}$, $\hat{P}_{\mathrm{S}}$) that are mapped into transverse polarization components of light through the Faraday rotation. The mechanical oscillator is characterized by canonical quadratures ($\hat{X}_{\mathrm{M}}$, $\hat{P}_{\mathrm{M}}$) that are mapped into the amplitude and phase components of light through optomechanical effects. The translation of light quadratures between the two systems is achieved by polarization optics converting polarization states into amplitude and phase states. The two systems have the same type of spectral response function[1]:

$$\chi_{\mathrm{S,M}}(\Omega) = \frac{\omega_{\mathrm{S,M}}}{\omega_{\mathrm{S,M}}^2 - \Omega^2 - i\Omega\gamma_{\mathrm{S,M}}}. \tag{11.4}$$

[1]The susceptibility of the spin is matched to the mechanics for the approximations presented in equation 2.35.

The interaction of the individual systems with light obeys the input-output relations of the form:

$$\begin{pmatrix} \hat{X}_{\mathrm{L}}^{\mathrm{out}} \\ \hat{P}_{\mathrm{L}}^{\mathrm{out}} \end{pmatrix} = \begin{pmatrix} \hat{X}_{\mathrm{L}}^{\mathrm{in}} \\ \hat{P}_{\mathrm{L}}^{\mathrm{in}} \end{pmatrix} + \sqrt{\Gamma_{\mathrm{S}}} \begin{pmatrix} 0 & \pm\zeta_{\mathrm{S,M}} \\ 1 & 0 \end{pmatrix} \begin{pmatrix} \hat{X}_{\mathrm{S,M}} \\ \hat{P}_{\mathrm{S,M}} \end{pmatrix}, \tag{11.5}$$

where the sign before the tensor interaction coefficient is determined by the effective mass of the oscillator. We can write up the simplified solution for the combined/joint input-output relation of the hybrid system when neglecting the losses of the systems,

$$\hat{P}_{\mathrm{L}}^{\mathrm{out}} = \hat{P}_{\mathrm{L}}^{\mathrm{in}} + \sqrt{\Gamma_{\mathrm{M}}}\hat{X}_{\mathrm{M}} + \sqrt{\Gamma_{\mathrm{S}}}\hat{X}_{\mathrm{S}}. \tag{11.6}$$

The solution for the input-output relation of light interacting with the lossless hybrid system, inserting the solution of $\hat{X}_{\mathrm{M}}$ and $\hat{X}_{\mathrm{S}}$, derived in appendix E:

$$\begin{aligned} \hat{P}_{\mathrm{L}}^{\mathrm{out}} \approx \hat{P}_{\mathrm{L}}^{\mathrm{in}} &+ \overbrace{\left[\Gamma_{\mathrm{S}}\chi_{\mathrm{S}} + \Gamma_{\mathrm{M}}\chi_{\mathrm{M}}\right] 2\hat{X}_{\mathrm{L}}^{\mathrm{in}}}^{\mathrm{BA}} \\ &+ \underbrace{2i\Gamma_{\mathrm{M}}\chi_{\mathrm{M}}\chi_{\mathrm{S}}\left[2\Gamma_{\mathrm{S}}[\zeta_{\mathrm{M}} - \zeta_{\mathrm{S}}]\hat{X}_{\mathrm{L}}^{\mathrm{in}} + \sqrt{\Gamma_{\mathrm{S}}}[\zeta_{\mathrm{M}} - \zeta_{\mathrm{S}}]\hat{F}_{\mathrm{S}}\right]}_{\text{dynamical BA}} \\ &+ \underbrace{\sqrt{\Gamma_{\mathrm{S}}}\chi_{\mathrm{S}}\hat{F}_{\mathrm{S}} + \sqrt{\Gamma_{\mathrm{M}}}\chi_{\mathrm{M}}\hat{F}_{\mathrm{M}}}_{\mathrm{TH}}. \end{aligned} \tag{11.7}$$

The expression for the light input-output relation with the hybrid system can be split into three contributions; back-action noise (BA), dynamical back-action noise (dynamical BA), and thermal noise (TH).

The spin ensemble can be configured to form a negative-mass reference frame (see section 2.1.1 for details), where the spin response is opposite to that of the mechanics. The ideal configuration for matching the susceptibilities is to have the following conditions; $\gamma_{\mathrm{S}} = \gamma_{\mathrm{M}}$ and $-\omega_{\mathrm{S}} = \omega_{\mathrm{M}}$, resulting in $-\chi_{\mathrm{S}} = \chi_{\mathrm{M}}$, in view of equation 11.4. Furthermore, the readout rate of the systems can be matched $\Gamma_{\mathrm{S}} = \Gamma_{\mathrm{M}}$, which results in a back-action evading measurement due to the cancellation of the BA term in equation 11.7. This has been realized in a previous experiment [Møller et al., 2017], showing measurement with a 1.8 dB reduction of the quantum back-action. However, the dynamical BA can also be evaded by matching $\zeta_{\mathrm{S}} = \zeta_{\mathrm{M}}$, still with the presents of dynamical broadening. While this yields an idealized example of quantum back-action evading measurements, a mismatch between the dynamical processes, $\zeta_{\mathrm{S}} < \zeta_{\mathrm{M}}$, in fact, contributes destructively to other noise processes, thereby improving entanglement generation [Huang et al., 2018].

The resonant hybrid system, with system parameters listed in appendix E, shows an overall reduction of the quantum back-action noise by 4.6 dB, additionally reducing the thermal spin noise by 2.5 dB from non-local dynamical cooling performed by the membrane. This reduces the unconditional variance from $V_{\mathrm{u}} = 6.07$ to $V_{\mathrm{u}} = 1.91$, transitioning from a non-evading to an evading measurement (with regard to the quantum back-action). This is close to the limit of a system free of dynamical effects, being in the ground-state for an unconditional variance of $V_{\mathrm{u}} = 1$ [Vasilyev et al., 2013], which can be exceeded when including dynamical effects [Huang et al., 2018]. The realized hybrid system can surpass the inseparability limit by conditioning the variance on prior measurements.

11.1.3 Conditional variance

The conditional variance is model-based by predicting the state from prior measurements, realized by the equations of motion for our system, with the knowledge of noise spectral densities for the input operators to estimate the optical filter for predicting the state of the hybrid system.

Figure 11.1 illustrates the simplified hybrid system. The light first interacts with the atomic ensemble then it is transmitted to interact with the optomechanical cavity. The two systems oscillate oppositely in phase space, illustrating the negative-mass reference frame constituted by the atomic spin ensemble. The output signal from the hybrid system is finally detected, resulting in the photocurrent $i(t)$. Next, we want to filter the photocurrent in order to optimally estimate the state of the hybrid system as illustrated by the exponential filter function, $K(t)$, in the upper right corner of figure 11.1.

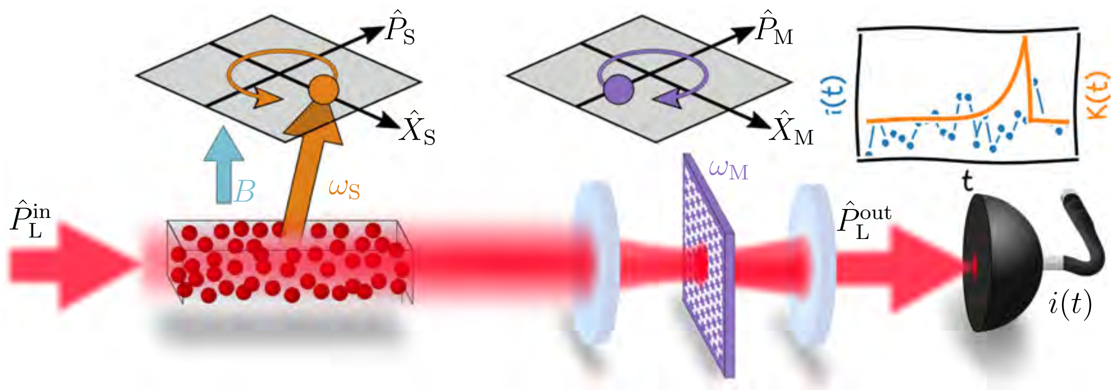

Figure 11.1: Illustration of the hybrid entanglement setup. A simplified depiction of the hybrid experiment, showing the interaction of a traveling light field with the spin and optomechanical subsystems. $i(t)$ is the measured photocurrent to be filtered by the Wiener filter $K(t)$. The figure is revisited in appendix E.

We want to track the quadratures of the hybrid system:

$$\mathbf{Q} = (\hat{X}_{\mathrm{M}}, \hat{P}_{\mathrm{M}}, \hat{X}_{\mathrm{S}}, \hat{P}_{\mathrm{S}}). \tag{11.8}$$

The tracking of the conditional trajectory of quadratures can be found by integrating the homodyne current up until that point using appropriate stationary filters;

$$\mathbf{Q}_{\mathrm{c}} = \int_0^t \mathbf{K}(t' - t, t) i(t') \, \mathrm{d}t'. \tag{11.9}$$

The appropriate filter for measuring a steady-state system is the Wiener filter [Wiener, 1964]. The Wiener filter can be calculated from the Wiener-Hopf equation, which involves the cross-correlations between the tracked quadratures and the photocurrent (see appendix E for details).

We can calculate the conditional covariance matrix, $\mathbf{V}_{\mathrm{c}}$, from the unconditional covariance matrix, $\mathbf{V}_{\mathrm{u}}$, by subtracting the unconditional covariance matrix of the best estimates obtained from optimal filtering:

$$\mathbf{V}_{\mathrm{c}} = \mathbf{V}_{\mathrm{u}} - \mathbf{V}_{\mathrm{be}}, \tag{11.10}$$

where the best estimate covariances can be calculated from the covariance between the unconditional and conditional tracking of the system:

$$\mathbf{V}_{\mathrm{be}}(t) = \mathrm{Cov}(\mathbf{Q}, \mathbf{Q}^c(t)). \tag{11.11}$$

In turn, the EPR variables can be constructed by appropriate weighting, $\mathbf{u}$, of the systems characterized by $\mathbf{Q}$.

$$\begin{aligned} \hat{\mathbf{X}}_{\mathrm{EPR}} &= \mathbf{u}^{\intercal}\mathbf{Q}, \\ \hat{\mathbf{X}}^{\mathrm{c}}_{\mathrm{EPR}} &= \mathbf{u}^{\intercal}\mathbf{Q}^{\mathrm{c}}. \end{aligned} \tag{11.12}$$

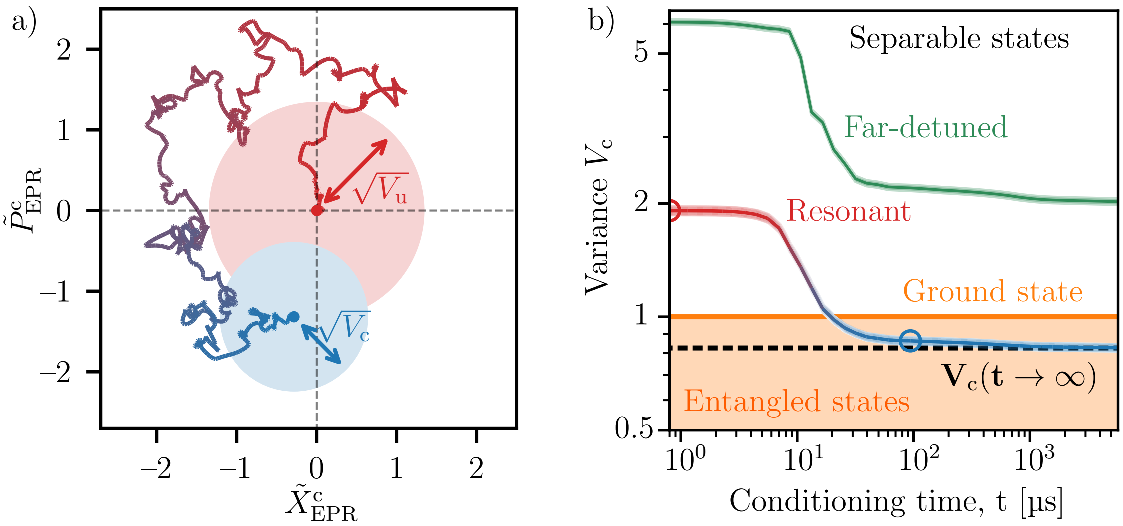

Figure 11.2: Conditional cooling of the EPR variance. a) phase space trajectory of the conditional EPR quadratures, evolving from red to blue. b) conditional variance as a function of time, acquiring prior information about the state, showing the bound for entangled states, having a variance below 1. The figure is revisited in appendix E.

The evolution of the conditional variance can be seen in figure 11.2. Figure a) shows the trajectory in the phase space of the conditional EPR pair. $\tilde{X}^{\mathrm{c}}_{\mathrm{EPR}}$ and $\tilde{P}^{\mathrm{c}}_{\mathrm{EPR}}$ denotes the quadrature signals obtained by demodulation at the oscillation frequency. The initial EPR state has the unconditional variance $V_\mathrm{c}(t \to 0) = V_\mathrm{u}$. The conditional EPR pair's variance is "cooled" by extracting information from the measurement record, therefore cooling by measurement. Figure b) shows the cooling of the initial unconditional variance of $V_\mathrm{u} = 1.91$ down below the ground-state variance of 1;

$$V_\mathrm{c} = \mathrm{Var}_\mathrm{c}[\hat{X}_{\mathrm{EPR}}] + \mathrm{Var}_\mathrm{c}[\hat{P}_{\mathrm{EPR}}] = 0.83 \pm 0.02 < 1, \tag{11.13}$$

showing an entangled state with uncertainties far below the inseparability limit. This can be compared to the variance of the far-detuned subsystems above the inseparability limit, which displays the absence of back-action evading effects, demonstrating the advantage of the negative-mass reference frame.

11.2 Improved hybrid system

Results in appendix E further project that a conditional variance of $V_c \approx 0.3$ can be achieved by improving experimental parameters; a reduction of the thermal noise introduced by the broadband noise from the spin by a factor of 3, improving the fractional coherent spin readout Γ_S/γ_{S0} by a factor of 3, reducing the optical losses between the two systems by 37%, and improving the cavity overcoupling to 98%.

The experiment has been rebuilt since the entanglement demonstration published in [Thomas et al., 2020]. Consequently, the experimental parameters have changed to further improve the hybrid system, which is detailed in this thesis:

- The overall thermal noise contribution from the broadband noise has been improved by a factor of 2 when comparing the ratio $A_{\mathrm{BBN}}/\Gamma_S$ (see chapter 8).
- The fractional coherent spin readout Γ_S/γ_{S0} has been improved by a factor of 3.6, reaching $\Gamma_S/\gamma_{S0} = 42$ (see chapter 10).
- We bought new cavity mirrors to improve the overcoupling and lower the mirror noise. The new mirrors show an overcoupling of $\approx$ 96% for the membrane placed in the position of maximum photon-phonon coupling.
- The quantum efficiency between the systems has also been significantly improved, as we were limited by the double pass of the atomic ensemble for readout enhancement [Thomas, 2020] and the limited coupling to the optomechanical cavity. The quantum efficiency between the systems has been improved by $\Delta\nu \approx 13\%$.
  - 5% arising from a Faraday isolator, which can be excluded in the single pass.
  - $\approx$ 0% by flipping the cascade order from having the first system being the atoms to the mechanics, as the out coupling of the two systems is similar.
  - $\approx$ 8% from improving mode overlap of the two systems. The mode overlap of the two systems was $\simeq$ 90%. This has been improved, in the flipped configuration, with preliminary results showing a mode overlap between the mode cleaning cavity and optomechanical cavity $\approx$ 98%.
- The detection efficiency has also been improved due to the reversed configuration of the setup from 77% to 91%, resulting in an improvement of the detection efficiency by $\Delta\eta = 14\%$.

The new experiment would have to be flipped due to the changed experimental configuration, introducing a square tophat beam. This would be a disadvantage for the non-local dynamical cooling of the spin oscillator in the old configuration, having the spin system as the dominating thermal noise contributor. Therefore, the flipped experiment would instead perform a non-local dynamical cooling of the mechanical oscillator. However, this does not significantly affect the new experimental parameters because the mechanical oscillator now has the largest thermal contribution.

The improved system parameters are close to the outlook of the future work that we present in appendix E. The newly achieved parameters would give a conditional variance of $V_\mathrm{c} \approx 0.45$ using the same cascaded model for calculating the conditional variance as presented in appendix E. This would imply that we are breaching the boundary for EPR steering $V_\mathrm{c}^\mathrm{steering} < 0.5$ [Huang et al., 2019], which would constitute a new regime for quantum protocols in hybrid quantum systems.

CHAPTER 12

Teleportation

Quantum teleportation is a crucial ingredient in entanglement distribution, for example, for quantum key distribution in communication and state transfer in quantum computing. The first experimental realization of quantum teleportation was the teleportation between light fields/modes [Bouwmeester et al., 1997]. Regarding experiments involving spin ensembles, teleportation of a coherent displacement of light to a spin ensemble [Sherson et al., 2006], and later teleportation between two spin ensembles [Krauter et al., 2013] have been realized. On the other hand, teleportation involving mechanical objects is still a relatively undeveloped field except for a recent discrete-variable demonstration of polarization state teleportation to mechanical objects [Fiaschi et al., 2021]. In particular, the teleportation between a material system and optomechanics is still unheard-of. Such experiments would open the possibility of preparing a non-classical state for the mechanical system and the teleportation of states to the mechanical resonator as a long-lived material system for the storage of quantum states.

Here, we present our efforts towards the teleportation of a quantum state from the spin ensemble to the mechanics using light as the meter field, building on our previous realization of spin-optomechanical entanglement. The teleportation can be achieved via a Bell measurement between the atomic ensemble and the light entangled with the mechanics. The Bell measurement is traditionally depicted as a Bell state $|\phi_{\text{BELL}}\rangle_{\text{M,L}}$ being the entangled link between mechanics and light, performing a Bell measurement for the light and the spin ensemble $|\psi\rangle_{\text{S}} \bigotimes |\phi_{\text{BELL}}\rangle_{\text{M,L}}$ measured in the basis of the EPR pair $\langle\psi_{\text{EPR}}|_{\text{S,L}}$ for the light and spin systems (see equation 11.2 for the equally weighted EPR pair of the spin-optomechanical system). This process is well-established for the discrete-variable teleportation [Bennett et al., 1993], and for continuous variables teleportation [Braunstein and Kimble, 1998] but it has still been unclear for non-projective measurements when collapsing the superposition of states onto a basis of observables [Wiseman and Milburn, 2009], until recent findings in [Fedorov and Zeuthen, 2023].

12.1 Prediction and retrodiction for hybrid spin-optomechanical teleportation

We want to teleport the spin state onto the mechanics by continuous state estimation for the teleportation protocol, requiring us to consider the collapse of states upon measuring, meaning filtering has to be implemented for optimal state estimation for the teleportation protocol: It is desired to predict the mechanical state since we want to estimate the state in which we want to teleport. This is employed by filtering, $f(t)$, the measurement current, $i(t)$;

$$\hat{b}_{\mathrm{M}}(\tau) = \int_0^{\tau} f(t)i(t)dt, \tag{12.1}$$

to predict the mechanical state, $\hat{b}_{\mathrm{M}}$, at time τ. And it is desired to retrodict the spin state since we want to estimate the prepared state that we want to teleport employed by estimating the spin state, $\hat{b}_{\mathrm{S}}(0)$ at time zero.

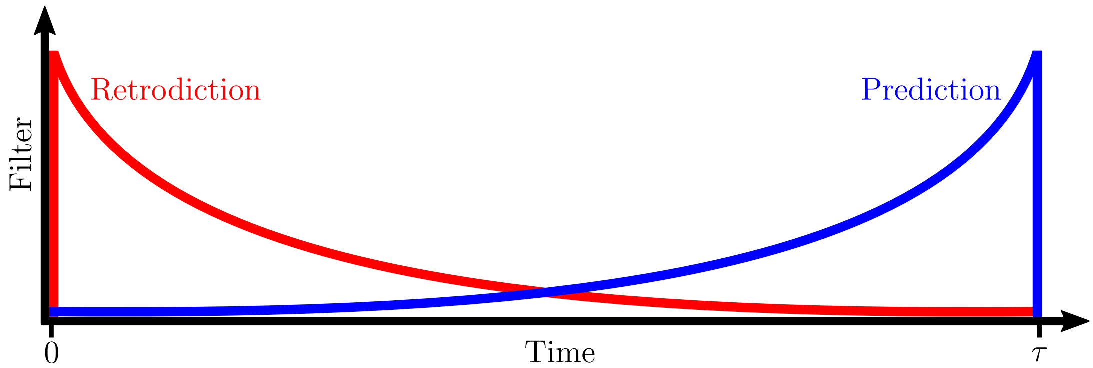

Figure 12.1: Filtering for prediction and retrodiction of the demodulated measurement current. Prediction of the state of the oscillator (mechanics) at the end of the measurement interval $\hat{b}_{\mathrm{M}}(\tau)$, and retrodiction of the state of the oscillator (spin) at the beginning of the measurement interval $\hat{b}_{\mathrm{S}}(0)$. Rising and falling exponentials to resemble the filters for prediction and retrodiction theory, respectively, for a continuous measurement in the time interval $t \in [0, \tau]$.

The concept of prediction was invoked in the context of entanglement generation in chapter 11, where it was used to achieve the conditional estimation of a state by filtering the measurement current. For the constant drive/readout rate $\Gamma(t) = \Gamma$ employed there, the optimal steady-state (Wiener) filter is a rising exponential. Contrary to the steady-state entanglement experiment, a more involved filter is generally required in the non-stationary context of a continuous measurement within a finite time interval, see figure 12.1, that is Kalman filtering; the Wiener filter is recovered in the stationary limit. The complementary procedure of retrodiction, concerned with estimating the initial system state at the beginning of the measurement interval, is qualitatively similar to prediction. Considering a constant drive/readout rate in the measurement interval, a falling filter function is required for the optimal estimation of the initial state.

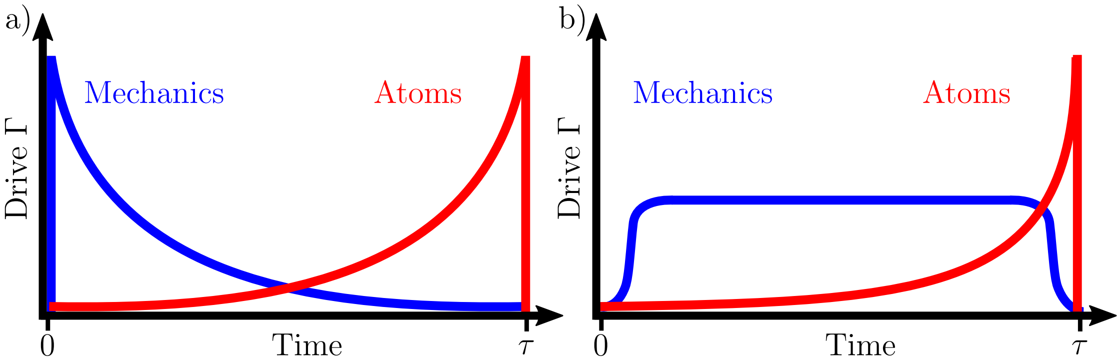

Figure 12.2: Drive to match the prediction and retrodiction filters. a) shaping of the mechanical and atomic drive to match the prediction and retrodiction filters. b) a smoothened flat drive of the mechanics to reduce optical spring effects and a raising drive of the atoms for matching the prediction and retrodiction filters.

Typical rising and falling filter functions for prediction and retrodiction can be seen in figure 12.1. The appropriate continuous Bell measurement on the hybrid system requires the simultaneous filtering of both retrodiction of the initial spin state and prediction of the mechanical state at τ after the entangling interaction with light; this superposition of prediction and retrodiction is referred to as pretrodiction in [Fedorov and Zeuthen, 2023]. This can be accomplished by shaping the drive envelopes $\Gamma_{\mathrm{S,M}}(t)$, represented by the readout rate, of both systems to match the optimal filters for the prediction and retrodiction components in order to enable the optimal pretrodiction of the final state of mechanics and the initial state of atoms. The matching of filters is achieved by a falling envelope of the drive for the subsystem to be predicted (mechanics) and a rising envelope of the drive for the subsystem to be retrodicted (atoms) seen in figure 12.2a. The time-varying envelope for the mechanical drive could be inconvenient due to the resulting time dependence of the induced optical spring effects [Aspelmeyer et al., 2014], which can be circumvented by smoothened flat pulses for the mechanical drive [Zwettler, 2019]. Appropriate reshaping of the atomic drive can ensure the matching of filters. This is achieved by a more sharply rising atomic drive envelope, as shown in figure 12.2b. Whereas the pairs of drive shapes shown in figure 12.2 are qualitative plots, the analytical theory of drive envelope matching is given in [Fedorov and Zeuthen, 2023].

12.2 Experimental setup for teleportation

The presented shaping of drive pulses has required significant changes to the experimental scheme, in addition flipping the system order of the oscillators, implementing a tophat beam, a new optical pumping scheme, a mode cleaning cavity, and a verification setup. Therefore, it has been necessary to perform a total disassembly of the experimental setup.

The new experimental setup, designed for teleportation from the atomic spin oscillator to the mechanical oscillator, can be seen in figure 12.3. Its layout can be divided into six sections:

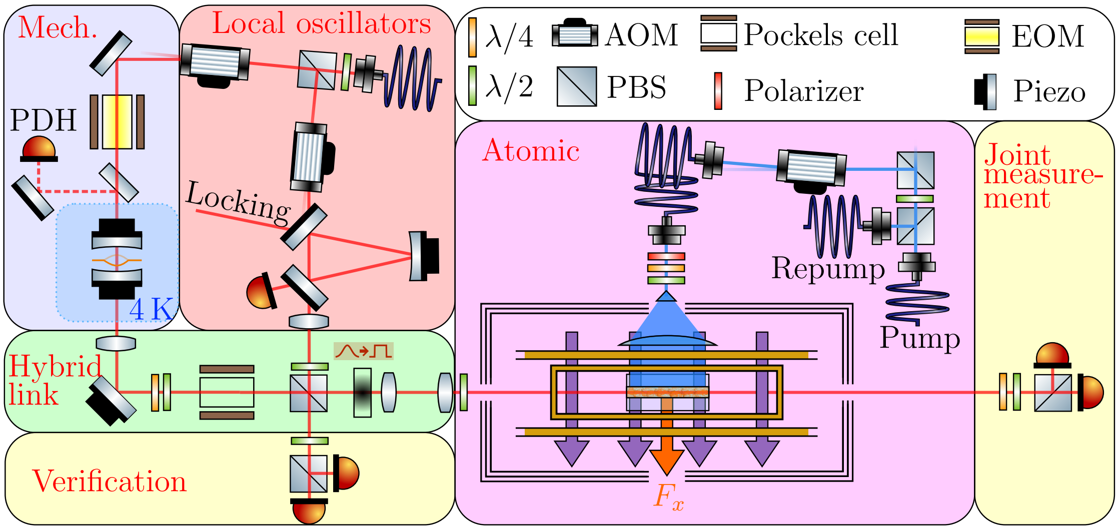

Figure 12.3: Teleportation setup. The setup is divided into six sections; local oscillators, mechanics, hybrid link, atomic, joint measurement, and verification. See the text for details.

Local oscillators

It is required for the local oscillators to be pulsed in the teleportation experiment; this pulse shaping is implemented by AOMs.

Another addition to the experimental setup is a mode cleaning cavity for cleaning the Gaussian mode to better mode match the mechanical and atomic systems, and for an improved detection efficiency of the mechanics. The mode cleaning cavity has to be locked to a counter-propagating beam for locking while pulsing the beams.

Mechanics

It is desirable to have an interaction with light dominated by the two-mode-squeezing type, $\zeta_{\mathrm{M}} < 0$, to have an efficient entangled link for the teleportation protocol [Fedorov and Zeuthen, 2023]. Since this implies optically-induced anti-damping of the oscillator, whereby no steady state exists, the teleportation protocol benefits from being pulsed. Moreover, the initial cooling can be performed before the protocol is initiated.

A Pound–Drever–Hall (PDH) lock [Black, 2001] stabilizes the cavity to the laser frequency.

Hybrid link

The hybrid link of the experiment is responsible for transporting and converting the light that has interacted with the mechanics so that it can interact with the atomic ensemble. The hybrid link also transports the measurement of the mechanical state after teleportation for the verification setup. A Pockels cell is implemented for switching the polarization, thereby directing the light to either the atomic ensemble or the verification setup. A fixed fraction of the local oscillator is split off to drive the atomic ensemble and the subsequent verification.

The mode of the local oscillator for the atomic drive and the sidebands of light having interacted with the mechanics are sent through a beam-shaping lens to shape the mode profile into a square tophat beam for probing the atomic ensemble (see chapter 8 for details).

Atomic

The atomic ensemble also benefits from the scheme being pulsed since initial cooling of the oscillator can be performed before initiating the protocol, cooling the oscillator to the ground state with an effective thermal occupancy of $n_{\mathrm{S}} = 0.042$ (see chapter 5 for details), which is ideal for spin state preparation.

The atomic ensemble needs to be prepared in an initial state for us to teleport. This could be drawn from a family of coherent states, which would be achieved by a magnetic RF excitation of the spin, with the size of coherent displacement referenced to the projection noise of the ensemble. By linearity, the teleportation protocol also allows for teleporting more interesting states, for instance, a squeezed state or a Fock state.

The atomic ensemble is to perform a measurement by the light entangled with the mechanics. The fidelity of the teleportation is, in principle, independent of the sideband asymmetry for the spin ensemble, ζ_{S}, in a cascaded setting under ideal circumstances. In contrary to a parallel scheme, where it is desirable to have an interaction dominated by the beam-splitter type of interaction $\zeta_{\mathrm{S}} > 0$, where it would be advantageous to the dynamical back-action of the subsystems oppositely matched; $\zeta_{\mathrm{S}} = -\zeta_{\mathrm{M}}$ [Fedorov and Zeuthen, 2023].

Joint measurement

The final step of the teleportation protocol is to perform the Bell measurement with a homodyne detector. Appropriate filtering of the photocurrent determines the feedback to be performed by the probe laser on the mechanical membrane in order to complete the teleportation of the initial state of the atomic ensemble to the mechanical system.

Verification

Verification of the teleported state is required to ascertain and characterize the performance of the protocol, typically quantified by the mean fidelity for a certain family of input states. The Pockels cell can be switched to send all the light, having interacted with mechanics, to the verification setup for characterization of the teleported state.

An alternative, simpler experimental setup would be tuning the laser frequency away from the transitions of the atomic ensemble for the verification, removing the Pockels cell, and using the homodyne detector of the joint measurement for verification instead. This might result in higher optical losses for the verification but lowers the complexity of the experimental setup. An experimental decision is still to be made in this regard.

We are concluding the present chapter on teleportation, having outlined the rebuilt/redesigned experimental setup, including the planned sequence for state teleportation.

Part VI

Summary and outlook

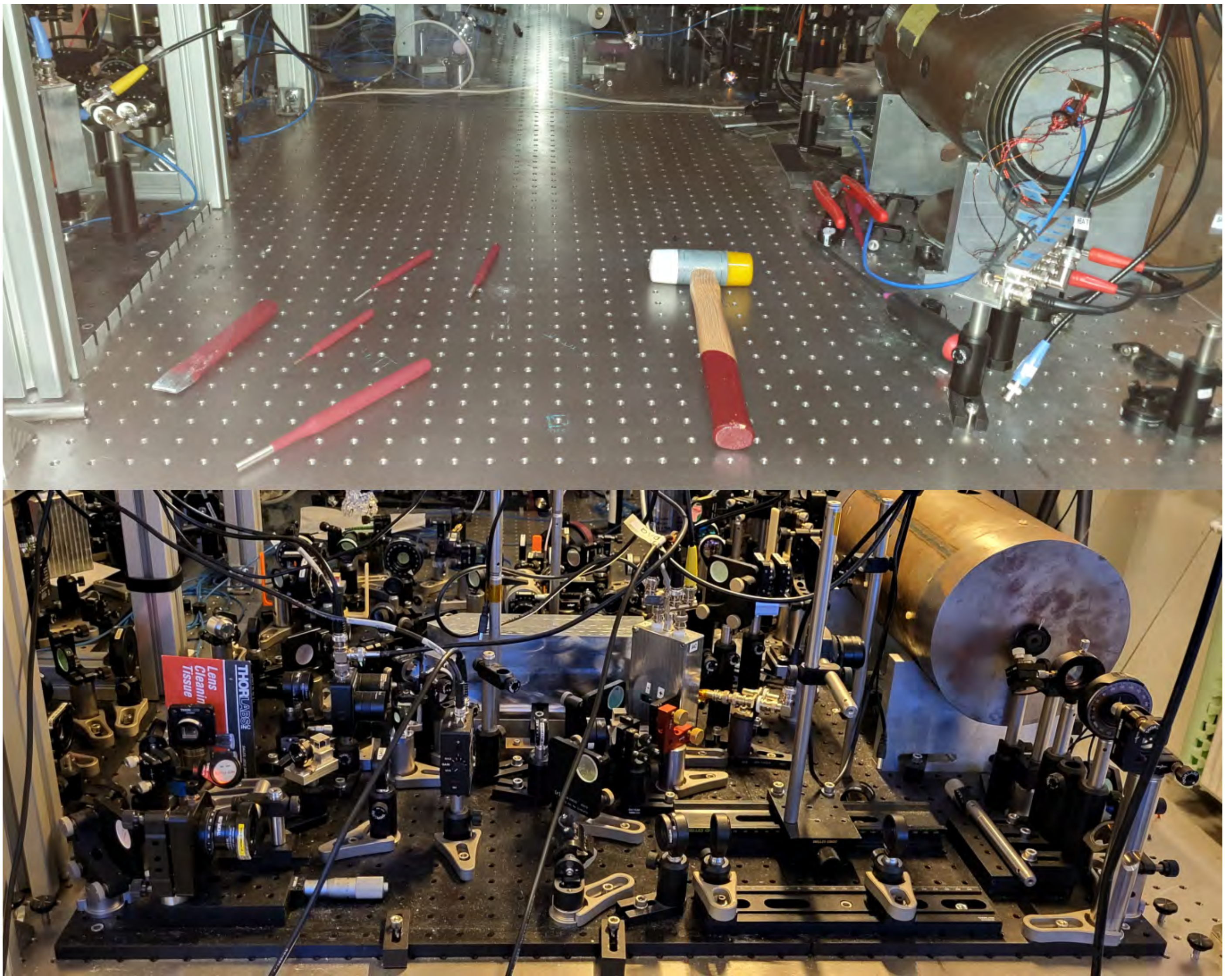

CHAPTER 13

Summary

In this thesis, we have presented the main results of this work: *Entanglement between distant macroscopic mechanical and spin systems* [Thomas et al., 2020] appended in appendix E, and *Squeezed light from an oscillator measured at the rate of oscillation* [Bærentsen et al., 2023] appended in appendix D. The presented work was initialized to bridge the gap between spin ensembles and mechanical resonators via entanglement generation. The accomplishment of spin-optomechanical entanglement and the development of a new calibration method, *Calibration of spin-light coupling by coherently induced Faraday rotation* [Thomas et al., 2021] appended in appendix F, were completed halfway into this work. The accomplishments lead us to shift our focus in a new direction towards quantum teleportation between spin ensembles and mechanical resonators. The previous work had given us much insight into the technical challenges and limitations of the experiment, therefore motivating us to restart from scratch and rethinking the entire experiment. The optical setup has been rebuilt for the presented work of this thesis. The abolition of the old setup is shown in the introductory image to this part VI. We having focused on the atomic spin ensemble in this thesis, and overcoming several technical challenges presented in part II for optical pumping and in part III for motional averaging, which has paved the way for measuring the spin ensemble in a new regime of high quantum cooperativity and of measurements faster than the oscillation frequency.

Summarizing the work of this thesis,

- Part I, we introduced the hybrid system of spin-optomechanics in chapter 1, with a detailed description of the macroscopic spin system of hot cesium atoms, presenting the framework for the dynamics of a hot spin ensemble in chapter 2. We finish the overview with an outline of the membrane in the-middle optomechanics in chapter 3.

- Part II, we presented the experimental methods for characterizing the spin ensemble, detailing the magneto-optical resonance signal, and the ground-state preparation of the spin ensemble, achieving a spin polarization of $p = 98.7\%$ and thermal occupancy of $n_{\mathrm{S}} = 0.042$ presented in chapter 5. Lastly, we introduced the coherent induced Faraday rotation (CIFAR) method in chapter 6.

- Part III, we investigated motional averaging in a hot vapor cell, introducing the effects of dephasing due to magnetic inhomogeneities in chapter 7. We detail the characterization and experimental implementation of a new coil system for the atomic ensemble, achieving a magnetic field with a standard deviation of $\sigma = 5\,\text{ppm}$ over the cell length of 40 mm, resulting in an improved spin dephasing of $\gamma_{\text{dephasing}} = 90\,\text{Hz}$. Next, in chapter 8, we introduced the broadband noise/fast decaying spin-modes from an inhomogeneous readout of the atomic ensemble arising from the loss of information in the dark. This problem was addressed by homogeneous probing of the spin ensemble using a square tophat beam, which allowed to lower the thermal contribution arising from the broadband noise by a factor of 3.4 compared to probing with a Gaussian beam. Last, concluding the topic of motional averaging by presenting the simulations of a hot spin ensemble in chapter 9, as a tool for predicting the implications of changing the cell geometry, beam shape, or other variables dependent on motional averaging, and for understand the phenomena of motional averaging.

- Part IV, we outlined the spin-induced light squeezing, which is the fruit of all the advancements realized for the spin ensemble, showcasing two measurement regimes for the atomic ensemble: measurements slower than the rate of oscillation, generating $11.5^{+2.5}_{-1.5}\,\text{dB}$ and detecting $8.5^{+0.1}_{-0.1}\,\text{dB}$ of squeezing in a tunable band, and measurements faster than the rate of oscillation, detecting a squeezing level of 6.5 dB and 4.7 dB of squeezing spanning more than one order of magnitude below the oscillation frequency with a readout rate twice the oscillation frequency, $\Gamma_{\text{S}} \approx 2\omega_{\text{S}}$, with an almost saturated imprecision product 20% above the Heisenberg uncertainty limit.

- Part V, we first, in chapter 11, outlined the entanglement in a hybrid spin-optomechanical system, estimated by an Einstein-Podolsky-Rosen (EPR) state, using Wiener filtering to condition the variance, achieving a conditional variance of EPR state: $V_c = 0.83 \pm 0.03 < 1$, below the inseparability limit of 1. Then, finally, we introduced, in chapter 12, the pinnacle of our quest; the road towards quantum teleportation between a spin ensemble and a mechanical resonator, outlining the principles of teleportation and updated experimental setup for our pursuit.

The achievements throughout this thesis have brought us closer to quantum teleportation, since many experimental parameters have been improved compared to the entanglement generation experiment. The summary of the experimental parameters is given in table 13.1.

Parameter	**Symbol**	**New value**	**Old - Ent.**
	Atomics		
Fractional coherent spin readout	Γ_S/γ_{S0}	42	12
Spin polarization	p	98.7%	82%
Spin thermal occupancy	n_S	0.042	0.8
Broadband noise	A_{BBN}/Γ_S	$BBN_{old}/2$	BBN_{old}
Intrinsic linewidth in the dark	$\gamma_{S0,dark}$	200 Hz	450 Hz
	Mechanics		
Cavity overcoupling	κ_{in}/κ	96%	93%
	Detection		
Quantum efficiency between systems	ν	66%	53%
System mode-matching (amplitude)		98%	90%
Detection efficiency	η	91%	77%
Verification detection efficiency	η_V	80%	

Table 13.1: Experimental parameters. The estimation of the new experimental parameters for the teleportation experiment compared to the entanglement experiment. The entanglement experiment was realized for a continuous measurement, and the teleportation experiment will be performed for a pulsed measurement. The thermal noise and the spin polarization should therefore not be compared as an experimental improvement. The entanglement experimental configuration has achieved a spin polarization close to $\sim 97\%$ for a pulsed measurement, therefore, the spin polarization is still improved for the new experimental realizations.

We can conclude by saying that teleportation between a spin ensemble and a mechanical resonator is attainable and within reach, in the light of the improved parameters of the rebuilt experimental setup. Setting the stage for the future realization of quantum teleportation between a spin ensemble and a mechanical resonator.

CHAPTER 14

Outlook

This outlook presents the prospects of generating non-classical states and performing quantum teleportation in a hybrid spin-optomechanical system, given the new improvements in the room-temperature atomic spin platform.

14.1 Atomic spin ensemble

The spin ensemble has been shown to achieve high quantum cooperativity, reaching $C_{\mathrm{Q}} = 15$ in the continuous measurement setting, which is a new benchmark for room-temperature spin ensembles. Furthermore, we demonstrated the fractional coherent spin readout of $\Gamma_{\mathrm{S}}/\gamma_{\mathrm{S0}} = 42$, and the ground state preparation with a thermal occupancy of $n_{\mathrm{S}} = 0.042$ for pulsed measurements. In the pulsed regime, this would correspond to the quantum cooperativity for the spin ensemble of $C_{\mathrm{Q}} = 40$. This would be a new milestone for quantum back-action dominated measurements, corresponding to only 2.5% of thermal noise compared to quantum back-action, which would put the spin ensembles on the pinnacle for quantum-limited measurements.

Low power requirements for D_2 light of $\approx 20\,\mathrm{mW}$ in combination with high levels of generated squeezing $11.5^{+2.5}_{-1.5}\,\mathrm{dB}$ in a tunable band, open the way for realizing compact squeezing-generating modules, competitive with the established nonlinear-crystal based ones.

Measurements faster than the rate of oscillation enable continuous generation of spin squeezing. This unlocks possibilities for using spin ensembles as magnetometers with quantum-enhanced sensitivity in a new, broadband, regime.

14.2 Hybrid spin-optomechanics

The verified entanglement in a spin-optomechanical system has opened the possibility for quantum-enhanced sensing, for instance, continuous force sensing in gravitational-wave detection [Zeuthen et al., 2019, Khalili and Polzik, 2018]. Moreover, the entanglement generation demonstrated the ability to access non-classical states in a spin-optomechanical system, paving the way for quantum teleportation.

Teleportation between a spin ensemble and a mechanical resonator would allow utilizing the low decoherence of a mechanical resonator for quantum memory. Alternatively, atomic ensembles can be utilized as a quantum memory for electromechanically coupled superconducting qubits [Mirhosseini et al., 2020].

Moreover, squeezed mechanical states has shown to be challenging task only showing small squeezing levels [Pirkkalainen et al., 2015, Wollman et al., 2015]. However, a squeezed state could be teleported to the mechanical resonator from the atomic ensemble, where it can be more easily prepared, e.g. by stroboscopic measurements [Vasilakis et al., 2015, Zheng et al., 2023], opening the possibility for mechanical squeezed force sensing.

Part VII

Supplementary information

APPENDIX A

Spin density operators in the x-basis

We have an atypical quantization axis along the x-direction. It is useful to write up the relevant operators as density operators to describe the spin dynamics [Julsgaard, 2003, Thomas, 2020]:

$$\begin{aligned}
\hat{F}_x &= \sum_m m\hat{\sigma}_{mm}, \\
\hat{F}_y &= \frac{1}{2}\sum_m C(F,m)\left(\hat{\sigma}_{m+1,m} + \hat{\sigma}_{m,m+1}\right), \\
\hat{F}_z &= \frac{1}{2i}\sum_m C(F,m)\left(\hat{\sigma}_{m+1,m} - \hat{\sigma}_{m,m+1}\right), \\
\hat{F}_+ &= \sum_m C(F,m)\hat{\sigma}_{m+1,m}, \\
\hat{F}_- &= \sum_m C(F,m)\hat{\sigma}_{m,m+1}.
\end{aligned} \tag{A.1}$$

The density operator $\hat{\sigma}_{a,b}$ is defined as $|a\rangle\langle b| = |F,a\rangle\langle F,b|$, $\hat{F}_\pm$ are the ladder operators for the spin and we have the following relation $C(F,m) = \sqrt{F(F+1) - m(m+1)}$. The following higher order relations are important for understanding the simplified Hamiltonian:

$$\begin{aligned}
\hat{F}_x\hat{F}_y + \hat{F}_y\hat{F}_x &= \frac{1}{2}\sum_m C(F,m)(2m+1)(\hat{\sigma}_{m+1,m} + \hat{\sigma}_{m,m+1}), \\
\hat{F}_x^2 &= \sum_m m^2\hat{\sigma}_{mm}, \\
\hat{F}_y^2 &= \frac{1}{4}(\hat{F}_+\hat{F}_+ + \hat{F}_-\hat{F}_- + \hat{F}_+\hat{F}_- + \hat{F}_-\hat{F}_+), \\
\hat{F}_z^2 &= -\frac{1}{4}(\hat{F}_+\hat{F}_+ + \hat{F}_-\hat{F}_- - \hat{F}_+\hat{F}_- - \hat{F}_-\hat{F}_+).
\end{aligned} \tag{A.2}$$

APPENDIX B

Curing of a paraffin coated vapor cells

A paraffin-coated vapor can change over time towards having high optical losses, a degrading atomic signal, or a decreasing lifetime of the transverse spin. These effects are all unwanted. However, they can all be restored in the process of curing the cell.

The entrusted method of curing atomic cells has been to create a heat gradient from the cell body decreasing towards the stem. This makes paraffin and cesium condense in the stem, leaving residue to vaporize from the cell's windows, walls, or micro-hole. This has historically been achieved by placing the body of the cell on a Peltier element to heat the cell body while placed in an oven of $60\,^{\circ}\mathrm{C}$, in the endeavor to create a $5-10\,^{\circ}\mathrm{C}$ heat gradient with a cell body temperature of $65-70\,^{\circ}\mathrm{C}$ and stem temperature of $60\,^{\circ}\mathrm{C}$. The baking time of the cell for curing has usually lasted for at least 24 hours to see a restored cell performance.

Another newly implemented method, similar to the entrusted method of curing mentioned above, is to wrap the stem in wet cotton while placed in an oven with a temperature of $70\,^{\circ}\mathrm{C}$. This should, in practice, create an even larger heat gradient, which has recently been introduced by our cell manufacturer and glass blower Mikhail V. Balabas.

A picture of an atomic cell with a degraded transmission is shown in figure B.1a, showing a cell window with paraffin spots collected on the cell window. The big circle on the window is the anti-reflection coating of the window, and the chip is the elongated shape with the atomic channel shown as the small dark square positioned in the chip. The small paraffin spots are the reason for this cell's transmission degradation. The degradation of cell transmission has empirically always been shown to come from deposits on cell windows.

We have experimented with a new method of removing residue from the cell windows by locally heating the cell without curing the entire cell. This has been desirable for cells with good characteristics such as a long lifetime of the spin and a significant optical depth. However, the curing of cells is working on the boundary of temperatures that the paraffin of the cell can handle. Therefore, we have only cured cells as a last resort to recover them. The new method can be seen in figure

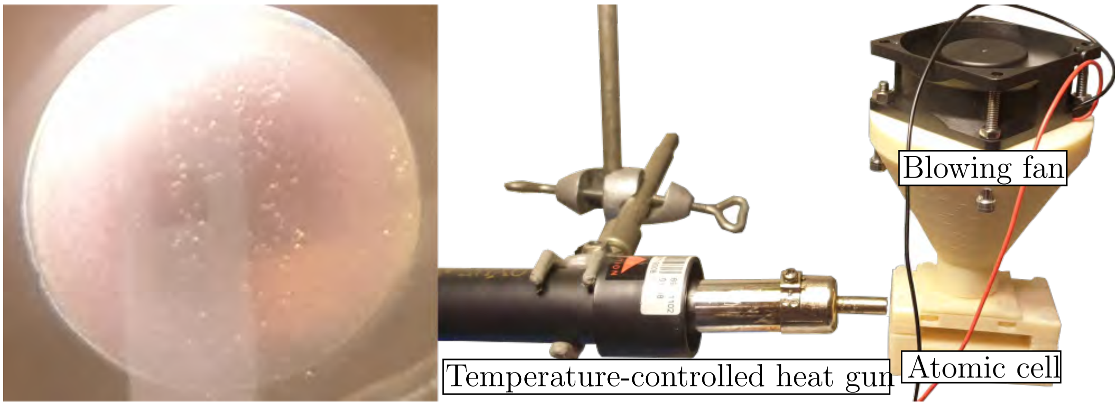

a) b)

Figure B.1: Deposits on cell window and removal. a) deposits of paraffin on a cell window; see text for details. b) setup for locally restoring the cell transmission from deposits blocking the cell window.

B.1b, using a temperature-controlled heat gun to locally heat the cell window to $90-100\,^{\circ}$C, simultaneously cooling the stem and cell body by attaching a fan blowing on the stem. This approach has shown the ability to remove deposits of the cell window, fully recovering the cell transmission without heating the cell body or the stem.

APPENDIX C

Proposal: Converting a square tophat beam into a Gaussian beam

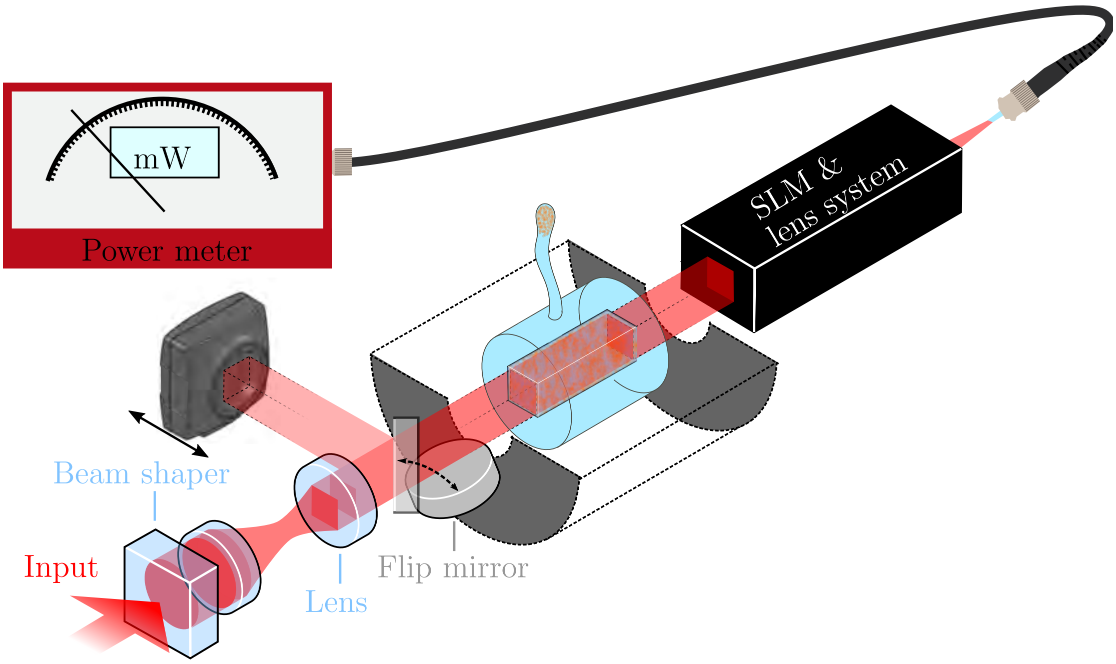

Figure C.1: The use of a spatial light modulator for Gaussian mode matching when converting from a square tophat beam. The square tophat beam is converted back into a Gaussian beam with a spatial light modulator (SLM) and lens system measured by a power meter.

This appendix proposes converting a square tophat beam into a Gaussian beam. We have investigated the use of a specially designed beam shaper for converting a square tophat beam into a Gaussian beam, having an opposite phase pattern of the beam shaper converting a Gaussian beam into a square tophat beam. Unfortunately, multiple companies refused to produce such a converter. Furthermore, an optical element with these properties would also have the disadvantage of maintaining a beam through diffraction and scattering of the cell windows changing the mode profile and using imperfect lenses, which limits transformation into a Gaussian mode.

The presented proposal uses a spatial light modulator (SLM) in combination with a spherical lens system for the generation of the square tophat beam to match the beam profile of the square tophat beam presented in chapter 8.2.2, so it can be converted into a Gaussian beam. We are going to take advantage of linear optical systems being reversible. First, performing a mode-matching optimization process, and second, inverting the beam propagation for the actual experiment.

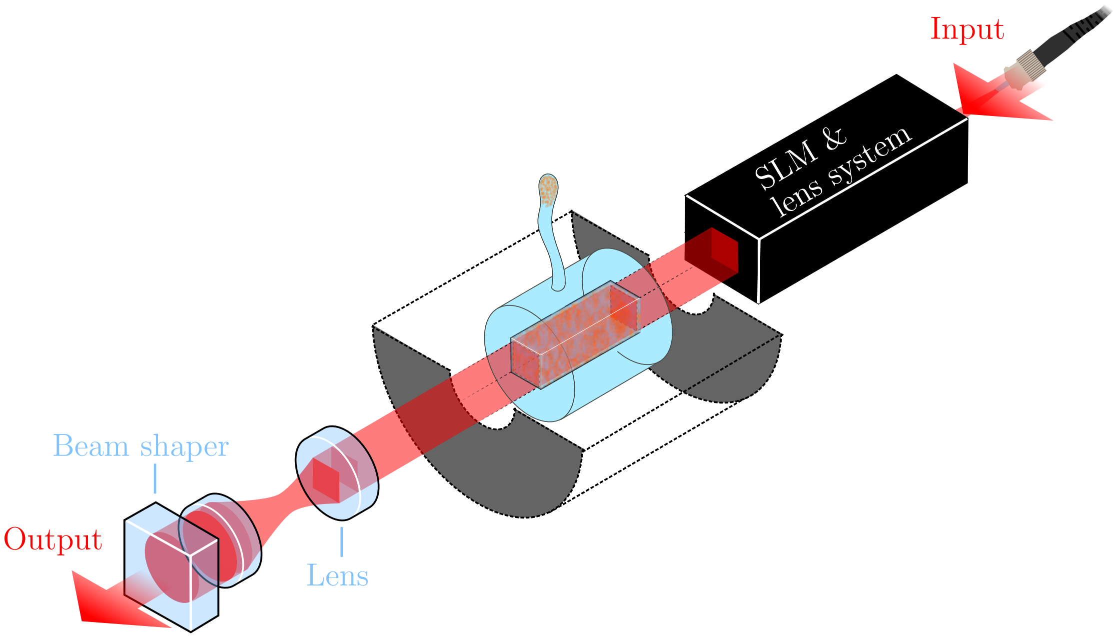

Figure C.2: Generation of square tophat beam with a spatial light modulator, and the conversion back into a Gaussian beam using a Beam shaper. The input and output are Gaussian beams. The setup uses the beam shaper to convert the square tophat beam into a Gaussian beam, reducing losses after interaction with the atomic ensemble.

The optical scheme for calibrating the system can be seen in figure C.1. The optical beam is generated using a beam shaper followed by spherical lenses, where a camera and the transmission of the atomic cell optimize the beam profile of the square tophat beam. The black box then converts the beam into a Gaussian beam, symbolizing a SLM in combination with a lens system for coupling to a fiber with a transverse electromagnetic 00 mode profile. The coupling to the fiber is optimized by measuring the injected power on a power meter to feedback on the mode profile generated by the SLM. The fiber could be supplemented by a cavity if required by the experimental settings.

The disadvantage of having the SLM system after the atomic cell is the transmission losses of the SLM system. However, the invertibility of the beam propagation allows us to exchange the power meter by a lasing source using the SLM for tophat beam generation, which can be seen in figure C.2 for the reverted beam propagation. In this experimental configuration, the input and output beam profiles are Gaussian.

This setup benefits from the low transmission losses of the beam shaper and lenses, only having low transmission losses after the atomic ensemble. The open question is the generation of a square tophat beam with a SLM system, which would have to be tested for the required resolution of the modulator.

The advantage of making the calibration setup first, before generating the tophat beam with the SLM system, is the quality of the tophat beam being determined by the lens system having the beam shaper, where the Gaussian beam transformation is determined by the SLM. A final (minor) tuning of the mode profile after the reverted beam propagation could still be performed for better Gaussian transformation since the spacial mode is already optimized for the best tophat beam performance.

APPENDIX D

Manuscript in review: Squeezed light from an oscillator measured at the rate of oscillation

Christian Bærentsen, Sergey A. Fedorov, Christoffer Østfeldt, Mikhail V. Balabas, Emil Zeuthen, and Eugene S. Polzik *Squeezed light from an oscillator measured at the rate of oscillation.* arXiv. 2302.13633 (2023).

Squeezed light from an oscillator measured at the rate of oscillation

Christian Bærentsen, Sergey A. Fedorov,* Christoffer Østfeldt,
Mikhail V. Balabas, Emil Zeuthen, and Eugene S. Polzik†
Niels Bohr Institute, University of Copenhagen, Copenhagen, Denmark
(Dated: February 28, 2023)

Continuous measurements of the position of an oscillator become projective on position eigenstates when the measurements are made faster than the coherent evolution. We evidence an effect of this transition on a spin oscillator within an ensemble of 2×10^{10} room-temperature atoms by observing correlations between the quadratures of the meter light field. These correlations squeeze the fluctuations of the light quadratures below the vacuum level. When the measurement is slower than the oscillation, we generate $11.5^{+2.5}_{-1.5}$ dB and detect $8.5^{+0.1}_{-0.1}$ dB of squeezing in a tunable band that is a fraction of the resonance frequency. When the measurement is as fast as the oscillation, we detect 4.7 dB of squeezing that spans more than one decade of frequencies below the resonance. Our results demonstrate a new regime of continuous quantum measurements on material oscillators, and set a new benchmark for the performance of a linear quantum sensor.

I. INTRODUCTION

Projective, or von Neumann, measurements collapse the observed quantum system on eigenstates of a Hermitian operator, while more general measurements, described by positive operator-valued measures, collapse the system on states from an overcomplete set [1]. A gradual transition between the two situations can be realized in continuous measurements using meter fields, a canonical example of which is an optical interferometric measurement of the position of a harmonic oscillator [2]. Position measurements are associated with mechanical resonators [3], collective atomic spins [4, 5], ferromagnetic solid-state media [6], single molecules [7], or density waves in liquids [8], that are linearly probed by traveling optical or microwave fields. The boundary between generalized and von Neumann measurements occurs at a certain value of the measurement rate [9]. When the rate is slower than the oscillation, measurements with the meter in the vacuum input state project the oscillator on coherent states. When the rate is faster than the oscillation, measurements project the oscillator on position-squeezed states.

In addition to the oscillator state, the rate of position measurement affects the output state of the meter field [9]. The quadratures of the meter are correlated, and their fluctuations can be below the vacuum level [10, 11]. In the slow measurement regime, the correlations and the associated squeezing exist in a narrow frequency band near the resonance, and have a strong frequency dependence due to the time-averaged response of the oscillator to the measurement backaction. When the measurement is faster than the oscillation, the correlations and squeezing are broadband and frequency-independent at low frequencies, where the oscillator responds to the backaction instantaneously. The detection of squeezing means observing the backaction-driven motion of the oscillator at frequencies much lower than the resonance, which is a necessary condition for position squeezing [9].

The squeezing of the meter light is both a valuable quantum resource and a figure of merit for the purity of the light-oscillator interaction. In the slow regime, we realize a measurement of a collective spin of a room-temperature atomic ensemble at a rate fifteen times higher than the rate of thermal decoherence. The generated squeezing of the meter light reaches $11.5^{+2.5}_{-1.5}$ dB at the output of the cell, exceeding the squeezing demonstrated previously using collective atomic spins [12–14], optomechanical cavities [15–17], levitated nanoparticles [18, 19], and compact on-chip sources utilizing material nonlinearity [20], while approaching the results achievable using bulk nonlinear crystals [21]. In the fast-measurement regime, we detect broadband squeezing in a bandwidth of several MHz while keeping the backaction-imprecision product [22] within 20 % from the value saturating the Heisenberg uncertainty relation. These results enable new regimes for sensing surpassing the standard quantum limit [23, 24], tests of uncertainty relations for past quantum states [25, 26], quantum control of material oscillators [27–30], and links between collective spins and other material systems [14, 31–33].

II. MEASUREMENTS OF SPIN OSCILLATORS

Linearly polarized light traveling through an oriented atomic medium (as illustrated in Fig. 1a-b) continuously measures the projection of the total spin on the propagation direction, $\hat{J}_z$, via polarization rotation. This measurement acts back on the spin via quantum fluctuations of ponderomotive torque. When the input light is in a strong coherent state, and the spin satisfies the Holstein-Primakoff approximation [34], the process can be described in terms of linearly coupled pairs of canonically conjugate position and momentum variables. The canonical variables of the spin, $\hat{X}_S$ and $\hat{P}_S$, are the normalized projections defined as $\hat{X}_S = \hat{J}_z/\sqrt{\hbar\langle J_x\rangle}$ and

* sergey.fedorov@nbi.ku.dk
† polzik@nbi.ku.dk

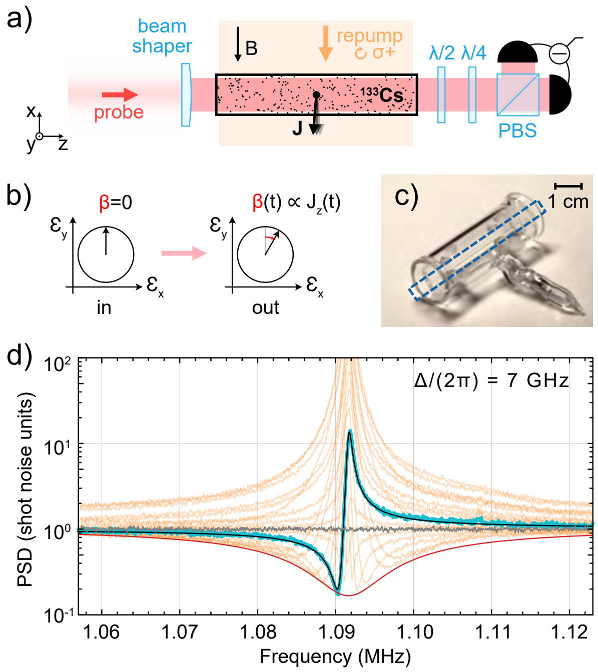

FIG. 1. a) An optical probe spatially shaped in a square tophat beam travels through an atomic ensemble with the total spin $\boldsymbol{J}$ in a magnetic field B, and is detected using balanced polarization homodyning. The detected quadrature is selected using the $\lambda/2$ and $\lambda/4$ waveplates. The total spin is oriented by the repump beam traveling along x. PBS: polarization beam splitter. b) The polarization angle β of the probe as a meter for the spin projection $\hat{J}_z$. c) A photograph of an anti-spin-relaxation coated cell. The channel with probed atoms is indicated by the blue rectangle. d) The orange curves show power spectral densities (PSD) of homodyne signals recorded at $\Delta/(2\pi) = 7\,\text{GHz}$ at different quadratures. The trace showing the largest squeezing is highlighted by the blue curve. The black curve is the theoretical prediction based on the global fit including all quadratures (see the SI). The gray curve is the shot-noise level. The red curve is the theoretical optimum-quadrature squeezing spectrum.

$\hat{P}_\text{S} = -\hat{J}_y/\sqrt{\hbar\langle J_x\rangle}$, which satisfy the commutation relation $[\hat{X}_\text{S}, \hat{P}_\text{S}] = i$. The variables of the light, $\hat{X}_\text{L}$ and $\hat{P}_\text{L}$, are the quadratures proportional to the amplitude and phase differences between the circularly polarized components, respectively. Their commutator is $[\hat{X}_\text{L}(t), \hat{P}_\text{L}(t')] = (i/2)\delta(t-t')$. The Heisenberg uncertainty principle constrains the two-sided spectral densities of the imprecision in the $\hat{P}_\text{L}$-quadrature measurements, S_imp, and the measurement backaction, S_BA, as $\sqrt{S_\text{imp}\, S_\text{BA}} \geq \hbar/2$ (see Ref. [22] and the SI). This uncertainty relation is saturated if the detection efficiency is perfect and there is no excess measurement noise.

When the ensemble is probed far-detuned from optical transitions, the total spin couples to the probe via the position-measurement Hamiltonian $\hat{H}_\text{int} = -2\hbar\sqrt{\Gamma}\,\hat{X}_\text{L}\hat{X}_\text{S}$, and modifies the probe variables according to the input-output relations [14, 35]

$$\hat{P}_\text{L}^\text{out}(t) = \hat{P}_\text{L}^\text{in}(t) + \sqrt{\Gamma}\,\hat{X}_\text{S}(t), \quad \hat{X}_\text{L}^\text{out}(t) = \hat{X}_\text{L}^\text{in}(t), \quad (1)$$

where Γ is the measurement rate proportional to the optical power. The measurement backaction force is $\hat{F}_\text{QBA} = 2\sqrt{\Gamma}\hat{X}_\text{L}^\text{in}$. The response of the spin to the measurement backaction in this situation is described by the Fourier-domain susceptibility $\chi[\Omega] = \Omega_\text{S}/(\Omega_\text{S}^2 - \Omega^2 - i\Omega\gamma_0)$, where Ω_S is the resonance Larmor frequency and γ_0 is the intrinsic decay rate. The response induces correlations between $\hat{X}_\text{L}^\text{out}$ and $\hat{P}_\text{L}^\text{out}$ that can be observed by detecting intermediate quadratures of light, $\hat{Q}_\text{L}^\phi = \sin(\phi)\hat{X}_\text{L}^\text{out} + \cos(\phi)\hat{P}_\text{L}^\text{out}$. The two-sided spectra of those quadratures, detected by a homodyne with efficiency η, are given by

$$S_\phi[\Omega] = 1/4 + (\eta\Gamma/2)\,\text{Re}\,(\chi[\Omega])\sin(2\phi) + \eta\Gamma(\Gamma + \gamma_\text{th})|\chi[\Omega]|^2\cos(\phi)^2, \quad (2)$$

where $\gamma_\text{th} = (2\,n_\text{th}+1)\gamma_0$ is the thermal decoherence rate. The term $\propto \cos(\phi)^2$ is due to the spin oscillator motion, and the term $\propto \sin(2\theta)$ is due to the cross-correlation between $\hat{X}_\text{S}$ and $\hat{X}_\text{L}^\text{out}$. Negative cross-correlation can squeeze $S_\phi[\Omega]$ below the vacuum level of 1/4.

In a more general situation, the internal dynamics of the collective spin are those of $2F$ harmonic oscillators, where F is the ground-state angular momentum number of the atomic species. Their annihilation operators,

$$\hat{b}_m = \frac{1}{\sqrt{\Delta N_m}}\sum_{j=1}^{N} |m+1\rangle_j\langle m|_j, \quad (3)$$

are introduced using the multilevel Holstein-Primakoff approximation [36]. In Eq. (3), m is the projection quantum number of the single-atom angular momentum on the x axis, $|m+1\rangle_j\langle m|_j$ are the jump operators between the states $|m\rangle_j$ and $|m+1\rangle_j$ of the individual atoms, and $\Delta N_m = N_{m+1} - N_m$ are the differences in the mean numbers of atoms in the corresponding states. The frequencies of the oscillators are the energy differences between $|m\rangle_j$ and $|m+1\rangle_j$, controlled by an external static magnetic field. The oscillator-light interaction is described by the Hamiltonian

$$\hat{H}_\text{int} = -2\hbar\sum_{m=-F}^{F-1}\sqrt{\Gamma_m}\left(\hat{X}_m\hat{X}_\text{L} + \zeta_m\hat{P}_m\hat{P}_\text{L}\right), \quad (4)$$

where the quadratures of the modes satisfy $[\hat{X}_m, \hat{P}_m] = i$, Γ_m are the measurement rates, and $\zeta_m = \zeta(2m+1)/7$ determine the strengths of dynamical backaction. The common factor ζ is a function of the optical detuning Δ and the level structure. The deviation of the interaction Hamiltonian (4) from that of pure position measurement, $\zeta = 0$, results in dynamical-backaction damping with rates $\gamma_{\text{DBA},m} = 2\zeta_m\Gamma_m$, and increases the quantum backaction-imprecision product by an amount proportional to ζ^2 (see the SI), which is small in all our

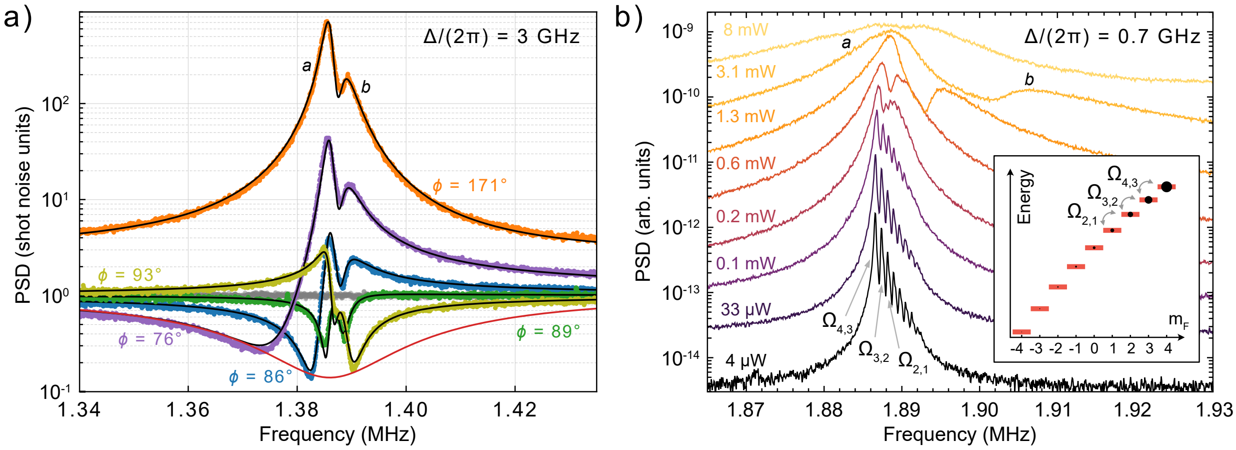

FIG. 2. a) Homodyne signal PSDs at $\Delta/(2\pi) = 3\,\mathrm{GHz}$ and different detection angles ϕ indicated in the figure. The points are experimental data. The green and orange traces are obtained close to $\hat{P}_{\mathrm{L}}$ and $\hat{X}_{\mathrm{L}}$, respectively, and the olive, blue and purple—at intermediate quadratures. The gray points show the shot-noise level. The black curves are theoretical predictions based on the global fit including the spectra at 15 quadratures (see the SI). The red curve is the optimum-quadrature squeezing spectrum predicted by the single-oscillator model. b) The spectra of classically driven motion of the collective spin. The eight peaks visible at low probe powers correspond to bare oscillator modes due to the transitions between adjacent m_F levels. Their frequencies are determined by the linear and quadratic Zeeman energies, and magnitudes are determined by the macroscopic populations of the m_F levels as shown in the inset. The spectra at high powers expose the hybridized oscillator modes.

experiments. The oscillators experience thermal decoherence due to the spontaneous scattering and the collisions of atoms. The thermal occupancy of the intrinsic damping bath is $n_{\mathrm{th}} = N_m/\Delta N_m$, experimentally found to be independent of m.

The multimode structure can affect the response of the spin to the measurement backaction at frequencies close to Ω_{S}, while far away from Ω_{S} the spin acts as a single oscillator with $\hat{X}_{\mathrm{S}} = \sum_m \sqrt{\Gamma_m/\Gamma}\hat{X}_m$ that is measured at the total rate $\Gamma = \sum_m \Gamma_m$ and experiences decoherence at the rate $\gamma_{\mathrm{th}} = \sum_m \gamma_{\mathrm{th},m}\Gamma_m/\Gamma$, where $\gamma_{\mathrm{th},m}$ are the individual decoherence rates of the modes. The quantum cooperativities for the individual modes are defined as the ratios of the measurement and decoherence rates. For the total spin, the cooperativity is $C_{\mathrm{q}} = \Gamma/\gamma_{\mathrm{th}}$.

III. EXPERIMENT

An ensemble of $N \approx 2\times 10^{10}$ cesium-133 atoms at $52\,^{\circ}\mathrm{C}$ is contained in the $1\,\mathrm{mm}\times 1\,\mathrm{mm}\times 4\,\mathrm{cm}$ channel of a glass chip, shown in Fig. 1c. The channel is coated with paraffin to reduce the spin decoherence from wall collisions [37], and is positioned in a homogeneous magnetic field directed along the x axis (Fig. 1a). The ensemble is continuously probed by a $y-$polarized laser beam propagating in the z direction that has the wavelength 852.3 nm, blue-detuned from the $F = 4 \to F' = 5$ transition of the D2 line by $\Delta/(2\pi) = 0.7 - 7\,\mathrm{GHz}$. The ensemble is also continuously repumped using circularly polarized light resonant with the $F = 3 \to F' = 2$ transition of the D2 line. The combination of spontaneous scattering of probe photons and repumping maintains a steady-state distribution of atoms over the magnetic sublevels of the $F = 4$ ground state, which has the macroscopic spin orientation along the magnetic field with polarization $\langle \hat{J}_x\rangle/(NF) \approx 0.78$. The steady-state populations are independent of the probe power in our regime, and correspond to the occupancy of the thermal bath $n_{\mathrm{th}} = 0.9 \pm 0.1$. The resonance frequencies of the oscillators are set by the Larmor frequency and split by $0 - 40\,\mathrm{kHz}$ in different regimes by the quadratic Zeeman and tensor Stark effects. The Larmor frequency can be positive or negative depending on the orientation of the magnetic field, setting the signs of the effective oscillator masses. We work in the negative-mass configuration [31], but the effects that we observe, in particular the squeezing levels, do not change upon the reversal of the sign of mass (see the SI). The output light is detected using balanced polarization homodyning, which enables shot-noise-limited detection at frequencies down to 10 kHz.

IV. RESULTS

In Fig. 1d, we present homodyne spectra recorded at the optical detuning $\Delta/(2\pi) = 7\,\mathrm{GHz}$ over a range of detection quadratures ϕ. In this measurement, dynamical backaction effects are small ($\zeta \approx 0.01$), and the probed spin behaves as a single oscillator subjected to position measurements. The data in Fig. 1d shows squeezing down to 7.5 dB, attained by the highlighted blue trace. From a global fit of the spectra at all quadratures, we infer the measurement rate $\Gamma/(2\pi) = 13\,\mathrm{kHz}$ and the

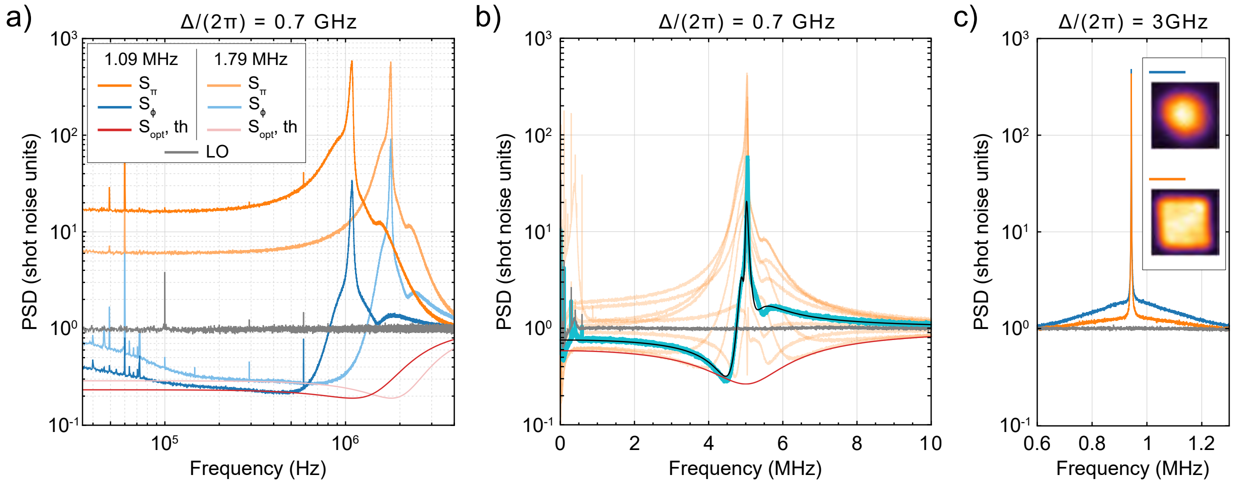

FIG. 3. a-b) Homodyne signal PSDs at $\Delta/(2\pi) = 0.7\,\mathrm{GHz}$. The gray curves show the experimental shot-noise levels, and the red curves are the theoretical optimum-quadrature squeezing spectra derived from Eq. (2). a) Spectra for $|\Omega_\mathrm{S}|/(2\pi) = 1.09\,\mathrm{MHz}$ and $1.79\,\mathrm{MHz}$. The orange and blue curves are measurements with the quadrature angle set to detect $\hat{P}_\mathrm{L}$ and a quadrature ϕ close to $\hat{X}_\mathrm{L}$, respectively. LO: local oscillator, th: theoretical. b) Orange curves show homodyne spectra recorded at $|\Omega_\mathrm{S}|/(2\pi) = 5\,\mathrm{MHz}$ and at different quadratures ϕ. The trace with the largest squeezing is highlighted by the blue curve. The black curve is the theoretical prediction based on the global fit including all quadratures (see the SI). c) The spectra taken at the $\hat{P}_\mathrm{L}$ quadrature when the probe beam is Gaussian (blue curve) and tophat (orange curve). The gray curve is the shot noise. The inset shows the beam intensity distributions over the $1\,\mathrm{mm}\times1\,\mathrm{mm}$ channel cross section recorded without the cell.

quantum cooperativity $C_\mathrm{q} = 11$. The measurement rate can be verified directly from Fig. 1d via the width $\Delta\Omega$ of the frequency band over which squeezing is present in any of the traces, which in the backaction-dominated regime is $\Delta\Omega \sim \Gamma$. The envelope of the traces in Fig. 1d is described by the spectrum given by Eq. (2) minimized over the detection quadrature at each frequency. Neglecting the imaginary part of the response, the optimum-quadrature spectrum is given by

$$S_\mathrm{min}[\Omega] = \frac{1}{4} - \frac{\eta}{2}\frac{\Gamma}{\Gamma+\gamma_\mathrm{th}}\, D\left(\frac{\Omega-\Omega_\mathrm{S}}{\Gamma+\gamma_\mathrm{th}}\right), \qquad (5)$$

where $D(x) = 1/\left(1+\sqrt{1+4x^2}\right)$. The red curve plotted in Fig. 1d additionally accounts for 0.7 shot noise units of excess $\hat{P}_\mathrm{L}$-quadrature noise from the thermal motion of fast-decaying spin modes (see Sec. V). This noise is the main limitation for the backaction-imprecision product in this measurement, which equals $1.5 \times (\hbar/2)$.

Due to the scaling $\Gamma \propto 1/\Delta^2$, higher measurement rates are achievable with the probe laser tuned closer to the atomic transition. In Fig. 2a we present data obtained at the optical detuning of $3\,\mathrm{GHz}$ using $8.4\,\mathrm{mW}$ of probe power. In this measurement $\zeta = 0.054$, in which case the dynamical backaction results in optical damping and hybridization of the oscillator modes, as well as optical squeezing in the $\hat{X}_\mathrm{L}$-quadrature (see the green trace in Fig. 2a). Since the thermal decoherence of the oscillators is due to baths at a temperature close to zero, the optical damping improves the maximum magnitude of squeezing by about $0.5\,\mathrm{dB}$. The minimum noise shown by the blue trace in Fig. 2a is $8.5^{+0.1}_{-0.1}\,\mathrm{dB}$ below the shot noise level. The overall detection efficiency of our setup is $\eta = (91 \pm 3)\,\%$, and the transmission loss at the exit window of the cell is $1.6\,\%$, which means that the magnitude of the squeezing at the exit of the cell is $11.5^{+2.5}_{-1.5}\,\mathrm{dB}$. The backaction-imprecision product in this measurement is $1.9 \times (\hbar/2)$, which is higher than in the measurement at $7\,\mathrm{GHz}$ detuning due to the higher excess $\hat{P}_\mathrm{L}$-quadrature noise (two shot noise units).

The experimental spectra in Fig. 2a can be understood as arising from the coupled dynamics of two nearly-degenerate bright modes of the spin, which we refer to as modes a and b. To extract their effective parameters, we globally fit the set of spectra recorded over an extended range of quadrature angles (see the SI). We find the total measurement rate to be $\Gamma/(2\pi) = 52\,\mathrm{kHz}$, the individual quantum cooperativities to be $C_\mathrm{q}^a = 12$ and $C_\mathrm{q}^b = 4$, and the total cooperativity to be $C_\mathrm{q} = 15$. The lower envelope of the experimental traces is in agreement with the optimum-quadrature spectrum predicted by the single-oscillator model using the same Γ and C_q.

The bright modes a and b emerge due to the coupling of the individual spin oscillators via the common reservoir of the probe optical modes with coupling rates proportional to ζ_m and Γ_m. To illustrate this effect, we set the laser detuning to $0.7\,\mathrm{GHz}$, where the dynamical backaction coefficient is larger, $\zeta = 0.18$, and excite the oscillators with classical white noise applied via a magnetic field. The spectra of the P quadrature of the output light at different probe powers are shown in Fig. 2b. At the lowest power, the eight bare spin oscillators due to the transitions between adjacent m_F levels are individually resolved. As the probe power is increased, the resonances first merge in two (the a and b modes) and then three. The macroscopic occupancies of different m_F levels in the atomic ensemble remain the same at all powers, as we separately check, which means that the change in the output spectrum is only due to the coupled dynamics of the collective oscillators.

At the detuning of 0.7 GHz from the optical transition, the measurement rate of the spin motion can be as high as the oscillation frequency. While around the Larmor resonance, in a frequency band of approximately one hundred kHz, the coupling between individual spin oscillators is pronounced, at frequencies much lower than the resonance the spin behaves as a single oscillator, and the quantum measurement backaction manifests via broadband squeezing of light. In Fig. 3a, we present spectra recorded using 12.8 mW of optical probe power at two resonance frequencies, 1.09 MHz and 1.79 MHz, in which the bandwidth of low-frequency squeezing extends down to 30 kHz. The minimum noise levels of the homodyne signals (6.5 dB below the shot noise for the 1.09 MHz data) are consistent with the quantum cooperativity $C_\mathrm{q} = 8$. The measurement rate can be estimated from the signal-to-shot-noise ratio on the P quadrature in Fig. 3a using the formula

$$S_{\phi=0}[0] = 1/4 + \eta\,(\Gamma/\Omega_\mathrm{S})^2\,, \tag{6}$$

which yields $\Gamma/(2\pi) \approx 2$ MHz, a value higher than the resonance frequencies. To further corroborate the measurement rate, we perform a quadrature sweep with the resonance frequency set to 5 MHz and using 10.2 mW of probe power (Fig. 3b). From fitting this data, we find $\Gamma/(2\pi) = 1.77$ MHz, which is consistent within ten percent with the previous estimate corrected for the difference in the probe powers. Theoretically, the optimum-quadrature noise levels should saturate as the Fourier frequency approaches zero, to a value around 0.22 shot-noise units for the 1.09 MHz data in Fig. 3a, while experimental noise levels increase at low frequencies due to excess noise from the atomic ensemble.

The backaction-imprecision product for the measurements in Fig. 3a is below $1.2 \times (\hbar/2)$ at frequencies higher than 100 kHz. This value is closer to saturating the Heisenberg uncertainty relation than the values in the slow-measurement experiments, because the fast-decaying modes are in the backaction-dominated regime, and do not contribute excess thermal noise. The limiting factors for the product in this case are the dynamical backaction and detection inefficiency.

V. FAST-DECAYING MODES

In addition to the collective oscillators described by the annihilation operators from Eq. (3), in which all atoms contribute equally, there are other modes of the spin in our system [38, 39]. The resonance frequencies of these modes coincide with Ω_S, but their decay rates are limited by the rate of atoms flying through the probe field ($\gamma_{0,\mathrm{flight}}/(2\pi) \approx 300$ kHz) rather than collisions with the walls and other atoms ($\gamma_{0,\mathrm{coll}}/(2\pi) \approx 200$ Hz). The annihilation operators of these modes are

$$\hat{b}'_m = \frac{1}{\sqrt{\Delta N_m\,\langle \Delta g(t)^2\rangle_c}} \sum_{j=1}^{N} \Delta g_j(t)\,|m\rangle_j\langle m+1|_j, \tag{7}$$

where $g_j(t)$ are the coupling rates between the optical probe and the individual atoms (see the SI) and $\langle \Delta g^2\rangle_c$ is the squared deviation of the coupling from the mean averaged over classical trajectories, assumed to be the same for all atoms. The measurement rate of the fast-decaying modes is $\propto \langle \Delta g^2\rangle_c$, while the measurement rate of the slow-decaying modes is $\propto \langle g\rangle_c^2$.

An enabling feature of our experiment is the high 3D uniformity of the optical probe field, achieved using a tophat beam configuration, which reduces $\langle \Delta g^2\rangle_c$ and thus the readout of the fast-decaying modes. In Fig. 3c, we compare the spectra recorded at the $\hat{P}_\mathrm{L}$-quadrature using a tophat and a wide Gaussian probe beam with equal optical powers in the slow-measurement regime. The thermal noise contributed by the fast-decaying modes is reduced from 1 to 0.3 shot-noise units on resonance upon switching from the Gaussian to the tophat probe. The absolute non-uniformity of the coupling [40, 41] for the tophat beam is estimated to be $\langle \Delta g^2\rangle_c/\langle g\rangle_c^2 = 0.6$ based on the camera imaging.

VI. OUTLOOK

Continuous measurements that combine high measurement rate, quantum cooperativity, and detection efficiency can be used for single-shot generation of spin-squeezed states and quantum state tomography [42]. The entanglement link between the material spin and traveling light entailed by the squeezing enables quantum-coherent coupling of spins with other material systems [14, 32]. While the backaction-imprecision product in all our measurements is already within a factor of two from the Heisenberg bound, it can be further improved by optimizing the probe power for measurements of the $\hat{P}_\mathrm{L}$-quadrature. Our measurements were optimized for quadratures intermediate between $\hat{X}_\mathrm{L}$ and $\hat{P}_\mathrm{L}$ (i.e. for "variational" readout [23]) which can yield superior results [43] in quantum sensing and control.

This work also establishes room-temperature atomic spin oscillators as a practical platform for engineering quantum light with high levels of squeezing, which is a basic resource for interferometric sensing and optical quantum information processing [20]. The highest demonstrated squeezing, reaching 8.5 dB at the detection, is narrowband, but its frequency can be tuned by the magnetic field without degrading the level within the range of approximately $0.8 - 5$ MHz in our experiments.

VII. ACKNOWLEDGEMENTS

The authors thank Michał Parniak, Jörg Müller, Rebecca Schmieg, and Ivan Galinskiy for general help and useful discussions. This work was supported by the European Research Council (ERC) under the Horizon 2020 (grant agreement No 787520) and by VILLUM FONDEN under a Villum Investigator Grant no. 25880. SF acknowledges funding from the European Union's Horizon 2020 research program under the Marie Sklodowska-Curie grant agreement No. 847523 "INTERACTIONS".

[1] H. M. Wiseman and G. J. Milburn, *Quantum Measurement and Control* (Cambridge University Press, Cambridge, 2009).
[2] V. B. Braginsky, F. Y. Khalili, and K. S. Thorne, *Quantum Measurement*, 1st ed. (Cambridge University Press, Cambridge England ; New York, NY, USA, 1992).
[3] T. P. Purdy, R. W. Peterson, and C. A. Regal, Observation of radiation pressure shot noise on a macroscopic object, Science **339**, 801 (2013).
[4] K. Hammerer, A. S. Sørensen, and E. S. Polzik, Quantum interface between light and atomic ensembles, Reviews of Modern Physics **82**, 1041 (2010).
[5] P. Grangier, J.-P. Poizat, P. Grelu, F. Castelli, L. Lugiato, and A. Sinatra, Back-action-induced Squeezed Light in a Detuned Quantum Non-demolition Scheme, Journal of Modern Optics **41**, 2241 (1994).
[6] J. Graf, H. Pfeifer, F. Marquardt, and S. Viola Kusminskiy, Cavity optomagnonics with magnetic textures: Coupling a magnetic vortex to light, Physical Review B **98**, 241406 (2018).
[7] P. Roelli, C. Galland, N. Piro, and T. J. Kippenberg, Molecular cavity optomechanics as a theory of plasmon-enhanced Raman scattering, Nature Nanotechnology **11**, 164 (2016).
[8] A. Shkarin, A. Kashkanova, C. Brown, S. Garcia, K. Ott, J. Reichel, and J. Harris, Quantum Optomechanics in a Liquid, Physical Review Letters **122**, 153601 (2019).
[9] C. Meng, G. A. Brawley, J. S. Bennett, M. R. Vanner, and W. P. Bowen, Mechanical Squeezing via Fast Continuous Measurement, Physical Review Letters **125**, 043604 (2020).
[10] C. Fabre, M. Pinard, S. Bourzeix, A. Heidmann, E. Giacobino, and S. Reynaud, Quantum-noise reduction using a cavity with a movable mirror, Physical Review A **49**, 1337 (1994).
[11] S. Mancini and P. Tombesi, Quantum noise reduction by radiation pressure, Physical Review A **49**, 4055 (1994).
[12] C. F. McCormick, V. Boyer, E. Arimondo, and P. D. Lett, Strong relative intensity squeezing by four-wave mixing in rubidium vapor, Optics Letters **32**, 178 (2007).
[13] V. Boyer, A. M. Marino, R. C. Pooser, and P. D. Lett, Entangled Images from Four-Wave Mixing, Science **321**, 544 (2008).
[14] R. A. Thomas, M. Parniak, C. Østfeldt, C. B. Møller, C. Bærentsen, Y. Tsaturyan, A. Schliesser, J. Appel, E. Zeuthen, and E. S. Polzik, Entanglement between distant macroscopic mechanical and spin systems, Nature Physics , 1 (2020).
[15] D. W. C. Brooks, T. Botter, S. Schreppler, T. P. Purdy, N. Brahms, and D. M. Stamper-Kurn, Non-classical light generated by quantum-noise-driven cavity optomechanics, Nature **488**, 476 (2012).
[16] A. H. Safavi-Naeini, S. Gröblacher, J. T. Hill, J. Chan, M. Aspelmeyer, and O. Painter, Squeezed light from a silicon micromechanical resonator, Nature **500**, 185 (2013).
[17] T. P. Purdy, P.-L. Yu, R. W. Peterson, N. S. Kampel, and C. A. Regal, Strong Optomechanical Squeezing of Light, Physical Review X **3**, 031012 (2013).
[18] L. Magrini, V. A. Camarena-Chávez, C. Bach, A. Johnson, and M. Aspelmeyer, Squeezed Light from a Levitated Nanoparticle at Room Temperature, Physical Review Letters **129**, 053601 (2022).
[19] A. Militaru, M. Rossi, F. Tebbenjohanns, O. Romero-Isart, M. Frimmer, and L. Novotny, Ponderomotive Squeezing of Light by a Levitated Nanoparticle in Free Space, Physical Review Letters **129**, 053602 (2022).
[20] Y. Zhang, M. Menotti, K. Tan, V. D. Vaidya, D. H. Mahler, L. G. Helt, L. Zatti, M. Liscidini, B. Morrison, and Z. Vernon, Squeezed light from a nanophotonic molecule, Nature Communications **12**, 2233 (2021).
[21] H. Vahlbruch, M. Mehmet, K. Danzmann, and R. Schnabel, Detection of 15 dB Squeezed States of Light and their Application for the Absolute Calibration of Photoelectric Quantum Efficiency, Physical Review Letters **117**, 110801 (2016).
[22] A. A. Clerk, M. H. Devoret, S. M. Girvin, F. Marquardt, and R. J. Schoelkopf, Introduction to quantum noise, measurement, and amplification, Reviews of Modern Physics **82**, 1155 (2010).
[23] S. P. Vyatchanin and A. B. Matsko, Quantum limit on force measurements, JETP **77**, 218 (1993).
[24] D. Mason, J. Chen, M. Rossi, Y. Tsaturyan, and A. Schliesser, Continuous force and displacement measurement below the standard quantum limit, Nature Physics **15**, 745 (2019).
[25] M. Tsang, Optimal waveform estimation for classical and quantum systems via time-symmetric smoothing, Physical Review A **80**, 033840 (2009).
[26] H. Bao, S. Jin, J. Duan, S. Jia, K. Mølmer, H. Shen, and Y. Xiao, Retrodiction beyond the Heisenberg uncertainty relation, Nature Communications **11**, 5658 (2020).
[27] D. J. Wilson, V. Sudhir, N. Piro, R. Schilling, A. Ghadimi, and T. J. Kippenberg, Measurement-based control of a mechanical oscillator at its thermal decoherence rate, Nature **524**, 325 (2015).
[28] M. Rossi, D. Mason, J. Chen, Y. Tsaturyan, and A. Schliesser, Measurement-based quantum control of mechanical motion, Nature **563**, 53 (2018).
[29] F. Tebbenjohanns, M. L. Mattana, M. Rossi, M. Frimmer, and L. Novotny, Quantum control of a nanoparticle optically levitated in cryogenic free space, Nature **595**, 10.1038/s41586-021-03617-w (2021).
[30] L. Magrini, P. Rosenzweig, C. Bach, A. Deutschmann-Olek, S. G. Hofer, S. Hong, N. Kiesel, A. Kugi, and M. Aspelmeyer, Real-time optimal quantum control of

mechanical motion at room temperature, Nature **595**, 373 (2021).

[31] C. B. Møller, R. A. Thomas, G. Vasilakis, E. Zeuthen, Y. Tsaturyan, M. Balabas, K. Jensen, A. Schliesser, K. Hammerer, and E. S. Polzik, Quantum back-action-evading measurement of motion in a negative mass reference frame, Nature **547**, 191 (2017).

[32] T. M. Karg, B. Gouraud, C. T. Ngai, G.-L. Schmid, K. Hammerer, and P. Treutlein, Light-mediated strong coupling between a mechanical oscillator and atomic spins 1 meter apart, Science **369**, 174 (2020).

[33] G.-L. Schmid, C. T. Ngai, M. Ernzer, M. B. Aguilera, T. M. Karg, and P. Treutlein, Coherent Feedback Cooling of a Nanomechanical Membrane with Atomic Spins, Physical Review X **12**, 011020 (2022).

[34] F. T. Arecchi, E. Courtens, R. Gilmore, and H. Thomas, Atomic Coherent States in Quantum Optics, Physical Review A **6**, 2211 (1972).

[35] K. Hammerer, E. S. Polzik, and J. I. Cirac, Teleportation and spin squeezing utilizing multimode entanglement of light with atoms, Physical Review A **72**, 052313 (2005).

[36] Z. Kurucz and K. Mølmer, Multilevel Holstein-Primakoff approximation and its application to atomic spin squeezing and ensemble quantum memories, Physical Review A **81**, 032314 (2010).

[37] M. V. Balabas, T. Karaulanov, M. P. Ledbetter, and D. Budker, Polarized Alkali-Metal Vapor with Minute-Long Transverse Spin-Relaxation Time, Physical Review Letters **105**, 070801 (2010).

[38] R. Shaham, O. Katz, and O. Firstenberg, Quantum dynamics of collective spin states in a thermal gas, Physical Review A **102**, 012822 (2020).

[39] Y. Tang, Y. Wen, L. Cai, and K. Zhao, Spin-noise spectrum of hot vapor atoms in an anti-relaxation-coated cell, Physical Review A **101**, 013821 (2020).

[40] J. Borregaard, M. Zugenmaier, J. M. Petersen, H. Shen, G. Vasilakis, K. Jensen, E. S. Polzik, and A. S. Sørensen, Scalable photonic network architecture based on motional averaging in room temperature gas, Nature Communications **7**, 11356 (2016).

[41] K. B. Dideriksen, R. Schmieg, M. Zugenmaier, and E. S. Polzik, Room-temperature single-photon source with near-millisecond built-in memory, Nature Communications **12**, 3699 (2021).

[42] M. R. Vanner, I. Pikovski, G. D. Cole, M. S. Kim, C. Brukner, K. Hammerer, G. J. Milburn, and M. Aspelmeyer, Pulsed quantum optomechanics, Proceedings of the National Academy of Sciences **108**, 10.1073/pnas.1105098108 (2011).

[43] H. Habibi, E. Zeuthen, M. Ghanaatshoar, and K. Hammerer, Quantum Feedback Cooling of a Mechanical Oscillator Using Variational Measurements:Tweaking Heisenberg's Microscope, Journal of Optics **18**, 084004 (2016).

Supplementary Information

Squeezed light from an oscillator measured at the rate of oscillation

Christian Bærentsen, Sergey A. Fedorov,* Christoffer Østfeldt,
Mikhail V. Balabas, Emil Zeuthen, and Eugene S. Polzik†
Niels Bohr Institute, University of Copenhagen, Copenhagen, Denmark

CONTENTS

Appendix A: Experimental setup

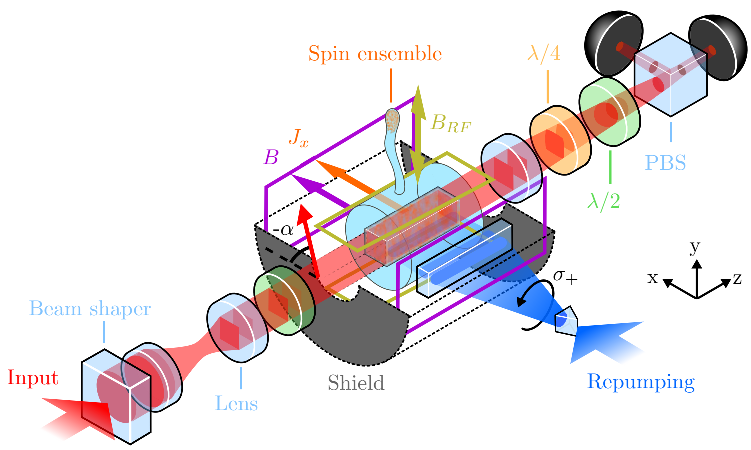

FIG. SI1. Experimental setup. A linearly polarized light probe is spatially shaped as a square-tophat beam. The probe interacts with an optically polarized ensemble of Cesium atoms located in a glass chip. The macroscopic atomic polarization J_x is oriented along the magnetic field B. The optical probe and the atomic ensemble interact via Faraday interaction in the dispersive regime. The output probe light is detected using a polarization self-homodyning setup. PBS: Polarizing beamsplitter. $\lambda/2$: Half wave plate. $\lambda/4$: Quarter wave plate. Beam shaper: Gaussian-to-tophat beam-shaping lens.

A detailed schematic of our experimental setup is presented in Fig. SI1. The probed cesium-133 atoms are located in a channel of a glass chip with 1 mm×1 mm cross-section and 40 mm length. The chip is enclosed in a glass cell, which has a stem attached to it that contains a piece of cesium metal providing a reservoir of atoms. The cell interior is coated with an anti-spin-relaxation paraffin coating to decrease the decoherence due to the collisions of atoms with walls. The cell is heated to $(52 \pm 2)\,^\circ$C and placed in a stationary homogeneous magnetic field directed along the x axis, which is created by a pair of rectangular coils parallel to the yz plane. Additional time-dependent magnetic field directed along the y axis can be created using another pair of coils parallel to the xz plane, which has the effect of applying a classical force to the atomic oscillator. The cell and the entire set of coils are enclosed in a multi-layer magnetic shield, including μ-metal layers to eliminate the magnetic field of the Earth and an aluminum layer to protect the spins from external high-frequency magnetic noise.

The atoms interact with two light beams: the probe, which is linearly polarized and propagates along the channel, and the repump, which is circularly polarized and propagates perpendicular to the channel, along the x axis. Both light beams have wavelengths around 852.3 nm, close to the D2 transition from the ground state of Cs. The ground state of Cs is split into two hyperfine levels, with the magnetic momentum numbers $F = 3$ and $F = 4$, and each hyperfine level is further split into $(2F + 1)$ magnetic sublevels. The repump beam is produced by a diode laser and has the power in the range of $8 - 10$ mW. It is blue-detuned by 80 MHz from the $F = 3 \to F' = 2$ transition of the D2 line, and resonant with all transitions $F = 3 \to F' = 2, 3, 4$ within the Doppler linewidth, where the primes denote electronically excited states. The cross-section of the chip channel containing atoms is chosen to be square to avoid lensing of the repump beam. In order to uniformly illuminate the elongated channel, the repump beam is shaped by a combination of a Powell lens and a cylindrical collimating lens. The repump transfers all atoms to $F = 4$ level, and simultaneously creates macroscopic spin orientation in the ensemble because of its circular polarization. The chirality of the polarization, σ_+ or σ_-, determines the sign of the mass of the oscillator [1]. Our experiments are done with a negative-mass oscillator, but the results, including the observed levels of squeezing, are largely independent of the sign of the mass (see Sec. E). The probe beam is blue-detuned by $0.7 - 7$ GHz from $F = 4 \to F' = 5$ transition; it is produced by a Ti:Sa laser and has the power up to 13 mW. The probe interacts with the ensemble in the dispersive regime, but the residual spontaneous scattering of photons from it contributes to the spin decoherence. The linear polarization of the probe is set along the y axis to maximize the optical damping by the dynamical backaction (which nevertheless remains small), and simultaneously decouple the spin from the classical intensity fluctuations. The small amount of optical damping in our experiments improves the maximum observed level of squeezing (see Sec. F). The decoherence rate due to the spontaneous scattering is proportional to the probe power, and is the primary limitation for the achievable quantum cooperativity in our work. The distribution of the atoms among the magnetic sublevels is determined by the interplay of the spontaneous scattering processes due to the probe and the repump beam, and is independent of the probe power and detuning within our range of parameters.

After the interaction with the atomic ensemble, the relevant quadratures of the probe beam are detected using polarization homodyning. The quadrature angle is selected using a combination of a quarter waveplate and a half waveplate. A key advantage of the polarization homodyning method is the perfect spatial overlap between the detected modes of light and the local oscillator. The electronic noise floor of the photodetector is typically about 30 dB below the shot noise level and hence is negligible.

The maximum narrowband squeezing of light observed in the regime when $\Gamma \ll |\Omega_S|$ is approximately independent of the Larmor frequency within the range of Larmor frequencies between 0.8 MHz and 5 MHz. At low frequencies, the limitation is due to classical noises acting on the spins, and at high frequencies due to the inhomogeneity of the magnetic field, which could be straightforwardly improved.

In order to minimize the coupling to the fast-decaying modes of the spin ensemble (see Sec. B), the probe beam is shaped into a square tophat beam using a high-transmission beam shaping lens (Topag GTH-3.6-1.75FA), and an additional system of regular spherical lenses described in Sec. G. The resulting beam has a supergaussian intensity cross section $I(x, y) \propto \exp(-2(x/w_x)^{2n} - 2(y/w_y)^{2n})$ with $n \approx 3.2$ and $2w_x \approx 2w_y \approx 0.84$ mm, which change negligibly in the z direction over the length of the cell channel. The on-resonance extraneous thermal noise in the slow-measurement regime was experimentally found to be lower by a factor of 3.6 for the tophat beam probe compared to the Gaussian beam probe with the maximum width allowed by the cell channel. The transmission of the probe beam through the cell reaches 96.8%, limited by the reflection and scattering of light upon hitting the cell windows, with the loss of light due to the clipping of the beam being negligible. In order to infer the generated level of squeezing from detected, we assume that the transmission loss is equally contributed by the input and the output windows.

Appendix B: The modes of an ensemble of moving atoms interacting with light

In this section, we describe N moving atoms interacting with the probe light field, and derive input-output relations for the optical quadratures in terms of two types of collective spin oscillator modes: usual Larmor precession modes, and modes scrambled by the atomic motion. Individual atoms interact with the light field with the strengths $g_k(t)$ (where $k = 1, .., N$ is the integer index that labels the atoms) that is proportional to the intensity of the light field at their instantaneous position. The interaction strengths randomly change in time as atoms move inside the cell. The motions of different atoms are assumed to have the same statistical properties and be uncorrelated between each other. The statistics of motion are characterized by decomposing the couplings into their mean value, $\bar{g}$, and deviations, $\Delta g_k(t)$,

$$g_k(t) = \bar{g} + \Delta g_k(t), \tag{SI B.1}$$

and specifying the motional correlation function, $R(\tau)$,

$$\frac{\langle \Delta g_k(t_1)\, \Delta g_l(t_2)\rangle_c}{\langle \Delta g(t)^2\rangle_c} = \delta_{kl} R(t_1 - t_2), \tag{SI B.2}$$

where δ_{kl} is the Kronecker symbol and $\langle\cdot\rangle_c$ denotes motional averaging (following the notation of Ref. [2], to separate from the quantum averaging $\langle\cdot\rangle$). The normalization factor, $\langle \Delta g(t)^2\rangle_c$, is the mean squared deviation among the individual atom-light couplings. According to the ergodic hypothesis, the result of the averaging is the same regardless of whether it is done over the time or the realizations of the ensemble.

The dispersive interaction between the light and the $k-$th atom in the ensemble is described by the Hamiltonian [3, 4]

$$\hat{H}^{(k)}_{\text{int}} = \hbar\, g_k(t) \left[a_0 \hat{I} + a_1 \hat{S}_z \hat{j}^{(k)}_z + a_2 \left(\hat{I}\, \hat{j}^{(k)}_z \hat{j}^{(k)}_z - 2\hat{S}_x \left(\hat{j}^{(k)}_x \hat{j}^{(k)}_x - \hat{j}^{(k)}_y \hat{j}^{(k)}_y\right) - 2\hat{S}_y \left(\hat{j}^{(k)}_x \hat{j}^{(k)}_y + \hat{j}^{(k)}_y \hat{j}^{(k)}_x\right)\right)\right], \tag{SI B.3}$$

where $\hat{S}_{x,y,z}$ are the Stokes parameters of the input light [3], $\hat{I}$ is the intensity of the input light, and the parameters $a_{0,1,2}$ are functions of the level structure and the laser detuning from the optical transition [5]. After linearization assuming a strong coherent y-polarized light probe with the mean amplitude $\bar{a}$, the Hamiltonian is expressed as

$$\hat{H}^{(k)}_{\text{int}} = \hat{H}^{(k)}_{\text{Stark}} - \hbar \frac{\bar{a} g_k(t)}{\sqrt{2}} \left[a_1 \hat{j}^{(k)}_z \hat{X}_{\text{L}} - 2a_2 \left(\hat{j}^{(k)}_x \hat{j}^{(k)}_y + \hat{j}^{(k)}_y \hat{j}^{(k)}_x\right) \hat{P}_{\text{L}}\right], \tag{SI B.4}$$

where the Stark Hamiltonian $\hat{H}^{(k)}_{\text{Stark}} = \hbar g_k(t) \left[a_0 + a_2 \left(\hat{j}^{(k)}_x \hat{j}^{(k)}_x - \hat{j}^{(k)}_y \hat{j}^{(k)}_y + \hat{j}^{(k)}_z \hat{j}^{(k)}_z\right)\right] \hat{I}$ describes the energy shifts due to the dynamic Stark effect, and $\hat{X}_{\text{L}}$ and $\hat{P}_{\text{L}}$ are the polarization quadratures of the light field normalized such that they satisfy the commutation relation

$$[\hat{X}_{\text{L}}(t_1), \hat{P}_{\text{L}}(t_2)] = (i/2)\delta(t_1 - t_2). \tag{SI B.5}$$

The spin components of individual atoms $\hat{j}^{(k)}_{x,y,z}$ can be expressed in terms of the jump operators $\hat{\sigma}^{(k)}_{n,m}$ between the ground state sublevels,

$$\hat{\sigma}^{(k)}_{n,m} = |n\rangle_k \langle m|_k, \tag{SI B.6}$$

where $m, n = -F, ..., F$ is the projection of the angular momentum on the x axis (which coincides with the direction of the magnetic field), and F is the total angular momentum quantum number of the ground state level. In this notation,

$$H^{(k)}_{\text{int}} = \hat{H}^{(k)}_{\text{Stark}} + \hbar \frac{\bar{a} g_k(t)}{2\sqrt{2}} \sum_{m=-F}^{F-1} C_m \left(i a_1 \left(\hat{\sigma}^{(k)}_{m+1,m} - \hat{\sigma}^{(k)}_{m,m+1}\right) \hat{X}_{\text{L}} + 2(2m+1) a_2 \left(\hat{\sigma}^{(k)}_{m+1,m} + \hat{\sigma}^{(k)}_{m,m+1}\right) \hat{P}_{\text{L}}\right), \tag{SI B.7}$$

where $\hat{H}^{(k)}_{\text{Stark}} = \hbar \sum_m g_k(t) \left(a_0 + a_2 m^2\right) \hat{I}\, \hat{\sigma}^{(k)}_{m,m}$ is the Stark energy, and $C_m = \sqrt{F(F+1) - m(m+1)}$ are Clebsch–Gordan coefficients. When transiting from Eq. (SI B.4) to Eq. (SI B.7) we neglected the terms involving second-order coherences that only couple to $\hat{I}$ and are negligibly small in our case.

The individual atomic spins are precessing in a homogeneous magnetic field directed along the x axis. Taking the zero of the energy scale to be the ground state energy of free atoms, the Hamiltonian of the precession is expressed as

$$\hat{H}^{(k)}_{\text{S}} = \sum_{m=-F}^{F} E_{\text{Zeem},m}\, \hat{\sigma}^{(k)}_{m,m}, \tag{SI B.8}$$

where $E_{\text{Zeem},m}$ are the Zeeman energies of the magnetic sublevels that include contributions linear and quadratic in m. The total Hamiltonian of all atoms,

$$\hat{H} = \sum_{k=1}^{N} \left(\hat{H}_{\text{S}}^{(k)} + \hat{H}_{\text{int}}^{(k)} \right), \tag{SI B.9}$$

can be expressed using collective operators: the total numbers of atoms in the magnetic sublevels, denoted by $\hat{N}_m$, and two sets of coherences between neighboring m levels, denoted by $\hat{\Sigma}_m$ and $\hat{\Sigma}'_m$. The operators are defined as

$$\hat{N}_m = \sum_{k=1}^{N} \hat{\sigma}_{m,m}^{(k)}, \qquad \hat{\Sigma}_m = \sum_{k=1}^{N} \hat{\sigma}_{m+1,m}^{(k)}, \qquad \hat{\Sigma}'_m = \frac{1}{\sqrt{\langle \Delta g^2 \rangle_c}} \sum_{k=1}^{N} \Delta g_k(t)\, \hat{\sigma}_{m+1,m}^{(k)}, \tag{SI B.10}$$

where $m = -F, ..., F-1$ for the Σ operators and $m = -F, ..., F$ for the N operators. The expression for the Hamiltonian, neglecting a small contribution due to the inhomogeneity of the Stark shift, is

$$\hat{H} = \sum_{m=-F}^{F} E_m \hat{N}_m + \hbar \sum_{m=-F}^{F-1} \frac{\bar{g}\bar{a}a_1}{2\sqrt{2}} C_m \left(i \left(\hat{\Sigma}_m - \hat{\Sigma}_m^\dagger \right) \hat{X}_{\text{L}} + \zeta_m \left(\hat{\Sigma}_m + \hat{\Sigma}_m^\dagger \right) \hat{P}_{\text{L}} \right)$$
$$+ \hbar \sum_{m=-F}^{F-1} \frac{\sqrt{\langle \Delta g^2 \rangle_c}\, \bar{a} a_1}{2\sqrt{2}} C_m \left(i \left(\hat{\Sigma}'_m - \hat{\Sigma}'^\dagger_m \right) \hat{X}_{\text{L}} + \zeta_m \left(\hat{\Sigma}'_m + \hat{\Sigma}'^\dagger_m \right) \hat{P}_{\text{L}} \right), \tag{SI B.11}$$

where $\zeta_m = 2(2m+1)a_2/a_1$, and $E_m = E_{\text{Zeem},m} + E_{\text{Stark},m}$ is the sum of the Zeeman and the Stark energies. In the limit of a large number of atoms in the ensemble, the two sets of $\hat{\Sigma}_m$ operators are independent and have constant commutators,

$$\left[\hat{\Sigma}_n, \hat{\Sigma}_m^\dagger \right] = \delta_{nm} \left(\hat{N}_{m+1} - \hat{N}_m \right) \quad \xrightarrow[N \gg 1]{} \quad \delta_{nm} \left(N_{m+1} - N_m \right), \tag{SI B.12}$$

$$\left[\hat{\Sigma}_n, \hat{\Sigma}'^\dagger_m \right] = \delta_{nm} \sum_k \frac{\Delta g_k(t)}{\sqrt{\langle \Delta g^2 \rangle_c}} \left(\hat{\sigma}_{m+1,m+1}^{(k)} - \hat{\sigma}_{m,m}^{(k)} \right) \quad \xrightarrow[N \gg 1]{} \quad 0, \tag{SI B.13}$$

$$\left[\hat{\Sigma}'_n, \hat{\Sigma}'^\dagger_m \right] = \delta_{nm} \sum_j \frac{\Delta g_j(t)^2}{\langle \Delta g^2 \rangle_c} \left(\hat{\sigma}_{m+1,m+1}^{(j)} - \hat{\sigma}_{m,m}^{(j)} \right) \quad \xrightarrow[N \gg 1]{} \quad \delta_{nm} \left(N_{m+1} - N_m \right), \tag{SI B.14}$$

where $m, n = -F, ..., F-1$, and $N_m = \langle \hat{N} \rangle$ are the average macroscopic populations of the magnetic sublevels. By normalizing the Σ operators to satisfy the canonic commutation relations, we can introduce two sets of bosonic modes, $\hat{b}_m$ and $\hat{b}'_m$, that appear in the main text,

$$\hat{b}_m = \hat{\Sigma}_m / \sqrt{\Delta N_m}, \qquad \hat{b}'_m = \hat{\Sigma}'_m / \sqrt{\Delta N_m}, \tag{SI B.15}$$

where $\Delta N_m = N_{m+1} - N_m$. The modes described by $\hat{b}_m$ are those usually identified with the Larmor precession of the spin ensemble as a whole. They experience coupling to the probe light that is averaged over the atomic trajectories [6], and their coherence time is high, limited by the reorientation of individual spins due to the collisions with the walls and between each other, and by the spontaneous scattering of probe photons. The modes described by $\hat{b}'_m$ experience additional damping and decoherence due to the atoms flying in and out of the probe beam. We refer to them as the fast-decaying modes. Introducing the quadratures of the spin oscillators,

$$\hat{X}_m \equiv \frac{1}{i\sqrt{2}} \left(\hat{b}_m - \hat{b}_m^\dagger \right), \quad \hat{P}_m \equiv -\frac{1}{\sqrt{2}} \left(\hat{b}_m + \hat{b}_m^\dagger \right), \quad \hat{X}'_m \equiv \frac{1}{i\sqrt{2}} \left(\hat{b}'_m - \hat{b}'^\dagger_m \right), \quad \hat{P}'_m \equiv -\frac{1}{\sqrt{2}} \left(\hat{b}'_m + \hat{b}'^\dagger_m \right), \tag{SI B.16}$$

which satisfy $[\hat{X}_m, \hat{P}_m] = i$ and $[\hat{X}'_m, \hat{P}'_m] = i$, and using the fact that, in the Holstein-Primakoff approximation, the numbers of atoms in the $m-$th levels satisfy

$$\hat{N}_m \approx N_m + \frac{1}{2} \left(\hat{b}_m^\dagger \hat{b}_m + \hat{b}'^\dagger_m \hat{b}'_m - \hat{b}_{m-1}^\dagger \hat{b}_{m-1} - \hat{b}'^\dagger_{m-1} \hat{b}'_{m-1} + \text{h.c.} \right), \tag{SI B.17}$$

the total Hamiltonian in Eq. (SI B.11) is expressed as

$$\hat{H} = \hbar \sum_{m=-F}^{F-1} \left[\frac{\Omega_m}{2} \left(\hat{X}_m^2 + \hat{P}_m^2 \right) + \frac{\Omega_m}{2} \left(\hat{X}'^2_m + \hat{P}'^2_m \right) \right.$$
$$\left. -2\sqrt{\Gamma_m} \left(\hat{X}_m \hat{X}_{\text{L}} + \zeta_m \hat{P}_m \hat{P}_{\text{L}} \right) - 2\sqrt{\Gamma'_m} \left(\hat{X}'_m \hat{X}_{\text{L}} + \zeta_m \hat{P}'_m \hat{P}_{\text{L}} \right) \right], \tag{SI B.18}$$

which is a Hamiltonian of $4F$ oscillators linearly coupled to a propagating field. The frequencies Ω_m are determined by the energy splittings between different magnetic sublevels due to the Zeeman and Stark effects,

$$\hbar\Omega_m = E_{\mathrm{Zeem},m} - E_{\mathrm{Zeem},m+1} - \hbar\bar{g}a_2 I(2m+1), \tag{SI B.19}$$

and the measurement rates for the slow- and the fast-decaying modes are identified as

$$\Gamma_m = \bar{g}^2(\bar{a}a_1\, C_m)^2\Delta N_m/16, \qquad \Gamma'_m = \langle\Delta g^2\rangle_c\,(\bar{a}a_1\, C_m)^2\Delta N_m/16. \tag{SI B.20}$$

The input-output relations for the quadratures of the light field are derived based on Eq. (SI B.18) as described in Ref. [7]. They are given by

$$\hat{X}_{\mathrm{L}}^{\mathrm{out}}(t) = \hat{X}_{\mathrm{L}}^{\mathrm{in}}(t) - \sum_{m=-F}^{F-1}\zeta_m\left(\sqrt{\Gamma_m}\hat{P}_m(t) + \sqrt{\Gamma'_m}\hat{P}'_m(t)\right), \tag{SI B.21}$$

$$\hat{P}_{\mathrm{L}}^{\mathrm{out}}(t) = \hat{P}_{\mathrm{L}}^{\mathrm{in}}(t) + \sum_{m=-F}^{F-1}\left(\sqrt{\Gamma_m}\hat{X}_m(t) + \sqrt{\Gamma'_m}\hat{X}'_m(t)\right), \tag{SI B.22}$$

and the Heisenberg equations of motion for the slow-decaying modes are

$$\frac{d}{dt}\hat{X}_m(t) = \Omega_m\hat{P}_m(t) - \sum_{n=-F}^{F-1}\zeta_m\sqrt{\Gamma_m}\left(\sqrt{\Gamma_n}\hat{X}_n(t) + \sqrt{\Gamma'_n}\hat{X}'_n(t)\right) - 2\zeta_m\sqrt{\Gamma_m}\hat{P}_{\mathrm{L}}^{\mathrm{in}}(t), \tag{SI B.23}$$

$$\frac{d}{dt}\hat{P}_m(t) = -\Omega_m\hat{X}_m(t) - \sum_{n=-F}^{F-1}\zeta_n\sqrt{\Gamma_m}\left(\sqrt{\Gamma_n}\hat{P}_n(t) + \sqrt{\Gamma'_n}\hat{P}'_n(t)\right) + 2\sqrt{\Gamma_m}\hat{X}_{\mathrm{L}}^{\mathrm{in}}(t). \tag{SI B.24}$$

Eq. (SI B.23-SI B.24) show that the oscillators experience damping or antidamping by dynamical backaction with the rates $\gamma_{\mathrm{DBA},m} = 2\zeta_m\Gamma_m$, and are coupled between each other at the rates $\sqrt{\gamma_{\mathrm{DBA},m}\gamma_{\mathrm{DBA},n}}$ due to the interaction with the common optical bath. For practical calculations, intrinsic dissipation due to the atomic collisions and spontaneous scattering is added to Eq. (SI B.23-SI B.24) using the usual quantum Langevin approach [4]. The temperatures of the effective thermal baths can be determined from the equilibrium numbers of excitation in the modes in the absence of probing, $n_{\mathrm{th}} \equiv \langle\hat{b}_m^\dagger\hat{b}_m\rangle = (N_m/\Delta N_m)$, which are calculated directly from the definitions of $\hat{b}_m$ under the assumption that the processes that determine the equilibrium populations N_m affect all atoms independently.

The Heisenberg equations of motion describing the evolution of the modes from the fast-decaying family are identical to Eq. (SI B.23-SI B.24), except that they include additional terms due to the explicit time dependence of their operators. These terms are more convenient to present for the annihilation operators than for the quadratures, they are given by

$$\frac{d}{dt}\hat{b}'_m(t) = -i\left[\hat{b}'_m, \hat{H}\right] + \frac{1}{\sqrt{\Delta N_m\,\langle\Delta g^2\rangle_c}}\sum_{k=1}^{N}\left(\frac{d}{dt}\Delta g_k(t)\right)\hat{\sigma}_{m+1,m}^{(k)}, \tag{SI B.25}$$

where $-i[\hat{b}'_m, \hat{H}]$ contributes the terms due to the coherent evolution and the coupling to the light field that are completely analogous to those present in Eq. (SI B.23-SI B.24). The added terms give rise to both extra dissipation and fluctuations. If the motional correlation function is exponential, $\langle\Delta g_k(t_1)\,\Delta g_k(t_2)\rangle \propto e^{-\gamma_b|t_1-t_2|/2}$, as it was suggested in [6], the stochastic evolution of $\Delta g_k(t)$ can be modeled by the Ornstein–Uhlenbeck process,

$$\frac{d}{dt}\Delta g_k(t) = -\frac{\gamma_b}{2}\Delta g_k(t) + \sqrt{\gamma_b}f_k(t), \tag{SI B.26}$$

where $\langle f_k(t_1)f_k(t_2)\rangle_c = \langle\Delta g^2\rangle_c\,\delta(t_1-t_2)$. In this case, the extra terms in the Heisenberg-Langevin equations for $\hat{b}'$ can be re-expressed as

$$\frac{d}{dt}\hat{b}'_m(t) = -i\left[\hat{b}'_m, \hat{H}\right] - \frac{\gamma_b}{2}\hat{b}'_m(t) + \sqrt{\gamma_b}\hat{\mathcal{F}}'_b(t), \tag{SI B.27}$$

where $\langle\hat{\mathcal{F}}_b'^\dagger(t_1)\hat{\mathcal{F}}'_b(t_2)\rangle = n_{\mathrm{th}}\delta(t_1-t_2)$ and $n_{\mathrm{th}} = N_m/\Delta N_m$ is the thermal occupancy of the bath. While the atomic motion increases the decoherence rate, the thermal bath occupancies for the fast- and slow-decaying modes are the same.

Appendix C: The backaction-imprecision product in homodyne detection

The two conjugated quadratures of the probe light that after interaction with the atomic ensemble, $\hat{X}_{\mathrm{L}}^{\mathrm{out}}$ and $\hat{P}_{\mathrm{L}}^{\mathrm{out}}$, as well as any intermediate quadrature $\hat{Q}_{\mathrm{L}}^{\phi}$,

$$\hat{Q}_{\mathrm{L}}^{\phi}(t) = \sin(\phi)\hat{X}_{\mathrm{L}}^{\mathrm{out}}(t) + \cos(\phi)\hat{P}_{\mathrm{L}}^{\mathrm{out}}(t), \tag{SI C.1}$$

can be detected by balanced polarization homodyning after passing the output light through a combination of a half and a quarter waveplates. The rotation angles of the waveplates allow setting the detection angle ϕ. The two-sided power spectral density (PSD) of the photocurrent signal is given by

$$S_{\phi}[\Omega] = \frac{1}{4}(1-\eta) + \eta \int_{-\infty}^{\infty} e^{i\Omega\tau} \left\langle \hat{Q}_{\mathrm{L}}^{\phi}(t+\tau)\, \hat{Q}_{\mathrm{L}}^{\phi}(t) \right\rangle d\tau, \tag{SI C.2}$$

where η is the detection efficiency. When the optical field is in the vacuum state, its correlation is given by $\langle \hat{Q}_{\mathrm{L}}^{\phi}(t+\tau)\, \hat{Q}_{\mathrm{L}}^{\phi}(t)\rangle = (1/4)\delta(\tau)$, and therefore $S_{\phi}[\Omega] = 1/4$; this value is the shot noise level. The observation $S_{\phi}[\Omega] < 1/4$ means that some of the Fourier-domain modes of light are in squeezed states.

The spectral density of the photocurrent when the homodyne is tuned to detect the P quadrature is given by

$$S_{\phi}[\Omega] = \frac{1}{4} + \eta\Gamma\, S_{X_S X_S}[\Omega] + \eta\, S_{PP,\mathrm{ext}}[\Omega], \tag{SI C.3}$$

where $S_{X_S X_S}[\Omega]$ is the spectrum of the total spin motion, and $S_{PP,\mathrm{ext}}[\Omega]$ is the extraneous noise. In the slow-measurement regime when $\Gamma \ll |\Omega_S|$, $S_{PP,\mathrm{ext}}$ comes from the thermal noise of fast-decaying modes (see Sec. D), and in the fast-measurement regime when $\Gamma \sim |\Omega_S|$, $S_{PP,\mathrm{ext}} = 0$. There is no detectable extraneous noise in the X quadrature of light in our experiments. The spectrum of the imprecision noise for measurements on the P quadrature is given by

$$S_{\mathrm{imp}}[\Omega] = \frac{1/4 + S_{PP,\mathrm{ext}}[\Omega]}{\eta\Gamma}, \tag{SI C.4}$$

The spectrum of the backaction noise is given by $S_{\mathrm{BA}}[\Omega] = \hbar^2 \left(\Gamma(1+\zeta^2) + \gamma_{\mathrm{sc}}\right)$, where γ_{sc} is the decoherence rate of the oscillator due to spontaneous scattering, which is proportional to the probe power. We conservatively estimate $\gamma_{\mathrm{sc}}/\Gamma$ as $1/\mathcal{C}_{\mathrm{q}}$ (as if all the decoherence of spin oscillators comes from spontaneous scattering). Overall, the backaction-imprecision product in terms of the two-sided spectral densities is found as

$$\sqrt{S_{\mathrm{imp}}\, S_{\mathrm{BA}}} = (\hbar/2)\sqrt{\frac{1}{\eta}\left(1 + \frac{S_{PP,\mathrm{ext}}}{\mathrm{SN}}\right)\left(1 + \zeta^2 + \frac{1}{\mathcal{C}_{\mathrm{q}}}\right)}. \tag{SI C.5}$$

where $\mathrm{SN} = 1/4$ is the shot noise level. This expression exposes how various imperfections of the measurements, including the finite detection efficiency, the extraneous noise, the "heating" due to spontaneous scattering, and the dynamical backaction, elevate the backaction-imprecision product above the quantum limit of $\hbar/2$ in our experiments.

Appendix D: The modeling of the experimental data

To process the experimental data, we model the homodyne spectrum as arising from the dynamics of several oscillator modes coupled to the probe field, using the input-output relations that are expressed analogously to Eqs.(SI B.21) and (SI B.22),

$$\hat{X}_{\mathrm{L}}^{\mathrm{out}}(t) = \hat{X}_{\mathrm{L}}^{\mathrm{in}}(t) - \sum_{i=1}^{n_{\mathrm{modes}}} \zeta_i \sqrt{\Gamma_i}\hat{P}_i(t), \qquad \hat{P}_{\mathrm{L}}^{\mathrm{out}}(t) = \hat{P}_{\mathrm{L}}^{\mathrm{in}}(t) + \sum_{i=1}^{n_{\mathrm{modes}}} \sqrt{\Gamma_i}\hat{X}_i(t). \tag{SI D.1}$$

and the Heisenberg equations of motion analogous to Eqs.(SI B.23) and (SI B.24),

$$\frac{d}{dt}\hat{X}_i(t) = \Omega_i \hat{P}_i(t) - \frac{\gamma_{0,i}}{2}\hat{X}_i(t) - \sum_{j=1}^{n_{\mathrm{modes}}} \zeta_i \sqrt{\Gamma_i \Gamma_j}\hat{X}_j(t) - 2\zeta_i\sqrt{\Gamma_i}\hat{P}_{\mathrm{L}}^{\mathrm{in}}(t) + \hat{F}_i^X(t), \tag{SI D.2}$$

$$\frac{d}{dt}\hat{P}_i(t) = -\Omega_i \hat{X}_i(t) - \frac{\gamma_{0,i}}{2}\hat{P}_i(t) - \sum_{j=1}^{n_{\mathrm{modes}}} \zeta_j \sqrt{\Gamma_i \Gamma_j}\hat{P}_j(t) + 2\sqrt{\Gamma_i}\hat{X}_{\mathrm{L}}^{\mathrm{in}}(t) + \hat{F}_i^P(t). \tag{SI D.3}$$

The index i counts the modes of the model, corresponding to the hybridized resonances we observe in the experimental spectra. The model accounts for the intrinsic dissipation of the modes characterized by the damping rates $\gamma_{0,i}$, and thermal forces $\hat{F}_i^{X,P}(t)$ via the quantum Langevin approach. The correlators of the thermal forces are

$$\left\langle \hat{F}_i^X(t_1)\hat{F}_j^X(t_2)\right\rangle = \left\langle \hat{F}_i^P(t_1)\hat{F}_j^P(t_2)\right\rangle = \delta_{ij}\gamma_{0,i}(n_{\mathrm{th}}+1/2)\delta(t_1-t_2), \quad \left\langle \hat{F}_i^X(t_1)\hat{F}_j^P(t_2)+\hat{F}_j^P(t_2)\hat{F}_i^X(t_1)\right\rangle = 0. \tag{SI D.4}$$

The intrinsic dissipation in our experiments is dominated by spin depolarization due to the atomic collisions and spontaneous scattering of probe photons, which is why we assume that it symmetrically affects X and P, and that the thermal noises are delta-correlated [5]. The thermal occupancy of the intrinsic bath is $n_{\mathrm{th}} = 0.9 \pm 0.1$, as extracted from the equilibrium macroscopic population distribution of atoms over the magnetic sublevels.

The fast-decaying modes are treated as one, because their frequency splitting is much smaller than their decoherence rates. This mode is accounted differently for different detunings of the optical probe. At large detunings, the measurement rate for the fast-decaying mode also is much smaller than its decoherence rate, and the dynamic backaction is negligible. In this case, it contributes incoherent thermal noise to the measurement of slow-decaying modes. The spectrum of this noise in the $\hat{P}_{\mathrm{L}}$ quadrature of the output light is given by

$$S_{PP,\mathrm{ext}}[\Omega] = \Gamma' \int_{-\infty}^{\infty} e^{i(\Omega-\Omega_S)\tau}\frac{\langle \Delta g(t+\tau)\Delta g(t)\rangle_c}{\langle \Delta g(t)^2\rangle_c}d\tau, \tag{SI D.5}$$

where Γ' is the measurement rate of the mode and $\langle \Delta g(t+\tau)\Delta g(t)\rangle_c$ is the correlation function of the atomic motion (introduced in Sec. B). Experimentally, we find that this spectrum at frequencies close to the resonance has a Gaussian shape (consistent with a non-Markovian thermal bath), and describe it using the expression

$$S_{PP,\mathrm{ext}}[\Omega]/\mathrm{SN} = A_b\, e^{-(\Omega-\Omega_{\mathrm{S}})^2/(2\gamma_b^2)}, \tag{SI D.6}$$

where A_b is the magnitude of the added noise on resonance in shot noise (SN) units, and γ_b is the characteristic decay rate. The spectral width of the broadband noise is closely related to the transition time τ of atoms through the probe beam, $\gamma_{\mathrm{b}} \sim 1/\tau = v_{\mathrm{th}}/w$, where w is the width of the beam, $v_{\mathrm{th}} = \sqrt{2k_{\mathrm{B}}T/M_{\mathrm{Cs}}} \approx 200\,\mathrm{m/s}$ is the thermal velocity atoms, $T = 52\,^{\circ}\mathrm{C}$ is the operating temperature, k_{B} is the Boltzmann constant and M_{Cs} is the mass of one atom.

At the detuning of the optical probe equal to 0.7 GHz, at which the measurement rate of the spin reaches the oscillation frequency, the fast-decaying mode of the atomic ensemble is in the backaction-dominated regime. We therefore include it as an extra oscillator in Eqs. (SI D.1—SI D.3). This approach effectively approximates the correlation function of the thermal motion of the mode by an exponential, which in the spectral domain may introduce an error in the frequency window of several hundreds of kHz around the resonance, much smaller than the full bandwidth of the fit (several MHz).

The full comparison between the model and the experimental data at different optical detunings is shown in Fig. SI2. The data obtained at 7 GHz optical detuning is described by the response of a single oscillator mode to the measurement backaction. The data obtained at 3 GHz detuning is described with $n_{\mathrm{modes}} = 2$. At 0.7 GHz, we include the fast-decaying mode in the model and describe the experiment with $n_{\mathrm{modes}} = 3$. The homodyne spectra at all quadratures are processed in one global fit, where the resonance frequencies Ω_i, the measurement rates Γ_i, the dynamical backaction coefficients ζ_i, the intrinsic damping rates $\gamma_{0,i}$, and the quadrature angles ϕ are free parameters, and the values of the thermal occupancy n_{th} and the detection efficiency η are taken from independent calibrations. When processing the broadband measurements at 0.7 GHz, we additionally correct for the frequency response of the measurement electronic chain. The total quantum cooperativity for the data in Fig. SI2c is 4.6.

Appendix E: The sign of the mass

Spin oscillators can have positive or negative effective masses depending on the orientation of the mean spin alignment $\langle \hat{J}_x \rangle$ with respect to the magnetic field. The sign of the mass determines the overall sign of the response $\chi[\Omega]$ of the oscillator to generalized forces, including the quantum backaction force when the oscillator is subjected to linear measurements. Negative-mass oscillators can cancel measurement backaction on regular material oscillators [1], and become entangled with them [4].

The sign of the oscillator mass, together with the detection angle and the Fourier frequency, determines the sign of the backaction-imprecision correlations observed in homodyne measurement records. For multiple resonances, it also inverts the signs of the frequency splittings due to the Stark and quadratic Zeeman effects. The total effect of inverting

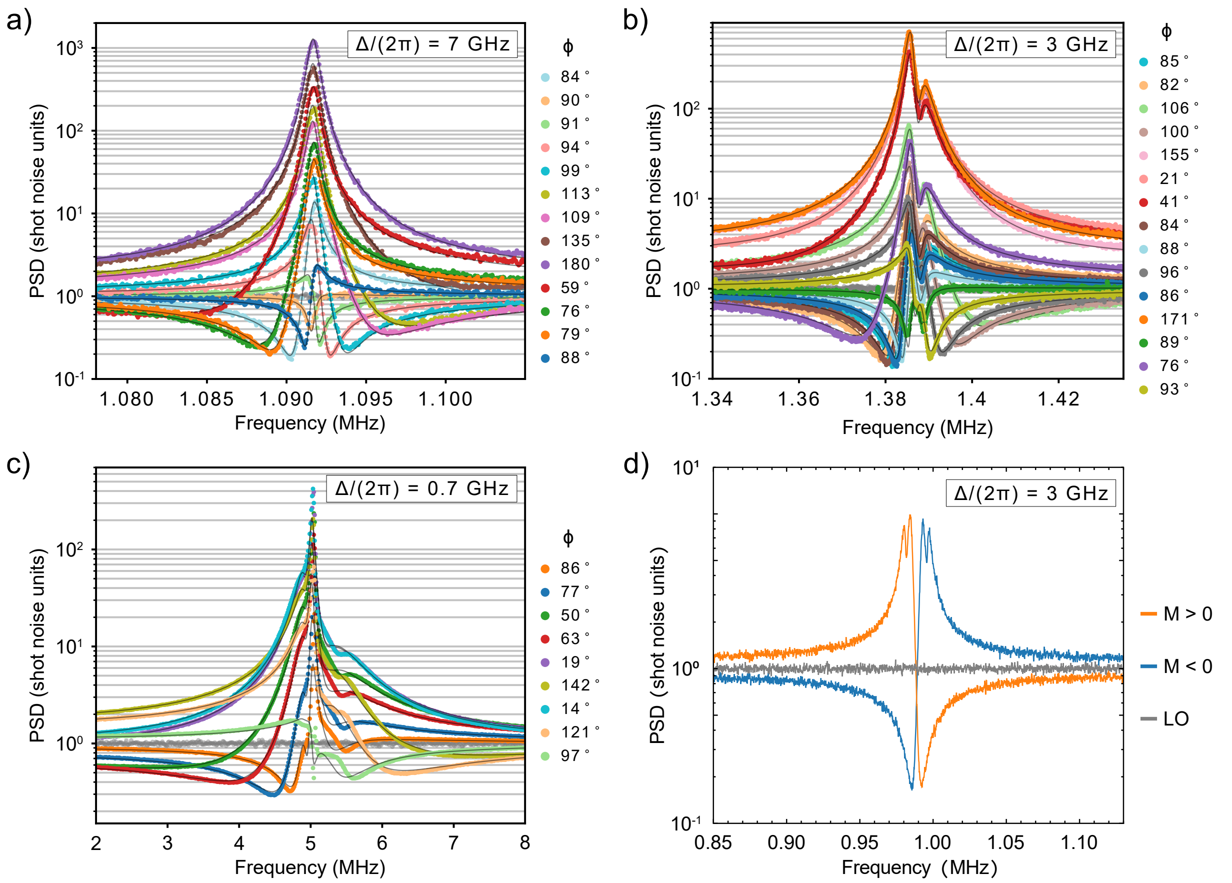

FIG. SI2. a)-c) Power spectral densities (PSD) of homodyne signals recorded at different quadrature angles ϕ and laser detunings Δ. The points of different colors show the experimental spectra for different quadrature angles as labeled in the legends. The black curves show the results of global fits at each detuning performed as described in Sec. D. Gray points show the local oscillator shot noise. Panel a) displays only part of the 17 traces fitted in total. d) The effect of changing the oscillator mass, M, on the homodyne spectrum measured at a quadrature intermediate between $\hat{X}_{\mathrm{L}}$ and $\hat{P}_{\mathrm{L}}$. The blue curve shows the spectrum recorded in a negative mass (M) configuration, the orange curve shows the spectrum recorded in a positive mass configuration, and the gray curve shows the local oscillator (LO) shot noise. The sign of the mass was changed by inverting the direction of the magnetic field with respect to the x axis. The spectra were recorded using a 12 mW probe detuned from the optical transition by 3 GHz.

the mass sign on homodyne spectra is therefore the reflection of the spectra with respect to the Larmor frequency. We observe this in Fig. SI2d, where we invert the sign of the mass by changing the direction of the magnetic field.

Appendix F: The spectrum of the homodyne signal in the presence of dynamical backaction

To illustrate the effect that the deviation of the interaction Hamiltonian from pure position measurement-type $(\zeta = 0)$ has on the detected spectra and the squeezing of light, we present an analytical solution for the optimum-quadrature homodyne spectrum in the single-oscillator model with arbitrary $\zeta \in [-1, 1]$ under the rotating-wave approximation (RWA). For a single mode, by solving Eqs. (SI D.2-SI D.3) and using the input-output relations given by Eq. (SI D.1), we find the spectrum of the output signal neglecting the detection losses as

$$S_\phi[\Omega]/\mathrm{SN} = 1 + 2\mathrm{Re}\left[\mathcal{A}\chi[\Omega]\right] + |\mathcal{A}\chi[\Omega]|^2 \left(1 + \frac{\gamma_{\mathrm{th}} + \gamma_0}{\Gamma(1+\zeta)}\right), \tag{SI F.1}$$

where SN $= 1/4$ is the shot noise level, $\chi[\omega] = -(1/2)/(\Delta\Omega + i\gamma/2)$ is the RWA force susceptibility, $\Delta\Omega = \Omega - \Omega_S$ is the Fourier-detuning from the oscillator resonance, $\gamma = \gamma_0 + 2\zeta\Gamma$ is the total oscillator linewidth, and the transduction factor $\mathcal{A}$ is

$$\mathcal{A} = i\Gamma(1+\zeta)\left((1+\zeta) + (1-\zeta)e^{-2i\phi}\right). \tag{SI F.2}$$

By minimizing Eq. (SI F.1) over the quadrature angle ϕ, we find the frequency-dependent maximum-squeezing angle $\phi_{\min}$ via

$$\tan(2\phi_{\min}[\Omega]) = -\frac{2\Delta\Omega}{\gamma_{\text{dec}}}, \tag{SI F.3}$$

where the total decoherence rate $\gamma_{\text{dec}} = \gamma_{\text{th}} + \gamma_{\text{QBA}}$ is the sum of the decoherence rates due to the intrinsic thermal noise, γ_{th} and the quantum backaction, γ_{QBA} which are defined as

$$\gamma_{\text{th}} = (2n_{\text{th}} + 1)\gamma_0, \qquad \gamma_{\text{QBA}} = \Gamma(1+\zeta^2). \tag{SI F.4}$$

The shot-noise normalized signal spectrum at the optimum quadrature is

$$S_{\phi_{\min}}[\Omega]/\text{SN} = 1 - \frac{2\gamma_{\text{DBA}}/\gamma}{1 + (2\Delta\Omega/\gamma)^2} - \frac{2\gamma_{\text{dec}}\Gamma/\gamma^2}{1 + (2\Delta\Omega/\gamma)^2}\left((1-\zeta^2)\sqrt{1 + \left(\frac{2\Delta\Omega}{\gamma_{\text{dec}}}\right)^2} - (1+\zeta^2)\right), \tag{SI F.5}$$

where $\gamma_{\text{DBA}} = 2\zeta\Gamma$ is the contribution of the dynamical backaction to the total oscillator linewidth (the optical damping). The absolute minimum of the spectrum is found by further minimizing $S_{\phi_{\min}}[\Omega]$ over $\Delta\Omega$, which can be done analytically in the general case, but yields a cumbersome result. Instead of presenting this result, we restrict the attention to the case $\zeta \ll 1$, which is relevant to our experiments, and estimate the minimum noise level by evaluating $S_{\phi_{\min}}[\Omega]$ at $\Delta\Omega_{\min,\zeta=0} = 1/2\sqrt{\gamma(2\gamma_{\text{dec}} + \gamma)}$, the optimum Fourier detuning for $\zeta = 0$. The result is

$$S_{\min} \approx 1 - \frac{\Gamma}{\gamma_{\text{dec}} + \gamma_0} - \frac{(\gamma_0 + \gamma_{\text{th}})\gamma_{\text{DBA}}}{(\gamma_0 + \gamma_{\text{dec}})^2}. \tag{SI F.6}$$

When the thermal occupancy of the intrinsic bath is close to zero, and the quantum cooperativity is in the intermediate regime, such that γ_{dec} has the same order of magnitude as γ_0, there is an improvement in the minimum noise level from a small positive optical damping.

Appendix G: The generation of the collimated tophat beam

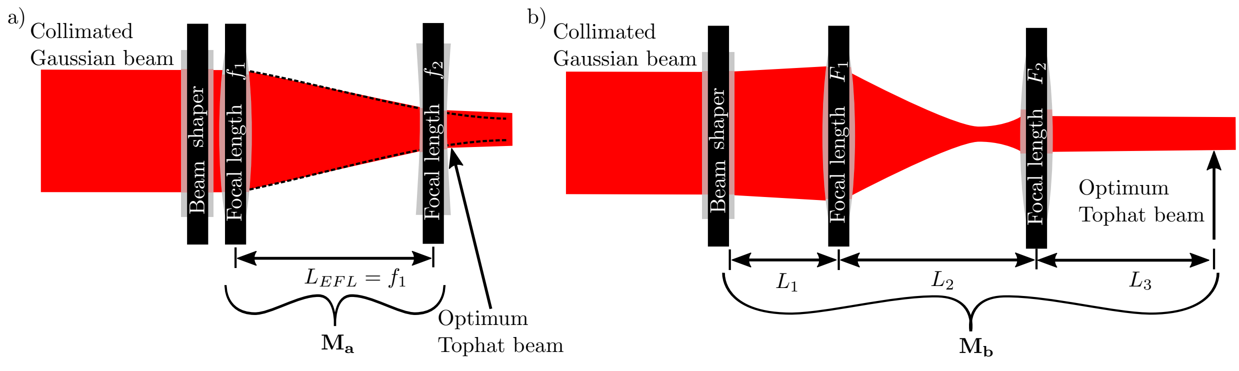

FIG. SI3. Optical setups for the generation of collimated tophat beams. $\mathbf{M}_{a,b}$ are ray transfer matrices. a) A simple setup. The dashed black line shows how the beam would propagate after passing the beam shaper and the lens f_1, but without passing the negative lens f_2. EFL: effective focal length. b) A realistic setup designed using the condition $\mathbf{M}_a = \mathbf{M}_b$. Beam shaper: Gaussian-to-tophat beam-shaping lens.

Optical beams with tophat transverse profiles are commonly produced by passing a collimated Gaussian beam through an aspherical beam shaper, and focusing the beam after the shaper using a spherical lens. In this configuration, the optimum tophat profile (giving the sharpest roll-off of the intensity distribution in the transverse direction) is realized before the focal point, and the beam is tightly focused. In our experiment, it is essential to create a beam in which the tophat profile coincides with the position of the beam waist, and has a relatively large transverse size, enabling a long Rayleigh length extending over the entire cell channel.

An intuition on how to produce a tophat beam that fulfills our criteria can be obtained by examining the setup shown in figure Fig. SI3a, which is a straightforward extension of the usual beam shaper application scheme with an addition of a negative lens f_2. The optimum tophat transverse profile is realized at a distance one effective focal length (EFL) away from the first lens. The transverse width is proportional to the focal length f_1. The beam is converging at the optimum point, because of the full fan angle of the tophat beam shaper (i.e. the divergence the shaper introduces in the beam). By placing an appropriate negative lens f_2 in the optimum point, the beam can be collimated, and its waist position made coincide with the optimum location of the transverse profile. The required focal length of the negative lens can be calculated given the size of the input Gaussian beam, w_{in}, and the full fan angle of the beam shaper, ϕ_{FA}, as $f_2 = \frac{\phi_{\mathrm{FA}}/w_{\mathrm{in}} f_1}{\phi_{\mathrm{FA}}/w_{\mathrm{in}} - 1/f_1}$.

The setup in Fig. SI3a would be challenging to implement directly, because the waist position of the beam is located inside the cell, where placing a lens is hardly realistic. However, one can find an optical setup with an identical ray transfer matrix to the one in Fig. SI3a, but realized using a different physical arrangement of lenses. Such a setup is shown in Fig. SI3b. The transfer matrices for the two setups, $\mathbf{M}_a$ and $\mathbf{M}_b$, are given by

$$\mathbf{M}_a = \mathbf{L}(f_2)\mathbf{S}(f_1)\mathbf{L}(f_1), \qquad \mathbf{M}_b = \mathbf{S}(L_3)\mathbf{L}(F_2)\mathbf{S}(L_2)\mathbf{L}(F_1)\mathbf{S}(L_1), \tag{SI G.1}$$

where the matrices for propagation in free space, $\mathbf{S}$, and passing through a lens, $\mathbf{L}$, respectively, are

$$\mathbf{S}(L) = \begin{bmatrix} 1 & L \\ 0 & 1 \end{bmatrix}, \qquad \mathbf{L}(f) = \begin{bmatrix} 1 & 0 \\ -1/f & 1 \end{bmatrix}. \tag{SI G.2}$$

In our experiment, the setup in Fig. SI3b is implemented using lenses of pre-determined focal lengths F_1 and F_2, while the separating distances L_1, L_2 and L_3 are adjusted to meet the condition $\mathbf{M}_a = \mathbf{M}_b$. Additionally, the matrix $\mathbf{M}_a$ is supplemented by an inversion in the transverse plane, which can be interpreted as passing the beam through an extra 4f optical system, which is done in order to have more flexibility in the choice of lenses and more control over the resulting distances.

* sergey.fedorov@nbi.ku.dk
† polzik@nbi.ku.dk

[1] C. B. Møller, R. A. Thomas, G. Vasilakis, E. Zeuthen, Y. Tsaturyan, M. Balabas, K. Jensen, A. Schliesser, K. Hammerer, and E. S. Polzik, Quantum back-action-evading measurement of motion in a negative mass reference frame, Nature **547**, 191 (2017).

[2] R. Shaham, O. Katz, and O. Firstenberg, Quantum dynamics of collective spin states in a thermal gas, Physical Review A **102**, 012822 (2020).

[3] J. Sherson, B. Julsgaard, and E. S. Polzik, Deterministic Atom–Light Quantum Interface, in *Advances In Atomic, Molecular, and Optical Physics*, Vol. 54, edited by P. R. Berman, C. C. Lin, and E. Arimondo (Academic Press, 2007) pp. 81–130.

[4] R. A. Thomas, M. Parniak, C. Østfeldt, C. B. Møller, C. Bærentsen, Y. Tsaturyan, A. Schliesser, J. Appel, E. Zeuthen, and E. S. Polzik, Entanglement between distant macroscopic mechanical and spin systems, Nature Physics , 1 (2020).

[5] D. V. Vasilyev, K. Hammerer, N. Korolev, and A. S. Sørensen, Quantum noise for Faraday light–matter interfaces, Journal of Physics B: Atomic, Molecular and Optical Physics **45**, 124007 (2012).

[6] J. Borregaard, M. Zugenmaier, J. M. Petersen, H. Shen, G. Vasilakis, K. Jensen, E. S. Polzik, and A. S. Sørensen, Scalable photonic network architecture based on motional averaging in room temperature gas, Nature Communications **7**, 11356 (2016).

[7] K. Hammerer, E. S. Polzik, and J. I. Cirac, Teleportation and spin squeezing utilizing multimode entanglement of light with atoms, Physical Review A **72**, 052313 (2005).

APPENDIX E

Published by Nature Physics: Entanglement between distant macroscopic mechanical and spin systems

Rodrigo A. Thomas, Michał Parniak, Christoffer Østfeldt, Christoffer B. Møller, **Christian Bærentsen**, Yeghishe Tsaturyan, Albert Schliesser, Jürgen Appel, Emil Zeuthen, and Eugene S. Polzik. *Entanglement between distant macroscopic mechanical and spin systems.* Nature Physics. 17, 228–233 (2021).

ARTICLES
https://doi.org/10.1038/s41567-020-1031-5

nature physics

Check for updates

Entanglement between distant macroscopic mechanical and spin systems

Rodrigo A. Thomas [1,5], Michał Parniak [1,5], Christoffer Østfeldt [1,5], Christoffer B. Møller [1,2,5], Christian Bærentsen [1], Yeghishe Tsaturyan [1,3], Albert Schliesser [1], Jürgen Appel [1,4], Emil Zeuthen [1] and Eugene S. Polzik [1] ✉

Entanglement is an essential property of multipartite quantum systems, characterized by the inseparability of quantum states of objects regardless of their spatial separation. Generation of entanglement between increasingly macroscopic and disparate systems is an ongoing effort in quantum science, as it enables hybrid quantum networks, quantum-enhanced sensing and probing of the fundamental limits of quantum theory. The disparity of hybrid systems and the vulnerability of quantum correlations have thus far hampered the generation of macroscopic hybrid entanglement. Here, we generate an entangled state between the motion of a macroscopic mechanical oscillator and a collective atomic spin oscillator, as witnessed by an Einstein–Podolsky–Rosen variance below the separability limit, $0.83 \pm 0.02 < 1$. The mechanical oscillator is a millimetre-size dielectric membrane and the spin oscillator is an ensemble of 10^9 atoms in a magnetic field. Light propagating through the two spatially separated systems generates entanglement because the collective spin plays the role of an effective negative-mass reference frame and provides—under ideal circumstances—a back-action-free subspace; in the experiment, quantum back-action is suppressed by 4.6 dB.

Entanglement is a key resource for quantum information processing[1], quantum-enhanced sensing[2] and fundamental tests of quantum theory[3,4]. Hybrid quantum systems often provide novel synergetic functionalities[5,6]. In particular, entangled states of motional and spin degrees of freedom have played a prominent role in quantum computing and simulation with trapped ions and atoms[7–9]. There, entanglement between motion and spin is generated by short-range interactions between individual atoms positioned at micrometre-scale distances, with motional and spin degrees of freedom associated with the same atoms.

A very different regime, focused on long-range macroscopic entanglement between the motion of one object and a spin of another, has been proposed in ref. [10] (see also ref. [11]). The key idea is to let an atomic spin in a magnetic field act as a negative-mass oscillator[10,12–14], enabling coherent quantum back-action (QBA) cancellation[15], thereby permitting travelling light to generate entanglement between the two objects. The negative-mass idea, which has been implicitly used in earlier experiments with two atomic ensembles[12,16–18], has been further developed in refs. [19–21] and has become the basis for quantum-mechanics-free subspaces[22].

Negative-mass-enabled instability[23] and strong coupling[24] have been recently demonstrated using the coupling of a motional degree of freedom to a spin system. In refs. [25,26], sympathetic cooling of a mechanical oscillator optically coupled to atoms has been shown. The negative-mass reference frame idea has also been utilized in proposals[27,28] by using an auxiliary mechanical system and multiple drive tones. In this way, entanglement has been generated between two micromechanical oscillators embedded in a common microwave cavity[29]. An approach to mechanical–mechanical entanglement based on single-photon detection was demonstrated in refs. [30,31].

Here we report an experimental implementation of Einstein–Podolsky–Rosen (EPR) entanglement in a hybrid system consisting of a mechanical oscillator and a spin oscillator[10], as depicted schematically in Fig. 1a. An out-of-plane vibrational mode of a soft-clamped, highly stressed dielectric membrane[32], which is embedded in a free-space optical cavity, constitutes the mechanical subsystem. The spin subsystem is prepared in a warm ensemble of optically pumped caesium atoms confined in a spin-preserving microcell[33]. The two oscillators are coupled to an itinerant light field and optically read out in a cascaded fashion. The basic ingredients of our hybrid set-up and the principle of QBA evasion using a negative-mass oscillator have been described in ref. [14].

The collective macroscopic spin $\hat{J}_x = \sum_{i=1}^{N} \hat{F}_x^{(i)}$ of $N \approx 10^9$ atoms, each with total angular momentum components $(\hat{F}_x^{(i)}, \hat{F}_y^{(i)}, \hat{F}_z^{(i)})$, is optically pumped in the direction x of the magnetic bias field B. In the limit where the magnitude of the mean longitudinal spin $J_x = |\langle \hat{J}_x \rangle|$ far exceeds the transverse collective spin components, $\hat{J}_y$ and $\hat{J}_z$, the latter can be mapped to the harmonic oscillator variables $\hat{X}_S = \hat{J}_z/\sqrt{\hbar J_x}$ and $\hat{P}_S = -\hat{J}_y/\sqrt{\hbar J_x}$, satisfying the canonical commutation relation $[\hat{X}_S, \hat{P}_S] = i$ (ref. [34]). The transverse components precess around the magnetic field at the Larmor frequency $\omega_S \propto B$ according to $\hat{H}_S = -\hbar\omega_S \hat{J}_x \approx -\hbar\omega_S J_x + (\hbar\omega_S/2)(\hat{X}_S^2 + \hat{P}_S^2)$, where the first term is a constant offset.

Since the optical pumping prepares the collective spin near the energetically highest Zeeman state, the collective spin realizes a negative-mass oscillator, that is, $\omega_S < 0$ (ref. [13]), with a counter-rotating trajectory (Fig. 1a). The 'negative mass' terminology arises by analogy to the standard harmonic oscillator Hamiltonian $\hat{H} = m\omega^2\hat{X}^2/2 + \hat{P}^2/(2m)$, in which the sign of the

[1]Niels Bohr Institute, University of Copenhagen, Copenhagen, Denmark. [2]Present address: ICFO - Institut De Ciencies Fotoniques, The Barcelona Institute of Science and Technology, Castelldefels, Spain. [3]Present address: Pritzker School of Molecular Engineering, University of Chicago, Chicago, IL, USA. [4]Present address: Danish Fundamental Metrology, Hørsholm, Denmark. [5]These authors contributed equally: Rodrigo A. Thomas, Michał Parniak, Christoffer Østfeldt, Christoffer B. Møller. ✉e-mail: polzik@nbi.ku.dk

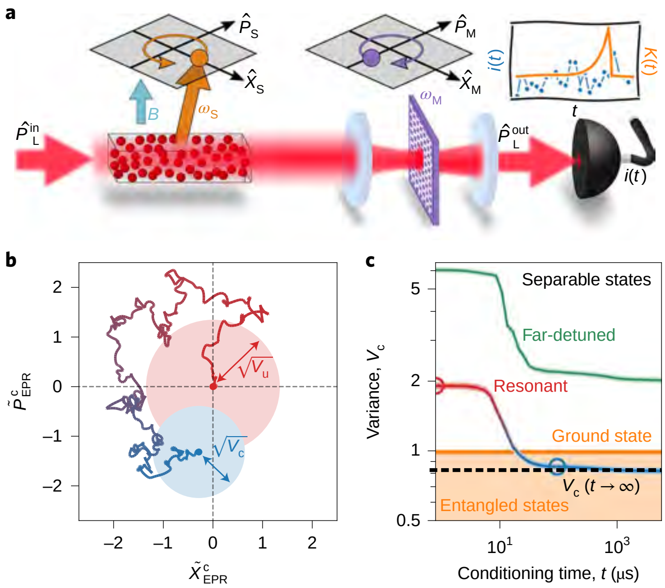

Fig. 1 | Tracking of the EPR oscillator. a, A simplified schematic of the entangled system, consisting of an atomic spin ensemble and a mechanical oscillator in a cavity, separated from the atoms by a 1 m distance, and probed by light in a cascaded manner. Phase spaces and the evolution for the spin $(\hat{X}_S, \hat{P}_S)$ and mechanical $(\hat{X}_M, \hat{P}_M)$ quantum degrees of freedom are shown above the respective systems. The measurement photocurrent $i(t)$ is convolved with a Wiener filter $K(t', t)$ (approximate envelope shown in the inset), to yield a conditional trajectory. **b**, Quantum phase-space trajectory of an EPR-entangled oscillator pair along with deterministic variance of the estimate $V_u = 1.91 \pm 0.05$ for $t = 0$ (red) and the approximately final conditional variance of $V_c = 0.83 \pm 0.02$ at $t = 110$ μs (blue). **c**, Evolution of the conditional variance V_c for the resonant (red to blue) and far-detuned (green), that is, for a joint and spectrally separated oscillators, respectively. The circle marks the variance at the end of the trajectory in **b**. The shaded areas mark the 1σ uncertainty of V_c.

mass m determines that of both the potential and kinetic energies, as does the sign of ω_S in $\hat{H}_S$.

Trajectory of an entangled EPR pair

Fundamentally, the non-commuting quadratures of motion $[\hat{X}_j(t), \hat{P}_j(t)] = i$ for the individual systems (where $j \in$ {S,M} labels spin and mechanics) cannot be known simultaneously with arbitrary precision due to the Heisenberg uncertainty principle; in particular, $\mathrm{Var}[\hat{X}_j] + \mathrm{Var}[\hat{P}_j] \geq 1$. This limit is enforced by the QBA of the meter field (for example, light) on the measured oscillator.

Such a limit does not apply to a commuting combination of variables such as $[\hat{X}_{EPR}, \hat{P}_{EPR}] \equiv [(\hat{X}_M - \hat{X}_S)/\sqrt{2}, (\hat{P}_M + \hat{P}_S)/\sqrt{2}] = 0$, that is, the sum of variances is no longer bounded from below. In fact, $V = \mathrm{Var}[\hat{X}_{EPR}] + \mathrm{Var}[\hat{P}_{EPR}] < 1$ (ref. [35]) implies entanglement between systems S and M, which is analogous to violating the single-system limit with the EPR variables. Since the EPR variables describe spatially separated systems, this effective oscillator is non-local.

We entangle the two oscillators by a back-action-evading collective position measurement. For matched frequencies, $-\omega_S = \omega_M \equiv \omega > 0$, the negative-mass spin oscillator's response to the perturbing optical field happens with a phase opposite to that of the positive-mass oscillator. The resulting information written onto the optical meter phase is $\hat{P}_L^{out} \propto \hat{X}_{EPR}(t) = \cos\omega t \hat{X}_{EPR}(0) + \sin\omega t \hat{P}_{EPR}(0)$, and thus only depends on the initial values of $\hat{X}_j$ and $\hat{P}_j$, in the absence of damping and intrinsic oscillator noise. Thus, under ideal conditions, the joint measurement on an EPR-entangled system produces a noiseless trajectory of one oscillator in the reference frame of the other[13].

In quantum theory, those trajectories arise as the expectation values of the dynamical variables with respect to the conditional quantum state $\hat{\rho}_c(t)$, that is, incorporating the information contained in the measurement record obtained at times $t' < t$. Tracking the conditional state evolution is relatively straightforward in the present case of Gaussian states, dynamics and measurements (Supplementary Section C), where $\hat{\rho}_c(t)$ is characterized solely by its first and second moments, which may be extracted by linear filtering of past measurement outcomes[36,37]. Optimal filter functions are determined from the equations of motion, noise statistics and the input–output relations for the light fields. The optimal filter that takes into account data from a time period [0, t] to estimate, for example, $\hat{X}_{EPR}$ is called the Wiener filter, a version of the Kalman filter widely used for state estimation[38]. In the simplest case, the filter envelope is an exponential with the rate defined by decoherence and readout processes, as pictorially shown in the inset in Fig. 1a. Such exponential filtering has been used in, for example, refs. [18,39]. From the Wiener filter K_X for $\hat{X}_{EPR}$ the conditional quadrature is obtained as

$$X^c_{EPR}(t) = \int_0^t dt' \, K_X(t' - t, t) i(t'), \qquad (1)$$

where $i(t)$ is the instantaneous photocurrent obtained by the homodyne detection of the optical quadrature $\hat{P}_L^{out}(t)$ of the transmitted light. To obtain the exact Wiener filter, we solve the Wiener–Hopf equations (Supplementary Section C), which involve the cross-correlation $C_{Xi}(t)$ between the oscillator signal $\hat{X}_{EPR}$ and $i(t)$ as well as $C_{ii}(t)$, the autocorrelation of $i(t)$.

The variance of the conditional state, the residual uncertainty in our knowledge about the system, is deterministic and given by $\mathrm{Var}_c[\hat{X}_{EPR}](t) \equiv \mathrm{Var}[\hat{X}_{EPR}(t) - X^c_{EPR}(t)] = \mathrm{Var}[\hat{X}_{EPR}] - \mathrm{Var}[X^c_{EPR}(t)]$, that is, the difference between the unconditional (steady-state) variance $\mathrm{Var}[\hat{X}_{EPR}]$ and the (ensemble) variance of our optimal estimate $\mathrm{Var}[X^c_{EPR}(t)] = \int_0^t dt' \, K_X(-t', t) C_{Xi}(t')$ (Supplementary Section C). We calculate $\mathrm{Var}[\hat{X}_{EPR}]$ and $C_{Xi}(t)$ using fitted model parameters. In this manner, a complete set of second moments and the full conditional covariance matrix for $(\hat{X}_{EPR}, \hat{P}_{EPR})$ are found. The raw experimental photocurrent $i(t)$ is used to obtain the stochastic first moments, fully defining the Gaussian state. $\mathrm{Var}[\hat{X}_{EPR}]$ contains contributions due to imperfect QBA cancellation and thermal fluctuations, but if the correlation of $\hat{X}_{EPR}$ with X^c_{EPR} is strong enough, it leads to entanglement as witnessed by $\mathrm{Var}_c[\hat{X}_{EPR}](t)$. Qualitatively speaking, conditioning suppresses the thermal noise.

We use Wiener filtering to continuously track the EPR oscillator $(\hat{X}_{EPR}, \hat{P}_{EPR})$ by inferring the conditional expectation values $X^c_{EPR} \approx (X^c_M - X^c_S)/\sqrt{2}$ and $P^c_{EPR} \approx (P^c_M + P^c_S)/\sqrt{2}$ (optimal weights of M and S variables are determined by the full model as presented in Supplementary Section D). Demodulating $i(t)$ with $\cos\omega t$ and $\sin\omega t$, respectively, we obtain the conditional system quadratures $(\tilde{X}^c_{EPR}, \tilde{P}^c_{EPR})$, describing the rotating-frame dynamics of the EPR-entangled system (Fig. 1b). As the conditioning progresses, we obtain a more precise estimate of the conditional system state, as witnessed by the decreasing conditional variance shown in Fig. 1c. In the long-conditioning-time limit, maximum information is extracted from past measurements, and the shape of the Wiener filter attains its steady-state form, $K(t' - t, t) \to K(t' - t)$. The corresponding steady-state conditional variance that we observe for a near-resonant case $(\omega_M \approx -\omega_S)$ is $V_c = \mathrm{Var}_c[\hat{X}_{EPR}] + \mathrm{Var}_c[\hat{P}_{EPR}] = 0.83 \pm 0.02 < 1$, certifying entanglement of the spin and mechanics. This can be directly compared with a case where the frequencies of the systems are not matched, and consequently the best value $V_c = 2.02 \pm 0.03$ is above the

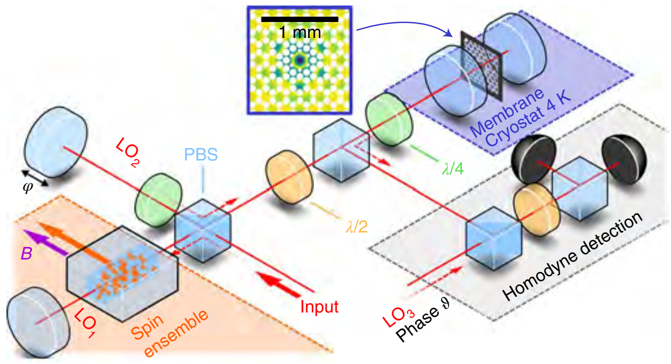

Fig. 2 | Experimental set-up for hybrid entanglement generation. The local oscillator LO_1 reads out the spin system precessing in the magnetic field B, with the quantum sideband fields written into the orthogonal light polarization. After splitting off LO_1, LO_2, phase shifted by φ relative to LO_1, is mixed with the sidebands. After projection into a common polarization, this light is sent to the mechanical system, which is probed in reflection. Final homodyne measurement of the cascaded hybrid system is performed with LO_3, with phase ϑ. $\lambda/2$, half-wave plate; $\lambda/4$, quarter-wave plate; PBS, polarizing beam splitter. See main text for details. Inset: mode shape of the mechanical mode under investigation (absolute displacement, linear scale).

entanglement limit. In the rest of the paper, we describe the experiment and analysis leading to the entanglement observation.

Experimental implementation

The layout of the hybrid system is outlined in Fig. 2 (see Supplementary Section A for further details). First, the light interacts with the collective spin of a caesium atomic ensemble, contained in a 300 μm × 300 μm × 10 mm glass cell. The spin anti-relaxation coating of the cell[40], along with magnetic shielding, provides a spin coherence lifetime of $T_2 = 0.7$ ms.

Light interacts with the spin ensemble in a double-pass configuration, thus increasing the light–spin interaction strength. The quantum operators of interest, $\hat{X}_{\rm L}^{\rm in}$ and $\hat{P}_{\rm L}^{\rm in}$, are the in-phase and in-quadrature vacuum fluctuations of the field polarized orthogonally to local oscillator 1 (LO_1). Light–matter mapping is well described by the Hamiltonian $\hat{H}_{\rm int}/\hbar \propto \sqrt{\Gamma_{\rm S}}(\hat{X}_{\rm S}\hat{X}_{\rm L} + \zeta_{\rm S}\hat{P}_{\rm S}\hat{P}_{\rm L})$, which is close to the quantum non-demolition (QND) interaction as $\zeta_{\rm S} \sim 0.03$. The interaction leads to a rotation of the input polarization state[16], with a coupling rate $\Gamma_{\rm S}/2\pi = 20$ kHz and the bandwidth $\gamma_{\rm S0}/2\pi = 1.7$ kHz (full-width at half-maximum) due to decoherence processes. The deviation from the QND interaction leads to light partially exchanging states with the oscillator[17,41], additionally broadening the spin oscillator[18] with rate $\delta\gamma_{\rm S}/2\pi \equiv 2\zeta_{\rm S}\Gamma_{\rm S} = 1.2$ kHz. The spin also couples to its own effective thermal bath with the net stochastic force $\hat{F}_{\rm S}$ originating from imperfect optical pumping, spin-exchange collisions and projection noise, resulting in the mean bath occupation $n_{\rm S} = 0.8$. After interaction with the spin system, quantum light is coupled to the mechanical oscillator (see Methods).

The mechanical oscillator is realized in a highly stressed silicon nitride membrane that is 13 nm thick and has millimetre-scale transverse dimensions. The membrane is periodically patterned, leading to the emergence of a phononic bandgap. The soft-clamped[32] mechanical mode is an out-of-plane, localized centre-of-mass vibrational mode (see inset in Fig. 2) with a frequency of $\omega_{\rm M0}/2\pi = 1.370$ MHz and a quality factor of $Q = 650 \times 10^6$, that is, a natural linewidth of $\gamma_{\rm M0}/2\pi = 2.1$ mHz, at cryogenic operating temperatures. The membrane is placed near the optical beam waist of a 2.6-mm-long cavity that has a linewidth of $\kappa/2\pi = 4.2$ MHz, and is strongly overcoupled in reflection by 93%.

The optomechanical system is mounted in a 4 K flow cryostat and optically probed. The effective thermal bath at 10 K acts as a stochastic driving force $\hat{F}_{\rm M}$ for the mechanical mode of interest. Light is detuned by $\Delta/2\pi \approx -0.7$ MHz from the cavity resonance, cooling the mechanical mode to near its motional quantum ground state with a mean phonon occupancy of roughly 2. This dynamical back-action cooling[4] broadens the mechanical response to $\gamma_{\rm M}/2\pi = 3.9$ kHz and redshifts its resonance frequency by 1 kHz to $\omega_{\rm M}/2\pi = 1.369$ MHz. The state of the mechanical system is extracted optically at a readout rate of $\Gamma_{\rm M}/2\pi = 15$ kHz.

Homodyne phase-quadrature measurement of the light reflected off the optomechanical cavity is performed with LO_3. The optical transmission between the spin and mechanical systems is $\nu = 0.53$, and the final EPR detection efficiency is $\eta = 0.77$, which includes optical losses in the path between the hybrid system and the detector and the detector quantum efficiency.

Model for the hybrid system

To construct the Wiener filter and deduce the entanglement from the data we derive the input–output relations for both systems individually and for the hybrid set-up.

The response equation for the individual oscillators is $\hat{X}_j = \chi_j[\hat{F}_j + 2\sqrt{\Gamma_j}(\hat{X}_{{\rm L},j}^{\rm in} \pm i\zeta_j\hat{P}_{{\rm L},j}^{\rm in})]$, where $\pm$ signifies ${\rm sign}(\omega_{j0})$. The effective Fourier-domain susceptibility is $\chi_{j(j0)}(\Omega) = \omega_{j0}/(\omega_j^2 - \Omega^2 - i\Omega\gamma_{j(j0)})$ including (excluding) the dynamical broadening $\delta\gamma_j \equiv \gamma_j - \gamma_{j0} = 2\zeta_j\Gamma_j$, parameterized in terms of the readout rate Γ_j and $1 > \zeta_j > -1$ (Ω is the Fourier frequency). Positive dynamical broadening $\zeta_j > 0$ provides beneficial cooling while adding extra QBA noise.

The input–output relation for the optical quadratures $\hat{\mathbf{X}}_{{\rm L},j}^{\rm in(out)} \equiv (\hat{X}_{{\rm L},j}^{\rm in(out)}, \hat{P}_{{\rm L},j}^{\rm in(out)})^\top$ probing the individual oscillators is $\hat{\mathbf{X}}_{{\rm L},j}^{\rm out} = \hat{\mathbf{X}}_{{\rm L},j}^{\rm in} + \sqrt{\Gamma_j}(\pm i\zeta_j, 1)^\top\hat{X}_j$, showing how $\zeta_j \neq 0$ entails the simultaneous mapping of the oscillator response into both light quadratures (see Supplementary Section B for details).

In the hybrid experiment light propagates from the spin ensemble to the mechanics, and the phases of the quadratures are adjusted by tuning the phase φ between LO_1 and LO_2 (Fig. 2) such that $\hat{\mathbf{X}}_{\rm L,M}^{\rm in} = -\sqrt{\nu}\hat{\mathbf{X}}_{\rm L,S}^{\rm out} + \sqrt{1-\nu}\hat{\mathbf{X}}_{{\rm L},\nu}$, where $\hat{\mathbf{X}}_{{\rm L},\nu}$ is the vacuum field due to intersystem losses $1-\nu$. Whenever $\zeta_{\rm M} \neq \zeta_{\rm S}$, a part of the spin response $\hat{X}_{\rm S}$ is mapped into the optical quadrature driving the mechanics, $\hat{X}_{\rm L,M}^{\rm in} + i\zeta_{\rm M}\hat{P}_{\rm L,M}^{\rm in}$; this enables non-local dynamical cooling of the combined EPR oscillator, a mechanism related to unconditional entanglement generation[18,21]. The EPR readout impinging on the detector is $\hat{\mathbf{X}}_{\rm L}^{\rm out} = \sqrt{\eta}\hat{\mathbf{X}}_{\rm L,M}^{\rm out} + \sqrt{1-\eta}\hat{\mathbf{X}}_{{\rm L},\eta}$, accounting for the finite EPR detection efficiency η.

Combining those relations, we obtain the EPR readout through the phase quadrature of light

$$\hat{P}_{\rm L}^{\rm out} = \hat{P}_{\rm L}^{\rm in\,\prime} + \sqrt{\eta}\left(\sqrt{\Gamma_{\rm M}}\hat{X}_{\rm M} - \sqrt{\nu\Gamma_{\rm S}}\hat{X}_{\rm S}\right) \tag{2A}$$

$$\begin{aligned}\approx \hat{P}_{\rm L}^{\rm in\,\prime} + \sqrt{\eta}\Big(&-\sqrt{\nu}\Big[\tfrac{\chi_{\rm S}}{\chi_{\rm S0}}\Gamma_{\rm M}\chi_{\rm M} + \tfrac{\chi_{\rm M}}{\chi_{\rm M0}}\Gamma_{\rm S}\chi_{\rm S}\Big]2\hat{X}_{\rm L,S}^{\rm in} \\ &+\sqrt{\Gamma_{\rm M}}\chi_{\rm M}[\hat{F}_{\rm M} + \sqrt{(1-\nu)\Gamma_{\rm M}}2\hat{X}_{{\rm L},\nu}] - \tfrac{\chi_{\rm M}}{\chi_{\rm MS}}\sqrt{\nu\Gamma_{\rm S}}\chi_{\rm S}\hat{F}_{\rm S}\Big),\end{aligned} \tag{2B}$$

where $\hat{P}_{\rm L}^{\rm in\,\prime}$ is the measurement imprecision noise including shot noise (SN) and broadband spin noise due to imperfect motional averaging[33]. The second line of equation (2B) contains the uncorrelated noise contributions driving the individual subsystems: intrinsic thermal and ground-state noise $\hat{F}_j$ and the extraneous QBA $\hat{X}_{{\rm L},\nu}$.

The thermal forces acting on subsystem j are suppressed due to the dynamical cooling $\delta\gamma_j > 0$ (contained in χ_j) occurring locally at each subsystem. Additionally, the thermal spin response $\chi_{\rm S}\hat{F}_{\rm S}$ is further

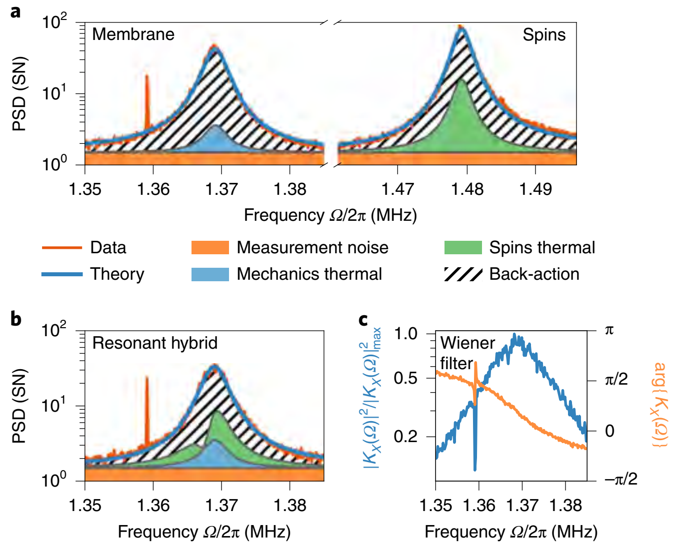

Fig. 3 | Quantum noise spectra of the hybrid system. a, Optical phase quadrature power spectral densities (PSD) for the measurements of the individual oscillators (detuned by 110 kHz), in units of shot noise (SN). The feature at ~1.359 MHz is due to laser phase noise. **b**, Joint spectrum of the EPR system for the spin oscillator tuned close to resonance with the mechanical oscillator. Notably, the relative (as well as absolute) amount of QBA noise in the joint signal is significantly reduced compared with that of the individual oscillators. **c**, Wiener filter normalized absolute square amplitude (blue, left axis) and phase (orange, right axis) for the resonant hybrid case. The filtering procedure discerns the hybrid system signal from experimental imperfections, for example, the laser phase noise peak.

suppressed by χ_M/χ_{MS} due to the non-local dynamical EPR cooling, introducing the cross-susceptibility $\chi_{MS}^{-1}(\Omega) \equiv \chi_{M0}^{-1}(\Omega) - i2\zeta_S\Gamma_M$.

The joint QBA term $\propto \hat{X}_{L,S}^{in}$ in the first line of equation (2B) embodies the central physical mechanism of our scheme resulting from the following two interfering processes: first, the spin system produces squeezed amplitude fluctuations $\hat{X}_{L,S}^{out} \sim (\chi_S/\chi_{S0})\hat{X}_{L,S}^{in}$ that map into the mechanical phase quadrature response according to $\Gamma_M\chi_M$; second, the spin QBA response $\hat{P}_{L,S}^{out} \sim \Gamma_S\chi_S\hat{X}_{L,S}^{in}$ is subsequently filtered by the mechanical system according to χ_M/χ_{M0}. We remark that the function χ_j/χ_{j0} suppresses near-resonant spectral components in a bandwidth γ_j with maximal suppression γ_{j0}/γ_j at $\Omega \sim \omega_j$ (for $\delta\gamma_j > 0$). Since $\gamma_{M0}/\gamma_M \ll 1$, this entails strong suppression of the spin QBA response, whereas the amplitude squeezing by the spin is more moderate $\gamma_{S0}/\gamma_S \approx 0.6$.

The prefactor to $\hat{X}_{L,S}^{in}$ may be rewritten as $\chi_M\chi_S/(\chi_{M0}\chi_{S0}) \times [\Gamma_M\chi_{M0} + \Gamma_S\chi_{S0}]$, highlighting the condition $\Gamma_M\chi_{M0} + \Gamma_S\chi_{S0} = 0$ for total broadband QBA cancellation (independent of dynamical broadening), which requires $\omega_M = -\omega_S$. In the case of unmatched intrinsic linewidths $\gamma_{M0} \neq \gamma_{S0}$, one still needs $\omega_M = -\omega_S$ to minimize the term. Equation (2B) demonstrates that dynamical broadening enhances QBA suppression substantially via the factors χ_j/χ_{j0}.

While QBA reduction is necessary to achieve $V < 1$, it is not sufficient, due to the inevitable presence of ground-state fluctuations contained in $\hat{F}_j$ (equation (2B)). These thermal fluctuations, along with residual QBA, can be suppressed by the conditional tracking and/or the coherent dynamical cooling mechanisms (local and non-local) discussed above; here we simultaneously employ both types of mechanism.

While equation (2) captures all essential aspects of the involved EPR dynamics, certain technical or peripheral effects were left out for simplicity. These include the finite overcoupling of the optical cavity and the option of introducing optical quadrature rotations between the subsystems as well as in the homodyne detection. Moreover, equation (2B) neglects the phase noise QBA contributions $\propto \hat{P}_{L,S}^{in}, \hat{P}_{L,\nu}$ to the EPR response, which are minor for the parameter regime considered here. The full model accounting for all the aforementioned effects was employed in analysing the experimental data (Supplementary Section B).

Back-action interference

The various noise suppression mechanisms of equation (2B) manifest themselves in the noise spectra of the optical readout $\hat{P}_L^{out}$ (Fig. 3). When the two oscillators are detuned by 110 kHz, by changing $\omega_S \propto B$, they are essentially probed separately (Fig. 3a). However, due to the finite detuning, the measurement noise for both subsystems is the sum of optical shot noise and broadband spin noise. The Lorentzian features $\propto |\chi_j|^2$ are the dynamically broadened responses to thermal noise and light QBA of the two systems. The mechanical motion is strongly dominated by QBA, its ratio to intrinsic thermal noise (TH) being QBA/TH = 19, whereas for the spin oscillator QBA/TH = 4.9.

When the spin oscillator is tuned close to the mechanical resonance (Fig. 3b), we observe strong overall noise reduction for the EPR oscillator. Firstly, the non-local dynamical cooling of the spin thermal noise amounts to a reduction of the joint noise due to stochastic forces $\hat{F}_M$ and $\hat{F}_S$ by 2.5 dB. Secondly, we observe the reduction of the QBA due to the destructive interference by 4.6 dB (striped area in Fig. 3b), compared with the sum of the QBA of the two separate systems (striped areas in Fig. 3a). As a result, the unconditional EPR variance is reduced by 5.0 dB, from 6.07 to 1.91, as has already been indicated in Fig. 1c. The asymmetrical features in Fig. 3b arise due to the small but finite spin-mechanics detuning and the choice of the LO_2 phase φ.

Conditional entanglement estimation

Having discussed the coherent suppression of the QBA and thermal noise, which reduces the unconditional EPR variance V_u in our experiment, we now return to the Wiener filtering method we apply to verify conditional entanglement $V_c < 1$. To focus on its essential properties, we here consider the QND limit $\gamma_j = \gamma_{j0}$ of equation (2).

Before considering the hybrid system, we apply the filtering method to the tracking of a single oscillator, specifically the mechanical one, by setting $\Gamma_S = 0$ (and $\Gamma_M \equiv 2\Gamma$). The same argument can be made for the tracking of the spin oscillator. In this case, the filtering reduces the variance from its unconditional value $V_u^{(1)} = (1 + 2n)(1 + 2C_q)$ to $V_c^{(1)} \approx \sqrt{1/(2\eta)}\sqrt{(\gamma/\Gamma)V_u^{(1)}} = \sqrt{1/\eta}\sqrt{1 + 1/(2C_q)}$, assuming the rotating wave approximation ($\omega \gg \gamma V_u^{(1)}, \Gamma$) and fast readout $\sqrt{8\eta V_u^{(1)}\Gamma/\gamma} \gg 1$ here and henceforth[42]. We have expressed the quantum cooperativity $C_q = \Gamma/(\gamma[2n + 1])$ in terms of the thermal bath occupancy n. Within the QND model, C_q = QBA/TH. An efficient measurement of a single system, $\eta = 1$ and $C_q \to \infty$, can bring the conditional variance to the ground-state value $V_c^{(1)} \to 1$, but not below.

In the idealized hybrid case with matched readout rates $\Gamma_M = \Gamma_S \equiv \Gamma$ and intrinsic susceptibilities $\chi_{M0} = -\chi_{S0}$ (implying $\omega_{M0} = -\omega_{S0} \equiv \omega$ and $\gamma_{M0} = \gamma_{S0} \equiv \gamma$), the tracking reduces the variance from the QBA-free unconditional value $V_u = 1 + 2n$ (where now $n = (n_S + n_M)/2$) to

$$V_c \approx \frac{1}{\sqrt{2\eta}}\sqrt{\frac{\gamma}{\Gamma}V_u} = \frac{1}{\sqrt{\eta}}\sqrt{\frac{1}{2C_q}}, \quad (3)$$

which shows that ideal QBA cancellation removes the lower bound $V_c^{(1)} \geq 1$ associated with the single-oscillator case.

It is clear from equation (3) that high QBA/TH $\gg 1$ and high efficiencies are imperative for generation of an entangled state.

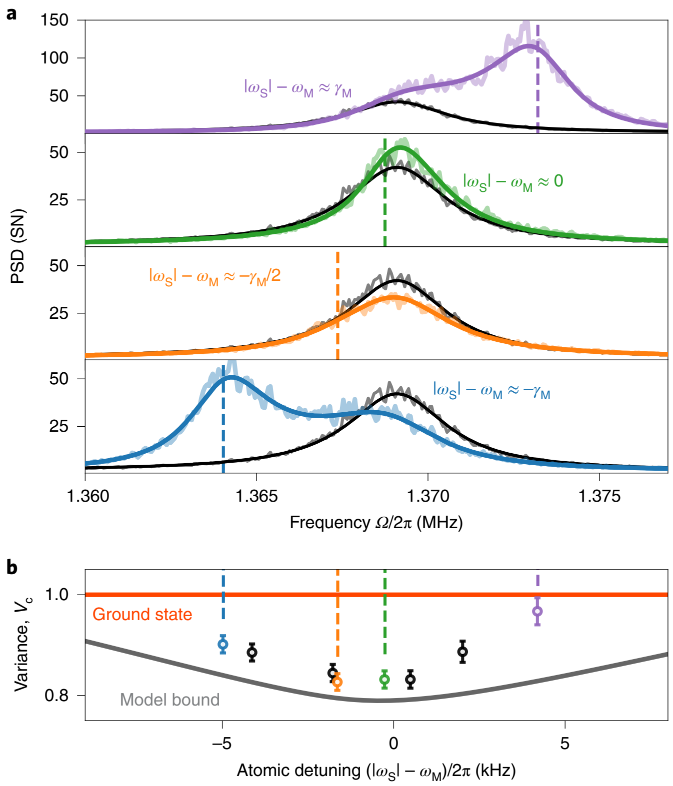

Fig. 4 | Entanglement tuning and optimization. We sweep the resonant (Larmor) frequency of the spin oscillator across the mechanical resonance. This tunes the distinguishability of the two oscillators in the measured light, thus varying the achievable conditional EPR entanglement. **a**,**b**, Spectra with respective fits (**a**) and resulting variance for different values of the mechanical–spin detuning (**b**). Black curves in **a** depict the mechanics-only spectrum. Dashed vertical lines indicate spin frequency. Grey curve in **b** depicts variances of optimized EPR combinations, calculated from theoretical spectra, given parameter values from the orange point. Excess experimental noise leads to expected deviations of this theoretical bound and experimental values. Error bars represent 1σ uncertainty of V_c, as calculated by the Markov chain Monte Carlo[47] method (see Methods). For the spectra corresponding to the black points see Supplementary Fig. 8.

Numerical simulation confirms the crucial role of those factors and shows that with an intermediate coupling strength QBA/TH ~ 1 and lower efficiencies, such as in ref. [14], entanglement generation is not possible. Key new experimental features include an enhanced quality factor of the mechanical oscillator, an enhanced spin–photon interaction due to the double pass and the overall improved efficiency of the hybrid set-up (Supplementary Table 1). The latter involves both better direct transmission efficiencies, as well as an optimized coupling of the probe beam to the collective spin mode leading to a substantial suppression of the broadband spin noise.

When applied to experimental data, the Wiener filter not only optimally discerns the EPR signal from white measurement noise, but also rejects other coloured, peaked or cross-correlated noises. Figure 3c presents the steady-state, frequency-domain Wiener filter $K_X(\Omega) \propto \int_{-\infty}^{\infty} d\tau\ \exp(i\Omega\tau)K_X(\tau)$ for the hybrid case of nearly resonant oscillators. It takes into account the full model of the joint system along with experimentally measured noise.

In the experiment, the conditional variance is determined by many factors, such as optical losses ν and η, as well as mismatched intrinsic linewidths $\gamma_{M0} \neq \gamma_{S0}$ and readout rates Γ_j. Figure 3 presents results for the case $\Gamma_M \approx \nu\Gamma_S$. Whereas in Fig. 3b we have matched frequencies $\omega_M \approx -\omega_S$, in Fig. 4a we present a series of spectra in which $|\omega_S|$ is swept through the mechanical resonance by tuning the B field. The resulting V_c for a set of such measurements (Fig. 4b) exhibits a smooth transition between the regimes of entangled and non-entangled states of the hybrid system. Notably, our system is rather resilient even to quite substantial oscillator detunings $|\omega_S| - \omega_M$. The bandwidth of V_c as a function of the detuning is affected by the readout rates, here amounting to several oscillator linewidths.

Conclusion and outlook

We have demonstrated entanglement between distant objects in a hybrid system consisting of a mechanical oscillator and an atomic spin ensemble. This constitutes a new milestone for hybrid macroscopic entanglement and for demonstration of noiseless trajectories in the negative-mass reference frame.

This enables quantum communication between distant mechanical and atomic systems using, for example, teleportation-based protocols[1], thereby adding a hitherto missing link to the hybrid systems landscape[6]. It paves the road towards, for example, an entanglement link between an electromechanically coupled superconducting qubit[43,44] and a distant atomic ensemble quantum memory. Moreover, the disparate entangled objects respond to very different perturbations and thus facilitate measurements of motion and fields with reduced quantum noise, for example, off-resonant continuous force detection in gravitational-wave interferometers[45,46], and resonant pulsed measurements based on state preparation and retrodiction[39].

Future work on enhancing entanglement and achieving practical detection of noiseless trajectories of motion will primarily concentrate on amending experimental imperfections. Specifically, a factor of 3 reduction of the broadband spin noise by better mode-matching of light to the atomic ensemble, reduction of intersystem optical losses down to 10%, improvement of cavity overcoupling to $\kappa_{in}/\kappa = 0.98$ and improvement of the fractional coherent spin readout Γ_S/γ_{S0} by a factor of 3 will lead to $V_c \approx 0.3$ (−5 dB) according to our model.

Online content

Any methods, additional references, Nature Research reporting summaries, source data, extended data, supplementary information, acknowledgements, peer review information; details of author contributions and competing interests; and statements of data and code availability are available at https://doi.org/10.1038/s41567-020-1031-5.

Received: 1 April 2020; Accepted: 6 August 2020;
Published online: 21 September 2020

References

1. Horodecki, R., Horodecki, P., Horodecki, M. & Horodecki, K. Quantum entanglement. *Rev. Mod. Phys.* **81**, 865–942 (2009).
2. Degen, C. L., Reinhard, F. & Cappellaro, P. Quantum sensing. *Rev. Mod. Phys.* **89**, 035002 (2017).
3. Chen, Y. Macroscopic quantum mechanics: theory and experimental concepts of optomechanics. *J. Phys. B* **46**, 104001 (2013).
4. Aspelmeyer, M., Kippenberg, T. J. & Marquardt, F. Cavity optomechanics. *Rev. Mod. Phys.* **86**, 1391–1452 (2014).
5. Kimble, H. J. The quantum internet. *Nature* **453**, 1023–1030 (2008).
6. Kurizki, G. et al. Quantum technologies with hybrid systems. *Proc. Natl. Acad. Sci. USA* **112**, 3866–3873 (2015).
7. Cirac, J. I. & Zoller, P. Quantum computations with cold trapped ions. *Phys. Rev. Lett.* **74**, 4091–4094 (1995).
8. Gross, C. & Bloch, I. Quantum simulations with ultracold atoms in optical lattices. *Science* **357**, 995–1001 (2017).
9. Brown, K. R., Kim, J. & Monroe, C. Co-designing a scalable quantum computer with trapped atomic ions. *npj Quant. Inf.* **2**, 16034 (2016).
10. Hammerer, K., Aspelmeyer, M., Polzik, E. S. & Zoller, P. Establishing Einstein-Poldosky-Rosen channels between nanomechanics and atomic ensembles. *Phys. Rev. Lett.* **102**, 020501 (2009).

11. Manukhova, A. D., Rakhubovsky, A. A. & Filip, R. Pulsed atom-mechanical quantum non-demolition gate. *npj Quant. Inf.* **6**, 4 (2020).
12. Julsgaard, B., Kozhekin, A. & Polzik, E. S. Experimental long-lived entanglement of two macroscopic objects. *Nature* **413**, 400–403 (2001).
13. Polzik, E. S. & Hammerer, K. Trajectories without quantum uncertainties. *Ann. Phys.* **527**, A15–A20 (2015).
14. Møller, C. B. et al. Quantum back-action-evading measurement of motion in a negative mass reference frame. *Nature* **547**, 191–195 (2017).
15. Tsang, M. & Caves, C. M. Coherent quantum-noise cancellation for optomechanical sensors. *Phys. Rev. Lett.* **105**, 123601 (2010).
16. Hammerer, K., Sørensen, A. S. & Polzik, E. S. Quantum interface between light and atomic ensembles. *Rev. Mod. Phys.* **82**, 1041–1093 (2010).
17. Muschik, C. A., Polzik, E. S. & Cirac, J. I. Dissipatively driven entanglement of two macroscopic atomic ensembles. *Phys. Rev. A* **83**, 052312 (2011).
18. Krauter, H. et al. Entanglement generated by dissipation and steady state entanglement of two macroscopic objects. *Phys. Rev. Lett.* **107**, 080503 (2011).
19. Stannigel, K., Rabl, P. & Zoller, P. Driven-dissipative preparation of entangled states in cascaded quantum-optical networks. *New J. Phys.* **14**, 063014 (2012).
20. Vasilyev, D. V., Muschik, C. A. & Hammerer, K. Dissipative versus conditional generation of Gaussian entanglement and spin squeezing. *Phys. Rev. A* **87**, 053820 (2013).
21. Huang, X. et al. Unconditional steady-state entanglement in macroscopic hybrid systems by coherent noise cancellation. *Phys. Rev. Lett.* **121**, 103602 (2018).
22. Tsang, M. & Caves, C. M. Evading quantum mechanics: engineering a classical subsystem within a quantum environment. *Phys. Rev. X* **2**, 031016 (2012).
23. Kohler, J., Gerber, J. A., Dowd, E. & Stamper-Kurn, D. M. Negative-mass instability of the spin and motion of an atomic gas driven by optical cavity backaction. *Phys. Rev. Lett.* **120**, 013601 (2018).
24. Karg, T. M. et al. Light-mediated strong coupling between a mechanical oscillator and atomic spins 1 meter apart. *Science* **369**, 174–179 (2020).
25. Jöckel, A. et al. Sympathetic cooling of a membrane oscillator in a hybrid mechanical–atomic system. *Nat. Nanotechnol.* **10**, 55–59 (2015).
26. Christoph, P. et al. Combined feedback and sympathetic cooling of a mechanical oscillator coupled to ultracold atoms. *New J. Phys.* **20**, 093020 (2018).
27. Tan, H., Buchmann, L. F., Seok, H. & Li, G. Achieving steady-state entanglement of remote micromechanical oscillators by cascaded cavity coupling. *Phys. Rev. A* **87**, 022318 (2013).
28. Woolley, M. J. & Clerk, A. A. Two-mode back-action-evading measurements in cavity optomechanics. *Phys. Rev. A* **87**, 063846 (2013).
29. Ockeloen-Korppi, C. F. et al. Stabilized entanglement of massive mechanical oscillators. *Nature* **556**, 478–482 (2018).
30. Riedinger, R. et al. Remote quantum entanglement between two micromechanical oscillators. *Nature* **556**, 473–477 (2018).
31. Lee, K. C. et al. Entangling macroscopic diamonds at room temperature. *Science* **334**, 1253–1256 (2011).
32. Tsaturyan, Y., Barg, A., Polzik, E. S. & Schliesser, A. Ultracoherent nanomechanical resonators via soft clamping and dissipation dilution. *Nat. Nanotechnol.* **12**, 776–783 (2017).
33. Borregaard, J. et al. Scalable photonic network architecture based on motional averaging in room temperature gas. *Nat. Commun.* **7**, 11356 (2016).
34. Holstein, T. & Primakoff, H. Field dependence of the intrinsic domain magnetization of a ferromagnet. *Phys. Rev.* **58**, 1098–1113 (1940).
35. Duan, L.-M., Giedke, G., Cirac, J. I. & Zoller, P. Inseparability criterion for continuous variable systems. *Phys. Rev. Lett.* **84**, 2722–2725 (2000).
36. Müller-Ebhardt, H. et al. Quantum-state preparation and macroscopic entanglement in gravitational-wave detectors. *Phys. Rev. A* **80**, 043802 (2009).
37. Rossi, M., Mason, D., Chen, J. & Schliesser, A. Observing and verifying the quantum trajectory of a mechanical resonator. *Phys. Rev. Lett.* **123**, 163601 (2019).
38. Wieczorek, W. et al. Optimal state estimation for cavity optomechanical systems. *Phys. Rev. Lett.* **114**, 223601 (2015).
39. Wasilewski, W. et al. Quantum noise limited and entanglement-assisted magnetometry. *Phys. Rev. Lett.* **104**, 133601 (2010).
40. Balabas, M. V. et al. High quality anti-relaxation coating material for alkali atom vapor cells. *Opt. Express* **18**, 5825–5830 (2010).
41. Geremia, J. M., Stockton, J. K. & Mabuchi, H. Tensor polarizability and dispersive quantum measurement of multilevel atoms. *Phys. Rev. A* **73**, 042112 (2006).
42. Lammers, J. *State Preparation and Verification in Continuously Measured Quantum Systems*. PhD thesis, Leibniz University Hannover (2018).
43. Higginbotham, A. P. et al. Harnessing electro-optic correlations in an efficient mechanical converter. *Nat. Phys.* **14**, 1038–1042 (2018).
44. Mirhosseini, M., Sipahigil, A., Kalaee, M. & Painter, O. Quantum transduction of optical photons from a superconducting qubit. Preprint at https://arxiv.org/abs/2004.04838 (2020).
45. Khalili, F. Y. & Polzik, E. S. Overcoming the standard quantum limit in gravitational wave detectors using spin systems with a negative effective mass. *Phys. Rev. Lett.* **121**, 031101 (2018).
46. Zeuthen, E., Polzik, E. S. & Khalili, F. Y. Gravitational wave detection beyond the standard quantum limit using a negative-mass spin system and virtual rigidity. *Phys. Rev. D* **100**, 062004 (2019).
47. Foreman-Mackey, D., Hogg, D. W., Lang, D. & Goodman, J. emcee: The MCMC hammer. *Publ. Astron. Soc. Pac.* **125**, 306–312 (2013).

Publisher's note Springer Nature remains neutral with regard to jurisdictional claims in published maps and institutional affiliations.

Methods

Coupling quantum optical signal from atoms to the mechanics. The LO_1 is filtered out after interacting with the spin, and the quantum optical signal emerging from the spin is spatially overlapped with LO_2. We mix the quantum signal with LO_2 in the same polarization with a waveplate and a polarizing beam splitter. This directly translates the optical polarization quadrature operators that interacted with the spin system into the amplitude and phase optical quadratures that are now coupled to the membrane-in-the-middle optomechanical system. The radiation pressure of those quadratures drives the mechanical oscillator[4] (Fig. 2).

Uncertainty estimation of conditional variance. Using the entire set of measurements we evaluated the uncertainty of the final result for V_c as further discussed in Supplementary Section E. We established priors for all experimental parameters by independent measurements, and used Markov chain Monte Carlo (MCMC) simulations[47] and log-likelihood optimization to obtain fit parameters and their uncertainties, in particular obtaining the uncertainty for the conditional EPR variance.

We calculated 1,000 values of V_c from a sub-sample of MCMC points, and found the mean and standard deviation for each spin–mechanics detuning, as shown in Supplementary Fig. 8.

Data availability

Data that support the plots within this paper and other findings of this study are available from the corresponding author upon reasonable request. Source data are provided with this paper.

Acknowledgements

We acknowledge conversations with K. Hammerer and J. H. Müller. X. Huang contributed theoretical simulations in the early stages of the project. We acknowledge M. Balabas for fabricating the coated caesium cells. This project has been supported by the European Research Council Advanced grant QUANTUM-N, the Villum Foundation and John Templeton Foundation. E.Z. acknowledges funding from the Carlsberg Foundation. M.P. was partially supported by the Foundation for Polish Science (FNP). R.A.T. was partially funded by the programme Science without Borders of the Brazilian Federal Government.

Author contributions

E.S.P. conceived and led the project. R.A.T., C.B.M., C.Ø. and M.P. built the experiment with the help of C.B. and J.A. The membrane resonator was conceived by A.S. and Y.T. designed and fabricated the device. R.A.T., M.P., C.Ø., C.B.M. and C.B. collected the data. E.Z. and M.P. developed the theory with input from J.A., E.S.P. and R.A.T. The paper was written by E.S.P., E.Z., R.A.T., M.P., C.Ø., C.B.M. and C.B., with contributions from other authors.

Competing interests

The authors declare no competing interests.

Additional information

Supplementary information is available for this paper at https://doi.org/10.1038/s41567-020-1031-5.

Correspondence and requests for materials should be addressed to E.S.P.

nature research
https://doi.org/10.1038/s41567-020-1031-5

Supplementary information

Entanglement between distant macroscopic mechanical and spin systems

In the format provided by the authors and unedited

Supporting Information

Entanglement between Distant Macroscopic Mechanical and Spin Systems

Rodrigo A. Thomas,* Michał Parniak,* Christoffer Østfeldt,* Christoffer B. Møller,*,† Christian Bærentsen, Yeghishe Tsaturyan,‡ Albert Schliesser, Jürgen Appel,§ Emil Zeuthen, and Eugene S. Polzik¶
Niels Bohr Institute, University of Copenhagen, Copenhagen, Denmark

CONTENTS

Appendix A: Experimental setup

1. Atomic spins

The atomic spin oscillator is prepared in a 50 °C warm ensemble of caesium atoms, confined in a spin anti-relaxation-coated microcell [1] (300 µm × 300 µm cross-section and 10 mm in length). The natural linewidth, in the absence of light, is $\gamma_{\mathrm{S0,dark}} = 1/(\pi T_2) = 450\,\mathrm{Hz}$, as measured by pulsed Magneto-Optical Resonance Signal (MORS) [2].

The microcell is positioned in a magnetic shield equipped with coils producing a homogeneous magnetic bias field orthogonal to the probe direction, and a heater to keep the interior at the desired temperature, effectively determining the total atom number. The magnetic field direction sets the quantization axis, denoted as the x-direction. The high thermal mass of the shield ensures a stable temperature throughout the experimental trials. The resonance frequency of the spin $|\omega_{\mathrm{S}}|$, i.e., the Larmor frequency, is controlled by the magnitude of the magnetic field.

The atoms travel through a Gaussian mode of the probe laser focused at the center of the microcell, with the beam waist ($w_0 \approx 80\,\mu\mathrm{m}$) optimised to maximise the filling factor without incurring extra optical losses. The laser frequency is blue-detuned by 3 GHz from the $F = 4 \to F' = 5$ D_2 transition. Even at this detuning the tensor interaction is non-negligible, which requires a careful choice of the input linear polarisation. The chosen polarisation is at the angle $\alpha \approx (60 \pm 2)^\circ$ with respect to the magnetic field such that the tensorial Stark shifts induced by the probe cancel the quadratic Zeeman splitting $\omega_{\mathrm{qzs}}/2\pi = 400\,\mathrm{Hz}$, as described by the atomic polarisability tensor (see Supplementary Information (SI) B 1 for more details).

The standard quantum Stokes variables $\hat{S}_x, \hat{S}_y, \hat{S}_z, \hat{S}_0$ – representing the light electric field in terms of its linear, diagonal, and circular polarisation states [3] and the total intensity – are redefined as $\{\hat{S}_\parallel = \hat{S}_x \cos 2\alpha - \hat{S}_y \sin 2\alpha, \hat{S}_\perp = \hat{S}_x \sin 2\alpha + \hat{S}_y \cos 2\alpha, \hat{S}_z, \hat{S}_0\}$. When mapping the polarisation variables into quadrature variables, we choose the parallel component as the classical variable – the local oscillator LO_1 with the photon flux $\langle \hat{S}_\parallel \rangle = \langle \hat{S}_0 \rangle = S_\parallel$, leaving

$\hat{S}_\perp, \hat{S}_z$ as quantum variables. We define the light quadratures as $\hat{X}_\mathrm{L} = \hat{S}_z/\sqrt{S_\parallel}$ and $\hat{P}_\mathrm{L} = -\hat{S}_\perp/\sqrt{S_\parallel}$. The photon flux determines the readout rate $\Gamma_\mathrm{S}/2\pi \propto J_x S_\parallel$ and the power broadening decoherence rate $\gamma_\mathrm{pb}/2\pi \propto S_\parallel$. In the experiment, the LO$_1$ power is $\sim 350\,\mu\mathrm{W}$. The decoherence rate of the oscillator is also affected by the optical pumping process, represented by the contribution γ_op. The total bandwidth of the spin resonance in the absence of dynamical processes is $\gamma_\mathrm{S0} = \gamma_\mathrm{S0,dark} + \gamma_\mathrm{pb} + \gamma_\mathrm{op}$. For the conditions of the current experiment, the ratio of quantum backaction to thermal noise contributions is QBA/TH = 4.9.

As the atoms move in and out of the beam, the scattered photons couple to various atomic motional modes. The motion of the atoms is fast (flight-through time $\sim$1 µs) and uncorrelated, leading to a motionally averaged coupling [4]. Phenomenologically, the long-lived correlations give rise to the mean spin mode – the mode of interest – and the short-time correlations to an uncorrelated spin contribution – the broadband spin mode. In the regime of operation both optical responses are harmonic, with the susceptibility of short-time correlations following a low-Q damped harmonic oscillator type, with resonance frequency Ω_S and linewidth $\gamma_\mathrm{bb}/2\pi \sim 1\,\mathrm{MHz}$ and coupling rate $\Gamma_\mathrm{S,bb}$.

We observe the response of the two spin modes to coherent drive tones $\hat{X}^\mathrm{drive}_\mathrm{L,S}$ in Figures SI1(a) and SI1(b) for different input modulation types $\hat{X}^\mathrm{drive}_\mathrm{L,S} = \hat{X}^\mathrm{in}_\mathrm{L,S}\cos\vartheta_\mathrm{in} + \hat{P}^\mathrm{in}_\mathrm{L,S}\sin\vartheta_\mathrm{in}$, measured by Coherent Induced FAraday Rotation (CIFAR) [5], a calibration technique which is inspired by the OptoMechanically Induced Transparency (OMIT) [6]. In short, CIFAR references the phase-sensitive response of the spin to an oscillating input polarisation at ω_RF; to the first order, the resulting interference between the drive and response, for $\Gamma_\mathrm{S}/\gamma_S \gg 1$ and $\vartheta_\mathrm{in} = \pm\pi/4$, gives rise to a dispersive feature in the detected field, with maximum destructive interference at $\pm\Gamma_\mathrm{S}$ away from $|\omega_\mathrm{S}|$. Under the assumption that both modes are uncorrelated, we fit these data to the input-output relations (equation (SI B.14)), allowing us to extract the readout rate Γ_S. The backaction on the broadband mode is negligible, i.e., $\Gamma_\mathrm{S,bb}/\gamma_\mathrm{S,bb} \ll 1$. For all noise spectra, we treat the broadband contribution as constant in the frequency range of interest, added incoherently with all other noise processes; effectively, it acts as added phase noise in the phase quadrature of light. The added spectral power at the resonance frequency due to extra spin noise, corrected for losses, is $\overline{S}_\mathrm{S,bb} = 1.68$ SN units. This noise depends on spatial properties of the beam and could be reduced by using a cell with larger cross section perfectly filled with a flat-top probe laser beam.

The spin oscillator is prepared by optically pumping the ensemble towards the $|F=4, m_F=4\rangle$ Zeeman sublevel. A repump laser is tuned to the $F=3 \rightarrow F'=2$ hyperfine transition in the D$_2$ line and a pump laser to the $F=4 \rightarrow F'=4$ hyperfine transition in the D$_1$ line, both circularly polarised. The pump laser directly couples to the coherences of interest, competing with the decoherence and depumping caused by the probe, adding $\gamma_\mathrm{op}/2\pi \sim 1\,\mathrm{kHz}$. The spin polarisation $p = 0.82 \pm 0.01$ is characterised by pulsed MORS [2], with the spectrum shown in Figure SI1(c). Due to the dominant role of the probing and pumping lasers, the Zeeman population distribution does not follow the spin temperature model. The fitting model follows Eq. (17) from Ref. [2] for arbitrary Zeeman population distribution. The spin polarisation is determined by assuming that the population of $|F=4, m_F=-4\rangle$ is negligible, which is guaranteed by the presence of the resonant pump laser. The spin oscillator variables $\hat{X}_\mathrm{S} = \hat{J}_z/\sqrt{\hbar J_x}$ and $\hat{P}_\mathrm{S} = -\hat{J}_y/\sqrt{\hbar J_x}$ are defined according to the steady-state spin polarisation, which defines J_x. From the population distribution we calculate the variance of the spin components, which leads to the added spin thermal occupancy $n_\mathrm{S} = 0.8$, meaning that incoherent processes drive towards an equilibrium with $\mathrm{Var}[\hat{X}_\mathrm{S}] = \mathrm{Var}[\hat{P}_\mathrm{S}] = n_\mathrm{S} + 1/2$.

The spin system can be operated in two regimes, which differ only by their effective masses. Optical pumping of the atoms to the highest energy state, i.e. spins aligned parallel with the bias magnetic field, leads to an effective negative mass, whereas pumping to the lowest energy state, i.e. spin aligned anti-parallel to the bias field, leads to an effective positive mass [7]. This choice defines the sign of the atomic susceptibility χ_S.

2. Optomechanics

The optomechanical system consists of a 13 nm thick, highly stressed, phononically patterned silicon nitride membrane featuring a soft-clamped [8], localised out-of-plane vibrational mechanical mode with a cryogenic Q-factor of 0.65×10^9 and resonance frequency of 1.37 MHz. This membrane is positioned close to the waist of a 2.6 mm long optical cavity along its axis and with maximum spatial overlap between the cavity mode and the localised mechanical mode. The cavity consists of two mirrors with 25 mm radius of curvature, and power transmissions of 20 ppm and 360 ppm, respectively. The entire optomechanical assembly is placed in a liquid helium flow cryostat, which is cooled to 4.4 K.

The basis of the light-mechanics coupling is the radiation pressure force of light on the membrane whose out-of-plane motion causes a dispersive shift of the cavity resonance frequency [9]. The placement of the membrane inside the cavity divides it into two sub-cavities, where the amount of light in each depends on the membrane position.

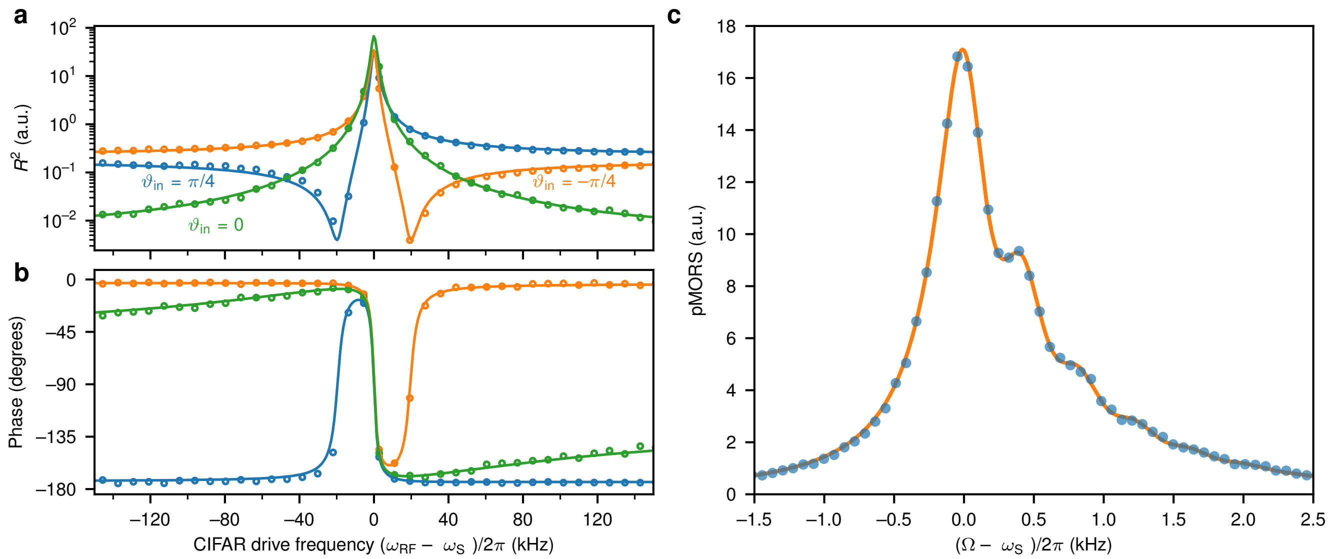

Figure SI1. **Spin oscillator calibrations.** **a** and **b** show the square amplitude (R^2) and phase of the demodulated spin response to a coherently driven light field with different $\theta_{\rm in}$. **c,** pulsed MORS spectrum for the distribution of atoms in the Zeeman levels corresponding to $p = 0.82 \pm 0.01$.

This system can be formally treated as a canonical end-mirror optomechanical system with just a single intracavity optical field. In this formalism adjusting the lengths of each subcavity, periodically modulates the canonical cavity parameters of optical linewidth, κ, resonance frequency, overcoupling $\kappa_{\rm in}/\kappa$ (where $\kappa_{\rm in}$ is the coupling rate of the input mirror), as well as the optomechanical single-photon coupling rate g_0.

The sub-cavities can be independently and electronically fine-tuned so as to simultaneously realise a high cooperativity optomechanical system, as well as tunability, in order to set an appropriate cavity detuning with respect to the probe of the atomic spin system. The various canonical optomechanical parameters are characterised through several independent measurements and a full list of these system parameters can be seen in Table SI1.

The cavity linewidth is characterised first by measuring the optical amplitude quadrature beatnote of a phase-modulation sideband transmitted through the cavity. In a second method, a single carrier is scanned across the cavity resonance on a timescale comparable to the cavity response time and the resultant beating ringdown signal is observed.

The cavity detuning is determined by combining the characterisation of the cavity dither lock error signal and knowledge of the cavity linewidth. By locating the turning point of the dither error signal we translate our locked error signal amplitude into an absolute detuning.

The effective mechanical bath temperature and field-enhanced optomechanical coupling rate $g = g_0|\alpha|$, where α is intra-cavity field, can be obtained by fitting the full optomechanical model to the ponderomotive squeezing spectra, seen in Fig. SI2. These spectra result from pumping the cavity from the high-reflector port and detecting the optical amplitude quadrature in transmission through the highly overcoupled port [10]. We fit the model to these two spectra simultaneously, using separately measured values for Δ, κ, and Q. From this characterisation the detection efficiency, with and without LO_3, can similarly be inferred. We observed up to 3 dB of ponderomotive squeezing. We note that while our system is not optimised for measuring maximum ponderomotive squeezing, nor operated in the optimum regime, we observe close to record amounts of squeezing for optomechanical systems.

A new feature of our optomechanical cavity compared to our previous work [7] is the full electronic control over the position of the membrane inside the standing wave of the cavity. Two piezos, each with an effective travel length of well over a half-wavelength at cryogenic conditions, allow us to scan the lengths of the two sub-cavities, so as to effectively position the membrane at any given intra-cavity position while keeping the cavity on resonance with the optical light field. By monitoring the cavity transmission as we scan the position of the membrane, we obtain knowledge about the position within the standing wave. We operate the optomechanical system at the point of highest total cavity linewidth, giving us the best overcoupling in reflection, as well as a high coupling rate g_0.

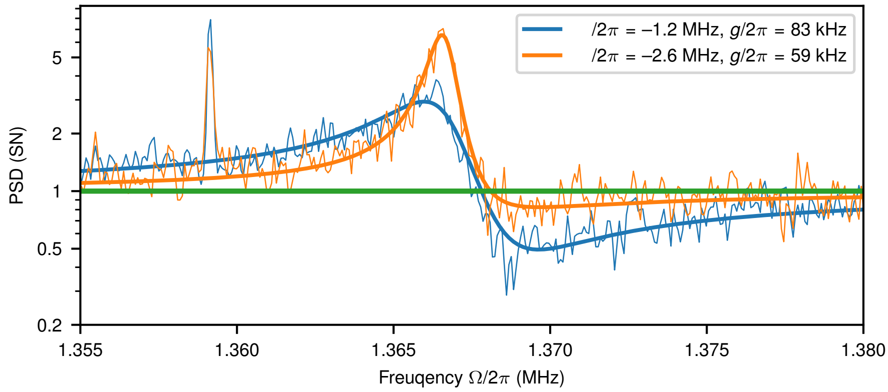

Figure SI2. **Ponderomotive squeezing spectra for different cavity detunings.** From these spectra we infer g, T, optical losses in the detection path etc. See SI A 2 for details. Using other system parameters, measured independently, we obtain an effective bath temperature of $T = (11.4 \pm 0.5)\,\mathrm{K}$.

3. Hybrid system matching & homodyne detection

The overall hybrid system consists of the cascaded optical readout of the spin and mechanical system by an itinerant light field, as outlined in the main text, see Fig. 2.

After interacting with the spin, LO_1 is filtered off the quantum signal, which is orthogonally polarisation to LO_1. The quantum signal is spatially overlapped with LO_2 on a PBS, after which the two beams co-propagate, but have different polarisation. To remedy this, we use a $\lambda/2$ plate and a second PBS to reject most of the LO_2 beam and retain most of the quantum signal, incurring a small (percent-scale) loss of the quantum signal. This directly translates the polarisation quadrature operators that interacted with the spin system into the amplitude and phase quadratures that are now coupled to the membrane-in-the-middle optomechanical system, in which radiation pressure of the LO_2 drives the mechanical oscillator.

The cascaded system, including the double pass nature of our atomic read out, makes our system susceptible to back-reflections from the optomechanical system to the spin system, since these reflections effectively amount to a self-driving force on the spins, leading to self-induced oscillations of the spin system. Therefore, the system necessitates the introduction of an optical isolator, leading to additional optical intersystem losses. Further, non-perfect rejection of LO_1 by the PBS separating LO_1 and the quantum signal leads to a part of LO_1 co-propagating with LO_2. These two LOs interfere, which effectively turns drifts in the LO_1-LO_2 phase φ into changes of the total optical power sent to the mechanical system.

The optical output of the spin system is spatially mode matched to the optomechanical cavity by using LO_1 as a proxy. By rotating waveplates, the LO_1 probe is directed to the cavity and modematched to it. The degree of modematching is characterised by the amount of ponderomotive squeezing observed in the optical amplitude quadrature in reflection.

Phase fluctuations of the light reflected off the optomechanical cavity are measured with homodyne detection as depicted in Fig. 2 of the main text. The reflected beam is spatially overlapped with LO_3 on a polarising beamsplitter (PBS), and the LO_3 is mode matched to the optical signal. The LO_3 and LO_2 plus quantum fluctuations are now co-propagating, but in different polarisation channels. They are transmitted through a $\lambda/2$ waveplate, set to rotate the polarisations by 45°. The mixed polarisation components are then respectively transmitted and reflected off the second PBS. Neglecting interference, this splits both components equally into the two ports. The total set of PBS-$\lambda/2$-PBS thus acts as an effective 50:50 beamsplitter. The light fields are now in the correct polarisation channels to interfere for homodyne detection.

We perform differential detection, by measuring the photocurrents of a photodetector in each arm, and electronically subtracting the two currents. The slow component is fed back to a piezo, controlling the optical path in the LO_3 arm, thus determining the homodyne detection angle ϑ. The optical powers are $\sim 2\,\mathrm{mW}$ of LO_3 and $\sim 9\,\mu\mathrm{W}$ of LO_2.

Experimental spectra are presented in the main text, Figs. 3 and 4, as well as in Figs. SI4 and SI8. In Fig. SI4 we present a wider frequency range, thus showing features such as out-of-bandgap mechanical modes, mechanical modes of the mirror substrates, higher-order mechanical modes in the bandgap, etc. In Fig. SI8 we present experimental spectra plus model fits for all atomic detunings presented in Fig. 4.

Appendix B: Theoretical model

In this section we will present the model used to fit the experimental data and to extract parameters necessary for the entanglement analysis and Wiener filtering. The latter also relies on signal and noise (cross-)correlation functions calculated from the (fitted) model.

For a function in the time domain $\hat{f}(t)$, we use the Fourier transform sign convention and property

$$\hat{f}(\Omega) = \mathcal{F}\{\hat{f}(t)\} = \int_{-\infty}^{\infty} \hat{f}(t) e^{i\Omega t}\,\mathrm{d}t, \qquad \mathcal{F}\left\{\frac{\mathrm{d}}{\mathrm{d}t}\hat{f}(t)\right\} = -i\Omega \hat{f}(\Omega). \tag{SI B.1}$$

For the localised optical cavity mode, we introduce the photon annihilation and creation operators obeying the commutation relation $[\hat{a}, \hat{a}^\dagger] = 1$, and, in turn, the light amplitude and phase quadratures (suppressing the time/Fourier-frequency dependence for brevity)

$$\hat{X}_\mathrm{L} = \frac{\hat{a} + \hat{a}^\dagger}{2} \qquad \hat{P}_\mathrm{L} = \frac{\hat{a} - \hat{a}^\dagger}{2i}, \tag{SI B.2}$$

which obey the same-time commutation relation $[\hat{X}_\mathrm{L}(t), \hat{P}_\mathrm{L}(t)] = i/2$.

All travelling optical fields, including additional (vacuum) noise fields introduced by optical losses, are described by amplitude and phase quadratures

$$\hat{X}_\mathrm{L}^{\mathrm{in(out)}} = \frac{\hat{a}_{\mathrm{in(out)}} + \hat{a}^\dagger_{\mathrm{in(out)}}}{2} \qquad \hat{P}_\mathrm{L}^{\mathrm{in(out)}} = \frac{\hat{a}_{\mathrm{in(out)}} - \hat{a}^\dagger_{\mathrm{in(out)}}}{2i}, \tag{SI B.3}$$

defined in terms of the quantum amplitudes

$$\hat{a}_{\mathrm{in(out)}}(t) = \frac{1}{2\pi}\int_{-\infty}^{\infty} \mathrm{d}\Omega\; e^{-i\Omega t} \hat{a}_{\mathrm{in(out)}}(\Omega) \qquad \hat{a}^\dagger_{\mathrm{in(out)}}(t) = \frac{1}{2\pi}\int_{-\infty}^{\infty} \mathrm{d}\Omega\; e^{+i\Omega t} \hat{a}^\dagger_{\mathrm{in(out)}}(\Omega) \tag{SI B.4}$$

where $\hat{a}_{\mathrm{in(out)}}$ is the field in a rotating frame with respect to the relevant optical carrier frequency ω_laser, so that $\hat{a}_{\mathrm{in(out)}}(\Omega)$ represents the field at absolute frequency $\Omega + \omega_\mathrm{laser}$. This expression is valid for Fourier frequencies close to the optical carrier, $|\Omega| \ll \omega_\mathrm{laser}$. According to the above considerations the Fourier transforms of the rotating-frame operators $\hat{a}_{\mathrm{in(out)}}(t)$ and $\hat{a}^\dagger_{\mathrm{in(out)}}(t)$ (see Eqs. (SI B.4)), using the convention in Eq. (SI B.1), are

$$\mathcal{F}\{\hat{a}_{\mathrm{in(out)}}(t)\} = \hat{a}_{\mathrm{in(out)}}(\Omega), \quad \mathcal{F}\{\hat{a}^\dagger_{\mathrm{in(out)}}(t)\} = \hat{a}^\dagger_{\mathrm{in(out)}}(-\Omega). \tag{SI B.5}$$

The non-vanishing commutation relations of the travelling field operators are $[\hat{X}_\mathrm{L}^{\mathrm{in(out)}}(t), \hat{P}_\mathrm{L}^{\mathrm{in(out)}}(t')] = (i/2)\delta(t-t')$. Accordingly, the symmetrised power spectral densities of the incoming vacuum light fields are

$$\overline{S}_{X_\mathrm{L}X_\mathrm{L}}(\Omega)\delta(\Omega-\Omega') = \frac{1}{2}\langle \hat{X}^{\mathrm{in}\dagger}_{\mathrm{L},j}(\Omega)\hat{X}^{\mathrm{in}}_{\mathrm{L},j}(\Omega') + \hat{X}^{\mathrm{in}}_{\mathrm{L},j}(\Omega')\hat{X}^{\mathrm{in}\dagger}_{\mathrm{L},j}(\Omega)\rangle = \frac{1}{4}\delta(\Omega-\Omega') \tag{SI B.6a}$$

$$\overline{S}_{P_\mathrm{L}P_\mathrm{L}}(\Omega)\delta(\Omega-\Omega') = \frac{1}{2}\langle \hat{P}^{\mathrm{in}\dagger}_{\mathrm{L},j}(\Omega)\hat{P}^{\mathrm{in}}_{\mathrm{L},j}(\Omega') + \hat{P}^{\mathrm{in}}_{\mathrm{L},j}(\Omega')\hat{P}^{\mathrm{in}\dagger}_{\mathrm{L},j}(\Omega)\rangle = \frac{1}{4}\delta(\Omega-\Omega'). \tag{SI B.6b}$$

For the mechanical (M) and spin (S) oscillators, we follow the commutation relation $[\hat{X}_j, \hat{P}_j] = i$ for $(j = \mathrm{M}, \mathrm{S})$; the effect of the thermal reservoirs $\hat{F}_j$ with mean thermal occupancy n_j is captured by the symmetrised correlation functions

$$\overline{S}_{F_S^X F_S^X}(\Omega)\delta(\Omega-\Omega') \equiv \frac{1}{2}\langle \hat{F}_\mathrm{S}^{\mathrm{X},\dagger}(\Omega)\hat{F}_\mathrm{S}^{\mathrm{X}}(\Omega') + \hat{F}_\mathrm{S}^{\mathrm{X}}(\Omega')\hat{F}_\mathrm{S}^{\mathrm{X},\dagger}(\Omega)\rangle = \gamma_{\mathrm{S0}}(n_\mathrm{S} + 1/2)\delta(\Omega-\Omega') \tag{SI B.7a}$$

$$\overline{S}_{F_S^P F_S^P}(\Omega)\delta(\Omega-\Omega') \equiv \frac{1}{2}\langle \hat{F}_\mathrm{S}^{\mathrm{P},\dagger}(\Omega)\hat{F}_\mathrm{S}^{\mathrm{P}}(\Omega') + \hat{F}_\mathrm{S}^{\mathrm{P}}(\Omega')\hat{F}_\mathrm{S}^{\mathrm{P},\dagger}(\Omega)\rangle = \gamma_{\mathrm{S0}}(n_\mathrm{S} + 1/2)\delta(\Omega-\Omega') \tag{SI B.7b}$$

$$\overline{S}_{F_M F_M}(\Omega)\delta(\Omega-\Omega') \equiv \frac{1}{2}\langle \hat{F}_\mathrm{M}^{\dagger}(\Omega)\hat{F}_\mathrm{M}(\Omega') + \hat{F}_\mathrm{M}(\Omega')\hat{F}_\mathrm{M}^{\dagger}(\Omega)\rangle = 2\gamma_{\mathrm{M0}}(n_\mathrm{M} + 1/2)\delta(\Omega-\Omega'). \tag{SI B.7c}$$

The diagrammatic representation of the fields and operations under considerations is presented in Fig. SI3.

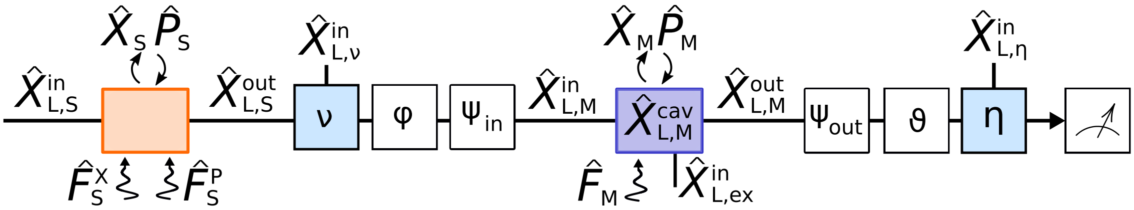

Figure SI3. **Diagramatic representation of the hybrid system.** Various optical fields, operators, thermal bath forces and rotations acting in the hybrid system, from input to detection. Spin (orange box) and mechanical system (blue box) along with driving optical and thermal forces. Light blue boxes represent beam-splitter-like losses. White boxes represent the various rotations applied to the optical fields.

1. Atomic ensemble

The atomic ensemble interacts dispersively with the light, leading to a mutual rotation of the light and spin variables according to the atomic polarizability tensor [11]

$$\hat{H}_\mathrm{S}/\hbar = -\omega_\mathrm{S}\hat{J}_x + g_\mathrm{S}\left[a_0\hat{S}_0\hat{J}_0 + a_1\hat{S}_z\hat{J}_z + 2a_2\left[\hat{S}_0\hat{J}_z^2 - \hat{S}_x(\hat{J}_x^2 - \hat{J}_y^2) - \hat{S}_y(\hat{J}_x\hat{J}_y + \hat{J}_y\hat{J}_x)\right]\right], \tag{SI B.8}$$

with a_0, a_1, and a_2 as the relative weights of the scalar, vector and tensor contributions [11], which can be tuned by the detuning of the laser with respect to the atomic resonance and g_S is the coupling rate. We work detuned 3 GHz to the blue from the $F = 4 \to F' = 5$ D_2 transition.

In the limit of high spin polarisation in the $F = 4$ hyperfine manifold and for a strong linearly polarised local oscillator polarised at an angle α to the quantization axis, the Hamiltonian can be simplified to [12]

$$\hat{H}_\mathrm{S}/\hbar = \frac{\omega_\mathrm{S}}{2}(\hat{X}_\mathrm{S}^2 + \hat{P}_\mathrm{S}^2) - 2\sqrt{\Gamma_\mathrm{S}}\left(\hat{X}_\mathrm{S}\hat{X}_\mathrm{L} + \zeta_\mathrm{S}\hat{P}_\mathrm{S}\hat{P}_\mathrm{L}\right), \tag{SI B.9}$$

where $\Gamma_\mathrm{S} = g_\mathrm{S}^2 a_1^2 S_\parallel J_x$ is the spin oscillator readout rate and $\zeta_\mathrm{S} = -14\frac{a_2}{a_1}\cos 2\alpha$ is the tensor correction factor, which for our choice of polarisation angle α has a value of ~ 0.028. We have omitted constant energy terms, as they do not affect the dynamics of the spin variables of interest. The canonical light variables are $\{\hat{X}_\mathrm{L} = \hat{S}_z/\sqrt{S_\parallel}, \hat{P}_\mathrm{L} = -\hat{S}_\perp/\sqrt{S_\parallel}\}$. In our experimental regime, as $\zeta > 0$, the spin-light interactions deviates from the QND interaction, introducing extra correlation terms and allowing for dynamical cooling of the spin ensemble, effectively changing the decay rate and bath occupation.

The dynamics follows from the Heisenberg-Langevin equations, which, in the steady state and in the frequency space, are

$$\begin{pmatrix} \gamma_{\mathrm{S}0}/2 + \zeta_\mathrm{S}\Gamma_\mathrm{S} - i\Omega & -\omega_\mathrm{S} \\ \omega_\mathrm{S} & \gamma_{\mathrm{S}0}/2 + \zeta_\mathrm{S}\Gamma_\mathrm{S} - i\Omega \end{pmatrix}\begin{pmatrix} \hat{X}_\mathrm{S} \\ \hat{P}_\mathrm{S} \end{pmatrix} = 2\sqrt{\Gamma_\mathrm{S}}\begin{pmatrix} 0 & -\zeta_\mathrm{S} \\ 1 & 0 \end{pmatrix}\begin{pmatrix} \hat{X}^\mathrm{in}_\mathrm{L,S} \\ \hat{P}^\mathrm{in}_\mathrm{L,S} \end{pmatrix} + \begin{pmatrix} \hat{F}^\mathrm{X}_\mathrm{S} \\ \hat{F}^\mathrm{P}_\mathrm{S} \end{pmatrix}, \tag{SI B.10}$$

$$\begin{pmatrix} \hat{X}^\mathrm{out}_\mathrm{L,S} \\ \hat{P}^\mathrm{out}_\mathrm{L,S} \end{pmatrix} = \begin{pmatrix} \hat{X}^\mathrm{in}_\mathrm{L,S} \\ \hat{P}^\mathrm{in}_\mathrm{L,S} \end{pmatrix} + \sqrt{\Gamma_\mathrm{S}}\begin{pmatrix} 0 & -\zeta_\mathrm{S} \\ 1 & 0 \end{pmatrix}\begin{pmatrix} \hat{X}_\mathrm{S} \\ \hat{P}_\mathrm{S} \end{pmatrix}, \tag{SI B.11}$$

for $2\zeta_\mathrm{S}\Gamma_\mathrm{S}$ as the tensor (dynamical) broadening, and $\hat{F}^\mathrm{X}_\mathrm{S}, \hat{F}^\mathrm{P}_\mathrm{S}$ as the effective force acting on the spins via the thermal bath. We proceed defining the shorthand matrix notation

$$\mathbf{Z} = \begin{pmatrix} 0 & -\zeta_\mathrm{S} \\ 1 & 0 \end{pmatrix}, \quad \mathbf{L} = \begin{pmatrix} \gamma_{\mathrm{S}0}/2 + \zeta_\mathrm{S}\Gamma_\mathrm{S} - i\Omega & -\omega_\mathrm{S} \\ \omega_\mathrm{S} & \gamma_{\mathrm{S}0}/2 + \zeta_\mathrm{S}\Gamma_\mathrm{S} - i\Omega \end{pmatrix}^{-1},$$
$$\hat{\boldsymbol{X}}^\mathrm{in(out)}_\mathrm{L,S} = \begin{pmatrix} \hat{X}^\mathrm{in(out)}_\mathrm{L,S} \\ \hat{P}^\mathrm{in(out)}_\mathrm{L,S} \end{pmatrix}, \quad \hat{\boldsymbol{X}}_\mathrm{S} = \begin{pmatrix} \hat{X}_\mathrm{S} \\ \hat{P}_\mathrm{S} \end{pmatrix}, \quad \hat{\boldsymbol{F}}_\mathrm{S} = \begin{pmatrix} \hat{F}^\mathrm{X}_\mathrm{S} \\ \hat{F}^\mathrm{P}_\mathrm{S} \end{pmatrix}, \tag{SI B.12}$$

and solve the equations for the atomic and light variables

$$\hat{\boldsymbol{X}}_\mathrm{S} = 2\sqrt{\Gamma_\mathrm{S}}\mathbf{L}\mathbf{Z}\hat{\boldsymbol{X}}^\mathrm{in}_\mathrm{L,S} + \mathbf{L}\hat{\boldsymbol{F}}_\mathrm{S} \tag{SI B.13}$$

$$\hat{\boldsymbol{X}}^\mathrm{out}_\mathrm{L,S} = \hat{\boldsymbol{X}}^\mathrm{in}_\mathrm{L,S} + \sqrt{\Gamma_\mathrm{S}}\mathbf{Z}\hat{\boldsymbol{X}}_\mathrm{S} = (\mathbf{1}_2 + 2\Gamma_\mathrm{S}\mathbf{Z}\mathbf{L}\mathbf{Z})\hat{\boldsymbol{X}}^\mathrm{in}_\mathrm{L,S} + \sqrt{\Gamma_\mathrm{S}}\mathbf{Z}\mathbf{L}\hat{\boldsymbol{F}}_\mathrm{S}, \tag{SI B.14}$$

where $\mathbf{1}_2$ is the 2×2 identity matrix.

In the main text we consider simpler, approximate versions of equations (SI B.13) and (SI B.14) valid in the limit $|\omega_\mathrm{S}| \gg \gamma_\mathrm{S}, |\Omega - |\omega_\mathrm{S}||$. In this limit, the effective thermal forces $\hat{F}_\mathrm{S}^\mathrm{X}$ and $\hat{F}_\mathrm{S}^\mathrm{P}$ can be combined into the single thermal force term $\hat{F}_\mathrm{S} \approx i\hat{F}_\mathrm{S}^\mathrm{X} + \hat{F}_\mathrm{S}^\mathrm{P}$. In this limit, the evolution equation for $\hat{X}_\mathrm{S}$ in terms of the susceptibility $\chi_\mathrm{S}(\Omega)$ arises from Eq. (SI B.13) (setting $\omega_\mathrm{S0} \equiv \omega_\mathrm{S}$),

$$\hat{X}_\mathrm{S} = \chi_\mathrm{S}\left[\hat{F}_\mathrm{S} + 2\sqrt{\Gamma_\mathrm{S}}\begin{pmatrix} 1 \\ -i\zeta_\mathrm{S} \end{pmatrix}^\intercal \hat{\boldsymbol{X}}_\mathrm{L,S}^\mathrm{in}\right] = \chi_\mathrm{S}[\hat{F}_\mathrm{S} + 2\sqrt{\Gamma_\mathrm{S}}(\hat{X}_\mathrm{L,S}^\mathrm{in} - i\zeta_\mathrm{S}\hat{P}_\mathrm{L,S}^\mathrm{in})], \tag{SI B.15}$$

as presented in the main text. Noting that $\hat{P}_\mathrm{S} \approx -\mathrm{sign}(\omega_\mathrm{S0})i\hat{X}_\mathrm{S}$, the simpler input-output relation discussed in the main text,

$$\boldsymbol{X}_\mathrm{L,S}^\mathrm{out} = \boldsymbol{X}_\mathrm{L,S}^\mathrm{in} + \sqrt{\Gamma_\mathrm{S}}\begin{pmatrix} -i\zeta_\mathrm{S} \\ 1 \end{pmatrix}\hat{X}_\mathrm{S}, \tag{SI B.16}$$

follows from Eq. (SI B.14).

The CIFAR modelling (see SI A 1) is based on equations (SI B.13) and (SI B.14), with the broadband response added as another atomic mode in the following manner

$$\hat{\mathbf{X}}_\mathrm{L,S}^\mathrm{out} = \hat{\mathbf{X}}_\mathrm{L,S}^\mathrm{in} + \sqrt{\Gamma_\mathrm{S}}\mathbf{Z}\hat{\mathbf{X}}_\mathrm{S} + \sqrt{\Gamma_\mathrm{S,bb}}\mathbf{Z}\hat{\mathbf{X}}_\mathrm{S,bb} \tag{SI B.17}$$

$$\hat{\mathbf{X}}_\mathrm{S,bb} = 2\sqrt{\Gamma_\mathrm{bb}}\mathbf{L}_\mathrm{bb}\mathbf{Z}\hat{\mathbf{X}}_\mathrm{L,S}^\mathrm{in}, \tag{SI B.18}$$

for $\mathbf{L}_\mathrm{bb}$ as $\mathbf{L}$ with $\gamma_\mathrm{S0} \to \gamma_\mathrm{bb}$, $\Gamma_\mathrm{S} \to \Gamma_\mathrm{S,bb}$ and $\Gamma_\mathrm{S,bb}$ as the broadband response readout rate. Incoherent thermal contributions were disregarded as the input field is modulated with large amplitude. The input field $\hat{\mathbf{X}}_\mathrm{L,S}^\mathrm{in}$ quadratures is rotated according to $\hat{\mathbf{X}}_\mathrm{L,S}^\mathrm{drive} = O_{\vartheta_\mathrm{in}}\hat{\mathbf{X}}_\mathrm{L,S}^\mathrm{in}$, in which $\boldsymbol{O}_\alpha$

$$\boldsymbol{O}_\alpha = \begin{pmatrix} \cos\alpha & -\sin\alpha \\ \sin\alpha & \cos\alpha \end{pmatrix} \tag{SI B.19}$$

is a rotation matrix. The result of the CIFAR modelling for various ϑ_in is presented in Fig. SI1. Fig. SI1(a) shows the amplitude squared R^2 of the detected field; Fig. SI1(b) presents the phase of detected field in respect to the drive.

2. Optomechanics

We start with the standard linearised optomechanical interaction between a mechanical degree of freedom with frequency ω_M and the intracavity field

$$\hat{H}_\mathrm{M}/\hbar = \frac{\omega_\mathrm{M}}{2}\left(\hat{X}_\mathrm{M}^2 + \hat{P}_\mathrm{M}^2\right) - \Delta\left(\hat{X}_\mathrm{L,M}^{\mathrm{cav}\,2} + \hat{P}_\mathrm{L,M}^{\mathrm{cav}\,2}\right) - 4g\left(\hat{X}_\mathrm{L,M}^\mathrm{cav}\cos\psi_\mathrm{in} + \hat{P}_\mathrm{L,M}^\mathrm{cav}\sin\psi_\mathrm{in}\right)\hat{X}_\mathrm{M}, \tag{SI B.20}$$

where $\Delta = \omega_\mathrm{L} - \omega_\mathrm{c}$ is the detuning of the laser with respect to the cavity resonance ω_c and g is the light-enhanced optomechanical coupling rate. The cavity linewidth κ has contributions from the the in-and-out-coupling mirror (κ_in) – we probe the cavity in reflection – and the highly-reflective (HR) back mirror ($\kappa_\mathrm{ex}^\mathrm{HR}$) as well as from intracavity losses ($\kappa_\mathrm{ex}^\mathrm{loss}$), such that $\kappa = \kappa_\mathrm{in} + \kappa_\mathrm{ex}$, with $\kappa_\mathrm{ex} = \kappa_\mathrm{ex}^\mathrm{HR} + \kappa_\mathrm{ex}^\mathrm{loss}$ where the subscript ex signifies any extra loss mechanism. Losses due to the HR mirror and due to intracavity scattering are mathematically equivalent. Finally, $\psi_\mathrm{in} = \arctan(2\Delta/\kappa)$ denotes the phase of the intracavity field relative to input field.

The time evolution of the optical and mechanical variables, including decay and fluctuations, is given by the Heisenberg-Langevin equations. In the frequency domain, and in the steady-state regime, the equations of motion are

$$\begin{pmatrix} \kappa/2 - i\Omega & \Delta & 2g\sin\psi_\mathrm{in} \\ -\Delta & \kappa/2 - i\Omega & -2g\cos\psi_\mathrm{in} \\ -4g\cos\psi_\mathrm{in} & -4g\sin\psi_\mathrm{in} & \chi_\mathrm{M00}^{-1} \end{pmatrix}\begin{pmatrix} \hat{X}_\mathrm{L,M}^\mathrm{cav} \\ \hat{P}_\mathrm{L,M}^\mathrm{cav} \\ \hat{X}_\mathrm{M} \end{pmatrix} = \begin{pmatrix} \sqrt{\kappa_\mathrm{in}}\hat{X}_\mathrm{L,M}^\mathrm{in} + \sqrt{\kappa_\mathrm{ex}}\hat{X}_\mathrm{L,M}^\mathrm{ex} \\ \sqrt{\kappa_\mathrm{in}}\hat{P}_\mathrm{L,M}^\mathrm{in} + \sqrt{\kappa_\mathrm{ex}}\hat{P}_\mathrm{L,M}^\mathrm{ex} \\ \hat{F}_\mathrm{M} \end{pmatrix}, \tag{SI B.21}$$

in which $\chi_\mathrm{M00}^{-1} \equiv (\omega_\mathrm{M0}^2 - \Omega^2 - i\Omega\gamma_\mathrm{M0})/\omega_\mathrm{M0}$ (the subscript denotes that this susceptibility excludes both dynamical broadening and optical spring effects) and $\hat{X}_\mathrm{L,M}^\mathrm{in}$ ($\hat{X}_\mathrm{L,M}^\mathrm{ex}$) is the input quantum field leaking in via the port 'in' ('ex'). The port 'in' corresponds to the main in/outcoupler, while mathematically port 'ex' corresponds to both the HR mirror and intra-cavity loss, which act in the same way since no light is present at the input of HR. The dynamics of the membrane momentum are calculated from the relation $-i\Omega\hat{X}_\mathrm{M} = \omega_\mathrm{M0}\hat{P}_\mathrm{M}$. The natural linewidth of the mechanical mode is γ_M0, and the mean occupation due to the thermal reservoir at temperature T is $n_\mathrm{M0} = \hbar\omega_\mathrm{M0}/k_B T$.

We are interested both in the effect of the mechanical mode on the light variables and in the dynamics of the oscillator itself. By defining the matrices

$$\mathbf{A} = \begin{pmatrix} \kappa/2 - i\Omega & \Delta \\ -\Delta & \kappa/2 - i\Omega \end{pmatrix}, \quad \mathbf{B} = \begin{pmatrix} 0 \\ -2g \end{pmatrix}, \quad \mathbf{C} = \begin{pmatrix} -4g & 0 \end{pmatrix}, \quad \hat{\boldsymbol{X}}^j_\mathrm{L,M} = \begin{pmatrix} \hat{X}^j_\mathrm{L,M} \\ \hat{P}^j_\mathrm{L,M} \end{pmatrix}, \tag{SI B.22}$$

$\boldsymbol{O}_\psi$ as the input-intracavity field phase rotation (see Eq. (SI B.19)) and the index $j \in \{\mathrm{cav}, \mathrm{in}, \mathrm{ex}\}$ for optical fields, we write Eq. (SI B.21) as system of matrix equations. Noting that the cavity response matrix $\mathbf{A}$ is invariant under quadrature rotations, $\boldsymbol{O}_\psi \mathbf{A} \boldsymbol{O}_\psi^\intercal = \mathbf{A}$, we find the intracavity field and the mechanical variable as a function of the input fluctuations and thermal bath

$$\hat{\boldsymbol{X}}^\mathrm{cav}_\mathrm{L,M} = \mathbf{A}^{-1}\left(\sqrt{\kappa_\mathrm{in}}\hat{\boldsymbol{X}}^\mathrm{in}_\mathrm{L,M} + \sqrt{\kappa_\mathrm{ex}}\hat{\boldsymbol{X}}^\mathrm{ex}_\mathrm{L,M}\right) - \mathbf{A}^{-1}\mathbf{O}_{\psi_\mathrm{in}}\mathbf{B}\hat{X}_\mathrm{M}, \tag{SI B.23}$$

$$\hat{X}_\mathrm{M} = \chi_\mathrm{M}\left[-\mathbf{C}\mathbf{A}^{-1}\mathbf{O}^\intercal_{\psi_\mathrm{in}}\left(\sqrt{\kappa_\mathrm{in}}\hat{\boldsymbol{X}}^\mathrm{in}_\mathrm{L,M} + \sqrt{\kappa_\mathrm{ex}}\hat{\boldsymbol{X}}^\mathrm{ex}_\mathrm{L,M}\right) + \hat{F}_\mathrm{M}\right], \tag{SI B.24}$$

in which $\chi_\mathrm{M} = (\chi^{-1}_\mathrm{M00} - \mathbf{C}\mathbf{A}^{-1}\mathbf{B})^{-1}$ is the effective mechanical susceptibility in the presence of optomechanical coupling. Substituting Eq. (SI B.24) in Eq. (SI B.23) solves the system for the cavity field

$$\hat{\boldsymbol{X}}^\mathrm{cav}_\mathrm{L,M} = \mathbf{O}_{\psi_\mathrm{in}}\mathbf{Y}^{-1}\mathbf{O}^\intercal_{\psi_\mathrm{in}}\left(\sqrt{\kappa_\mathrm{in}}\hat{\boldsymbol{X}}^\mathrm{in}_\mathrm{L,M} + \sqrt{\kappa_\mathrm{ex}}\hat{\boldsymbol{X}}^\mathrm{ex}_\mathrm{L,M}\right) - \mathbf{O}_{\psi_\mathrm{in}}\mathbf{Y}^{-1}\mathbf{B}\chi_\mathrm{M00}\hat{F}_\mathrm{M}, \tag{SI B.25}$$

where $\mathbf{Y} = \mathbf{A} - \mathbf{B}\chi_\mathrm{M00}\mathbf{C}$ is the effective cavity response matrix in the presence of optomechanical coupling. This quantity can also be used to express the mechanical response (SI B.24) as

$$\hat{X}_\mathrm{M} = -\chi_\mathrm{M00}\mathbf{C}\mathbf{Y}^{-1}\mathbf{O}^\intercal_{\psi_\mathrm{in}}\left(\sqrt{\kappa_\mathrm{in}}\hat{\boldsymbol{X}}^\mathrm{in}_\mathrm{L,M} + \sqrt{\kappa_\mathrm{ex}}\hat{\boldsymbol{X}}^\mathrm{ex}_\mathrm{L,M}\right) + \chi_\mathrm{M}\hat{F}_\mathrm{M}. \tag{SI B.26}$$

Finally, we detect the reflected field off port 1 in a homodyne measurement. The phase of the outgoing classical carrier field with respect to the cavity field is given by $\psi_\mathrm{out} = \arctan(2\Delta/(\kappa_\mathrm{in} - \kappa_\mathrm{ex}))$. Overall, the total phase shift with respect to the input field is $\psi_\mathrm{out} + \psi_\mathrm{in}$. The cavity input-output relations, taking account for the acquired phase shift with respect to the input, from Eq. (SI B.25), is

$$\begin{aligned}\hat{\boldsymbol{X}}^\mathrm{out}_\mathrm{L,M} &= \mathbf{O}^\intercal_{\psi_\mathrm{in}+\psi_\mathrm{out}}(-\hat{\boldsymbol{X}}^\mathrm{in}_\mathrm{L,M} + \sqrt{\kappa_\mathrm{in}}\hat{\boldsymbol{X}}^\mathrm{cav}_\mathrm{L,M}) \\ &= \mathbf{O}^\intercal_{\psi_\mathrm{out}}(\kappa_\mathrm{in}\mathbf{Y}^{-1} - \mathbf{1}_2)\mathbf{O}^\intercal_{\psi_\mathrm{in}}\hat{\boldsymbol{X}}^\mathrm{in}_\mathrm{L,M} + \sqrt{\kappa_\mathrm{in}\kappa_\mathrm{ex}}\mathbf{O}^\intercal_{\psi_\mathrm{out}}\mathbf{Y}^{-1}\mathbf{O}^\intercal_{\psi_\mathrm{in}}\hat{\boldsymbol{X}}^\mathrm{ex}_\mathrm{L,M} - \sqrt{\kappa_\mathrm{in}}\mathbf{O}^\intercal_{\psi_\mathrm{out}}\mathbf{Y}^{-1}\mathbf{B}\chi_\mathrm{M00}\hat{F}_\mathrm{M},\end{aligned} \tag{SI B.27}$$

where in the second line we have substituted the solution for the intracavity field (SI B.25).

Above we have developed the exact Fourier-domain solution to a (linearised) cavity-optomechanical system, in particular the mechanical response (SI B.24) and the optomechanical input-output relation (SI B.23). We now derive the simplified versions of these equations used in the main text to emphasise the essential physics of our scheme. We note that the cavity response matrix can be expressed in terms of the complex Lorentzian sideband amplitudes $\mathcal{L}(\Omega) \equiv (\kappa/2)/[\kappa/2 - i(\Omega + \Delta)]$ with phase $\Theta(\Omega) \equiv \mathrm{Arg}[\mathcal{L}(\Omega)]$ as

$$\mathbf{A}^{-1} = \frac{1}{\kappa}\begin{pmatrix} \mathcal{L}(\Omega) + \mathcal{L}^*(-\Omega) & i[\mathcal{L}(\Omega) - \mathcal{L}^*(-\Omega)] \\ -i[\mathcal{L}(\Omega) - \mathcal{L}^*(-\Omega)] & \mathcal{L}(\Omega) + \mathcal{L}^*(-\Omega) \end{pmatrix} \tag{SI B.28}$$

$$= \frac{|\mathcal{L}(\Omega)| + |\mathcal{L}(-\Omega)|}{\kappa} e^{i[\Theta(\Omega)-\Theta(-\Omega)]/2}\mathbf{O}_{[\Theta(\Omega)+\Theta(-\Omega)]/2}\left[\mathbf{1}_2 + i\frac{|\mathcal{L}(\Omega)| - |\mathcal{L}(-\Omega)|}{|\mathcal{L}(\Omega)| + |\mathcal{L}(-\Omega)|}\mathbf{O}_{-\pi/2}\right]. \tag{SI B.29}$$

Assuming that the dependence of $\mathcal{L}(\Omega)$ on the Fourier frequency Ω is negligible over the bandwidth of interest, we may approximate $\mathcal{L}(\pm\Omega) \approx \mathcal{L}(\pm\omega_\mathrm{M})$ (and accordingly $\Theta(\pm\Omega) \approx \Theta(\pm\omega_\mathrm{M})$). Within this approximation, we can achieve the simplified mechanical response and input-output equations employed in the main text by introducing the rotated quadrature basis

$$\boldsymbol{X}^{\mathrm{in(ex)}\prime}_\mathrm{L,M} \equiv e^{i[\Theta(\omega_\mathrm{m})-\Theta(-\omega_\mathrm{m})]/2}\mathbf{O}_{[\Theta(\omega_\mathrm{m})+\Theta(-\omega_\mathrm{m})]/2}\mathbf{O}^\intercal_{\psi_\mathrm{in}}\boldsymbol{X}^\mathrm{in(ex)}_\mathrm{L,M}. \tag{SI B.30}$$

In this way, using Eqs. (SI B.29) and (SI B.30) to reexpress the QBA force on the mechanical mode (i.e., Eq. (SI B.24), 1st term in square brackets), we find

$$-\mathbf{C}\mathbf{A}^{-1}\mathbf{O}^\intercal_{\psi_\mathrm{in}}\left(\sqrt{\kappa_\mathrm{in}}\hat{\boldsymbol{X}}^\mathrm{in}_\mathrm{L,M} + \sqrt{\kappa_\mathrm{ex}}\hat{\boldsymbol{X}}^\mathrm{ex}_\mathrm{L,M}\right) \approx 2\sqrt{\Gamma_\mathrm{M}}\begin{pmatrix} 1 \\ i\zeta_\mathrm{M} \end{pmatrix}^\intercal\left(\sqrt{\kappa_\mathrm{in}/\kappa}\hat{\boldsymbol{X}}^{\mathrm{in}\prime}_\mathrm{L,M} + \sqrt{\kappa_\mathrm{ex}/\kappa}\hat{\boldsymbol{X}}^{\mathrm{ex}\prime}_\mathrm{L,M}\right), \tag{SI B.31}$$

where we have introduced the mechanical readout rate and sideband asymmetry parameter,

$$\Gamma_{\mathrm{M}} \equiv \frac{4g^2}{\kappa}(|\mathcal{L}(\omega_{\mathrm{M}})| + |\mathcal{L}(-\omega_{\mathrm{M}})|)^2, \quad \zeta_{\mathrm{M}} \equiv \frac{|\mathcal{L}(\omega_{\mathrm{M}})| - |\mathcal{L}(-\omega_{\mathrm{M}})|}{|\mathcal{L}(\omega_{\mathrm{M}})| + |\mathcal{L}(-\omega_{\mathrm{M}})|}, \tag{SI B.32}$$

respectively. Finally, we ignore the finite cavity overcoupling by setting $\kappa_{\mathrm{in}} = \kappa$ (and hence $\kappa_{\mathrm{ex}} = 0$) in Eq. (SI B.31) to arrive at the main-text expression for the response of $\hat{X}_{\mathrm{M}}$. Noting that $-\mathbf{1}_2 + \kappa \mathbf{A}^{-1} = e^{i[\Theta(\omega_{\mathrm{m}}) - \Theta(-\omega_{\mathrm{m}})]}\mathbf{O}_{\Theta(\omega_{\mathrm{m}})+\Theta(-\omega_{\mathrm{m}})}$, we find in the same limit that the rotated output quadrature

$$\boldsymbol{X}^{\mathrm{out}\prime}_{\mathrm{L,M}} \equiv e^{-i[\Theta(\omega_{\mathrm{M}})-\Theta(-\omega_{\mathrm{M}})]/2}\mathbf{O}^{\intercal}_{[\Theta(\omega_{\mathrm{M}})+\Theta(-\omega_{\mathrm{M}})]/2}\mathbf{O}^{\intercal}_{\psi_{\mathrm{in}}}\boldsymbol{X}^{\mathrm{out}}_{\mathrm{L,M}}, \tag{SI B.33}$$

obeys

$$\boldsymbol{X}^{\mathrm{out}\prime}_{\mathrm{L,M}} = \boldsymbol{X}^{\mathrm{in}\prime}_{\mathrm{L,M}} + \sqrt{\Gamma_{\mathrm{M}}}\begin{pmatrix} i\zeta_{\mathrm{M}} \\ 1 \end{pmatrix}\hat{X}_{\mathrm{M}}, \tag{SI B.34}$$

as follows from $\hat{\boldsymbol{X}}^{\mathrm{out}}_{\mathrm{L,M}} = -\hat{\boldsymbol{X}}^{\mathrm{in}}_{\mathrm{L,M}} + \sqrt{\kappa_{\mathrm{in}}}\hat{\boldsymbol{X}}^{\mathrm{cav}}_{\mathrm{L,M}}$ combined with Eq. (SI B.23), again assuming $\kappa_{\mathrm{in}} = \kappa$. Dropping the primes on the quadrature variables in Eq. (SI B.34) for brevity we arrive at the input-output relation presented in the main text.

3. Hybrid system I/O relations

The subsystems are coupled following the relation

$$\hat{\boldsymbol{X}}^{\mathrm{in}}_{\mathrm{L,M}} = \mathbf{O}_{\varphi}(\sqrt{\nu}\hat{\boldsymbol{X}}^{\mathrm{out}}_{\mathrm{L,S}} + \sqrt{1-\nu}\hat{\boldsymbol{X}}_{\mathrm{L},\nu}), \tag{SI B.35}$$

where optical transmission losses between the systems are modelled as a beam splitter with power transmission ν, and $\hat{\boldsymbol{X}}^{\mathrm{out}}_{\mathrm{L,S}}$ is defined Eq. (SI B.14). In general, the mechanical oscillator is not only coupled to light and its own thermal bath, but effectively also to the spin oscillator

$$\begin{aligned}\hat{X}_{\mathrm{M}} = -\chi_{\mathrm{M00}}\mathbf{C}\mathbf{Y}^{-1}\mathbf{O}^{\intercal}_{\psi_{\mathrm{in}}}\Big(\sqrt{\nu\kappa_{\mathrm{in}}}\mathbf{O}_{\varphi}[(\mathbf{1}_2 + 2\Gamma_{\mathrm{S}}\mathbf{ZLZ})\hat{\boldsymbol{X}}^{\mathrm{in}}_{\mathrm{L,S}} + \sqrt{\Gamma_{\mathrm{S}}}\mathbf{ZL}\hat{\boldsymbol{F}}_{\mathrm{S}}] + \sqrt{(1-\nu)\kappa_{\mathrm{in}}}\mathbf{O}_{\varphi}\hat{\boldsymbol{X}}_{\mathrm{L},\nu} + \sqrt{\kappa_{\mathrm{ex}}}\hat{\boldsymbol{X}}^{\mathrm{ex}}_{\mathrm{L,M}}\Big) \\ + (\chi^{-1}_{\mathrm{M00}} - \mathbf{C}\mathbf{A}^{-1}\mathbf{B})^{-1}\hat{F}_{\mathrm{M}},\end{aligned} \tag{SI B.36}$$

as follows by combining Eqs. (SI B.26), (SI B.35), and (SI B.14). At the output of the optical cavity, the field is homodyned at a quadrature of choice defined by the phase ϑ, $\hat{\boldsymbol{X}}^{\mathrm{meas}}_{\mathrm{L}} = \sqrt{\eta}\mathbf{O}_{\vartheta}\hat{\boldsymbol{X}}^{\mathrm{out}}_{\mathrm{L,M}} + \sqrt{1-\eta}\hat{\boldsymbol{X}}_{\mathrm{L},\eta}$, accounting for mode-matching and optical losses on the way to the final detector by the efficiency η. The detected field, including all contributions from losses, rotations and oscillator couplings is

$$\begin{aligned}\hat{\boldsymbol{X}}^{\mathrm{meas}}_{\mathrm{L}} = \sqrt{\eta}\mathbf{O}_{\vartheta}\mathbf{O}^{\intercal}_{\psi_{\mathrm{out}}}(\kappa_{\mathrm{in}}\mathbf{Y}^{-1} - \mathbf{1}_2)\mathbf{O}^{\intercal}_{\psi_{\mathrm{in}}}\Big(\sqrt{\nu}\mathbf{O}_{\varphi}[(\mathbf{1}_2 + 2\Gamma_{\mathrm{S}}\mathbf{ZLZ})\hat{\boldsymbol{X}}^{\mathrm{in}}_{\mathrm{L,S}} + \sqrt{\Gamma_{\mathrm{S}}}\mathbf{ZL}\hat{\boldsymbol{F}}_{\mathrm{S}}] + \sqrt{1-\nu}\mathbf{O}_{\varphi}\hat{\boldsymbol{X}}_{\mathrm{L},\nu}\Big) \\ + \sqrt{\eta\kappa_{\mathrm{in}}\kappa_{\mathrm{ex}}}\mathbf{O}_{\vartheta}\mathbf{O}^{\intercal}_{\psi_{\mathrm{out}}}\mathbf{Y}^{-1}\mathbf{O}^{\intercal}_{\psi_{\mathrm{in}}}\hat{\boldsymbol{X}}^{\mathrm{ex}}_{\mathrm{L,M}} - \sqrt{\eta\kappa_{\mathrm{in}}}\mathbf{O}_{\vartheta}\mathbf{O}^{\intercal}_{\psi_{\mathrm{out}}}\mathbf{Y}^{-1}\mathbf{B}\chi_{\mathrm{M00}}\hat{F}_{\mathrm{M}} + \sqrt{1-\eta}\hat{\boldsymbol{X}}_{\mathrm{L},\eta}.\end{aligned} \tag{SI B.37}$$

Note that the homodyne measurement only allows us to access one component of $\hat{\boldsymbol{X}}^{\mathrm{meas}}_{\mathrm{L}}$ for a given choice of ϑ.

The equations (SI B.13), (SI B.36), and (SI B.37) contain the full information needed to fit the experimental data and quantify correlations among the various constituents. To ease the handling of the theory, we construct a rectangular transformation matrix $\mathbf{U}$ in the input basis of the forces acting on the systems $\boldsymbol{Q}_{\mathrm{in}} \equiv (\hat{F}^X_{\mathrm{S}}, \hat{F}^P_{\mathrm{S}}, \hat{F}_{\mathrm{M}}, \hat{X}^{\mathrm{in}}_{\mathrm{L,S}}, \hat{P}^{\mathrm{in}}_{\mathrm{L,S}}, \hat{X}^{\mathrm{in}}_{\mathrm{L},\nu}, \hat{P}^{\mathrm{in}}_{\mathrm{L},\nu}, \hat{X}^{\mathrm{in}}_{\mathrm{L,ex}}, \hat{P}^{\mathrm{in}}_{\mathrm{L,ex}}, \hat{X}^{\mathrm{in}}_{\mathrm{L},\eta}, \hat{P}^{\mathrm{in}}_{\mathrm{L},\eta})^{\intercal}$ such that

$$\boldsymbol{Q}_{\mathrm{out}} = \mathbf{U}\boldsymbol{Q}_{\mathrm{in}} \tag{SI B.38}$$

and the output basis $\boldsymbol{Q}_{\mathrm{out}} \equiv (\hat{X}_{\mathrm{M}}, \hat{P}_{\mathrm{M}}, \hat{X}_{\mathrm{S}}, \hat{P}_{\mathrm{S}}, \hat{P}^{\mathrm{meas}}_{\mathrm{L}})^{\intercal}$, which are all the output operators we might potentially be interested in.

The various power (and cross) spectral densities are calculated by taking the absolute square of the vector $\boldsymbol{Q}_{\mathrm{out}}$ given the input matrix of spectral densities

$$\bar{\mathbf{S}}_{\mathrm{in}}\delta(\Omega - \Omega') = \frac{1}{2}\langle \boldsymbol{Q}^{\dagger}_{\mathrm{in}}(\Omega)[\boldsymbol{Q}_{\mathrm{in}}(\Omega')]^{\intercal} + \boldsymbol{Q}_{\mathrm{in}}(\Omega)[\boldsymbol{Q}^{\dagger}_{\mathrm{in}}(\Omega')]^{\intercal}\rangle, \tag{SI B.39}$$

where $\intercal$ signifies a row-vector, while $\dagger$ indicates Hermitian conjugation of the individual vector elements, not the vector as a whole. $\bar{\mathbf{S}}_{\text{in}}$ is a square matrix with diagonal entries

$$\text{diag}(\bar{\mathbf{S}}_{\text{in}}) = \left(\bar{S}_{F_{\text{S}}^X F_{\text{S}}^X}, \bar{S}_{F_{\text{S}}^P F_{\text{S}}^P}, \bar{S}_{F_{\text{M}} F_{\text{M}}}, \bar{S}_{X_{\text{L}} X_{\text{L}}}, \bar{S}_{P_{\text{L}} P_{\text{L}}}, \bar{S}_{X_{\text{L}} X_{\text{L}}}, \bar{S}_{P_{\text{L}} P_{\text{L}}} + \frac{\nu}{1-\nu}\bar{S}_{\text{S,bb}}, \bar{S}_{X_{\text{L}} X_{\text{L}}}, \bar{S}_{P_{\text{L}} P_{\text{L}}}, \bar{S}_{X_{\text{L}} X_{\text{L}}}, \bar{S}_{P_{\text{L}} P_{\text{L}}}\right), \tag{SI B.40}$$

and all other elements equal to zero. Notably, for an easier theoretical treatment, the broadband noise is added via the inter-system loss port in the $\hat{P}^{\text{in}}_{\text{L},\nu}$ field. As defined above, it effectively experiences the same losses and rotation as the narrowband atomic noise. The various power spectral densities above are defined in equations (SI B.6) and (SI B.7), with Fourier frequency dependencies Ω dropped for brevity. The diagonal entries related to light variables are all vacuum, therefore the indistinguishable labelling.

This allows us to calculate the spectral densities of the output signals as follows

$$\bar{\mathbf{S}}_{\text{out}} = \mathbf{U}^\dagger \bar{\mathbf{S}}_{\text{in}} \mathbf{U}, \tag{SI B.41}$$

where $\mathbf{U}^\dagger$ is conjugate-transpose matrix w.r.t. to $\mathbf{U}$. For instance, the (1,1) element of $\bar{\mathbf{S}}_{\text{out}}$ is the power spectral density of the mechanical oscillator position $\bar{S}_{X_{\text{M}} X_{\text{M}}}$.

We may now calculate the steady-state unconditional covariance matrix in the spin-mechanics subspace. For this we integrate $\bar{\mathbf{S}}_{\text{MS}}$, which we define as the submatrix of $\bar{\mathbf{S}}_{\text{out}}$ containing the first 4 rows and columns, leading to the unconditional covariance matrix

$$\mathbf{V}_u = \int_{-\infty}^{\infty} \frac{\text{d}\Omega}{2\pi} \bar{\mathbf{S}}_{\text{MS}}(\Omega). \tag{SI B.42}$$

Figures SI5a, SI6a, and SI7a present examples of $\mathbf{V}_u$ in different cases and bases.

Appendix C: Wiener filtering

In this Appendix we detail the central concepts of the conditional quantum state and the Wiener filtering procedure employed to extract conditional expectation values from measurement data.

A strong projective measurement of the initial system state $\hat{\rho}$ with a set of measurement operators $\{\hat{\Pi}_i\}$ generates a conditional quantum state $\hat{\rho}_c = \hat{\Pi}_i \hat{\rho} \hat{\Pi}_i / \text{Tr}(\hat{\Pi}_i \hat{\rho} \hat{\Pi}_i)$. In a quasi-continuous (multi-step) weak measurement, we replace the projection operators with a set of generalised measurement operators (positive operator-valued measures) acting repeatedly on the initial state [13, 14]. In general, prediction of the conditional state would require knowledge of operators associated with each measured value. For Gaussian states, the situation simplifies so that a linear, stationary filter can be used.

Given the weak, continuous character of our optical probing, useful measurement results must necessarily be obtained as (weighted) averages over finite segments of the homodyne measurement current. The appropriate temporal filter functions are defined by the system evolution during probing and the meter noise characteristics, necessitating precise knowledge of the equations of motion and the input-output relations. The methodology outlined here is known in classical physics and engineering as Kalman filtering, and its applicability to Gaussian quantum systems was proven in Refs. [15, 16] in a manner that we will now describe.

We note that our optical probing has the following two "classical" properties: First, the operators associated with the measurement current obtained at different times t and t' commute, $[\hat{P}^{\text{out}}_{\text{L}}(t), \hat{P}^{\text{out}}_{\text{L}}(t')] = 0$, implying their *simultaneous measurability*; second, causality entails that the measurement current at a given time t does not respond to the future system evolution (at times $t' > t$), in turn leading to the property $[\hat{P}^{\text{out}}_{\text{L}}(t), \hat{X}(t')] = 0$, $t' > t$, with $\hat{X}$ being any quadrature of a hybrid spin-mechanics system. Hence, the only manifestation of quantum mechanics in our probing scheme is that it enforces the presence of amplitude and phase (quantum) noise in the meter field according to the Heisenberg uncertainty relation. As the microscopic origin of the noise is immaterial to (classical) Wiener filtering theory, it follows from the above observations that it is applicable to our Gaussian quantum system.

As necessary prerequisites we introduce the PSD of the measurement current as $\bar{S}_{ii} \equiv \bar{S}_{P^{\text{meas}}_{\text{L}} P^{\text{meas}}_{\text{L}}}$ since $i(t)$ is the result of a quadrature measurement. In general, we aim to track the entire hybrid system characterised by $\boldsymbol{Q} = (\hat{X}_{\text{M}}, \hat{P}_{\text{M}}, \hat{X}_{\text{S}}, \hat{P}_{\text{S}})^\intercal$. Furthermore, we need to consider the signal-current correlation (cross-spectral density) row vector $\bar{\mathbf{S}}_{\boldsymbol{Q}i}$, which is the last row of $\bar{\mathbf{S}}_{\text{out}}$, Eq. (SI B.41). The spectral densities $\bar{S}(\Omega)$ are used to compute temporal correlation functions $\bar{C}(\tau)$ using the inverse Fourier transform thanks to the Wiener-Khinchin theorem.

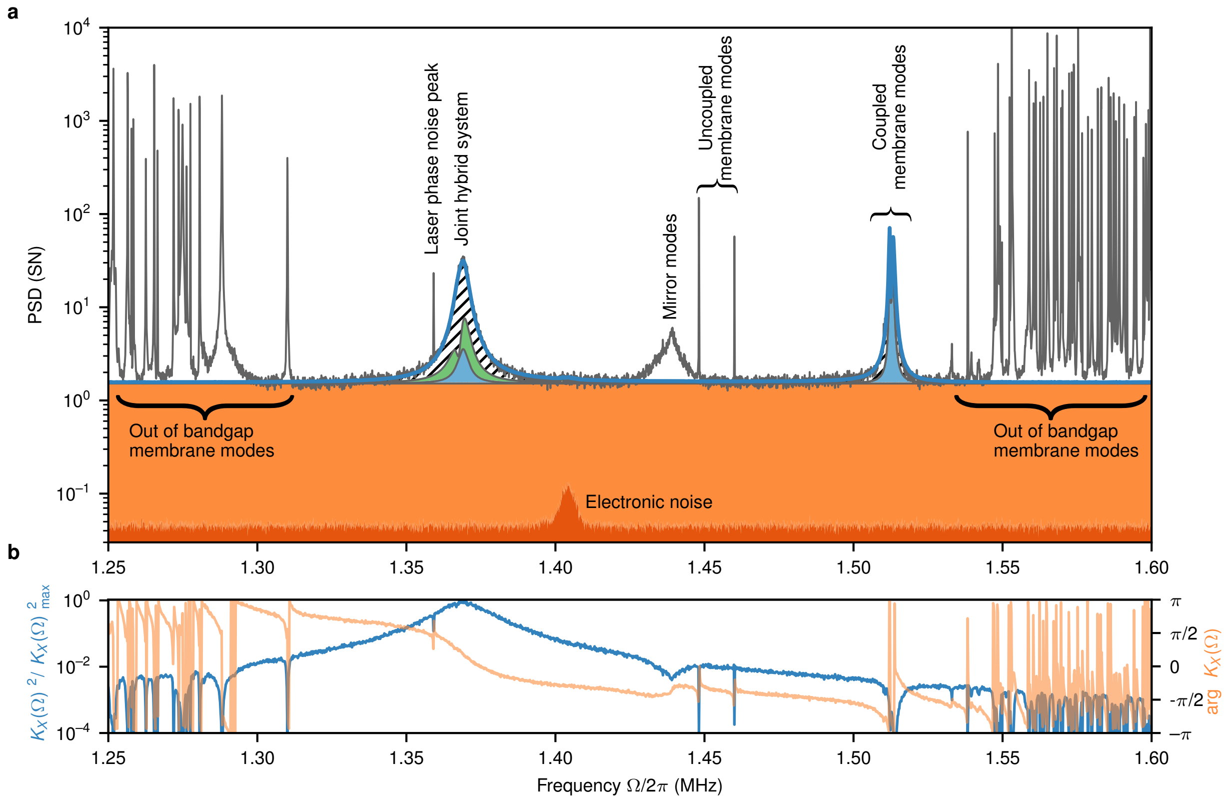

Figure SI4. **Spectra from Fig. 3b and associated Wiener filter from Fig. 3c shown in a wider range. a,** the spectrum is again decomposed into the same components as in Fig. 3b, yet including the electronic detection noise (dark orange). Furthermore, additional membrane modes are visible in the experimental data. We model two of those modes, around 1.52 MHz, including their back-action. Those are the only high-Q modes in the bandgap that are significantly coupled to light, which stretches from 1.31 to 1.54 MHz. Notably, the additional modes are treated as noise in the process of detecting the motion of the main defect mode of interest and the motion of spins. **b,** Wiener filter for the hybrid EPR system (squared normalised amplitude, left axis, phase, right axis). The filter automatically allows efficient tracking of the main EPR signal with other sources of noise removed in the form of frequency notch filters. Notably, the Wiener filter is significantly broader than the linewidth of the system itself.

Our hybrid system is driven solely by optical and thermal forces with wide-sense stationary noise statistics (i.e., constant first and second moments of all noises, and all covariances depending only on the time difference $t-t'$) [17]. Under these circumstances the appropriate set of causal filters $\mathbf{K}$ for purposes of estimating the system first and second moments is the so-called *Wiener filter* [18]. Convolving the filter with the measurement current yields the best unbiased estimate of the system variables (i.e., with the minimum mean-square error):

$$\boldsymbol{Q}^c_\infty(t) = \int_{-\infty}^{t} \mathbf{K}(t'-t) i(t')\,\mathrm{d}t', \tag{SI C.1}$$

where $\boldsymbol{Q}^c = (X^c_{\mathrm{M}}, P^c_{\mathrm{M}}, X^c_{\mathrm{S}}, P^c_{\mathrm{S}})^\intercal$ is the conditional trajectory in the steady-state scenario, i.e., for the case where we have $i(t)$ for all previous times available. In a more general case, where upon conditioning we increase the length of past data, we generally write:

$$\boldsymbol{Q}^c(t) = \int_{0}^{t} \mathbf{K}(t'-t, t) i(t')\,\mathrm{d}t', \tag{SI C.2}$$

where $\mathbf{K}(\tau, t)$ is the filter function, t' is the running argument of convolution and t is the length of the conditioning interval.

To find the Wiener filters $\mathbf{K}$, we solve the Wiener-Hopf equations, which state that the optimal $\boldsymbol{Q}^c(t)$ must obey

$$\bar{\mathbf{C}}_{\boldsymbol{Q}^c i}(t') = \bar{\mathbf{C}}_{\boldsymbol{Q} i}(t'), \tag{SI C.3}$$

for all t' within the conditioning window. In the limit of infinite conditioning time, the Wiener-Hopf equation (SI C.3) is typically stated as

$$\int_0^\infty \mathbf{K}^\intercal(-t'')\bar{C}_{ii}(t'-t'')\,\mathrm{d}t'' = \bar{\mathbf{C}}_{\boldsymbol{Q} i}(t') \quad \forall\, t' \geq 0, \tag{SI C.4}$$

where $\bar{\mathbf{C}}_{\boldsymbol{Q} i}(t')$ is the cross-correlation between $\boldsymbol{Q}$ and i calculated as the inverse Fourier transform of $\bar{\mathbf{S}}_{\boldsymbol{Q} i}(\Omega)$, which is a row vector of cross-spectral densities (first four elements of the last row of $\bar{\mathbf{S}}_{\mathrm{out}}$, Eq. (SI B.41)). The vector form of the above equation should here be understood as 4 independent equations.

If we only have data available for a finite past, we limit the above infinite integral to t and find the finite-input response filter $\mathbf{K}(t', t)$ as a solution of

$$\int_0^t \mathbf{K}^\intercal(-t'', t)\bar{C}_{ii}(t'-t'')\,\mathrm{d}t'' = \bar{\mathbf{C}}_{\boldsymbol{Q} i}(t') \quad \forall\, t' \in [0, t]. \tag{SI C.5}$$

In this form, the Wiener-Hopf equation can also be easily discretised and cast in a matrix equation form. The solution is then obtained via the Levinson–Durbin recursion algorithm. It is noteworthy that in the finite-time limit, the Wiener filter $\mathbf{K}(t', t)$ is only defined for $-t < t' < 0$, in accordance with the integration domain in Eq. (SI C.2).

While the trajectory $\boldsymbol{Q}^c$ is stochastic, the variance of residual fluctuations is deterministic; it can be calculated as the difference between the *unconditional* covariance matrix $\mathbf{V}_u$ and the (ensemble) covariance matrix of the best estimates $\mathbf{V}_{\mathrm{be}}$,

$$\mathbf{V}_c = \mathbf{V}_u - \mathbf{V}_{\mathrm{be}}, \tag{SI C.6}$$

where

$$\mathbf{V}_{\mathrm{be}} = \int_0^\infty \mathbf{K}(-t)\bar{\mathbf{C}}_{\boldsymbol{Q} i}(t)\,\mathrm{d}t = \mathrm{Cov}(\boldsymbol{Q}, \boldsymbol{Q}^c_\infty), \tag{SI C.7}$$

is the 4 by 4 covariance matrix of the best estimates and $\boldsymbol{Q}^c(t)$ is given by Eq. (SI C.1). In the case of a finite conditioning interval, we again limit the integration:

$$\mathbf{V}_{\mathrm{be}}(t) = \int_0^t \mathbf{K}(-t', t)\bar{\mathbf{C}}_{\boldsymbol{Q} i}(t')\,\mathrm{d}t' = \mathrm{Cov}(\boldsymbol{Q}, \boldsymbol{Q}^c(t)), \tag{SI C.8}$$

where $\boldsymbol{Q}^c(t)$ is defined by Eq. (SI C.2). Again, Eq. (SI C.6) holds, and hence captures how the conditional variance evolves as we increase the conditioning time t. The relation $\mathbf{V}_{\mathrm{be}}(t) = \mathrm{Cov}(\boldsymbol{Q}, \boldsymbol{Q}^c(t))$ implied by Eq. (SI C.8) follows directly from the Wiener-Hopf equation (SI C.3) by convolving it with $\mathbf{K}$ (as does the special case (SI C.7)).

We present the obtained Wiener filter, for the point with best entanglement (see SI D), in Fig. 3 of the main text, and for a wider frequency range in Fig. SI4. The time evolution of the conditional variance is shown in Fig. 1, and the final V_{c} is shown in Fig. 4.

Finally, it is noteworthy that the Wiener filter shares many characteristics with the widely used Kalman filter. In fact, the Wiener filter is a specific case of a Kalman filter where it can be obtained from the Wiener-Hopf equations since both noise and signal are wide-sense stationary. This still applies to our case of a finite-input response filter $\mathbf{K}(t', t)$, as to find it we assume stationary noise. In fact, the finite-input response (FIR) Wiener filters are widely used in engineering contexts. In a more general case one needs to solve Kalman equations that are qualitatively different.

Appendix D: Entanglement estimation

Let us now analyse the properties of the covariance matrices, obtained using the hybrid system model (SI B) and Wiener filtering (SI C), and estimate the entanglement of the bipartite state. In Fig. SI5(a) the covariance matrix $\mathbf{V}_u$ corresponding to the case with best entanglement is presented. Diagonal elements represent the occupations of individual oscillators. The conditioning procedure is then applied to obtain $\mathbf{V}_c$ in Fig. SI5(b). Notably, we observe strong positive correlation between $\hat{X}_{\mathrm{M}}$ and $\hat{X}'_{\mathrm{S}}$ as well as negative correlation between $\hat{P}_{\mathrm{M}}$ and $\hat{P}'_{\mathrm{S}}$. Furthermore, we can see that the conditioning procedure mostly allow us to decrease the conditional occupation of the mechanical subsystem, which is most efficiently measured. The spin variables here are rotated, i.e., $\hat{X}'_{\mathrm{S}} = \hat{X}_{\mathrm{S}} \cos\beta + \hat{P}_{\mathrm{S}} \sin\beta$, $\hat{P}'_{\mathrm{S}} = \hat{P}_{\mathrm{S}} \cos\beta - \hat{X}_{\mathrm{S}} \sin\beta$ such the anti-diagonal of $\mathbf{V}_c$ is nulled.

The estimation of the best entangled state involves the construction the general EPR variables

$$\hat{X}_{\mathrm{EPR}} = (\hat{X}_{\mathrm{M}} - a\hat{X}'_{\mathrm{S}})/\sqrt{1+a^2} = \boldsymbol{u}_X^{\intercal}\boldsymbol{Q}, \tag{SI D.1}$$

$$\hat{P}_{\mathrm{EPR}} = (\hat{P}_{\mathrm{M}} + a\hat{P}'_{\mathrm{S}})/\sqrt{1+a^2} = \boldsymbol{u}_P^{\intercal}\boldsymbol{Q}, \tag{SI D.2}$$

$$\hat{\boldsymbol{X}}_{\mathrm{EPR}} = \mathbf{u}^{\intercal}\boldsymbol{Q} \tag{SI D.3}$$

(with matrix $\mathbf{u}$ having vectors $\boldsymbol{u}_X$ and $\boldsymbol{u}_P$ as columns) along with canonically conjugated variables

$$\hat{X}'_{\mathrm{EPR}} = (\hat{X}_{\mathrm{M}} + a\hat{X}'_{\mathrm{S}})/\sqrt{1+a^2} \tag{SI D.4}$$

$$\hat{P}'_{\mathrm{EPR}} = (\hat{P}_{\mathrm{M}} - a\hat{P}'_{\mathrm{S}})/\sqrt{1+a^2} \tag{SI D.5}$$

where a is the relative weight of the spin component with respect to mechanics and β is the rotation angle of the spin component, and $\boldsymbol{u}_X$ and $\boldsymbol{u}_P$ are unit-length vectors. The EPR variance (conditional or unconditional) $V = \mathrm{Var}[\hat{X}_{\mathrm{EPR}}] + \mathrm{Var}[\hat{P}_{\mathrm{EPR}}]$ is evaluated using the covariance matrix $\mathbf{V}$ as

$$V_{a,\beta} = \boldsymbol{u}_X^{\intercal}\mathbf{V}\boldsymbol{u}_X + \boldsymbol{u}_P^{\intercal}\mathbf{V}\boldsymbol{u}_P. \tag{SI D.6}$$

For the present data, $a \approx 0.85$, which is approximately constant for all data point, and $\beta \approx 20°$ for the point of best entanglement. For different spin-mechanics detuning optimal β varies by tens of degrees. We have minimised the EPR variance $V = \min_{a,\beta} V_{a,\beta}$ for both parameters individually for each dataset.

Having defied the EPR basis we can now also plot the same matrix as in Fig. SI5 in the new basis, see Fig. SI6. Here, we observe that for $\mathbf{V}_c$ the variance of the EPR components on the diagonal indeed reaches below the classical limit of 0.5.

Finally, we compared the entangled case with the far-detuned case, presented in Fig. SI7. Here we observe negligible off-diagonal correlation terms, and also significantly lower unconditional occupation for mechanics, as it is not driven by the spin noise. Furthermore, the conditioning procedure can now distinguish the systems and efficiently brings down their respective conditional variances.

To generate the conditional trajectory in Fig. 1(c) we first solve Eq. (SI C.5) for a set of conditioning times t and find a collection of Wiener filters $\mathbf{K}(t', t)$. We then use the filters to get $\boldsymbol{Q}^c(t)$ as given by Eq. (SI C.2) as well as conditional covariance matrices $\mathbf{V}_c(t)$ (see Eqs. (SI C.6) and (SI C.8)). We then find the optimal a and β for the $\mathbf{V}_c$ associated with $t \to \infty$, which gives us $\mathbf{u}$. Subsequently, $\boldsymbol{X}^c_{\mathrm{EPR}} = \mathbf{u}^{\intercal}\boldsymbol{Q}^c$ is calculated. Finally we move to a rotating frame by $\tilde{\boldsymbol{X}}^c_{\mathrm{EPR}} = \mathbf{O}_{\omega t}\boldsymbol{X}^c_{\mathrm{EPR}}$ with $\omega/2\pi = 1.37\,\mathrm{MHz}$, which is rather an arbitrary choice since for the EPR oscillator there is no single distinguished frequency unless $\omega_{\mathrm{M}} = |\omega_{\mathrm{S}}|$ exactly, which is not the case.

We observe $\mathrm{Var}[\hat{X}] \approx \mathrm{Var}[\hat{P}]$ for all cases (Figs. SI5–SI7) consistent with our system operating within the regime of validity for the Rotating Wave Approximation.

Appendix E: Uncertainties

We apply elaborate statistical techniques to deduce the statistical uncertainty for the value of the degree of entanglement.

Spectra corresponding to points in Fig. 4b are fitted collectively to the same model. A subset of the parameters is shared between all spectra, while others are allowed to fluctuate from spectrum to spectrum, representing small short-timescale fluctuations.

The parameters that are allowed to change from spectrum to spectrum are atomic frequency, $\mathrm{LO}_1{+}\mathrm{LO}_2$ phase φ, cavity detuning Δ, and mechanical coupling rate g. The drift of the latter two can be explained by a spurious interference, which turns drifts in φ into drifts in optical power in LO_2, which in turns leads to a change in Δ and thus also g. The typical size of drifts of φ is ~ 3 degrees.

We establish prior probabilities for all parameters by independent measurements and calibrations, many of which we explain above. We use those priors for our parameters, together with the spectra and their statistical uncertainties to perform a log-likelihood optimisation. We use Gaussian priors for the parameters and assume a relative Gaussian error of 8 %, stemming from the number of samples for each spectrum $N_{\mathrm{samp}} = 200$, i.e., the statistical variance of the

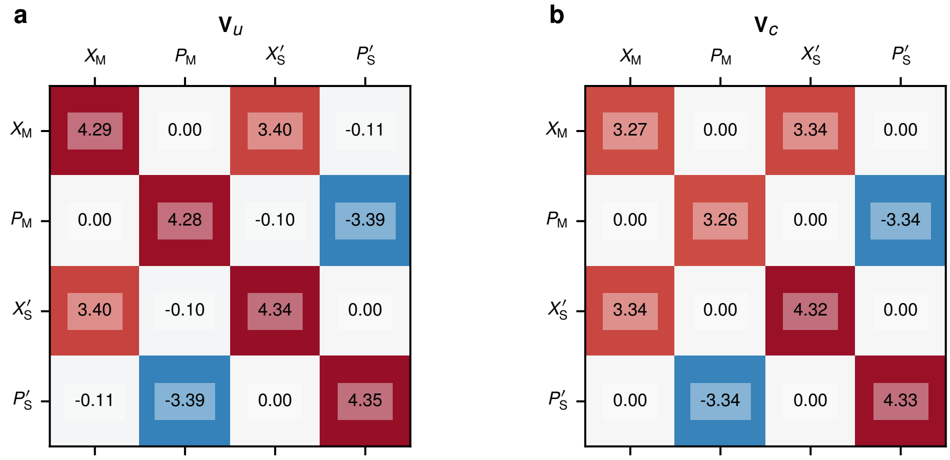

Figure SI5. **Covariance matrices in the individual single-system basis**, for the dataset with $|\omega_S| - \omega_M \approx -\gamma_M/2$. Angle β is adjusted so that anti-diagonal in **b** is 0. **a,** Unconditional and **b,** conditional covariance matrices.

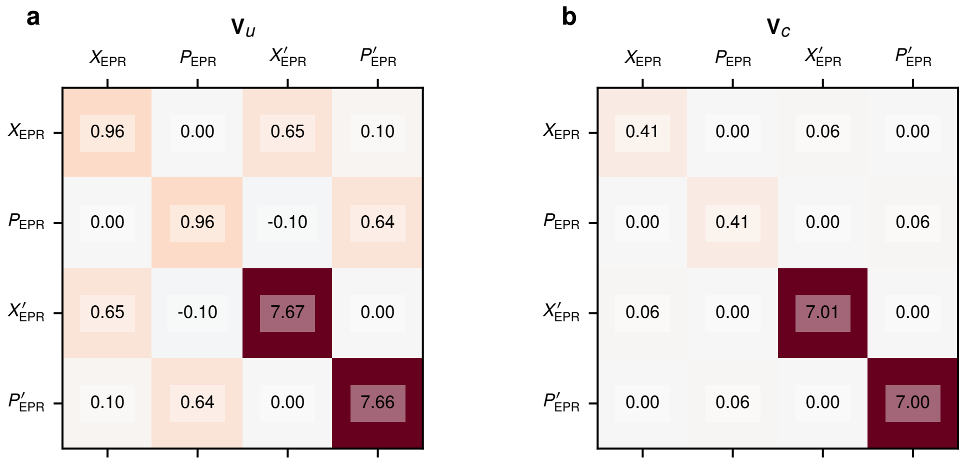

Figure SI6. **Covariance matrices in the EPR basis**, for the dataset with $|\omega_S| - \omega_M \approx -\gamma_M/2$. **a,** Unconditional and **b,** conditional covariance matrices.

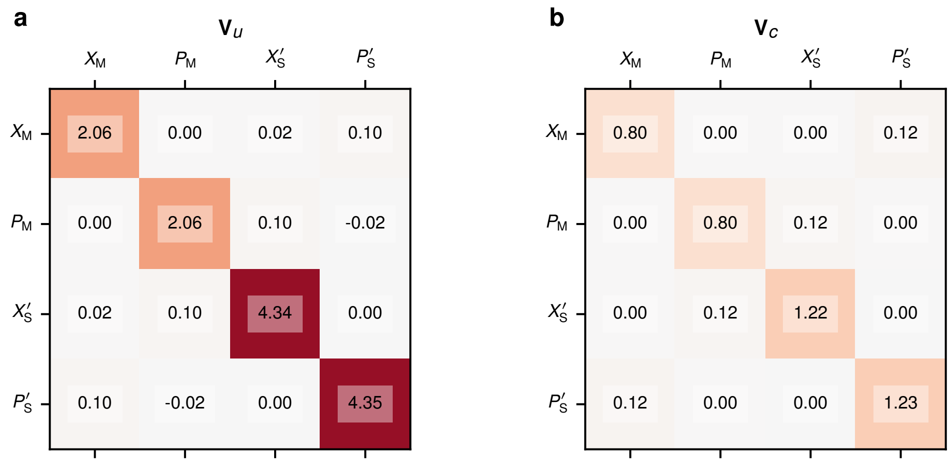

Figure SI7. **The covariance matrices in the detuned case**, expressed in the individual system basis. Same rotation angle β as in Fig. SI5 for the atomic subsystem is applied here. **a,** Unconditional and **b,** conditional covariance matrices.

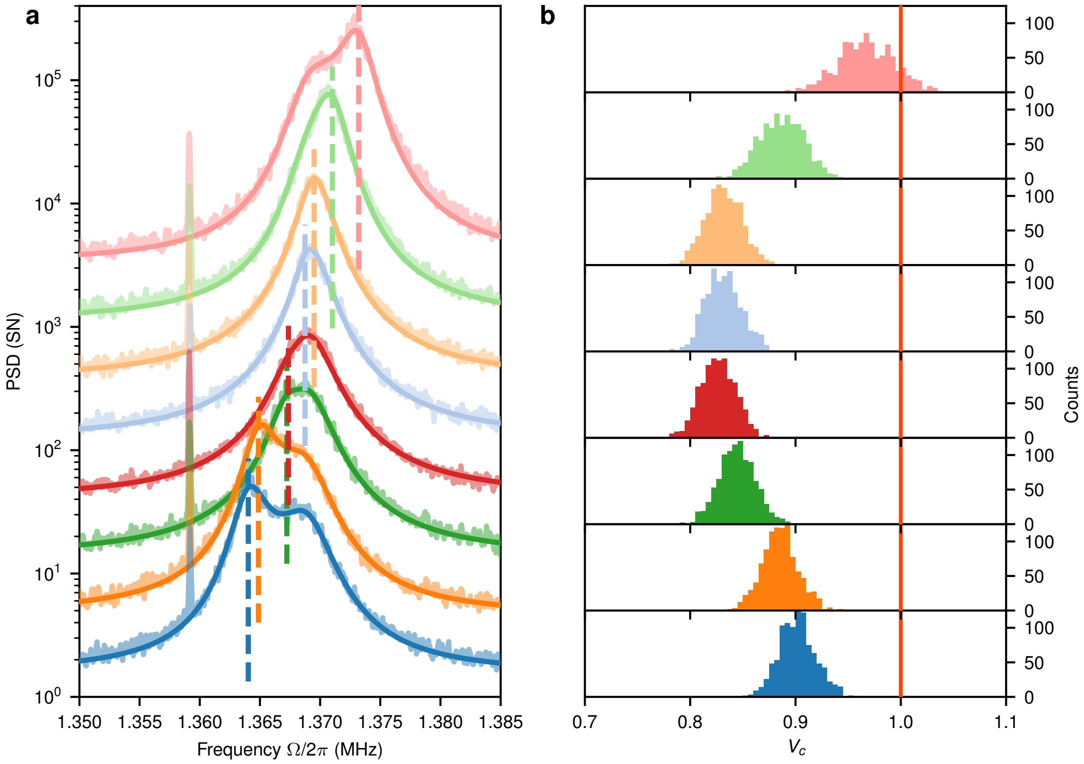

Figure SI8. **Entanglement tuning and optimisation. a,** Fit results for varied atomic frequencies ω_S for all points shown in Fig. 4. For clarity, subsequent lines are offset vertically by multiplying by a constant factor. **b,** MCMC results for the conditional variance for all atomic detunings. Mean and standard deviation leads to the points in Fig. 4b.

periodogram estimator, and additional uncertainty due to shot-noise level calibration. We additionally assume the level of data uncertainty to have an extra constant offset of 0.1 SN units to account for the presence of small mirror mode peaks beneath the signal.

Due to the vast parameter space, originating partly from the collective fitting with both shared and non-shared parameters, we perform the optimisation with Markov Chain Monte Carlo (MCMC) simulations [19]. We run 150 walkers with 4000 burn-in steps and subsequent 6000 sampling steps. From these 900 000 points, we select 1000 random samples for which we compute entanglement. This sampling of the log-likelihood landscape leads directly to posterior probabilities for the parameters for each spectrum, and, more importantly, also for derived values, such as the conditional variance. The choice of the number of samples for the entanglement calculation is determined by the computational cost of evaluating the conditional variance. Sampling those 1000 points from a larger set of MCMC points reduces the co-variance of the points sampling of the posterior log-likelihood landscape.

The MCMC fitting routine results in a set of parameters with good agreement between priors and posteriors for almost all parameters. The main discrepancy is for the case of inter-system quantum efficiency; here, the posterior value of $\nu = 0.53$ is significantly lower than the anticipated value of $\nu_{\text{prior}} = 0.65 \pm 0.03$. In addition, we obtain a slightly lower posterior detection efficiency $\eta = 0.77$ than $\eta_{\text{prior}} = 0.80 \pm 0.03$ and higher overcoupling $(\kappa_{\text{in}}/\kappa) = 0.925 \pm 0.005$ than $(\kappa_{\text{in}}/\kappa)_{\text{prior}} = 0.91 \pm 0.01$. The extra optical losses are currently unaccounted for, with possible explanations for this discrepancy that include mode matching and polarisation-dependent losses of our quantum signal. We should stress that this discrepancy leads only to a reduction of the obtained entanglement. The atomic parameters are kept reasonably within the prior bounds with $\Gamma_{\text{S,prior}}/2\pi = (18 \pm 1)$ kHz and posterior $\Gamma_{\text{S}}/2\pi = (20.3 \pm 0.4)$ kHz as well as $n_{\text{S,prior}} = 0.72 \pm 0.05$ and posterior $n_{\text{S}} = 0.81 \pm 0.05$.

* These authors contributed equally to the work
*,† These authors contributed equally to the work; Currently at: ICFO – Institut De Ciencies Fotoniques, The Barcelona Institute of Science and Technology, Castelldefels, Spain
‡ Currently at: Pritzker School of Molecular Engineering, University of Chicago, Chicago, USA
§ Currently at: Danish Fundamental Metrology, Hørsholm, Denmark
¶ Corresponding author: polzik@nbi.ku.dk

[1] Balabas, M. V. *et al.* High quality anti-relaxation coating material for alkali atom vapor cells. *Opt. Express* **18**, 5825–5830 (2010).
[2] Julsgaard, B., Sherson, J., Sørensen, J. L. & Polzik, E. S. Characterizing the spin state of an atomic ensemble using the magneto-optical resonance method. *Journal of Optics B: Quantum and Semiclassical Optics* **6**, 5 (2004).
[3] Agarwal, G. S. & Chaturvedi, S. Scheme to measure quantum stokes parameters and their fluctuations and correlations. *Journal of Modern Optics* **50**, 711–716 (2003).
[4] Borregaard, J. *et al.* Scalable photonic network architecture based on motional averaging in room temperature gas. *Nature Communications* **7**, 11356 (2016).
[5] Thomas, R. A., *et al.* Atomic Spin System Calibrations by Coherently Induced Faraday Rotation. In preparation.
[6] Weis, S. *et al.* Optomechanically induced transparency. *Science* **330**, 1520–1523 (2010).
[7] Møller, C. B. *et al.* Quantum back-action-evading measurement of motion in a negative mass reference frame. *Nature* **547**, 191–195 (2017).
[8] Tsaturyan, Y., Barg, A., Polzik, E. S. & Schliesser, A. Ultracoherent nanomechanical resonators via soft clamping and dissipation dilution. *Nature Nanotechnology* **12**, 776–783 (2017).
[9] Jayich, A. M. *et al.* Dispersive optomechanics: A membrane inside a cavity. *New Journal of Physics* **10**, 095008 (2008).
[10] Nielsen, W. H. P., Tsaturyan, Y., Møller, C. B., Polzik, E. S. & Schliesser, A. Multimode optomechanical system in the quantum regime. *Proceedings of the National Academy of Sciences* **114**, 62–66 (2017).
[11] Julsgaard, B. *Entanglement and Quantum Interactions with Macroscopic Gas Samples.* PhD dissertation, University of Aarhus (2003).
[12] Wasilewski, W. *et al.* Generation of two-mode squeezed and entangled light in a single temporal and spatial mode. *Opt. Express* **17**, 14444–14457 (2009).
[13] Carmichael, H. *An Open Systems Approach to Quantum Optics* (Springer, Berlin, Heidelberg, 1993).
[14] Helstrom, C. W. *Quantum detection and estimation theory* (Academic Press, 1976).
[15] Müller-Ebhardt, H. *et al.* Quantum-state preparation and macroscopic entanglement in gravitational-wave detectors. *Phys. Rev. A* **80**, 043802 (2009).
[16] Miao, H. *Exploring Macroscopic Quantum Mechanics in Optomechanical Devices.* Ph.D. thesis, University of Western Australia (2010).
[17] Broersen, P. M. T. *Automatic Autocorrelation and Spectral Analysis* (Springer-Verlag, Berlin, Heidelberg, 2006).
[18] Wiener, N. *Extrapolation, Interpolation, and Smoothing of Stationary Time Series: With Engineering Applications.* Massachusetts Institute of Technology : Paperback series (M.I.T. Press, 1964).
[19] Foreman-Mackey, D., Hogg, D. W., Lang, D. & Goodman, J. emcee: The MCMC hammer. *Publications of the Astronomical Society of the Pacific* **125**, 306–312 (2013).

Parameter	Symbol	Value
	Atomic spin oscillator	
Decoherence rate in the dark	$\gamma_{\mathrm{S0,dark}}/2\pi$	450 Hz
Intrinsic linewidth	$\gamma_{\mathrm{S0}}/2\pi$	1.7 kHz
Effective linewidth (incl. dynamical damping)	$\gamma_{\mathrm{S}}/2\pi$	2.9 kHz
Tensor contribution	ζ_{S}	0.028
LO_1 driving power		350 µW
Readout rate	$\Gamma_{\mathrm{S}}/2\pi$	20 kHz
Spin Polarisation	p	0.82
Spin thermal occupancy	n_{S}	0.8
Microcell temperature		50°C
	Mechanical oscillator and cavity	
Intrinsic mechanical frequency	$\omega_{\mathrm{M0}}/2\pi$	1.370 MHz
Intrinsic damping rate	$\gamma_{\mathrm{M0}}/2\pi$	2.1 mHz
Optical damping rate	$\gamma_{\mathrm{M}}/2\pi$	3.9 kHz
Cavity detuning	$\Delta/2\pi$	−0.7 MHz
Total cavity linewidth	$\kappa/2\pi$	4.2 MHz
LO_2 drive power		∼8 µW
Intracavity photons	N	1.6×10^6
Single photon coupling rate	$g_0/2\pi$	6×10^1 Hz
Readout rate	$\Gamma_{\mathrm{M}}/2\pi$	15 kHz
Cavity overcoupling	$\kappa_{\mathrm{in}}/\kappa$	0.93
Thermal bath temperature	T	11 K
Bath occupancy	n_{M0}	173×10^3
Mean occupancy	n_{M}	~ 2
Quantum cooperativity	$C_{\mathrm{q}}^{\mathrm{M}}$	15
	Hybrid & detection	
Quantum efficiency between systems	ν	0.53
Cavity mode-matching (amplitude)		0.9
Power transmission between systems		0.8
Detection efficiency	η	0.77
Homodyning visibility		0.96
Power transmission and detector QE		0.87
LO_1–LO_2 phase	φ	∼180°
Detection phase	ϑ	2°

Table SI1. **Summary of notation and experimental parameters.** When applicable, we quote the posterior mean values from the MCMC simulation.

APPENDIX F

Published by Optics Express: Calibration of spin-light coupling by coherently induced Faraday rotation

Rodrigo A. Thomas, Christoffer Østfeldt, **Christian Bærentsen**, Michał Parniak, and Eugene S. Polzik, *Calibration of spin-light coupling by coherently induced Faraday rotation*. Optics Express 29, 23637-23653 (2021)

Research Article | Vol. 29, No. 15 / 19 July 2021 / *Optics Express* 23637
Optics EXPRESS

Calibration of spin-light coupling by coherently induced Faraday rotation

RODRIGO A. THOMAS,[1,*] CHRISTOFFER ØSTFELDT,[1] CHRISTIAN BÆRENTSEN,[1] MICHAŁ PARNIAK,[1,2] AND EUGENE S. POLZIK[1]

[1] *Niels Bohr Institute, University of Copenhagen, Copenhagen, Denmark*
[2] *Centre for Quantum Optical Technologies, Centre of New Technologies, University of Warsaw, Warsaw, Poland*
[*] *rathomas@nbi.ku.dk*

Abstract: Calibrating the strength of the light-matter interaction is an important experimental task in quantum information and quantum state engineering protocols. The strength of the off-resonant light-matter interaction in multi-atom spin oscillators can be characterized by the readout rate Γ_S. Here we introduce the method named Coherently Induced FAraday Rotation (CIFAR) for determining the readout rate. The method is suited for both continuous and pulsed readout of the spin oscillator, relying only on applying a known polarization modulation to the probe laser beam and detecting a known optical polarization component. Importantly, the method does not require changes to the optical and magnetic fields performing the state preparation and probing. The CIFAR signal is also independent of the probe beam photo-detection quantum efficiency, and allows direct extraction of other parameters of the interaction, such as the tensor coupling ζ_S, and the damping rate γ_S. We verify this method in the continuous wave regime, probing a strongly coupled spin oscillator prepared in a warm cesium atomic vapour.

1. Introduction

The off-resonant interface of light with atomic ensembles has been widely explored in the last decades [1–4] in ultra-cold, cold and warm alkali implementations. The spin degree of freedom in the atomic ground state coherences and its coupling to light has been used in protocols ranging from fundamental [5–8] to technological [9–11] applications. Furthermore, the collective spin excitations of the highly polarized atomic ensembles in a static magnetic field can be well approximated by harmonic oscillator-like degrees of freedom – a spin oscillator [12]. The oscillator mapping, i.e., the effective description of the collective spin system as single harmonic oscillator, helps facilitate the interface with nano-mechanical oscillators via back-action evasion [13] and entangling [14] measurements, which promises sensitivity improvements in future gravitational wave detectors [15] and optical quantum control of the hybrid spin-mechanical system [16].

In the interface between atoms and light, characterizing the strength with which the systems couple is paramount for understanding their dynamics. According to the principles of quantum mechanics, the statistical nature of the quantum measurement process leads to fundamental limits in estimation of a systems state at a given instant of time [17]. Optimizing the measurement performed by the optical probe interacting with the spin oscillator, according to the application or protocol in mind, is key to optimally estimating the state of the system.

While the method discussed in this paper can be described in a fully classical manner, it is relevant to experiemnts in which quantum noise plays an important role. For instance, the optical readout of a highly polarized atomic ensemble prepared in a spin oscillator state contains contributions arising from [18]: optical shot noise, inherent to the quantum nature of light in the process of photo-detection; coherent spin state or ground state noise, from the zero-point energy required to satisfy the Heisenberg uncertainty principle; thermal noise, originating from the extra

#425613 https://doi.org/10.1364/OE.425613
Journal © 2021 Received 25 Mar 2021; revised 8 Jun 2021; accepted 8 Jun 2021; published 12 Jul 2021

spin fluctuations of the oscillator having non-zero mean occupancy n_S due to imperfect optical pumping; and lastly, quantum back-action noise, originating from the perturbations of the optical readout in the oscillator's dynamics. As we obtain information about the oscillator by performing measurements on the light that has interacted with the system, it is of key importance to faithfully characterize the weight of each of these contributions, which scale differently with Γ_S.

The standard quantum limit (SQL) for a measurement of mechanical displacements, for example, sets the sensitivity to external fields in conventional interferometric measurements [19]. At the SQL, the detection shot noise and measurement back-action contribute equally to the measurement imprecision. Another figure of merit that quantifies the efficiency of the coupling is the quantum cooperativity C_q, here defined as $C_q = \frac{\Gamma_S}{2\gamma_S(n_S+1/2)}$. Working in the regime $C_q \gg 1$, in which the coupling is strong, indicates that the measurement significantly influences the oscillator dynamics, allowing for its control and manipulation. A highly efficient mapping of the oscillator state to light requires the quantum back-action to dominate over the coupling to the thermal environment [4]. Common to these protocols is the importance of the interaction strength parameter between light and the oscillator, here defined as the readout rate Γ_S (also commonly known as the measurement rate in the optomechanics community [20]). Knowledge of this constant facilitates evaluating the regime of interaction, but also allows quantifying the sensitivity in absolute terms or with respect to the SQL.

In this paper, we show how the parameter Γ_S may be extracted from a measurement based on the interference of the induced Faraday rotation, i.e., the oscillator response to a classical optical polarization modulation, with the modulation itself. We call it Coherently Induced FAraday Rotation, or CIFAR, signal. The method further allows extraction of the damping rate, γ_S, and the tensorial part of the interaction, ζ_S, describing the deviation from the idealized quantum non-demolition (QND) interaction. Crucially this method relies on the same alignment of magnetic and optical fields as well as optical pumping of the atomic ensemble, as used for experiments such as [13,14], and thus does not require any modifications to the experimental setup to perform the characterisation. The CIFAR method is applicable in all experimental implementations of spin oscillators, from ultra-cold to warm vapors, in ensembles with total angular momentum (per atom) equal to or larger than $\frac{1}{2}$. The coherent drive also allows for probing the atomic motion through the laser beam [21] and characterizing the coupling to fast decaying spin modes [22], which give rise to a broadband spin response. We verify the CIFAR in the continuous regime, probing a spin oscillator in the strong coupling regime, prepared in a warm cesium atomic vapour. Lastly, we also explore the limits of our linearized oscillator description by driving the system with large classical polarization modulation.

Our experimental setup is depicted in Fig. 1. We use a spin-polarized atomic spin ensemble prepared in an uniform magnetic field, probed by an optical local oscillator that is weakly polarization modulated. This interaction drives the collective spin which again induces a Faraday rotation of the light polarization, which is detected in a self-homodyning configuration. The following signal is referred to as the CIFAR signal. See the experimental section for a specific description of the technical details.

The content will be outlined as follows, In Section 2 the theoretical framework will by laid out, in Section 3 the technical specifics of our experiment will be put forward, while in Section 4 the data and model fitting is presented, before discussing further work and limitations of our work in Section 5.

The technique here described is especially suited for continuous wave measurement of (single) spin oscillators, which should be contrasted with the mean value transfer method [10] and thermal noise scaling [23], which rely on time consuming measurements and more dramatic changes of the experimental setup. We nonetheless highlight that this technique can also be employed in the canonical state-preparation-probing experimental cycle. Furthermore, the signal depends only on the interference between the drive and response, it is independent of the overall detection

Optics EXPRESS

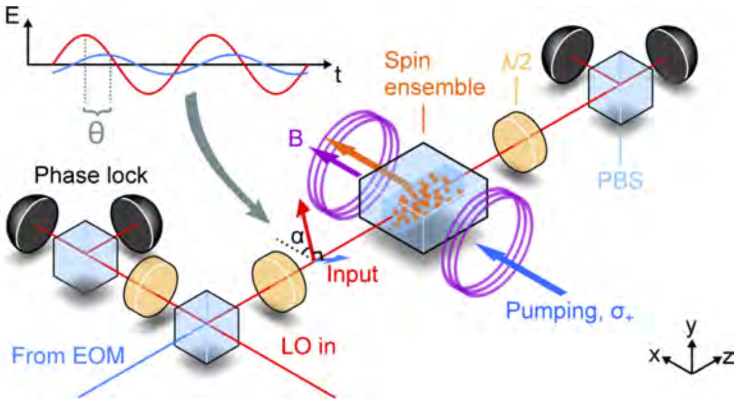

Fig. 1. Experimental setup. A strong linearly polarized LO (red) is mode matched to a weaker, phase modulated beam from an EOM (blue) on a PBS. Part of the light is sent to a polarization sensitive detection setup, which is used to stabilize the relative phase between the two beams. The atomic input is sent through an optically polarized room temperature alkali spin ensemble (orange circles), situated in a homogeneous magnetic field B (purple). The collective total spin vector (orange) modulates the input light polarization due to the Faraday interaction, while the light also drives the spin. The field at the output of the ensemble is detected in a polarization self-homodyning setup. Technical details are more thoroughly described in Section 3, experimental implementation. EOM: Electro-optic modulator. LO: Local Oscillator. PBS: Polarizing beamsplitter. $\lambda/2$: Half wave plate.

quantum efficiency and thermal noise calibrations, as the calibration used in [13]. The CIFAR method is similar to the Optomechanically Induced Transparency (OMIT)-response measurement technique [24], used to characterize optomechanical coupling parameters [25].

2. Theory

The interaction between an atomic ensemble and light has been widely studied in the context of optical pumping [1] and quantum information applications [4]. For a far detuned monochromatic optical field with intensity much below saturation, the effective atom-light interaction is given by the coupling of the electronic-ground-state magnetic sublevels to the light polarization. The interaction can be seen as a mutual rotation of the light and spin variables, the Stokes operators $\{\hat{S}_x, \hat{S}_y, \hat{S}_z, \hat{S}_0\}$ and spin operators $\{\hat{J}_x, \hat{J}_y, \hat{J}_z, \hat{J}_0\}$ respectively, in the form of polarization-dependent ac Stark shifts of the ground state levels and spin-state-dependent index of refraction, according to the atomic polarizability tensor [26,27]. The collective macroscopic spin being represented as $\hat{J}_{x,y,z} = \sum_{i=1}^{N} \hat{F}^{(i)}_{x,y,z}$, where $\hat{F}^{(i)}_{x,y,z}$ are the Cartesian decomposition of the total angular momentum operator of a single atom.

The light-matter interaction, along with the contribution from an external bias magnetic field applied in the x-direction, gives the spin Hamiltonian for a single atom

$$\begin{aligned}\hat{H}^{(i)}_{\mathrm{S}}/\hbar = \pm\omega_{\mathrm{S}}\hat{F}^{(i)}_x + g_{\mathrm{S}}\Big[&a_0\hat{S}_0 + a_1\hat{S}_z\hat{F}^{(i)}_z + \\ &2a_2\left[\hat{S}_0(\hat{F}^{(i)}_z)^2 - \hat{S}_x((\hat{F}^{(i)}_x)^2 - (\hat{F}^{(i)}_y)^2) - \hat{S}_y(\hat{F}^{(i)}_x\hat{F}^{(i)}_y + \hat{F}^{(i)}_y\hat{F}^{(i)}_x)\right]\Big],\end{aligned} \tag{1}$$

where the first term refers to the the linear Zeeman effect induced bias magnetic field, shifting adjacent ground state magnetic sublevels by $\pm\omega_{\mathrm{S}}$, with sign depending on the direction of the magnetic field with respect to the x-axis. The coefficients a_0, a_1, and a_2 as the relative weights of the scalar, vector and tensor contributions of the polarizability tensor [27], and g_S is the single-photon coupling rate. The relative weights of the contributions depend on the level structure of the atom and can be controlled by the laser detuning from the atomic resonance. The vector and tensor contributions are related to circular and linear birefringence of the atomic medium, respectively. The scalar component leads to a polarization independent phase shift.

We now focus in the specific case of cesium-133 [26]. For a laser beam detuned by Δ from the $F = 4 \longrightarrow F' = 5$ transition in the D_2 cesium line interacting with atoms in the $F = 4$ ground state manifold, the a_i parameters are given by

$$\begin{aligned} a_0 &= \frac{1}{4}\left(\frac{1}{1+\Delta_{35}/\Delta} + \frac{7}{1+\Delta_{45}/\Delta} + 8\right) \\ a_1 &= \frac{1}{120}\left(-\frac{35}{1+\Delta_{35}/\Delta} - \frac{21}{1+\Delta_{45}/\Delta} + 176\right) \\ a_2 &= \frac{1}{240}\left(\frac{5}{1+\Delta_{35}/\Delta} - \frac{21}{1+\Delta_{45}/\Delta} + 16\right), \end{aligned} \tag{2}$$

with $\Delta_{35}/2\pi = 452\,\mathrm{MHz}$ and $\Delta_{45}/2\pi = 251\,\mathrm{MHz}$ as the excited state hyperfine splittings between $F' = 3$ and $F' = 5$, and $F' = 4$ and $F' = 5$ [28], respectively. A detuning $\Delta{>}0$ ($\Delta{<}0$) corresponds to the case with laser frequency above (below) the $F = 4 \longrightarrow F' = 5$ transition. In our experiments, the probe laser is detuned by $\Delta/2\pi = 3\,\mathrm{GHz}$, where relative weights are $a_0 \sim 3.83$, $a_1 \sim 1.05$, and $a_2 \sim 0.004$.

The interaction between light and the atomic ensemble in Eq. (1) can be simplified and linearized in the case of large ground state spin polarization and a polarized laser field with mean amplitude much larger than the vacuum fluctuations. These approximations (discussed before Eq. (3)) constitute the mapping of the spin system to an oscillator system. As we will describe in the next section, the ensemble is optically pumped such that the mean spin length is $J_x = \langle \hat{J}_x \rangle$ and transverse spin components are $\langle \hat{J}_y \rangle, \langle \hat{J}_z \rangle \ll J_x$ at any instant of time. Therefore, imperfect spin polarization will reduce the macroscopic spin length.

The probe is a strong classical field linearly polarized at an angle α to the magnetic field, which is also the quantization axis. The angle α controls the relative contributions of the vector and tensor effects described by the Hamiltonian (3). For simplicity, we change basis of the polarization variables such that the component $\hat{S}_\parallel$ describes the strong field as a classical variable with mean photon flux $\langle \hat{S}_\parallel \rangle = \langle \hat{S}_0 \rangle = S_\parallel$, leaving $\hat{S}_\perp, \hat{S}_z$ as zero-mean quantum variables. Mathematically, we rotate the polarization variables around the $\hat{S}_z$ components as $\{\hat{S}_\parallel = \hat{S}_x \cos 2\alpha - \hat{S}_y \sin 2\alpha, \hat{S}_\perp = \hat{S}_x \sin 2\alpha + \hat{S}_y \cos 2\alpha, \hat{S}_z, \hat{S}_0\}$.

For a highly polarized ensemble in the $F = 4$ hyperfine manifold, the Hamiltonian in Eq. (1) can be simplified [29]. In the limit of high steady state spin polarization, where only the two extreme magnetic sublevels, i.e., either $m_F = +4, +3$ or $m_F = -4, -3$, are populated, we perform the Holstein-Primakoff approximation [30] and map the spin variables to effective position and momentum variables

$$\hat{H}_S/\hbar = \mp\frac{\omega_S}{2}(\hat{X}_S^2 + \hat{P}_S^2) - 2\sqrt{\Gamma_S}\left(\hat{X}_S\hat{X}_L + \zeta_S\hat{P}_S\hat{P}_L\right). \tag{3}$$

The canonical variables for light and spins are $\{\hat{X}_L = \hat{S}_z/\sqrt{S_\parallel}, \hat{P}_L = -\hat{S}_\perp/\sqrt{S_\parallel}\}$ and $\{\hat{X}_S = \hat{J}_z/\sqrt{|J_x|}, \hat{P}_S = -\mathrm{sgn}(J_x)\hat{J}_y/\sqrt{|J_x|}\}$, respectively, satisfying $[\hat{X}_L(t), \hat{P}_L(t')] = (i/2)\delta(t-t')$ and $[\hat{X}_S, \hat{P}_S] = i$. Notably, the quadratic terms present in equation (1) are simplified here and the resulting Hamiltonian is linear in both atomic and light variables. The quantity $\mathrm{sgn}(J_x)$ refers to the sign of the mean spin, being positive (negative) for the negative (positive) mass oscillator cases. Notice that the sign before ω_S carries information about the mutual orientation of J_x and the external bias magnetic field. In the harmonic oscillator language, the mutual orientation defines the effective mass of the spin oscillator, with $-\omega_S$ $(+\omega_S)$ referring to the negative (positive) mass. In the derivation of Eq. (3), we have omitted constant energy terms, as they do not affect the dynamics of the variables of interest.

The parameters

$$\Gamma_S = g_S^2 a_1^2 S_{\|} J_x \tag{4}$$

$$\zeta_S = -14\frac{a_2}{a_1}\cos 2\alpha, \tag{5}$$

are the spin oscillator readout rate and the tensor coupling parameter, respectively. If $\zeta_S = 0$ the light-spins interaction is of the Quantum Non-Demolition (QND) type. In our experimental regime, as $\zeta_S \neq 0$, the spin-light interactions deviates from the QND interaction, allowing for dynamical cooling/heating of the spin oscillator and changing the total decay rate and effective bath occupation [14,31] in similar fashion to the effects of light interaction with a mechanical oscillator in the field of optomechanics [32].

In practice, the ensemble is not perfectly polarized due to limited optical pumping efficiency and decay due to, e.g., wall collisions, natural lifetime and optical de-pumping. Since the expression for ζ_S above is derived for perfect spin polarization, the effective value observed experimentally differs somewhat from that given by Eq. (5). As shown in Section 3, our full model with ζ_S as a free parameter describes the measured response sufficiently well. Further, the imperfect spin polarization gives rise to a thermal, stochastic distribution of the spins in the different magnetic sublevels, which shows as thermal noise in the detection.

The spin system evolves coherently due to the Hamiltonian given in Eq. (3), and incoherently due to spin decay and coupling to an external effective spin bath [33]. Furthermore, atomic motion leads to a time-dependent light-spin coupling. There is, in principle, an infinite set of collective spin modes that evolve in time accordingly to the ensemble geometry, collisions, dephasing, and diffusion [22]. Here, we focus on the so called *flat* spin mode corresponding to the total spin $\hat{J}_k = \sum_{i=1}^{N} \hat{F}_k^{(i)}$, the mode which is the most resilient to motional dephasing as it is fully symmetric with respect to shuffling atomic positions. In the linearized language introduced above, we assign effective position and momentum variables, $\hat{X}_S, \hat{P}_S$ to this mode. Later on, we will also introduce effective variables to describe the dynamics of the fast decaying spin modes, here denominated as the *broadband response*, and also introduce a qualitative model that describes its response to light.

The dynamics of the spin variables due to the Hamiltonian presented in Eq. (3) for the case with effective positive mass, including the non-Hamiltonian decay by natural and optically induced channels [33], is

$$\frac{\mathrm{d}}{\mathrm{d}t}\begin{pmatrix}\hat{X}_S\\ \hat{P}_S\end{pmatrix} = \begin{pmatrix}-\gamma_S/2 & \omega_S\\ -\omega_S & -\gamma_S/2\end{pmatrix}\begin{pmatrix}\hat{X}_S\\ \hat{P}_S\end{pmatrix} + 2\sqrt{\Gamma_S}\begin{pmatrix}0 & -\zeta_S\\ 1 & 0\end{pmatrix}\begin{pmatrix}\hat{X}_L^{\mathrm{in}}\\ \hat{P}_L^{\mathrm{in}}\end{pmatrix}, \tag{6}$$

with $\gamma_S/2 = \gamma_{S0}/2 + \zeta_S\Gamma_S$ as the dynamical damping rate, including tensor effects [34]. Here, γ_{S0} includes the natural (in the dark) damping rate, and laser induced contributions (from the pumping and probing lasers). For notation purposes, we write the light and spin variables in the matrix form as

$$\mathbf{X}_L^{\mathrm{in(out)}} = \begin{pmatrix}X_L^{\mathrm{in(out)}}\\ P_L^{\mathrm{in(out)}}\end{pmatrix}, \qquad \mathbf{X}_S = \begin{pmatrix}X_S\\ P_S\end{pmatrix}, \tag{7}$$

where the superscripts *in* (*out*) denote the optical mode before (after) the interaction with the spin oscillator, to be presented below. In the CIFAR experiments, as we will discuss in Section 3, the oscillator is coherently excited, e.g., with a drive $X_L^{\mathrm{in}} \propto \sin\omega_{\mathrm{RF}}t$. Since the system is driven by a classical driving field, the system response can also be considered to be classical, and we drop the operator description from here on.

Given the linear system of Eqs. (6) and a sinusoidal drive input $\mathbf{X}_\mathrm{L}^\mathrm{in}$, a solution in the complex plane can be found using the ansatz $X_\mathrm{S}(t) = X_\mathrm{S}(\omega_\mathrm{RF})e^{-i\omega_\mathrm{RF}t}, P_\mathrm{S}(t) = P_\mathrm{S}(\omega_\mathrm{RF})e^{-i\omega_\mathrm{RF}t}$, where $X_\mathrm{S}(\omega_\mathrm{RF})$ and $X_\mathrm{S}(\omega_\mathrm{RF})$ are complex numbers. We write this as

$$\mathbf{X}_\mathrm{S} = 2\sqrt{\Gamma_\mathrm{S}}\mathbf{L}\mathbf{Z}\mathbf{X}_\mathrm{L}^\mathrm{in}, \tag{8}$$

where the matrices $\mathbf{L}$ and $\mathbf{Z}$ parametrize the interaction dynamics as

$$\mathbf{Z} = \begin{pmatrix} 0 & -\zeta_\mathrm{S} \\ 1 & 0 \end{pmatrix} \tag{9}$$

$$\mathbf{L} = \begin{pmatrix} \gamma_\mathrm{S}/2 - i\omega_\mathrm{RF} & -\omega_\mathrm{S} \\ \omega_\mathrm{S} & \gamma_\mathrm{S}/2 - i\omega_\mathrm{RF} \end{pmatrix}^{-1} = \chi_\mathrm{S}(\omega_\mathrm{RF}) \begin{pmatrix} \gamma_\mathrm{S}/2 - i\omega_\mathrm{RF} & \omega_\mathrm{S} \\ -\omega_\mathrm{S} & \gamma_\mathrm{S}/2 - i\omega_\mathrm{RF} \end{pmatrix}, \tag{10}$$

with $\chi_\mathrm{S}(\omega_\mathrm{RF}) = \left(\omega_\mathrm{S}^2 + \left(\frac{\gamma_\mathrm{S}}{2} - i\omega_\mathrm{RF}\right)^2\right)^{-1}$ as the spin susceptibility. All spin and light variables are understood to be functions of drive frequency, ω_RF, the notation of which we suppress from now on.

The output light field, after the interaction with the spin oscillator given in Eq. (8), is

$$\mathbf{X}_\mathrm{L}^\mathrm{out} = \mathbf{X}_\mathrm{L}^\mathrm{in} + \sqrt{\Gamma_\mathrm{S}}\mathbf{Z}\mathbf{X}_\mathrm{S} = (\mathbf{1}_2 + 2\Gamma_\mathrm{S}\mathbf{Z}\mathbf{L}\mathbf{Z})\mathbf{X}_\mathrm{L}^\mathrm{in}, \tag{11}$$

where $\mathbf{1}_2$ is the 2×2 identity matrix. The equation above shows that the output light field will have two contributions: one directly from the input field and another from the response of the spin oscillator to the input. Having the light field as a common source, these two contributions can interfere.

By inserting (9) and (10) into (11), we get the expressions for output optical quadratures after the interaction with the spin ensemble

$$\begin{pmatrix} X_\mathrm{L}^\mathrm{out} \\ P_\mathrm{L}^\mathrm{out} \end{pmatrix} = \begin{pmatrix} 1 - 2\Gamma_\mathrm{S}\zeta_\mathrm{S}\left(\frac{\gamma_\mathrm{S}}{2} - i\omega_\mathrm{RF}\right)\chi_\mathrm{S} & -2\Gamma_\mathrm{S}\zeta_\mathrm{S}^2\omega_\mathrm{S}\chi_\mathrm{S} \\ 2\Gamma_\mathrm{S}\omega_\mathrm{S}\chi_\mathrm{S} & 1 - 2\Gamma_\mathrm{S}\zeta_\mathrm{S}\left(\frac{\gamma_\mathrm{S}}{2} - i\omega_\mathrm{RF}\right)\chi_\mathrm{S} \end{pmatrix} \begin{pmatrix} X_\mathrm{L}^\mathrm{in} \\ P_\mathrm{L}^\mathrm{in} \end{pmatrix}. \tag{12}$$

In general, we are able to select arbitrary input $\mathbf{X}_\mathrm{L}^\mathrm{in}$ and the detection $\mathbf{X}_\mathrm{L}^\mathrm{out}$ components by controlling the ellipticity of the polarization state by the phases θ and ϕ, respectively. The input light state, without loss of generality, is assumed to be generated from a pure phase modulation $G = |G|e^{i\varphi}$ that, when referenced to a local oscillator (LO) in a Mach-Zehnder interferometer, as we have in Fig. 1, can be arbitrarily decomposed into polarization variables and effective input amplitude and phase quadratures. Here, by convention, we have chosen $X_\mathrm{L}^\mathrm{in} = G, P_\mathrm{L}^\mathrm{in} = 0$ for $\theta = 0$. Path length difference ΔL control in the Mach-Zehnder interferometer ($\theta \propto \Delta L$, see inset of Fig. 1) allows for mixing the drive components via a basis rotation, and polarization homodyning angle (ϕ) allows for selecting the detection quadrature, as

$$\begin{pmatrix} X_\mathrm{L}^\mathrm{in} \\ P_\mathrm{L}^\mathrm{in} \end{pmatrix} = \begin{pmatrix} \cos\theta & -\sin\theta \\ \sin\theta & \cos\theta \end{pmatrix} \begin{pmatrix} G \\ 0 \end{pmatrix} = \begin{pmatrix} \cos\theta \\ \sin\theta \end{pmatrix} G, \qquad \begin{pmatrix} X_\mathrm{L}^\mathrm{det} \\ P_\mathrm{L}^\mathrm{det} \end{pmatrix} = \begin{pmatrix} \cos\phi & -\sin\phi \\ \sin\phi & \cos\phi \end{pmatrix} \begin{pmatrix} X_\mathrm{L}^\mathrm{out} \\ P_\mathrm{L}^\mathrm{out} \end{pmatrix}. \tag{13}$$

By inserting the Eqs. (13) in Eq. (12), we get to the final form of the Coherently Induced FAraday Rotation (CIFAR) signal. We typically define the measured quadrature as $P_\mathrm{L}^\mathrm{det}$, such

Optics EXPRESS

that the absolute squared of the detected spin response to an arbitrary input optical modulation is

$$\begin{aligned}|\mathrm{CIFAR}|^2 \equiv \left|P_{\mathrm{L}}^{\mathrm{det}}\right|^2 &= \left|P_{\mathrm{L}}^{\mathrm{out}} \cos\phi + X_{\mathrm{L}}^{\mathrm{out}} \sin\phi\right|^2 \\ &= \Big|\left(1 - 2\Gamma_{\mathrm{S}}\zeta_{\mathrm{S}}\left(\tfrac{\gamma_{\mathrm{S}}}{2} - i\omega_{\mathrm{RF}}\right)\chi_{\mathrm{S}}\right)\sin(\theta+\phi) \\ &+\Gamma_{\mathrm{S}}\omega_{\mathrm{S}}\chi_{\mathrm{S}}\left[(1-\zeta_{\mathrm{S}}^2)\cos(\theta-\phi) + (1+\zeta_{\mathrm{S}}^2)\cos(\theta+\phi)\right]\Big|^2 |G|^2.\end{aligned} \tag{14}$$

This equation is the main result of this section, being applicable to the description of a single collective spin mode, e.g., the flat spin mode, response to light.

In a broader view, it becomes necessary to consider other spin modes which in contrast to the total spin will have some spatial dependencies. We consider collective operators corresponding to the transverse spin components of mode n given by $\hat{J}_{z,y}^n = \sqrt{V}\sum_{i=1}^N u_n(\mathbf{x}_i)\hat{F}_{z,y}$ where $u_n(\mathbf{x})$ represents the spatial shape of the spin mode, V is the volume of cell (for the purpose of proper normalization) and $\mathbf{x}_i$ is the position of i-th atom. The coherent evolution of each mode (collective operator) is then governed by Eq. (3) with the readout rate Γ_{S}^n now taking into account the overlap between the spin mode and the Gaussian light mode I_n^{G}, such that $\Gamma_{\mathrm{S}}^n \sim |I_n^{\mathrm{G}}|^2$ [22]. At the same time, the incoherent part will depend on motion and wall collisions. It has been shown that even in the paraffin- or alkene-coated cells [35–38] or cells with dilute buffer gas [39] the atomic motion can be effectively described by the diffusion equation with adequate wall boundary condition. The cells with coated walls will feature a slow decay for the flat mode ($u_0(\mathbf{x}_i) = 1/\sqrt{V}$) which depends on intrinsic dynamics and wall decay, and much faster decay for all other modes, which is given by $\gamma_{\mathrm{S}}^n = Dk_n^2$, where D is the effective diffusion constant and k_n is the characteristic wavenumber of n-th mode [22].

For the case of quantum noise, it becomes necessary to consider both thermal contributions of each mode (added incoherently), and the coherent interaction of each mode the the Gaussian beam. These broadband spin noises affect the atomic ensembles serving as magnetometers [40] or quantum memories [22]. In our case we can consider only the coherent interaction and thus each spatial spin mode responds to the same light modulation. Therefore, we may simply modify Eq. (11) to the multimode case:

$$\mathbf{X}_{\mathrm{L}}^{\mathrm{out}} = \left(\mathbf{1}_2 + \sum_n 2\Gamma_{\mathrm{S}}^n \mathbf{Z}\mathbf{L}_n\mathbf{Z}\right)\mathbf{X}_{\mathrm{L}}^{\mathrm{in}}, \tag{15}$$

with $\mathbf{L}_n$ contains the susceptibility with the respective damping rate γ_{S}^n. In our case we shall work in a two-mode approximation for which the zeroth mode is the flat, long-lived mode, and the other mode has $\gamma_{\mathrm{S}}/2\pi \sim 1\,\mathrm{MHz}$. We justify this approach by noticing that broad modes contribute a similar flat background around the resonance which we primarily study here. In our system, the main fundamental mode is much longer lived than all other modes. As long as we try to determine the response around the resonance at ω_{S}, the tails of the response that may have non-Lorentzian shape due to the presence of more than one broad mode, will not contribute significantly. Following this approach we obtain a two-component CIFAR signal in which the narrow (with damping rate γ_{S} and readout rate Γ_{S}) and broad parts (with damping rate $\gamma_{\mathrm{S,BB}}$ and readout rate $\Gamma_{\mathrm{S,BB}}$) of the response may interfere according to their phase relation. In the following sections we will nevertheless give simplified formulas for the single mode case to facilitate understanding, and use the two-component model for fitting.

Given the input and detection angles, as well as the spin oscillator parameters and coupling to light, the CIFAR signal exhibits a characteristic frequency response. For developing intuition about the response, let us focus initially in the special case of $\theta = 45°$ and $\phi = 0°$, corresponding to detecting the phase quadrature of light $P_{\mathrm{L}}^{\mathrm{out}}$ and driving with an equal superposition of amplitude $X_{\mathrm{L}}^{\mathrm{in}}$ and phase modulation $P_{\mathrm{L}}^{\mathrm{in}}$. For the choice of phases described above, the detected signal goes as

$$|\mathrm{CIFAR}(\theta = 45°, \phi = 0°)|^2 = |1 - 2\Gamma_\mathrm{S}(-\omega_\mathrm{S} + \zeta_\mathrm{S}(\gamma_\mathrm{S}/2 - i\omega_\mathrm{RF}))\chi_\mathrm{S}|^2\, |G|^2. \tag{16}$$

Notably, the drive, represented by the constant term, and the spin response, proportional to the susceptibility χ_S, are added coherently and interfere. In particular, the readout rate Γ_S plays an important role in the interference pattern, modulating its strength. In the high-Q limit ($\gamma_\mathrm{S} \ll \omega_\mathrm{S}$) and around resonance ($\omega_\mathrm{RF} \sim \omega_\mathrm{S}$), the spin susceptibility is $\chi_\mathrm{S} \sim -\chi_{\mathrm{S}0}/\omega_\mathrm{S}$, for $\chi_{\mathrm{S}0} = \frac{1}{2}(\Delta_\mathrm{RF} + i\gamma_\mathrm{S}/2)^{-1}$, with $\Delta_\mathrm{RF} = \omega_\mathrm{RF} - \omega_\mathrm{S}$ as the detuning between the spin resonance and the input modulation tone. In this limit, the Eq. (16) becomes

$$|\mathrm{CIFAR}|^2/|G|^2 \sim |1 - 2\Gamma_\mathrm{S}(1 + i\zeta_\mathrm{S})\chi_{\mathrm{S}0}|^2 = 1 + \frac{\Gamma_\mathrm{S}^2(1 + \zeta_\mathrm{S}^2) - 2\Gamma_\mathrm{S}(\Delta_\mathrm{RF} + \zeta_\mathrm{S}\gamma_\mathrm{S})}{\Delta_\mathrm{RF}^2 + (\gamma_\mathrm{S}/2)^2}. \tag{17}$$

For exemplifying the procedure to extract the readout rate parameter Γ_S, let us consider two specific cases. First, we analyze the case of $\zeta_\mathrm{S} = 0$, that is, the light-matter interaction is of the QND type. Here,Eq. (17) reduces to

$$|\mathrm{CIFAR}_0|^2/|G|^2 = 1 + \frac{\Gamma_\mathrm{S}^2 - 2\Gamma_\mathrm{S}\Delta_\mathrm{RF}}{\Delta_\mathrm{RF}^2 + (\gamma_{\mathrm{S}0}/2)^2}. \tag{18}$$

The CIFAR_0 signal is a combination of a constant, a Lorentzian, and a dispersive term, representing the drive, the spin response and the interference between the drive and response, respectively. Importantly, the minimum and maximum of the signal are separated by $\sim \sqrt{\Gamma_\mathrm{S}^2 + \gamma_\mathrm{S}^2} \sim \Gamma_\mathrm{S}$ in the limit of high coupling, $\Gamma_\mathrm{S} \gg \gamma_\mathrm{S}$. The readout rate can thus be extracted just by noting this frequency difference, directly from the sweep figure, such as Fig. 2.

For the second specific case, when $\zeta_\mathrm{S} \neq 0$, Eq. (17) leads to a correction of the separation, as the maximum and minimum are separated by $\sim \sqrt{(1 + \zeta_\mathrm{S}^2)(\Gamma_\mathrm{S}^2(1 + \zeta_\mathrm{S}^2) + \gamma_\mathrm{S}^2 - 2\Gamma_\mathrm{S}\gamma_\mathrm{S}\zeta_\mathrm{S})}$. In the high-coupling limit, $\Gamma_\mathrm{S} \gg \gamma_\mathrm{S}$, this simplifies to $\sim \Gamma_\mathrm{S}(1 + \zeta_\mathrm{S}^2)$.

Having derived the needed expressions, we now turn to an experimental investigation of the CIFAR signal under different situations.

Optics EXPRESS

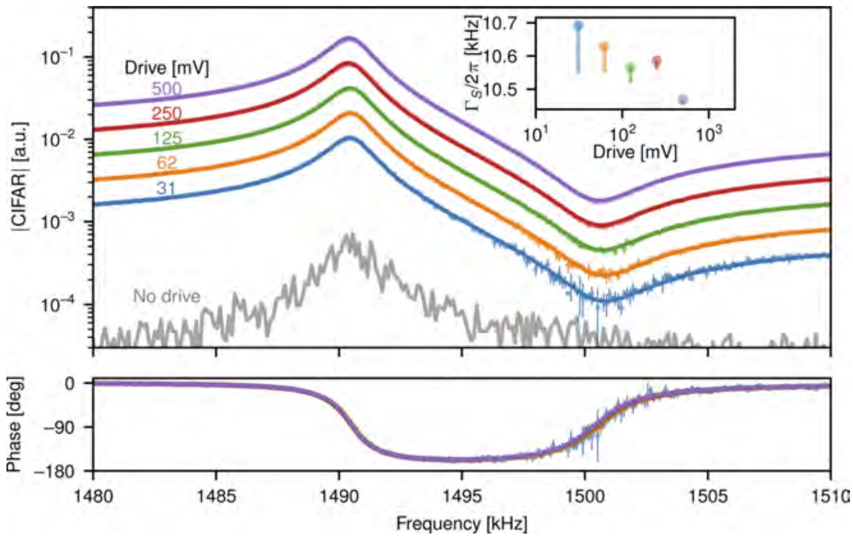

Fig. 2. CIFAR as a function of modulation amplitude. CIFAR response amplitude (top) and phase (bottom) for different electrical EOM drive voltage G. The average of 3 scans (dots) is presented along with their statistical 1σ uncertainty error bars (vertical bars). The solid lines are the model fits to the individual curves. The grey line in the top panel is the measured response without any modulation at the input. Inset: fitted readout rate and (asymmetric) error bars as function of the drive voltage. For a discussion of the error bars, see the main text.

3. Experimental implementation

The following section describes the experimental setup depicted in Fig. 1. We start by describing the atomic spin ensemble and the optical probing. The atomic spin ensemble is a warm gas consisting of $N \approx 10^8 - 10^9$ cesium-133 atoms, confined to a spin anti-relaxation-coated microcell [41] with a 300 µm × 300 µm cross-section and 10 mm in length. The system is probed with a Gaussian beam that has a waist of $w_0 \sim 80$ µm in radius $(1/e^2)$, propagating the in z-direction. The sub-millimeter transverse dimensions of the cell allow for fast motional averaging [21], ensuring an integrated interaction between all atoms and the light. The microcell is positioned in a magnetic shield which contains coils producing a homogeneous magnetic bias field B in the x-direction. The strength of the bias field splits the magnetically sensitive Zeeman levels by $|\omega_S|$, i.e., the Larmor frequency. Here, the Larmor frequency is in the range $\omega_S/2\pi \sim 0.3$ MHz to 1.5 MHz. The intrinsic (in the dark) spin damping rate at 59 °C and 1.5 MHz Larmor frequency is $\gamma_{S0,\mathrm{dark}}/2\pi = 450$ Hz. The relatively intense probe beam adds power broadening, and allows for collective broadening/narrowing the spin resonance. The decay mechanisms are included in the expression for the damping rate γ_S, as presented in Eq. (6). The steady state spin polarization is set by the competing contributions from the linearly polarized probe, propagating orthogonally to the bias magnetic field, and the circularly polarized resonant optical pumping beams, propagating along the bias field. The CIFAR method is sensitive to the single atom and collective decay channels and to the mean spin length. The steady state spin polarization in the experiments presented here is about ∼ 80%.

The remaining part of the setup in Fig. 1 sets the phase sensitive control of the excitation and detection of the optical signal. We effectively generate an arbitrary polarization of the input light by combining two laser beams, here named local oscillator (LO) and modulation, with orthogonal polarizations on a polarization beam splitter (PBS) with a phase delay θ. The modulation beam

Optics EXPRESS

is phase modulated at a RF frequency ω_{RF} in a fiber electro-optic modulator (EOM) according to $E_{\mathrm{EOM}}\mathrm{e}^{i\theta}\mathrm{e}^{iG\sin\omega_{\mathrm{RF}}t}$, for G as the modulation strength. An arbitrary optical polarization state can be set by choosing a given θ and relative intensities of the beams. One of the output ports of the PBS is sent to the spin ensemble and the other is used for a polarization detection setup (phase lock).

We now describe the input polarization to the spin ensemble. The electric field of the laser light after the PBS is $E_{\mathrm{LO}}(t)\hat{\mathrm{e}}_x + E_{\mathrm{EOM}}(t)\hat{\mathrm{e}}_y \sim |E_{\mathrm{LO}}|\hat{\mathrm{e}}_x + |E_{\mathrm{EOM}}|\mathrm{e}^{i\theta}(1 + iG\sin\omega_{\mathrm{RF}}t)\hat{\mathrm{e}}_y$, to the first order in G. Assuming $|E_{\mathrm{EOM}}| \ll |E_{\mathrm{LO}}|$, the equivalent input Stokes parameters [42] can be written, to the first order in $|E_{\mathrm{EOM}}|$, as

$$\begin{pmatrix} S_x^{\mathrm{in}} \\ S_y^{\mathrm{in}} \\ S_z^{\mathrm{in}} \end{pmatrix} = \begin{pmatrix} |E_{\mathrm{LO}}|^2/2 \\ |E_{\mathrm{LO}}||E_{\mathrm{EOM}}|(\sin\theta + G\sin\omega_{\mathrm{RF}}t\cos\theta) \\ |E_{\mathrm{LO}}||E_{\mathrm{EOM}}|(\cos\theta - G\sin\omega_{\mathrm{RF}}t\sin\theta) \end{pmatrix}. \tag{19}$$

The phase θ controls the relative contributions of circular and diagonal components, represented by S_y^{in} and S_z^{in}, in the input polarization state. The DC (static) components will lead to a small rotation in the local oscillator's polarization; the AC components will induce CIFAR signal. In the linearized quadrature language, the effective AC input drive is written as $(-X_{\mathrm{L}}^{\mathrm{in}}\sin\theta + P_{\mathrm{L}}^{\mathrm{in}}\cos\theta)G\sin\omega_{\mathrm{RF}}t$.

In the port that is directed to the phase lock output, the DC frequency interferometric signal, given in Eq. (19) is used for stabilizing θ, the path length difference between the LO and the EOM arms, and therefore the input modulation to the spin ensemble. Deviations from the ideal phase shift induced by birrefringent elements, e.g., half wave plates in Fig. 1, leads to a further mixing between S_y^{in} and S_z^{in} in Eq. (19), complicating the calibration of θ. The same argument applies to setting the detection angle ϕ. Experimentally, we first drive the spin oscillator with a RF magnetic field [43] to set ϕ. The detection half-wave plate is set to give the maximum photo-detected response to the applied magnetic field, which happens at $\phi = 0°$. Subsequently, we switch to a polarization modulation drive and find the effective $\theta = 90°$ when the spin response has a Lorentzian line-shape.

The polarization modulation at frequency ω_{RF} leads to a phase coherent interaction between the oscillator and light according to Eq. (12). The signal is recorded by balanced polarimetry photodetection and processed by a lock-in amplifier phase-referenced to the drive, allowing us to extract the slowly varying amplitude R and phase components. In a experimental protocol very similar to the one used in continuous wave Magneto-Optical Resonance Signal measurements [43], scanning ω_{RF} around the resonant frequency ω_{S} at a rate much smaller than the spin damping rates, we ensure the steady-state performance and extract the signal of interest. To extract the useful parameters from the data, we implemented non-linear optimization and curve fitting routine to a two spin-modes model based in Eq. (15).

For experimental implementations that operate in the pulsed regime [5,7,10], in which the probing follows a spin-state preparation stage, the CIFAR signal can be extracted in a similar manner to the one prescribed in the continuous readout. For example, during a single repetition, a fixed-frequency polarization modulated probe can map out the time-evolving signal, thus obtaining a single point in the interference signal. Repeating the experiment with different drive frequencies allows for mapping a signal similar to those presented in the Results section. The data analysis therefore borrows the analysis discussed in the Theory section.

4. Results

We will now present experimental support to the model described in Section 2. We fit the CIFAR model given in Eq. (14) to the recorded data, present its performance on different experimental conditions and discuss the overall validity of the model.

We start by the studying the response of spin oscillator to increasing modulation amplitudes G. In the data present in Figs. 2 to 4, we fix $\theta = 45°$, the probe power at 500 µW, and cancel the non-linear quadratic Zeeman shift with tensor Stark shifts [44] by setting $\alpha \sim 60°$. In Fig. 2, for each modulation amplitude, we record 3 scans and show the average as points, and the statistical 1σ uncertainty error bars (vertical bars). We double the amplitude starting from 31 mV (in blue) until 500 mV (in purple), showing |CIFAR| (top panel) and the phase response (bottom panel), the amplitude and phase of the CIFAR signal, respectively. The grey line is the response of the spin oscillator to a shot noise-limited drive, in which the coherent polarization modulation is turned off. We see that the amplitude of the CIFAR signal follows the drive increase, doubling as the amplitude doubles. As the drive amplitude increases, the coherent response dominates the signal and the spread around the mean values decreases.

The averaged traces for each drive amplitude in Fig. 2 is fit by the CIFAR model. The fits are displayed as solid lines, showing the good agreement to the measured amplitude and phase data. In the Fig. 2 inset, we show the readout rate $\Gamma_S/2\pi$ returned by the fitting routine as a function of the drive amplitude. For the 31 mV drive amplitude, the value for the readout rate is $\Gamma_S/2\pi = 10.685^{+0.008}_{-0.18}$kHz. For increasing drive, nonetheless, the trend is that the fitting routine returns smaller values (see inset of Fig. 2), a trend we will discuss below.

The asymmetric parameter errors are obtained with the `conf_invertal` function of the `lmfit` Python package [45]. The function returns the parameter values for which $\chi^2 = \chi^2_{min} + 1$, i.e., the interval containing the usual 68.27% probability, which for a Gaussian parameter error corresponds to the 1σ uncertainty. Similar results was obtained by Markov Chain Monte Carlo [46] optimization (not shown). The asymmetry arises due to a strong correlation between Γ_S and other fit parameters, mainly the parameter describing the overall response $\propto G$.

We further note that successfully fitting the model to the data relies on reliably ascribing errors to the individual data points; the individual traces spans 2 orders of magnitude, and failing to account for this in the optimization routine leads to discrepancies in either the peak or valley of the traces. Curiously, the data errors largely inherit the shape of the undriven atomic ensemble, i.e., a Lorentzian centered on the spin frequency (not shown). This places the condition that to obtain good fit values, all measurements must be repeated a number of times, to obtain trustworthy statistics.

Looking at the fitting residuals for the different traces, presented in Fig. 3, we see that structured deviations between model and data appear as the spin oscillator is driven with larger amplitudes. The residuals to the traces with drive voltages above 250 mV, shown in red and purple points, present significant deviations from our model. Some structure may be seen even for the green trace (125 mV drive). We believe that the deviations from our model appear as we start to drive the spin system significantly away from the small oscillation amplitude approximation that takes the system beyond the linearized oscillator model. We have, therefore, experimentally found the range of drive strengths that our model can describe. A more thorough investigation of the spin response beyond the linearized regime is left for a future work. We are thus left with two trends as the drive increases; the best-fit value for Γ_S decreases, while the trustworthiness of the model also decreases. What the absolute optimum drive amplitude is, and whether the low-drive regime is free of systematic effects, our data cannot answer at this point.

In Fig. 4 we present the dependence of the readout rate on J_x, the mean spin length. According to Eq. (4), $\Gamma_S \propto J_x$. The spin length is controlled by the temperature of the vapor cell, which sets number of atoms. When heated, the cesium vapor pressure increases [28]. For the data on Fig. 4, we record CIFAR scans while the cell is heated from ~34 °C (blue points) to ~59 °C (purple points). The solid lines are fits to the data, with the frequency axis shifted according to Δ_{RF} and re-scaled to the returned spin damping rate γ_S. The extracted readout rate increases from 1.1 kHz to 10.0 kHz. As the temperature, and consequently J_x, is increased, the peak signal increases and the minimum is shifted up in frequency. Importantly, the frequency detuning Δ_{RF}

Optics EXPRESS

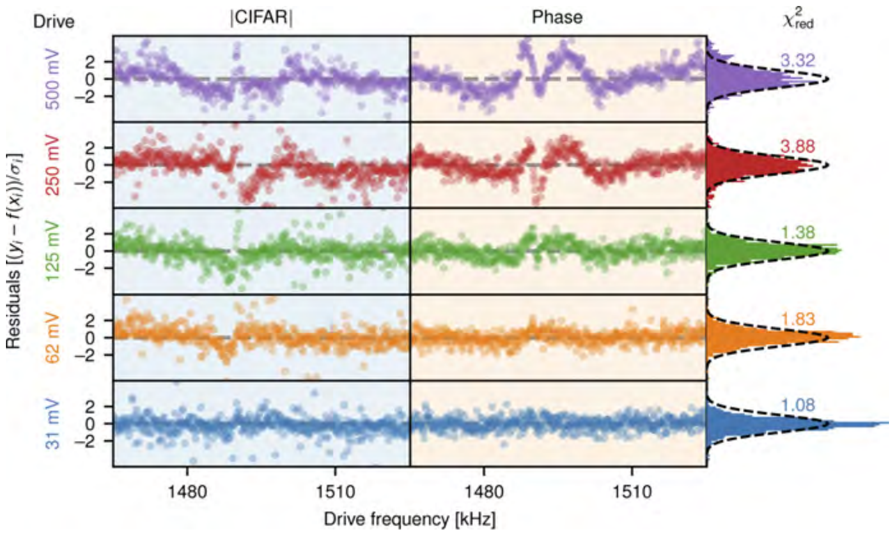

Fig. 3. Scaled fit residuals from Fig. 2. Residuals between the model and data, both in CIFAR amplitude (left column) and phase (right column), for the various drive voltages shown in Fig. 2. In the right-most column we show the histogram of the residuals along with a unity width Gaussian curve (dashed lines) to guide the eye. We also print the reduced χ^2. Some outliers are not shown.

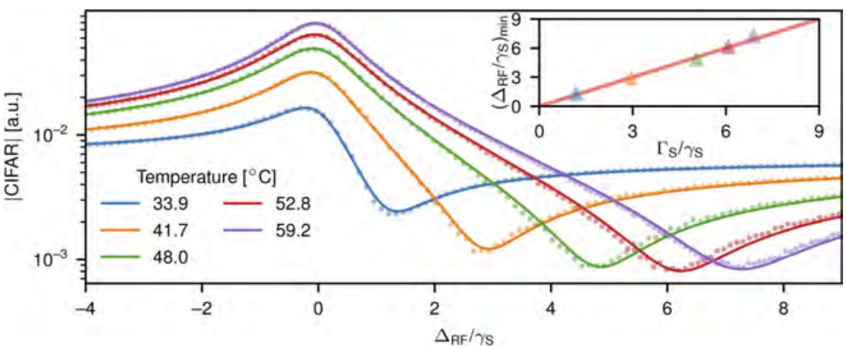

Fig. 4. CIFAR scans for different Γ_S/γ_S. We vary the readout rate by changing the temperature of the cell from ~34 °C to ~59 °C. Inset: The location of the minimum of the CIFAR response in units of Δ_{RF}/γ_S as a function of the normalized readout rate Γ_S/γ_S. Solid line: line with slope 1.

for which the CIFAR signal is minimal follows the readout rate Γ_S, as shown in the inset. There is, approximately, a one-to-one correspondence between Γ_S/γ_S and the frequency of the CIFAR signal minimum value, as shown by the line with slope 1 (solid line). Therefore, by choosing the input modulation type $\theta = 45°$, an approximate readout rate can be easily extracted from the CIFAR signal as the frequency difference between the maximum and minimum of the trace. We also note that at the highest temperature setting (~59 °C), with damping rate $\gamma_{S0}/2\pi = 1.3$ kHz and estimated spin thermal occupation $n_S \sim 0.75$ [47], we have $\Gamma_S/\gamma_S \sim 7$ and estimate $C_q \sim 3$, indicating that the spin oscillator is strongly coupled to light.

In Fig. 5, we present the CIFAR signal for different strengths of the tensor coupling parameter ζ_S. For a given detuning from the atomic resonance Δ, it is modified by selecting α, the angle between the LO linear polarization and the magnetic field B direction. According to Eq. (5), the angle $\alpha = 45°$ turns off the tensor coupling. For this experiment, we reduced the spin resonance frequency to $\omega_S/2\pi \sim 400$ kHz to avoid non-linear Zeeman splitting [43], the probe power was set to 250 µW to reduce probe-induced power broadening, and the temperature to $T = 55°$. In Fig. 5, we show the amplitude of the CIFAR signal for $\theta = 45°$ (top panel) and $\theta = 90°$ (bottom panel). The data for $\alpha = \{0°, 45°, 90°\}$ are shown in blue, orange and green dots, respectively. The choice of $\theta = 45°$ gives responses similar to those presented in Fig. 2. For this data set, we have $\Gamma_S/2\pi = 4.9$ kHz. The setting $\theta = 90°$, nonetheless, gives a rather different picture. According to Eq. (14), the detected signal goes as

$$\begin{aligned}|\mathrm{CIFAR}(\theta = 90°, \phi = 0)/G|^2 &= \left|1 - 2\Gamma_S\zeta_S\left(\tfrac{\gamma_S}{2} - i\omega_{RF}\right)\chi_S\right|^2 \\ &\sim 1 - \frac{\zeta_S\Gamma_S\gamma_S}{\Delta_{RF}^2 + (\gamma_S/2)^2},\end{aligned} \tag{20}$$

where in the last passage we used the high-Q ($\gamma_S \ll \omega_S$ and $\omega_{RF} \sim \omega_S$), and the small tensor coupling ($\zeta_S \ll 1$) limit. For this configuration, the CIFAR is dominated by the constant term, since we mostly detect the input modulation. Near the spin resonance, the oscillator will add ($\zeta_S<0$) or remove ($\zeta_S>0$) signal according to the tensor coupling sign. The obtained tensor coupling parameters are $\zeta_S = -0.045 \pm 0.002$ and $\zeta_S = 0.040 \pm 0.003$ for $\alpha = 0°$ and $\alpha = 90°$, respectively. For reference, the expected tensor parameter for a perfectly spin polarized ensemble is $|\zeta_S^{th}| = 0.053$. For $\alpha = 45°$ the spin contribution is, according to our theory, null; the returned value is $\zeta_S = 0.000 \pm 0.001$.

In our last study we present the broadband spin contributions to the CIFAR signal. The measurements presented in Fig. 6 are taken in the same experimental conditions as the data in Fig. 2, but now scanning the drive tone in a ~ 600 kHz band around ω_S. The CIFAR signal amplitude (top panels) and phase (bottom panels), including the model fits, are shown for $\theta \in \{-45°, 0°, 45°\}$ in blue, orange and green, respectively. Apart from the symmetric changes in the response as θ is changed from $-45°$ to $45°$, the $\theta \sim 0°$ amplitude and phase responses display characteristic features of a broadband spin response. The broadband spin response can be clearly seen by setting $\Gamma_S = 0$ (dashed orange line) or in our full model fit (dark orange line). The light orange line corresponds to the predicted response of the spin oscillator in the case $\Gamma_{S,BB} = 0$. The broadband spin response, having a damping rate $\gamma_{S,BB}/2\pi = 0.93$ MHz, couples to the drive with rate $\Gamma_{S,BB}/2\pi = 33.4$ kHz, distorting the phase response and adding a pedestal to the detected amplitude. Remarkably, although having a potentially complex origin [22], the broadband response is qualitatively well described by a single effective mode. The good match to data here justifies our two-mode approach in this case.

Optics EXPRESS

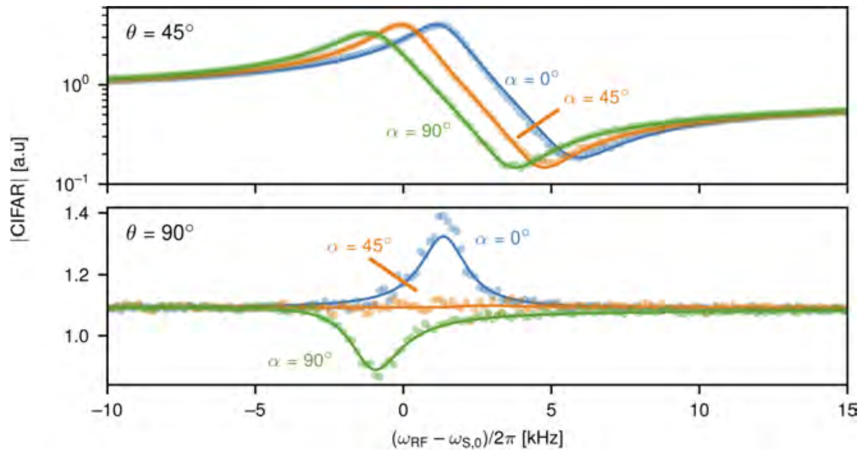

Fig. 5. CIFAR signal for different tensor coupling parameters ζ_S. The overall response of the spin oscillator to light depends on ζ_S, here controlled by the angle α between the input linear polarization LO and the direction of the magnetic bias field B. The CIFAR signals for input modulation with $\theta = 45°$ (top panel, logarithmic scale) and with $\theta = 90°$ (bottom panel, linear scale), and $\alpha = \{0°, 45°, 90°\}$ are shown in blue, orange and green, respectively.

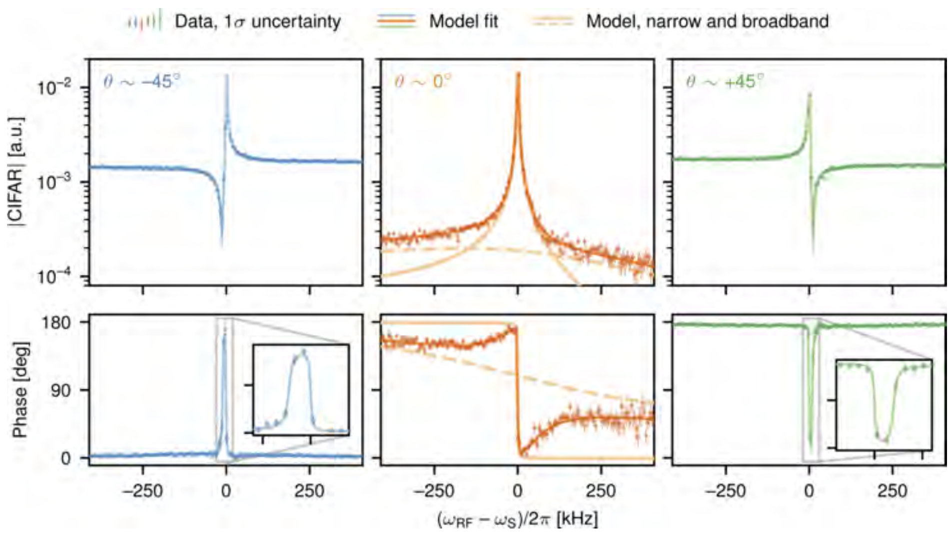

Fig. 6. Coherent interference between the responses of the narrow and broadband spin modes. CIFAR response amplitude (top row) and phase (bottom row) data (points with error bars) and fits (dark solid lines) as a function of the frequency detuning for three different modulation phases, $\theta \in \{-45°, 0°, 45°\}$. The data was taken under the same experimental conditions as the 62 mV drive trace (orange curve) in Fig. 2. For $\theta = 0°$ we also plot the fit result evaluated with the broadband readout rate set to $\Gamma_{S,BB} = 0$ (solid light orange curves, top and bottom panels) and narrowband readout rate $\Gamma_S = 0$ (dashed light orange curves).

Optics EXPRESS

5. Conclusion

In summary, we have presented a novel approach for calibrating the light-matter interaction between off-resonant optical beams and collective spin systems, the CIFAR technique. Experimentally, the calibration method relies only on applying a known input modulation and detecting a known optical quadrature, the variables parametrized by θ and ϕ, respectively. Supplied with the input-output relations of the spin-light interaction, a simple procedure for determining the interaction parameters, among those most importantly the readout rate Γ_S, is described. Fitting the recorded signal to the full model provides a full characterization of the system parameters. The technique does not rely on knowing the photo-detection efficiency or the ensemble spin polarization. We have verified the good agreement between data and the CIFAR method by continuously probing a strong coupled spin oscillator prepared in a warm cesium atomic vapour.

Theoretical refinement of our model can be envisioned with the consideration of the full Zeeman structure of the ground state manifold [48] ($F = 4$, in the present example). With that, the model will be able to account for the non-unity spin polarization and return consistent values for the tensor parameter. Furthermore, in the case of large excursions by the transverse angular momentum variables induced by the drive light, going beyond the linearized regime may potentially allow us to account for the mismatch between theory and data shown in our residuals analysis.

The technique here presented is also a powerful method for studying the coupling of light to the spin modes under diffusion and spatial averaging [22]. Our works provides an evidence for the coherent coupling and classical back-action of the short-lived spin modes with light, as opposed to previous observations of just broadband spin noise [37]. As these couplings to higher-order modes can now be calibrated, it would be worth to include shaping of the probe beam in the model to determine the full mode spectrum of the interaction. Applications are twofold: in the experiments such as the current one, where motional averaging is desired, this can be used to minimize couplings to higher modes. On the other hand, cells with buffers gas can incorporate multimode interfaces, for which it may be desired to design a stronger or selective interaction with higher modes.

The CIFAR technique also paves the way for probing and engineering the optical coupling of higher order spin modes to light, a source of inefficiencies and unwanted noise in quantum limited measurements. By preparing the optical field in a suitable spatial mode, the multimode capabilities of the spin-light platform can be utilized.

Funding. John Templeton Foundation; European Research Council (QUANTUM-N); Villum Fonden (Villum Investigator Grant 25880).

Acknowledgments. The authors acknowledge Jörg H. Müller and Emil Zeuthen for enlightening conversations. M.P. is also supported by the MAB/2018/4 project "Quantum Optical Technologies", carried out within the International Research Agendas program of the Foundation for Polish Science co-financed by the European Union under the European Regional Development Fund.

Disclosures. The authors declare no conflicts of interest.

Data availability. Data underlying the results presented in this paper are not publicly available at this time but may be obtained from the authors upon reasonable request.

References

1. W. Happer, “Optical pumping,” Rev. Mod. Phys. **44**(2), 169–249 (1972).
2. D. Budker and M. Romalis, “Optical magnetometry,” Nat. Phys. **3**(4), 227–234 (2007).
3. S. R. de Echaniz, M. Koschorreck, M. Napolitano, M. Kubasik, and M. W. Mitchell, “Hamiltonian design in atom-light interactions with rubidium ensembles: A quantum-information toolbox,” Phys. Rev. A **77**(3), 032316 (2008).
4. K. Hammerer, A. S. Sørensen, and E. S. Polzik, “Quantum interface between light and atomic ensembles,” Rev. Mod. Phys. **82**(2), 1041–1093 (2010).
5. B. Julsgaard, A. Kozhekin, and E. S. Polzik, “Experimental long-lived entanglement of two macroscopic objects,” Nature **413**(6854), 400–403 (2001).

6. B. Julsgaard, J. Sherson, J. I. Cirac, J. Fiurášek, and E. S. Polzik, "Experimental demonstration of quantum memory for light," Nature **432**(7016), 482–486 (2004).
7. G. Vasilakis, V. Shah, and M. V. Romalis, "Stroboscopic backaction evasion in a dense alkali-metal vapor," Phys. Rev. Lett. **106**(14), 143601 (2011).
8. H. Krauter, D. Salart, C. Muschik, J. M. Petersen, H. Shen, T. Fernholz, and E. S. Polzik, "Deterministic quantum teleportation between distant atomic objects," Nat. Phys. **9**(7), 400–404 (2013).
9. V. Acosta, M. P. Ledbetter, S. M. Rochester, D. Budker, D. F. Jackson Kimball, D. C. Hovde, W. Gawlik, S. Pustelny, J. Zachorowski, and V. V. Yashchuk, "Nonlinear magneto-optical rotation with frequency-modulated light in the geophysical field range," Phys. Rev. A **73**(5), 053404 (2006).
10. W. Wasilewski, K. Jensen, H. Krauter, J. J. Renema, M. V. Balabas, and E. S. Polzik, "Quantum noise limited and entanglement-assisted magnetometry," Phys. Rev. Lett. **104**(13), 133601 (2010).
11. K. Jensen, R. Budvytyte, R. A. Thomas, T. Wang, A. M. Fuchs, M. V. Balabas, G. Vasilakis, L. D. Mosgaard, H. C. Stærkind, J. H. Müller, T. Heimburg, S.-P. Olesen, and E. S. Polzik, "Non-invasive detection of animal nerve impulses with an atomic magnetometer operating near quantum limited sensitivity," Sci. Rep. **6**(1), 29638 (2016).
12. E. S. Polzik and K. Hammerer, "Trajectories without quantum uncertainties," Ann. Phys. **527**(1-2), A15–A20 (2015).
13. C. B. Møller, R. A. Thomas, G. Vasilakis, E. Zeuthen, Y. Tsaturyan, M. Balabas, K. Jensen, A. Schliesser, K. Hammerer, and E. S. Polzik, "Quantum back-action-evading measurement of motion in a negative mass reference frame," Nature **547**(7662), 191–195 (2017).
14. R. A. Thomas, M. Parniak, C. Østfeldt, C. B. Møller, C. Bærentsen, Y. Tsaturyan, A. Schliesser, J. Appel, E. Zeuthen, and E. S. Polzik, "Entanglement between distant macroscopic mechanical and spin systems," Nat. Phys. **17**(2), 228–233 (2021).
15. E. Zeuthen, E. S. Polzik, and F. Y. Khalili, "Gravitational wave detection beyond the standard quantum limit using a negative-mass spin system and virtual rigidity," Phys. Rev. D **100**(6), 062004 (2019).
16. T. M. Karg, B. Gouraud, C. T. Ngai, G.-L. Schmid, K. Hammerer, and P. Treutlein, "Light-mediated strong coupling between a mechanical oscillator and atomic spins 1 meter apart," Science **369**(6500), 174–179 (2020).
17. V. Braginsky, F. Khalili, and K. Thorne, *Quantum Measurement* (Cambridge University, 1992).
18. M. Auzinsh, D. Budker, D. F. Kimball, S. M. Rochester, J. E. Stalnaker, A. O. Sushkov, and V. V. Yashchuk, "Can a quantum nondemolition measurement improve the sensitivity of an atomic magnetometer?" Phys. Rev. Lett. **93**(17), 173002 (2004).
19. V. Braginsky, "Classical and quantum restrictions on the detection of weak disturbances of a macroscopic oscillator," Zh. Eksp. Teor. Fiz **53**, 1434–1441 (1967).
20. M. Rossi, D. Mason, J. Chen, Y. Tsaturyan, and A. Schliesser, "Measurement-based quantum control of mechanical motion," Nature **563**(7729), 53–58 (2018).
21. J. Borregaard, M. Zugenmaier, J. M. Petersen, H. Shen, G. Vasilakis, K. Jensen, E. S. Polzik, and A. S. Sørensen, "Scalable photonic network architecture based on motional averaging in room temperature gas," Nat. Commun. **7**(1), 11356 (2016).
22. R. Shaham, O. Katz, and O. Firstenberg, "Quantum dynamics of collective spin states in a thermal gas," Phys. Rev. A **102**(1), 012822 (2020).
23. H. Krauter, "Generation and application of entanglement of room temperature ensembles of atoms," Ph.D. thesis, University of Copenhagen (2011).
24. S. Weis, R. Rivière, S. Deléglise, E. Gavartin, O. Arcizet, A. Schliesser, and T. J. Kippenberg, "Optomechanically induced transparency," Science **330**(6010), 1520–1523 (2010).
25. W. H. P. Nielsen, Y. Tsaturyan, C. B. Møller, E. S. Polzik, and A. Schliesser, "Multimode optomechanical system in the quantum regime," Proc. Natl. Acad. Sci. **114**(1), 62–66 (2017).
26. B. Julsgaard, "Entanglement and quantum interactions with macroscopic gas samples," PhD dissertation, University of Aarhus (2003).
27. I. H. Deutsch and P. S. Jessen, "Quantum control and measurement of atomic spins in polarization spectroscopy," Opt. Commun. **283**(5), 681–694 (2010).
28. D. A. Steck, "Cesium D Line Data," Available online at http://steck.us/alkalidata (revision 2.2.1, 21 November 2019).
29. W. Wasilewski, T. Fernholz, K. Jensen, L. S. Madsen, H. Krauter, C. Muschik, and E. S. Polzik, "Generation of two-mode squeezed and entangled light in a single temporal and spatial mode," Opt. Express **17**(16), 14444–14457 (2009).
30. T. Holstein and H. Primakoff, "Field dependence of the intrinsic domain magnetization of a ferromagnet," Phys. Rev. **58**(12), 1098–1113 (1940).
31. C. A. Muschik, E. S. Polzik, and J. I. Cirac, "Dissipatively driven entanglement of two macroscopic atomic ensembles," Phys. Rev. A **83**(5), 052312 (2011).
32. M. Aspelmeyer, T. J. Kippenberg, and F. Marquardt, "Cavity optomechanics," Rev. Mod. Phys. **86**(4), 1391–1452 (2014).
33. D. V. Vasilyev, K. Hammerer, N. Korolev, and A. S. Sørensen, "Quantum noise for faraday light–matter interfaces," J. Phys. B: At., Mol. Opt. Phys. **45**(12), 124007 (2012).
34. K. Jensen, "Quantum information, entanglement and magnetometry with macroscopic gas samples and non-classical light," Ph.D. thesis, University of Copenhagen (2011).

35. N. Sekiguchi and A. Hatakeyama, "Non-negligible collisions of alkali atoms with background gas in buffer-gas-free cells coated with paraffin," Appl. Phys. B **122**(4), 81 (2016).
36. A. Hatakeyama, T. Kuroda, N. Sekiguchi, and K. Ishikawa, "Analysis of background gas in an alkali-metal vapor cell coated with paraffin," Appl. Phys. B **125**(7), 133 (2019).
37. Y. Tang, Y. Wen, L. Cai, and K. Zhao, "Spin-noise spectrum of hot vapor atoms in an anti-relaxation-coated cell," Phys. Rev. A **101**(1), 013821 (2020).
38. S. N. Atutov, F. A. Benimetskiy, A. I. Plekhanov, V. A. Sorokin, and A. V. Yakovlev, "Diffusion of rb atoms in paraffin-coated resonant vapor cells," Eur. Phys. J. D **71**(1), 12 (2017).
39. M. Parniak and W. Wasilewski, "Direct observation of atomic diffusion in warm rubidium ensembles," Appl. Phys. B **116**(2), 415–421 (2014).
40. V. G. Lucivero, N. D. McDonough, N. Dural, and M. V. Romalis, "Correlation function of spin noise due to atomic diffusion," Phys. Rev. A **96**(6), 062702 (2017).
41. M. V. Balabas, K. Jensen, W. Wasilewski, H. Krauter, L. S. Madsen, J. H. Müller, T. Fernholz, and E. S. Polzik, "High quality anti-relaxation coating material for alkali atom vapor cells," Opt. Express **18**(6), 5825–5830 (2010).
42. G. Agarwal and S. Chaturvedi, "Scheme to measure quantum stokes parameters and their fluctuations and correlations," J. Mod. Opt. **50**(5), 711–716 (2003).
43. B. Julsgaard, J. Sherson, J. L. Sørensen, and E. S. Polzik, "Characterizing the spin state of an atomic ensemble using the magneto-optical resonance method," J. Opt. B: Quantum Semiclassical Opt. **6**(1), 5–14 (2004).
44. K. Jensen, V. M. Acosta, J. M. Higbie, M. P. Ledbetter, S. M. Rochester, and D. Budker, "Cancellation of nonlinear zeeman shifts with light shifts," Phys. Rev. A **79**(2), 023406 (2009).
45. M. Newville, R. Otten, A. Nelson, A. Ingargiola, T. Stensitzki, D. Allan, A. Fox, F. Carter, Michał, D. Pustakhod, lneuhaus, S. Weigand, R. Osborn, Glenn, C. Deil, Mark, A. L. R. Hansen, G. Pasquevich, L. Foks, N. Zobrist, O. Frost, A. Beelen, Stuermer, kwertyops, A. Polloreno, S. Caldwell, A. Almarza, A. Persaud, B. Gamari, and B. F. Maier, "LMFIT: Non-Linear Least-Square Minimization and Curve-Fitting for Python," https://zenodo.org/record/4516651 (2021).
46. D. Foreman-Mackey, D. W. Hogg, D. Lang, and J. Goodman, "emcee: The MCMC hammer," Publ. Astron. Soc. Pac. **125**(925), 306–312 (2013).
47. R. Thomas, "Optical spin-mechanics quantum interface: entanglement and back-action evasion," PhD dissertation, University of Copenhagen (2020).
48. G. Colangelo, R. J. Sewell, N. Behbood, F. M. Ciurana, G. Triginer, and M. W. Mitchell, "Quantum atom–light interfaces in the gaussian description for spin-1 systems," New J. Phys. **15**(10), 103007 (2013).

Bibliography

[Appelt et al., 1998] Appelt, S., Baranga, A. B.-A., Erickson, C. J., Romalis, M. V., Young, A. R., and Happer, W. (1998). Theory of spin-exchange optical pumping of ^{3}He and ^{129}Xe. *Phys. Rev. A*, 58:1412–1439.

[Arute et al., 2019] Arute, F., Arya, K., Babbush, R., Bacon, D., Bardin, J. C., Barends, R., Biswas, R., Boixo, S., Brandao, F. G. S. L., Buell, D. A., Burkett, B., Chen, Y., Chen, Z., Chiaro, B., Collins, R., Courtney, W., Dunsworth, A., Farhi, E., Foxen, B., Fowler, A., Gidney, C., Giustina, M., Graff, R., Guerin, K., Habegger, S., Harrigan, M. P., Hartmann, M. J., Ho, A., Hoffmann, M., Huang, T., Humble, T. S., Isakov, S. V., Jeffrey, E., Jiang, Z., Kafri, D., Kechedzhi, K., Kelly, J., Klimov, P. V., Knysh, S., Korotkov, A., Kostritsa, F., Landhuis, D., Lindmark, M., Lucero, E., Lyakh, D., Mandrà, S., McClean, J. R., McEwen, M., Megrant, A., Mi, X., Michielsen, K., Mohseni, M., Mutus, J., Naaman, O., Neeley, M., Neill, C., Niu, M. Y., Ostby, E., Petukhov, A., Platt, J. C., Quintana, C., Rieffel, E. G., Roushan, P., Rubin, N. C., Sank, D., Satzinger, K. J., Smelyanskiy, V., Sung, K. J., Trevithick, M. D., Vainsencher, A., Villalonga, B., White, T., Yao, Z. J., Yeh, P., Zalcman, A., Neven, H., and Martinis, J. M. (2019). Quantum supremacy using a programmable superconducting processor. *Nature*, 574(7779):505–510.

[Aspect et al., 1981] Aspect, A., Grangier, P., and Roger, G. (1981). Experimental tests of realistic local theories via bell's theorem. *Phys. Rev. Lett.*, 47:460–463.

[Aspect et al., 1982] Aspect, A., Grangier, P., and Roger, G. (1982). Experimental realization of einstein-podolsky-rosen-bohm gedankenexperiment: A new violation of bell's inequalities. *Phys. Rev. Lett.*, 49:91–94.

[Aspelmeyer et al., 2014] Aspelmeyer, M., Kippenberg, T. J., and Marquardt, F. (2014). Cavity optomechanics. *Rev. Mod. Phys.*, 86:1391–1452.

[Balabas et al., 2010] Balabas, M. V., Karaulanov, T., Ledbetter, M. P., and Budker, D. (2010). Polarized alkali-metal vapor with minute-long transverse spin-relaxation time. *Phys. Rev. Lett.*, 105:070801.

[Bao et al., 2020] Bao, H., Duan, J., Jin, S., Lu, X., Li, P., Qu, W., Wang, M., Novikova, I., Mikhailov, E. E., Zhao, K.-F., Mølmer, K., Shen, H., and Xiao, Y. (2020). Spin squeezing of 1011 atoms by prediction and retrodiction measurements. *Nature*, 581(7807):159–163.

[Bayram et al., 2018] Bayram, M., Partal, T., and Buyukoz, G. O. (2018). Numerical methods for simulation of stochastic differential equations. *Advances in Difference Equations*, 2018(1).

[Bell, 1964] Bell, J. S. (1964). On the einstein podolsky rosen paradox. *Physics Physique Fizika*, 1:195–200.

[Bennett et al., 1993] Bennett, C. H., Brassard, G., Crépeau, C., Jozsa, R., Peres, A., and Wootters, W. K. (1993). Teleporting an unknown quantum state via dual classical and einstein-podolsky-rosen channels. *Phys. Rev. Lett.*, 70:1895–1899.

[Bernien et al., 2017] Bernien, H., Schwartz, S., Keesling, A., Levine, H., Omran, A., Pichler, H., Choi, S., Zibrov, A. S., Endres, M., Greiner, M., Vuletić, V., and Lukin, M. D. (2017). Probing many-body dynamics on a 51-atom quantum simulator. *Nature*, 551(7682):579–584.

[Black, 2001] Black, E. D. (2001). An introduction to pound–drever–hall laser frequency stabilization. *American Journal of Physics*, 69(1):79–87.

[Borregaard et al., 2016] Borregaard, J., Zugenmaier, M., Petersen, J. M., Shen, H., Vasilakis, G., Jensen, K., Polzik, E. S., and Sørensen, A. S. (2016). Scalable photonic network architecture based on motional averaging in room temperature gas. *Nature Communications*, 7(1).

[Bouwmeester et al., 1997] Bouwmeester, D., Pan, J.-W., Mattle, K., Eibl, M., Weinfurter, H., and Zeilinger, A. (1997). Experimental quantum teleportation. *Nature*, 390(6660):575–579.

[Braginskiĭ et al., 1970] Braginskiĭ, V. B., Manukin, A. B., and Tikhonov, M. Y. (1970). Investigation of Dissipative Ponderomotive Effects of Electromagnetic Radiation. *Soviet Journal of Experimental and Theoretical Physics*, 31:829.

[Braginsky and Manukin, 1967] Braginsky, V. B. and Manukin, A. B. (1967). Ponderomotive Effects of Electromagnetic Radiation. *Soviet Physics Journal of Experimental and Theoretical Physics*, 52:986+.

[Braginsky et al., 1980] Braginsky, V. B., Vorontsov, Y. I., and Thorne, K. S. (1980). Quantum nondemolition measurements. *Science*, 209(4456):547–557.

[Braunstein and Kimble, 1998] Braunstein, S. L. and Kimble, H. J. (1998). Teleportation of continuous quantum variables. *Phys. Rev. Lett.*, 80:869–872.

[Bærentsen et al., 2023] Bærentsen, C., Fedorov, S. A., Østfeldt, C., Balabas, M. V., Zeuthen, E., and Polzik, E. S. (2023). Squeezed light from an oscillator measured at the rate of oscillation.

[Cao et al., 2020] Cao, M., Hoffet, F., Qiu, S., Sheremet, A. S., and Laurat, J. (2020). Efficient reversible entanglement transfer between light and quantum memories. *Optica*, 7(10):1440–1444.

[Chan et al., 2011] Chan, J., Alegre, T. P. M., Safavi-Naeini, A. H., Hill, J. T., Krause, A., Gröblacher, S., Aspelmeyer, M., and Painter, O. (2011). Laser cooling of a nanomechanical oscillator into its quantum ground state. *Nature*, 478(7367):89–92.

[Corsini et al., 2013] Corsini, E. P., Karaulanov, T., Balabas, M., and Budker, D. (2013). Hyperfine frequency shift and zeeman relaxation in alkali-metal-vapor cells with antirelaxation alkene coating. *Phys. Rev. A*, 87:022901.

[Dang et al., 2010] Dang, H. B., Maloof, A. C., and Romalis, M. V. (2010). Ultrahigh sensitivity magnetic field and magnetization measurements with an atomic magnetometer. *Applied Physics Letters*, 97(15):151110.

[Dean, 1996] Dean, D. S. (1996). Langevin equation for the density of a system of interacting langevin processes. *Journal of Physics A: Mathematical and General*, 29(24):L613.

[Deutsch and Jessen, 2010] Deutsch, I. H. and Jessen, P. S. (2010). Quantum control and measurement of atomic spins in polarization spectroscopy. *Optics Communications*, 283(5):681–694.

[Dideriksen, 2021] Dideriksen, K. B. (2021). *A room-temperature single-photon source with built-in memory.* PhD thesis, University of Copenhagen.

[Dideriksen et al., 2021] Dideriksen, K. B., Schmieg, R., Zugenmaier, M., and Polzik, E. S. (2021). Room-temperature single-photon source with near-millisecond built-in memory. *Nature Communications*, 12(1).

[Dowling and Milburn, 2003] Dowling, J. P. and Milburn, G. J. (2003). Quantum technology: the second quantum revolution. *Philosophical Transactions of the Royal Society of London. Series A: Mathematical, Physical and Engineering Sciences*, 361(1809):1655–1674.

[Duan et al., 2000] Duan, L.-M., Giedke, G., Cirac, J. I., and Zoller, P. (2000). Inseparability criterion for continuous variable systems. *Phys. Rev. Lett.*, 84:2722–2725.

[Ebadi et al., 2021] Ebadi, S., Wang, T. T., Levine, H., Keesling, A., Semeghini, G., Omran, A., Bluvstein, D., Samajdar, R., Pichler, H., Ho, W. W., Choi, S., Sachdev, S., Greiner, M., Vuletić, V., and Lukin, M. D. (2021). Quantum phases of matter on a 256-atom programmable quantum simulator. *Nature*, 595(7866):227–232.

[Einstein et al., 1935] Einstein, A., Podolsky, B., and Rosen, N. (1935). Can quantum-mechanical description of physical reality be considered complete? *Phys. Rev.*, 47:777–780.

[Eksmaoptics-manual, 2023] Eksmaoptics-manual (2023). GAUSS-TO-TOP-HAT BEAM SHAPING LENS – GTH-3.6-1.75FA. `https://eksmaoptics.com/out/media/EKSMA_Optics_Gauss_Top_Hat_Lenses_GTH-3.6-1.75FA.pdf`. [Online; accessed 27-March-2023].

[Enzian et al., 2022] Enzian, G., Wang, Z., Simonsen, A., Mathiassen, J., Vibel, T., Tsaturyan, Y., Tagantsev, A., Schliesser, A., and Polzik, E. S. (2022). Phononically shielded photonic-crystal mirror membranes for cavity quantum optomechanics.

[Fedorov and Zeuthen, 2023] Fedorov, S. A. and Zeuthen, E. (2023). Prediction-retrodiction measurements for teleportation and conditional state transfer.

[Fiaschi et al., 2021] Fiaschi, N., Hensen, B., Wallucks, A., Benevides, R., Li, J., Alegre, T. P. M., and Gröblacher, S. (2021). Optomechanical quantum teleportation. *Nature Photonics*, 15(11):817–821.

[Greenwood, 2002] Greenwood, J. (2002). The correct and incorrect generation of a cosine distribution of scattered particles for monte-carlo modelling of vacuum systems. *Vacuum*, 67(2):217–222.

[Hammerer et al., 2009] Hammerer, K., Aspelmeyer, M., Polzik, E. S., and Zoller, P. (2009). Establishing einstein-poldosky-rosen channels between nanomechanics and atomic ensembles. *Phys. Rev. Lett.*, 102:020501.

[Harris et al., 2006] Harris, M. L., Adams, C. S., Cornish, S. L., McLeod, I. C., Tarleton, E., and Hughes, I. G. (2006). Polarization spectroscopy in rubidium and cesium. *Phys. Rev. A*, 73:062509.

[Hensen et al., 2015] Hensen, B., Bernien, H., Dréau, A. E., Reiserer, A., Kalb, N., Blok, M. S., Ruitenberg, J., Vermeulen, R. F. L., Schouten, R. N., Abellán, C., Amaya, W., Pruneri, V., Mitchell, M. W., Markham, M., Twitchen, D. J., Elkouss, D., Wehner, S., Taminiau, T. H., and Hanson, R. (2015). Loophole-free bell inequality violation using electron spins separated by 1.3 kilometres. *Nature*, 526(7575):682–686.

[Holstein and Primakoff, 1940] Holstein, T. and Primakoff, H. (1940). Field dependence of the intrinsic domain magnetization of a ferromagnet. *Phys. Rev.*, 58:1098–1113.

[Huang et al., 2019] Huang, X., Zeuthen, E., Gong, Q., and He, Q. (2019). Engineering asymmetric steady-state einstein-podolsky-rosen steering in macroscopic hybrid systems. *Phys. Rev. A*, 100:012318.

[Huang et al., 2018] Huang, X., Zeuthen, E., Vasilyev, D. V., He, Q., Hammerer, K., and Polzik, E. S. (2018). Unconditional steady-state entanglement in macroscopic hybrid systems by coherent noise cancellation. *Phys. Rev. Lett.*, 121:103602.

[Julsgaard, 2003] Julsgaard, B. (2003). *Entanglement and Quantum Interactions with Macroscopic Gas Samples*. PhD thesis, University of Copenhagen.

[Julsgaard et al., 2001] Julsgaard, B., Kozhekin, A., and Polzik, E. S. (2001). Experimental long-lived entanglement of two macroscopic objects. *Nature*, 413(6854):400–403.

[Julsgaard et al., 2004] Julsgaard, B., Sherson, J., Cirac, J. I., Fiurášek, J., and Polzik, E. S. (2004). Experimental demonstration of quantum memory for light. *Nature*, 432(7016):482–486.

[Julsgaard et al., 2003] Julsgaard, B., Sherson, J., Sørensen, J. L., and Polzik, E. S. (2003). Characterizing the spin state of an atomic ensemble using the magneto-optical resonance method. *Journal of Optics B: Quantum and Semiclassical Optics*, 6(1):5.

[Kepler, 1619] Kepler, J. (1619). *De cometis libelli tres ...* De cometis libelli tres. Typis Andreæ Apergeri, sumptibus Sebastiani Mylii bibliopolæ Augustani.

[Khalili and Polzik, 2018] Khalili, F. Y. and Polzik, E. S. (2018). Overcoming the standard quantum limit in gravitational wave detectors using spin systems with a negative effective mass. *Phys. Rev. Lett.*, 121:031101.

[Kimble, 1998] Kimble, H. J. (1998). Strong interactions of single atoms and photons in cavity qed. *Physica Scripta*, 1998(T76):127.

[Kimble, 2008] Kimble, H. J. (2008). The quantum internet. *Nature*, 453(7198):1023–1030.

[Kirschvink, 1992] Kirschvink, J. L. (1992). Uniform magnetic fields and double-wrapped coil systems: Improved techniques for the design of bioelectromagnetic experiments. *Bioelectromagnetics*, 13(5):401–411.

[Knudsen, 1967] Knudsen, M. (1967). The cosine law in the kinetic theory of gases.

[Kozhekin et al., 2000] Kozhekin, A. E., Mølmer, K., and Polzik, E. (2000). Quantum memory for light. *Phys. Rev. A*, 62:033809.

[Krauter et al., 2013] Krauter, H., Salart, D., Muschik, C. A., Petersen, J. M., Shen, H., Fernholz, T., and Polzik, E. S. (2013). Deterministic quantum teleportation between distant atomic objects. *Nature Physics*, 9(7):400–404.

[Kurizki et al., 2015] Kurizki, G., Bertet, P., Kubo, Y., Mølmer, K., Petrosyan, D., Rabl, P., and Schmiedmayer, J. (2015). Quantum technologies with hybrid systems. *Proceedings of the National Academy of Sciences*, 112(13):3866–3873.

[Kuzmich et al., 1998] Kuzmich, A., Bigelow, N. P., and Mandel, L. (1998). Atomic quantum non-demolition measurements and squeezing. *Europhysics Letters*, 42(5):481.

[Kuzmich et al., 1997] Kuzmich, A., Mølmer, K., and Polzik, E. S. (1997). Spin squeezing in an ensemble of atoms illuminated with squeezed light. *Phys. Rev. Lett.*, 79:4782–4785.

[Madsen et al., 2022] Madsen, L. S., Laudenbach, F., Askarani, M. F., Rortais, F., Vincent, T., Bulmer, J. F. F., Miatto, F. M., Neuhaus, L., Helt, L. G., Collins, M. J., Lita, A. E., Gerrits, T., Nam, S. W., Vaidya, V. D., Menotti, M., Dhand, I., Vernon, Z., Quesada, N., and Lavoie, J. (2022). Quantum computational advantage with a programmable photonic processor. *Nature*, 606(7912):75–81.

[Mathiassen, 2019] Mathiassen, J. B. (2019). Characterising and modelling thermal substrate noise for a membrane in the middle optomechanical cavity. Master's thesis, University of Copenhagen.

[Meng et al., 2020] Meng, C., Brawley, G. A., Bennett, J. S., Vanner, M. R., and Bowen, W. P. (2020). Mechanical squeezing via fast continuous measurement. *Phys. Rev. Lett.*, 125:043604.

[Mielec et al., 2018] Mielec, N., Altorio, M., Sapam, R., Horville, D., Holleville, D., Sidorenkov, L. A., Landragin, A., and Geiger, R. (2018). Atom interferometry with top-hat laser beams. *Applied Physics Letters*, 113(16):161108.

[Mirhosseini et al., 2020] Mirhosseini, M., Sipahigil, A., Kalaee, M., and Painter, O. (2020). Superconducting qubit to optical photon transduction. *Nature*, 588(7839):599–603.

[Møller et al., 2017] Møller, C. B., Thomas, R. A., Vasilakis, G., Zeuthen, E., Tsaturyan, Y., Balabas, M., Jensen, K., Schliesser, A., Hammerer, K., and Polzik, E. S. (2017). Quantum back-action-evading measurement of motion in a negative mass reference frame. *Nature*, 547(7662):191–195.

[Møller, 2018] Møller, C. B. (2018). *Quantum Back-Action Evasion in a Hybrid Spin-Optomechanical System*. PhD thesis, University of Copenhagen.

[Newell and Tiesinga, 2019] Newell, D. and Tiesinga, E. (2019). The international system of units (si), 2019 edition.

[Nielsen, 2016] Nielsen, W. H. P. (2016). *Qantum cavity optomechanics with phononic bandgap shielded silicon nitride membranes*. PhD thesis, University of Copenhagen.

[Pearman et al., 2002] Pearman, C. P., Adams, C. S., Cox, S. G., Griffin, P. F., Smith, D. A., and Hughes, I. G. (2002). Polarization spectroscopy of a closed atomic transition: applications to laser frequency locking. *Journal of Physics B: Atomic, Molecular and Optical Physics*, 35(24):5141.

[Pirkkalainen et al., 2015] Pirkkalainen, J.-M., Damskägg, E., Brandt, M., Massel, F., and Sillanpää, M. A. (2015). Squeezing of quantum noise of motion in a micromechanical resonator. *Phys. Rev. Lett.*, 115:243601.

[Polzik and Hammerer, 2015] Polzik, E. S. and Hammerer, K. (2015). Trajectories without quantum uncertainties. *Annalen der Physik*, 527(1-2):A15–A20.

[Purdy et al., 2013] Purdy, T. P., Yu, P.-L., Peterson, R. W., Kampel, N. S., and Regal, C. A. (2013). Strong optomechanical squeezing of light. *Phys. Rev. X*, 3:031012.

[Savukov and Romalis, 2005] Savukov, I. M. and Romalis, M. V. (2005). Effects of spin-exchange collisions in a high-density alkali-metal vapor in low magnetic fields. *Phys. Rev. A*, 71:023405.

[Schmieg, 2018] Schmieg, R. (2018). *Coherent dynamics of atomic vapors*. Project report, University of Copenhagen.

[Schmieg, 2019] Schmieg, R. (2019). Observation of non-classical photon pairs from roomtemperature atomic ensembles through suppression of four-wave mixing and classical noise sources. Master's thesis, University of Copenhagen.

[Schmieg, 2023] Schmieg, R. (2023). *Room-temperature spin-oscillators for quantum information technologies*. PhD thesis, University of Copenhagen.

[Schroeder, 2014] Schroeder, D. V. (2014). *An introduction to thermall physics*. Person education limited.

[Sekiguchi and Hatakeyama, 2016] Sekiguchi, N. and Hatakeyama, A. (2016). Non-negligible collisions of alkali atoms with background gas in buffer-gas-free cells coated with paraffin. *Applied Physics B*, 122(4).

[Sekiguchi et al., 2018] Sekiguchi, N., Hatakeyama, A., Okuma, K., and Usui, H. (2018). Scattering of an alkali-metal atomic beam on anti-spin-relaxation coatings. *Phys. Rev. A*, 98:042709.

[Shaham et al., 2020] Shaham, R., Katz, O., and Firstenberg, O. (2020). Quantum dynamics of collective spin states in a thermal gas. *Phys. Rev. A*, 102:012822.

[Sherson et al., 2006] Sherson, J. F., Krauter, H., Olsson, R. K., Julsgaard, B., Hammerer, K., Cirac, I., and Polzik, E. S. (2006). Quantum teleportation between light and matter. *Nature*, 443(7111):557–560.

[Steck, 1998] Steck, D. A. (1998). Cesium D Line Data. available online at `http://steck.us/alkalidata` (revision 2.2.1, 21 November 2019).

[Thiel et al., 2007] Thiel, F., Schnabel, A., Knappe-Grüneberg, S., Stollfuß, D., and Burghoff, M. (2007). Demagnetization of magnetically shielded rooms. *Review of Scientific Instruments*, 78(3):035106.

[Thomas, 2020] Thomas, R. A. (2020). *Optical spin-mechanics quantum interface: entanglement and back-action evasion*. PhD thesis, University of Copenhagen.

[Thomas et al., 2021] Thomas, R. A., Østfeldt, C., Bærentsen, C., Parniak, M., and Polzik, E. S. (2021). Calibration of spin-light coupling by coherently induced faraday rotation. *Opt. Express*, 29(15):23637–23653.

[Thomas et al., 2020] Thomas, R. A., Parniak, M., Østfeldt, C., Møller, C. B., Bærentsen, C., Tsaturyan, Y., Schliesser, A., Appel, J., Zeuthen, E., and Polzik, E. S. (2020). Entanglement between distant macroscopic mechanical and spin systems. *Nature Physics*, 17(2):228–233.

[Tsaturyan, 2019] Tsaturyan, Y. (2019). *Ultracoherent soft-clamped mechanical resonators for quantum cavity optomechanics.* PhD thesis, University of Copenhagen.

[Tsaturyan et al., 2017] Tsaturyan, Y., Barg, A., Polzik, E. S., and Schliesser, A. (2017). Ultracoherent nanomechanical resonators via soft clamping and dissipation dilution. *Nature Nanotechnology*, 12(8):776–783.

[Vahlbruch et al., 2016] Vahlbruch, H., Mehmet, M., Danzmann, K., and Schnabel, R. (2016). Detection of 15 db squeezed states of light and their application for the absolute calibration of photoelectric quantum efficiency. *Phys. Rev. Lett.*, 117:110801.

[Vasilakis et al., 2015] Vasilakis, G., Shen, H., Jensen, K., Balabas, M., Salart, D., Chen, B., and Polzik, E. S. (2015). Generation of a squeezed state of an oscillator by stroboscopic back-action-evading measurement. *Nature Physics*, 11(5):389–392.

[Vasilyev et al., 2013] Vasilyev, D. V., Muschik, C. A., and Hammerer, K. (2013). Dissipative versus conditional generation of gaussian entanglement and spin squeezing. *Phys. Rev. A*, 87:053820.

[Wasilewski et al., 2010] Wasilewski, W., Jensen, K., Krauter, H., Renema, J. J., Balabas, M. V., and Polzik, E. S. (2010). Quantum noise limited and entanglement-assisted magnetometry. *Phys. Rev. Lett.*, 104:133601.

[Wehner et al., 2018] Wehner, S., Elkouss, D., and Hanson, R. (2018). Quantum internet: A vision for the road ahead. *Science*, 362(6412):eaam9288.

[Weis et al., 2010] Weis, S., Rivière, R., Deléglise, S., Gavartin, E., Arcizet, O., Schliesser, A., and Kippenberg, T. J. (2010). Optomechanically induced transparency. *Science*, 330(6010):1520–1523.

[Wiener, 1964] Wiener, N. (1964). *Extrapolation, Interpolation, and Smoothing of Stationary Time Series: With Engineering Applications.* Massachusetts Institute of Technology : Paperback series. M.I.T. Press.

[Wiseman and Milburn, 2009] Wiseman, H. M. and Milburn, G. J. (2009). *Quantum Measurement and Control.* Cambridge University Press, Cambridge.

[Wollman et al., 2015] Wollman, E. E., Lei, C. U., Weinstein, A. J., Suh, J., Kronwald, A., Marquardt, F., Clerk, A. A., and Schwab, K. C. (2015). Quantum squeezing of motion in a mechanical resonator. *Science*, 349(6251):952–955.

[Yde, 2020] Yde, R. (2020). Room temperature spin ensembles for precision measurements. Master's thesis, University of Copenhagen.

[Zeuthen et al., 2019] Zeuthen, E., Polzik, E. S., and Khalili, F. Y. (2019). Gravitational wave detection beyond the standard quantum limit using a negative-mass spin system and virtual rigidity. *Phys. Rev. D*, 100:062004.

[Zheng et al., 2023] Zheng, W., Wang, H., Schmieg, R., Oesterle, A., and Polzik, E. S. (2023). Entanglement-enhanced magnetic induction tomography.

[Zwettler, 2019] Zwettler, T. (2019). Suppression of heating mechanisms for deep optomechanical ground-state cooling. Master's thesis, University of Copenhagen.

[Østfeldt, 2022] Østfeldt, C. (2022). *Quantum optomechanics for hybrid spin–membrane entanglement*. PhD thesis, University of Copenhagen.